Exploration of Metal–Organic Framework Phase Formation and Design

by

Derek Robert Du Bois

A dissertation submitted in partial fulfillment
of the requirements for the degree of
Doctor of Philosophy
(Chemistry)
in the University of Michigan
2023

Doctoral Committee:

Professor Adam J. Matzger, Chair
Assistant Professor Tim A. Cernak
Professor Zhan Chen
Professor Anne J. McNeil

Derek R. Du Bois

duboisd@umich.edu

ORCID iD: 0000-0002-1966-1437

Dedication

For Jim and Amber. The impact of having people who believe in you and push you to become better is impossible to quantify. These are two people who helped me start.

Acknowledgements

Professor Matzger has provided meaningful mentorship and ample opportunity to grow while in graduate school. I believe him to be the best boss I've ever had. I am especially grateful for opportunities to experience independent research, grant writing, collaboration, and leadership. Where it counts and when it has counted, Professor Matzger has always provided meaningful and material support that has enabled me to achieve *my* goals as a graduate student. I cannot overstate the value of his contribution in my development as a scientist.

My committee includes Professor Anne J. McNeil, Professor Zhan Chen, and Associate Professor Tim A. Cernak. My academic committee has provided their time, engagement, and advice on my project over multiple meetings, both within the structure of the department requirements and outside of it. Thank you for taking an interest in my research and my development.

I learned research skills under Dr. Hyunjun Yang in the laboratory of Professor Nowick. Both still show investment and interest in my development as a scientist. When people demonstrate continued commitment towards your journey, those are people deserving of appreciation and praise. Thank you, Dr. Yang and Professor Nowick.

There are many reasons to thank my laboratory coworkers/friends. From them, I have received specific research advice and learned research skills. They have contributed their perspectives on life and have provided emotional support. I have made friendships which will hopefully last beyond my time as a graduate student. I want to

highlight three coworkers: Dr. Leila Foroughi who has been so supportive to me as a person; Dr. Ren Wiscons who was my first role model as a researcher in the Matzger laboratory; and Dr. Mike Bellas whose opinions on research I value and trust.

I am truly lucky to have many long-lasting friendships. I wouldn't be here without my friends. I wouldn't be this version of me without the care and support they have provided. I have learned so much from the people I have had the joy to build relationships with. I credit my friends who have been my emotional rock and have taught me how to be a better person. Thank you to too many of you.

I want to thank my Father and my Stepmother. My Father raised me and struggled with me, pretty much an explosively dangerous child. To survive with me for 18 years while I fought him on everything is not easy. I am grateful for his patience and his continued support both materially and in trying to guide me towards a meaningful life. Nancy, my Stepmother, has been a role model for me. She is a powerhouse whose work ethic has never been matched by anyone I have met. On top of this, she has provided me unconditional love and affection. She has been my cheerleader through it all.

A couple lines for Jean, my therapist. I am intense, willful, and combative. Patiently, you have been there for me through it all. Thank you. Thank you...

Usually, in considering the important people, I am thinking of people who I have known for years. Steph, you've had an outsized impact for the brevity of time.

There are more people I am thankful for, many, many more. A person is not an island. We are grown and supported by many hands. Thank you, all of you.

My last thank you goes to Amber for being my role model and friend for years when I perceived I had none.

Table of Contents

List of Tables

List of Figures

List of Appendices

Abstract

Metal–organic frameworks (MOFs) are a class of porous materials comprised of metal, often in the form of metal–acetate clusters, and organic linker which form 3-dimensional crystalline structures featuring tantalizing porosity comfortably ranging the micro- and mesoscale as well as record-breaking surface area. For MOFs, an abundance of applications has been proposed to leverage their coveted properties including as battery materials for energy storage, as the solid phase for separations, and as the either the catalyst support or the catalytically active material in catalysis. Despite having desirable properties, industrial applications remain limited due to obstacles such as material stability and scaleup. Fundamental studies of MOF formation and design provide direct answers to some of these obstacles; an example: seeded MOF synthesis can be used to overcome synthesis limitations at high concentrations of metal and linker. This dissertation centers phase formation in MOFs.

Chapter 2 provides a mechanism for MOF-74 formation which employs a linker that coordinates via carboxylate *and* oxo moieties. MOFs which form from multiple coordination types to the linker were previously not investigated from a mechanism of formation perspective. Metastable phases which exclusively employ carboxylate coordination form before MOF-74, with dissolution of the metastable phase and redeposition of the MOF phase being the mechanism by which the MOF forms. The literature contains diverse examples of MOF formation deviating from classical nucleation

theory. Acknowledging this diversity, understanding MOF formation will enable more robust phase selection, an understanding of defect modes, and improved manufacturability.

Chapter 3 demonstrates a seeding methodology employed to increase expression of MOF phases at high synthesis concentrations of metal and linker which normally thwart MOF formation. Industrial scaleup of MOF synthesis will likely require similar input as process chemistry does in the industrial setting. A diversity of synthesis tools will benefit efforts in helping MOFs achieve industrial relevance. Seeding is commonly leveraged in pharmaceutical research but rarely applied to MOFs. Using MOF seeds to direct the formation the desired MOF phase, enabled much greater expression of the desired MOF phase than in conditions that did not employ the seeding methodology. Four MOF systems, employing a variety of linker and secondary building unit types, were investigated for seeding methodology. Three of four MOFs responded to seeding, and it was observed that seed dissolution prevented phase direction for SNU-70 synthesis. This chapter demonstrates that seeding can be applied to phase direct for desired MOF formation and provides a framework through which MOF synthesis can be optimized for reduced solvent waste.

Chapter 4 details phase distribution as a result of postsynthetic modification, a covalent method applied to modify MOFs at the linker. As a linker is modified, the resultant material is differentiated from the original MOF, thus delineating it as a separate phase. Before the research in this chapter, it was unknown whether covalent modification of the framework would apply uniformly throughout the framework or localize at the shell before progressing towards functionalizing the whole MOF. Through a combination electron

microscopy, elemental analysis, and nuclear magnetic resonance spectroscopy, it was determined that reagent reactivity, predominately, and solvent choice affect the distribution of functionality after postsynthetic modification. Additionally, understanding the effect of reagent reactivity and solvent choice on the distribution of functionality within the MOF allows for design of MOFs with controlled distributions of functionality, ie. designed microstructure.

Taken together, the chapters described above center on phase formation in MOFs. Mechanistic insights into MOF-74 formation lend support to the idea that MOF formation deviates from classical nucleation theory in many cases. Seeding as applied to MOF synthesis enables control over phase expression even under high concentration conditions that normally undermine MOF formation. Postsynthetic modification enables control over microstructure in MOFs. As a result, MOFs can be created with delineated phases contained within a single crystal. The work described in this dissertation provides tools for MOF synthesis and modification which leverages the advancements to understanding MOF formation and modification also discussed in this dissertation.

Chapter 1: Introduction

1.1 Metal–Organic Frameworks: Identity, Properties, and Applications

Metal–organic frameworks (MOFs) are materials heavily investigated in hopes of leveraging sought after properties such as porosity and record-setting surface area for applications in fuel storage, catalysis, and separations, to name a few.[1] MOFs are comprised of organic linkers and metal, combining to form crystalline frameworks (Figure 1.1). Depending on the identity of the linker and the metal, MOF identity and properties can change drastically. Organic linkers and metal secondary building units (SBUs) will each have a quantity of points of connection which are often depicted as simplified shapes in cartoon representations or even crystal structures (Figure 1.1). Different combinations of metal and linker produce diverse materials which may be differentiated based on many factors including but not limited to the topicity of the components, the chemical moieties available for interaction, and the stability of the framework.

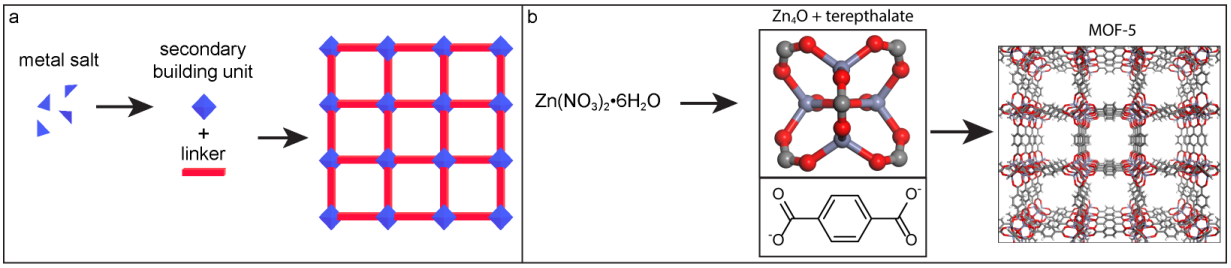

Figure 1.1 (a) Cartoon representation of MOF formation with (b) translation of cartoon to formation of MOF-5, where $Zn_4O(-COO)_6$ is shown coordinated to the carboxylate of the linker and, representing the SBU, and terepthalate is the linker.

1.2 MOF Formation

Research in the MOF field began ~25 years ago with the innovative and groundbreaking work of Professor Yaghi at Arizona State University,[2] although initial progress in the creation of what would later be called MOFs began with research conducted by Professor Robson at the University of Melbourne.[3,4] Since that time, many MOFs have been created, and while the umbrella term of MOF is adequate to describe these materials, the chemistry of each framework differs and demands nuanced attention before MOF formation can be adequately understood.[5] An examination of some iconic MOFs can provide context on how metal and linker choice can affect material properties. The most well-known MOF is MOF-5[6] which forms a cubic crystal structure from the combination of ditopic terepthalic acid and zinc nitrate hexahydrate which forms the octahedrally coordinating $Zn_4O(-COO)_6$ SBU in the MOF (Figure 1. top). The resulting material features intrinsic porosity which translates to high surface area: 3500 m^2/g. MOF-5 can function as a sorbent for fuel storage, a catalyst, or even as stationary phase for separations. One challenge that faces implementation of MOF-5 as a material for commercial application are concerns related to stability. It is known that MOF-5 material quality is reduced upon exposure to atmospheric water.[7] Such stability limitations are known, and enhancing the stability of these frameworks is a point of interest in the field.[8] Research focused on MOF-5, despite over 20 years of history, is ongoing, with exciting developments in drug delivery[9] and postsynthetic methodology[10–12] coming from the Matzger laboratory alone within the last few years. HKUST-1[13] is comprised of a tritopic linker, benzenetribenzoate, and a square planar coordinating SBU, known as a copper paddlewheel (Figure 1.2 bottom). The resulting material has a 'net topology' labeled **tbo**.

Features of the **tbo** framework include incorporation of multiple pore types and availability of the axial coordination sites on the copper paddlewheel to function as coordinatively unsaturated metal (CUS) sites after evacuating the framework of solvent in a process known as "activation". Stability of HKUST-1 is enhanced by the copper paddlewheel SBU which is known to be more stable against atmospheric water than $Zn_4O(–COO)_6$ SBUs, a desirable property in MOFs.[14]

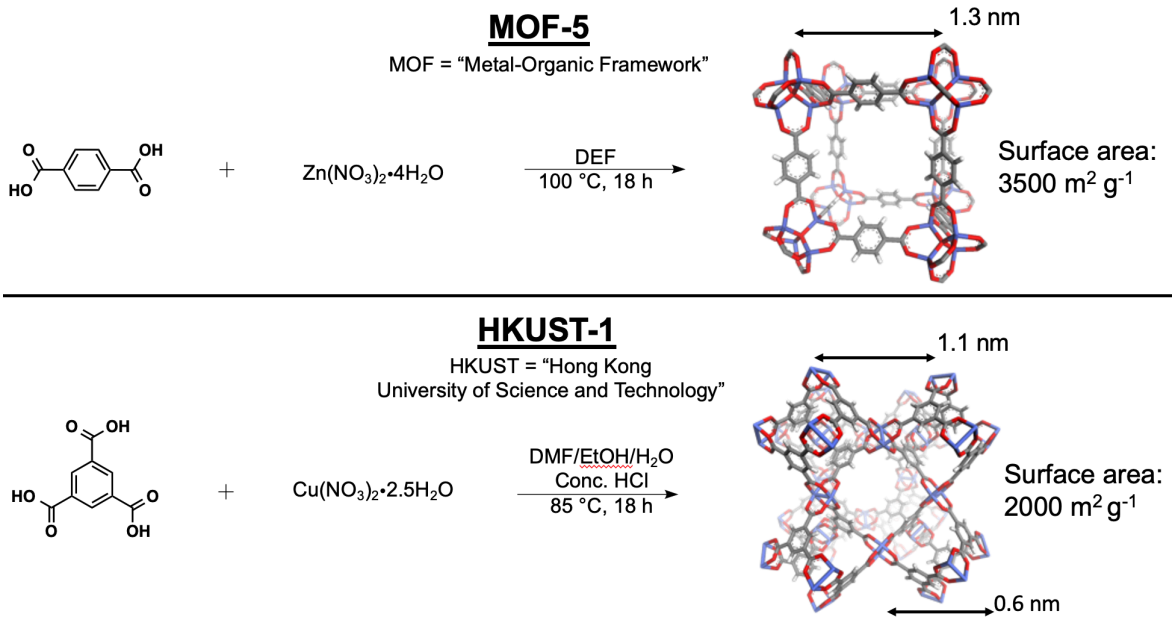

Figure 1.2 Examples of two iconic MOFs: MOF-5 and HKUST-1.

1.3 Challenges in MOF research

Despite having desirable properties, translating the material properties of MOFs into industrially relevant materials for applications remains a challenge. Industrial applications for MOFs remain limited,[15,16] and research in the field aims to overcome obstacles such as material instability/degradation,[17,18] storage capacity,[19,20] and limited scale-up of catalytic applications. Within each example above, there are more granular obstacles. In catalytic applications, for example, synthetic conditions must be compatible with the physical and chemical properties maintaining the integrity of the MOF.

Additionally, ensuring that catalysis employs the porosity of the MOF is relevant, and surface catalysis outside of the pores may thwart efforts to employ the porosity of the MOF to enable, for instance, size-selective catalysis. The quantity and complexity of challenges impeding widespread use of MOF technology remains daunting; however, over the course of ~25 years, the field has grown year-over-year and relevant applications appear within reach. Some fundamental insight into MOF production can help to contextualize how research bridges the gap between potential and actualized application.

MOF synthesis requires conditions that enable controlled production of coordinatively labile species which combine in a defined lattice to form the crystalline target. The most heavily employed method of MOF synthesis requires heat, making it a solvothermal synthesis. The solvent medium most commonly incorporates formamide solvents which slowly degrade *in situ* to form the base necessary to deprotonate the linker and enable formation of SBUs. However, MOF synthesis is not only the combination of linker and metal. The formation of crystals is a field of study[21] that requires consideration within the context of MOF formation. Since MOF formation incorporates elements of molecular synthesis in concert with crystal formation, the study of MOF synthesis has generated some surprising findings.[22–24] Classical nucleation theory describes crystal formation as being divided into the nucleation phase and the growth phase. The assumption is that increasing energy advantages from lattice formation and intermolecular interactions will gradually overcome any energy advantages as a solute. After this point, the crystal is free to grow. MOF crystal growth *may* follow the previously described trajectory, or it may follow a different path such as solid-to-solid transformation[25,26] or dissolution of an intermediate phase and redeposition of the desired

MOF phase.[27] Other MOF synthesis methods such as microwave synthesis or ball-mill synthesis have advantages and disadvantages to each and require careful consideration before employing them as an alternative to solvothermal synthesis.

Another, usually necessary, process employed in generating MOFs is activation, the process by which all guests are removed from the framework, enabling access to the porosity of the MOF (Figure 1.3 bottom). Unactivated MOFs may employ a process such as washing (removal of one solvent and addition of another or the same) to incorporate new guests into the framework or replace old guests within the framework (Figure 1.3 top). Often, washing and activation are both employed to yield MOFs which are more stable and retain less unwanted guests.[28,29] The Matzger laboratory has investigated methods of washing and activation,[17] concluding that care and deliberation go into the choosing the process through which a formed MOF must traverse before it is ready for application, whether that be for research or towards a practical implementation goal. Complications arise when considering phenomena common to MOFs such as framework instability[30] or the presence of CUS sites.[31] Evacuating a framework of guests generates empty space within the framework which is useful for applications such as fuel storage; however, the presence of solvent stabilizes MOFs, and framework instability can quickly result in collapse or reduced material quality. The solvents used for activation often feature low surface tension to reduce applied capillary forces to the framework during activation.[29] Fragile frameworks may even employ supercritical activation with CO_2 to overcome the associated capillary forces.[30] Alternatively, the presence of CUS sites may require more robust activation techniques which must, nonetheless, remain compatible with the overall stability of the framework.

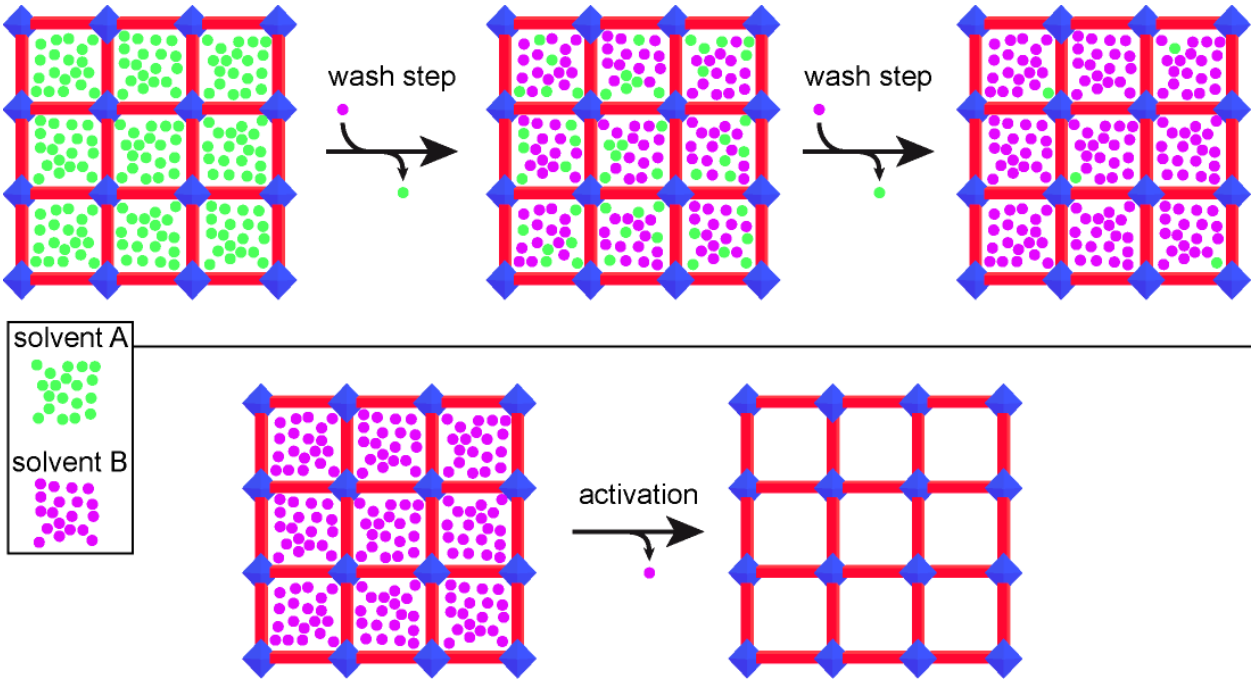

Figure 1.3 Cartoon representations of (top) washing solvent B replacing solvent A over multiple wash steps and (bottom) MOF activation.

MOF systems each have unique characteristics that govern which applications are achievable as well as what properties are limiting. Navigating the nuances of MOF chemistry requires broad understanding of chemistry, experimental experience working with MOF materials, and familiarity with the literature of the field. The methods of analysis which are commonly employed to characterize MOFs and assess their applications are discussed below.

1.4 Methods of analysis

Elucidating MOF properties and conducting research benefits from a suite of analytical techniques. Material properties of interest are tested in common ways, shared widely within the field. Surface area analysis is one of the most employed analyses for MOFs. The Brunauer–Emmett–Teller (BET) method is, as of this writing, the default for determining MOF surface areas.[32] Surface area in older publications may be conveyed

with an alternative "Langmuir" surface area. For these data, comparing the relative surface area between materials using the same surface area calculation method is of greater importance than understanding the theoretical differences between methods and deciding which to apply (the Langmuir method tends to overestimate true surface area). Sorption measurements are taken isothermally with measured gas uptake compared against pressure. The resulting sorption isotherm data (Figure 1.4 top) convey more information than just the surface area. Pore sizes can be calculated and observation of shape of the isotherm graph or hysteresis (inconsistency between the adsorptive and desorptive isotherm) can and do impact what conclusions may be drawn from the data (Figure 1.4 bottom). What does this data contribute to the field of MOF study? Applications of increased surface area may relate directly to increased capacity in fuel storage and selective capture of contaminants from mixtures (liquid or gas),[33] as examples.

BET surface area = 1680 m²/g
C constant = 5641.207
Correlation coefficient = 0.999999
BET fitting range = [0.0039, 0.0239]

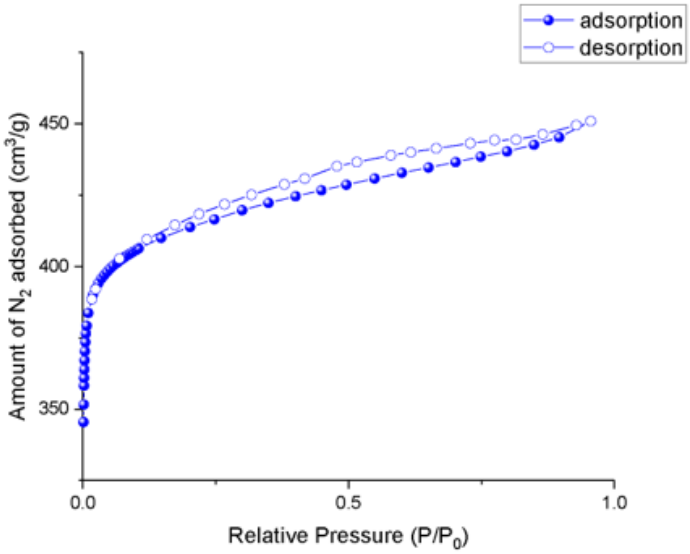

BET surface area = 173 m^2/g
C constant = 26.310
Correlation coefficient = 0.999934
BET fitting range = [0.048, 0.2978]

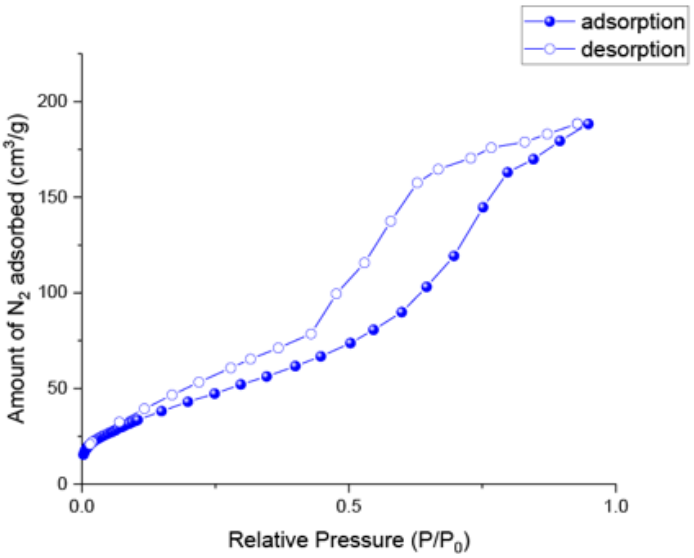

Figure 1.4 Sorption isotherm data for Mg-MOF-74 synthesis at (top) standard concentrations of reagents and at (bottom) 5× the concentration of reagents. At 5× the concentration of reagents, hysteresis is observable along with a reduction in surface area.

X-ray diffraction provides information on the organization of atoms within a repeating unit called a unit cell (Figure 1.5 left). Ideally, the quality of a crystal for diffraction enables full determination of the crystal lattice as well as information about where solvent may coordinate or what moieties in the lattice are disordered or have less than full occupancy. If crystalline targets for X-ray diffraction are not ideal for full characterization, powder X-ray diffraction (PXRD) provides data as diffractograms (Figure 1.5 right), the peaks of which are characteristic for unique materials, except for isostructural materials which can have the same lattice constants. Optimizing for crystal quality can overcome obstacles in characterizing isostructural materials, because single-crystal X-ray diffraction (SCXRD) can then be employed for full crystallographic characterization. Provided with X-ray diffraction data, MOF properties such as pore size, the presence of coordinatively unsaturated metal sites, or interatomic spacing among

others can be determined. These data often provide the basis for understanding material properties such as stability, porosity, reactivity, etc.

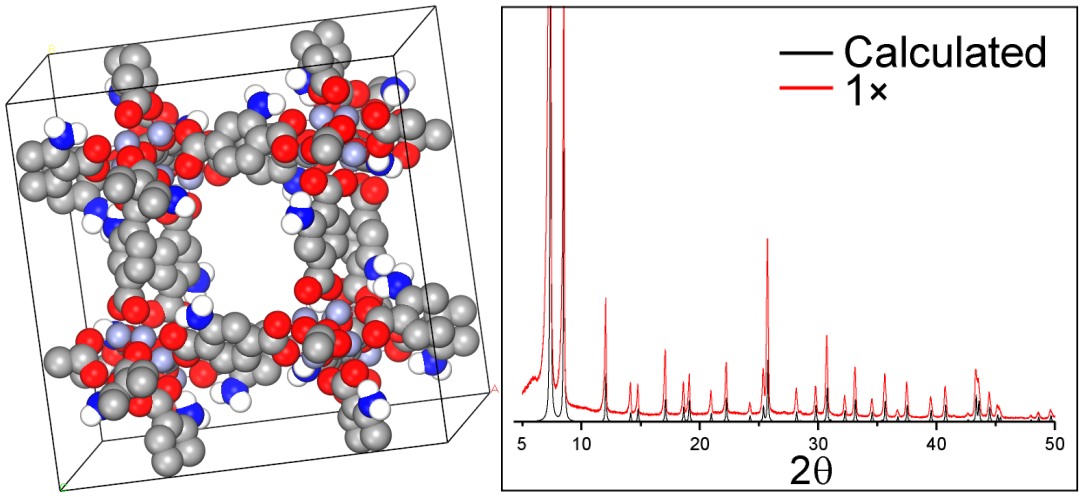

Figure 1.5 (left) Example of the IRMOF-3 unit cell in which the lattice is represented in the space-filling modality. Carbon-bonded protons removed for clarity. (right) Example of a UiO-66 PXRD diffractogram in which the standard synthesis (1×) and the calculated PXRD diffractogram are compared.

Thermal analysis such as thermogravimetric analysis (TGA) or differential scanning calorimetry (DSC) provide important information on material stability and activation in MOF research. MOF stability is one of the obstacles that must be addressed when considering future applications of MOFs. TGA specifically measures mass change as a function of temperature (Figure 1.6 top). TGA provides data on phenomena such as the loss of solvent from a framework or the actual degradation of the framework and its constituent pieces. DSC reports the change in heat flow of the material as a function of the change in temperature (Figure 1.6 bottom). DSC analysis is often used to evaluate endothermic and exothermic changes in the material and marks phase transitions, an indicator of material stability or of phase stability. In the MOF field, these data combined can help determine optimal conditions for material activation, a process by which guest molecules are removed from the framework, allowing for expression of material sorptive

properties. The data can be used to determine conditions under which material degradation may be observed. Additionally, MOF phase transitions to other materials can be observed which is relevant when considering that MOF formation does not always follow classical nucleation theory and may sometimes undergo solid-to-solid phase transitions.

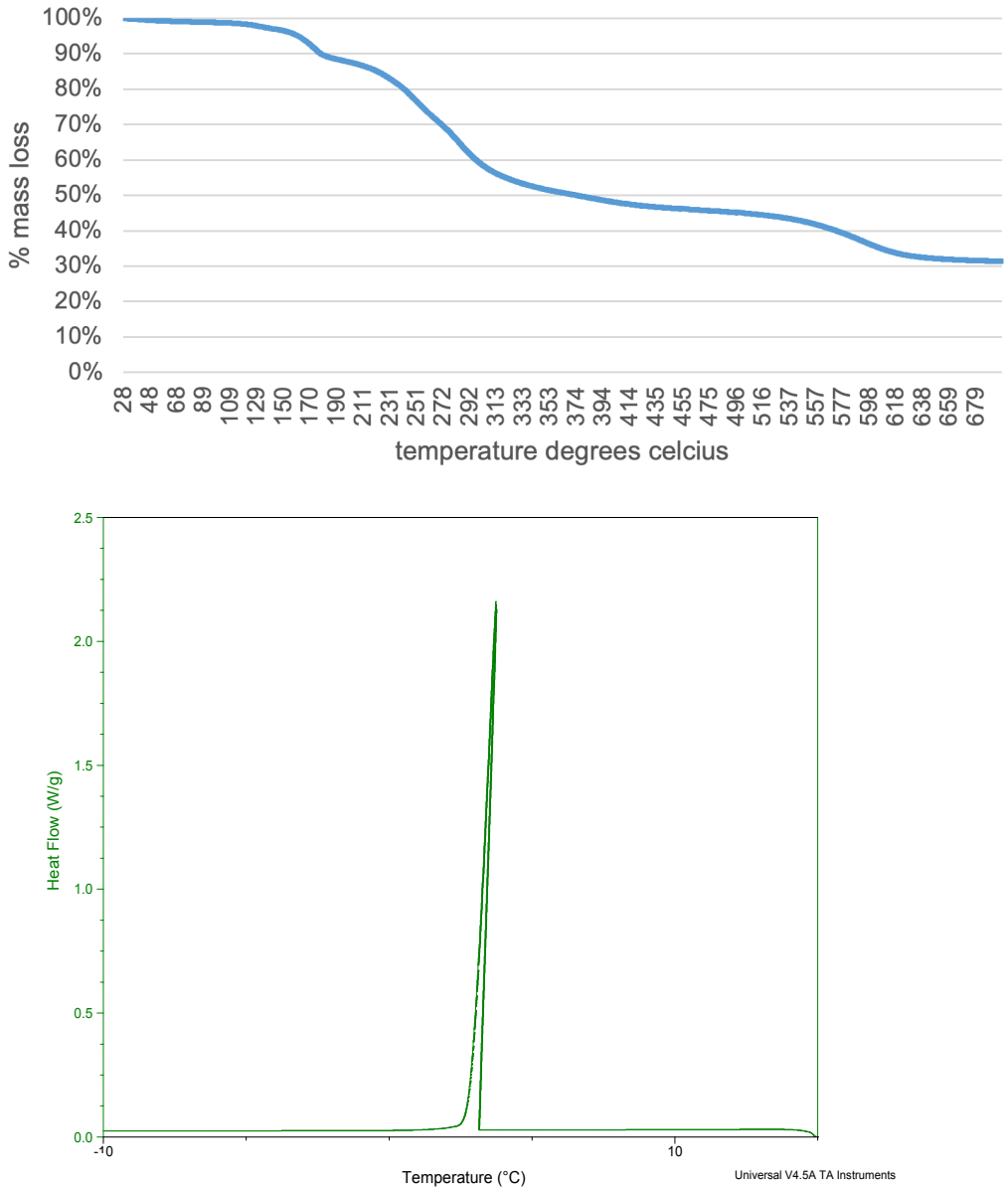

Figure 1.6 (top) TGA of DMF as guest in Mg-MOF-74 at 5× synthesis concentrations where mass loss is recorded as temperature increases. (bottom) DSC of cyclohexane as guest in SNU-70 where the endothermic melting of cyclohexane at ~5 °C is marked by a peak.

Nuclear magnetic resonance (NMR) spectroscopy is a technique which is used in chemistry to characterize intramolecular organization (Figure 1.7). Depending on what nucleus is targeted, intermolecular and ionic interactions can also be elucidated. In MOF research, NMR can provide information on molecular level transformations to the framework components, such as with linker modification.[11] Additionally, NMR data can show the presence of MOF guests which may be trapped in pores[34] or which may be strongly coordinated to the framework, an example of information which might not be readily observable by even SCXRD.

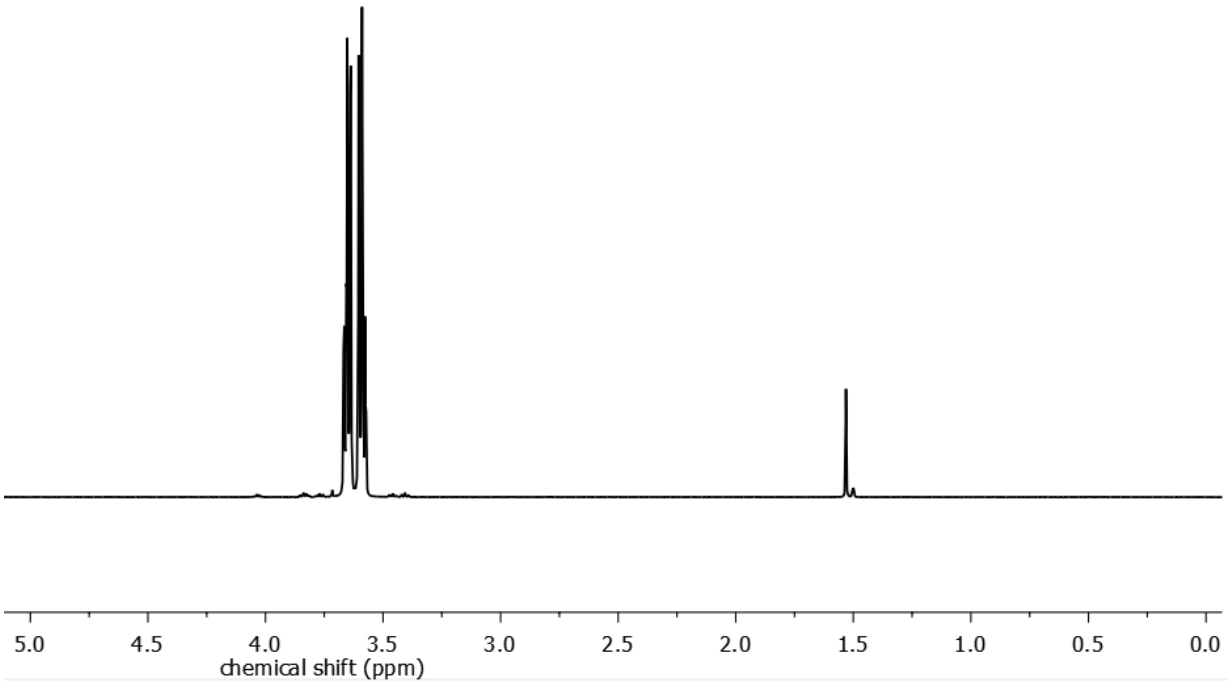

Figure 1.7 ^{1}H NMR of chloroethyl isocyanate where adjacent methylene protons show characteristic splitting patterns around 3.5 ppm.

Raman and Fourier-transform infrared (Figure 1.8) spectroscopies both provide vibrational data on intramolecular and, to an extent, intermolecular interactions, often observed as peak shifts when comparing similar materials. Vibrational spectroscopy can provide molecular characterization and is especially powerful for showing the presence

and identity of functional groups. Application of Beer's law enables quantification of sample components and can provide information on kinetic or thermodynamic properties. Applications for these techniques are extensive, and sophisticated experiments may provide even more nuanced insights such as structural information, allowing for determination of intermolecular interaction strengths, material properties, etc.

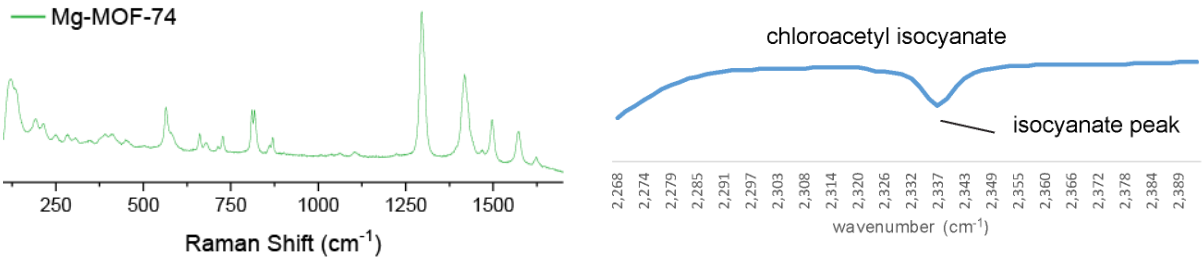

Figure 1.8 (left) Raman spectra of Mg-MOF-74. (right) Fourier-transform infrared spectroscopy data for chloroacetyl isocyanate in chloroform.

Scanning electron microscopy (SEM) enables visualization of materials at scales down to tens of nanometers and smaller under the correct conditions (Figure 1.9). This capability allows for researchers to distinguish morphology of small crystallites, distinguish between phases, and measure crystal size. A capability which is often attached to SEM is energy-dispersive X-ray spectroscopy (EDS). EDS provides elemental analysis, and in combination with SEM, EDS can provide spatially resolved information about where elements are contained in materials.[11]

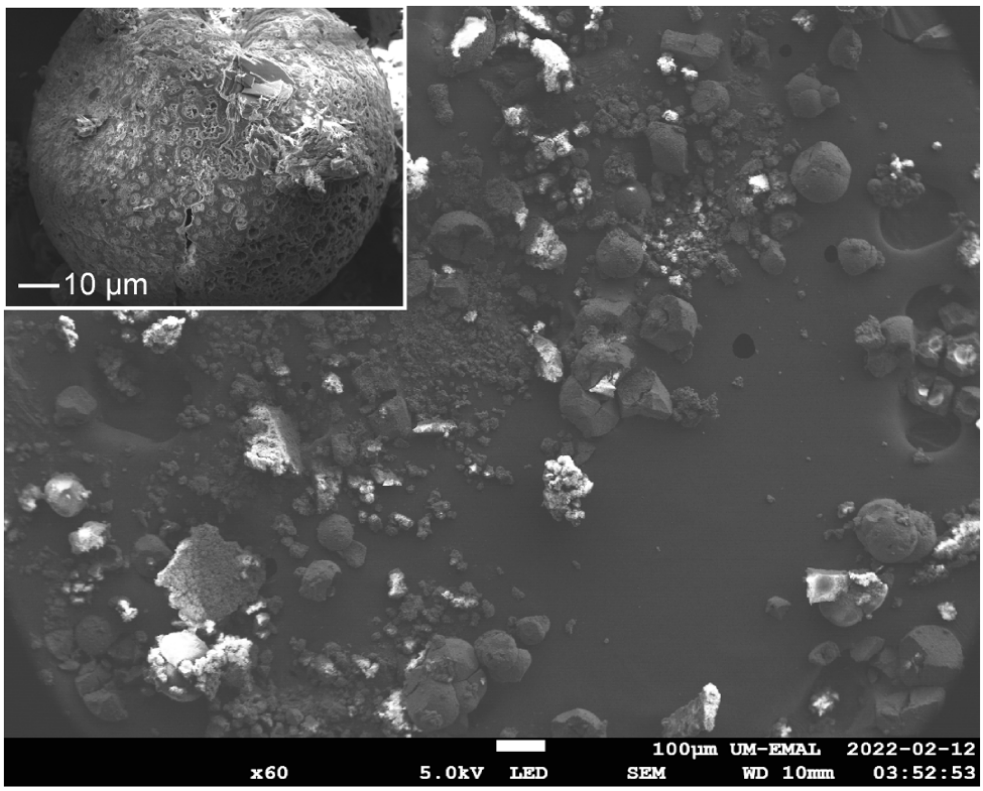

Figure 1.9 Scanning electron microscopy enables visualization of Mg-MOF-74 synthesized at 5× synthesis concentrations. The inset shows off-target phase morphology.

A wealth of other analytical techniques are commonly applied for more niche applications in MOF research. The methods of analysis described above are relevant to the work described in this dissertation. Where additional analytical techniques not described here are used, an explanation of their application to the research will follow.

1.5 Outline of the Dissertation

This dissertation focuses on the formation of MOF phases. A phase, in common vernacular, usually describes the delineation between states of matter such as gas, liquid, or solid. However, in materials chemistry, the delineation of a particular phase also includes chemical and crystallographic uniformity. Distinguishing phase change is not always straight forward, as in the case of morphological changes which do not necessarily

affect chemical and physical uniformity of the material (Figure 1.10). In contrast, a material may be visually comparable but of a different phase (Figure 1.10). An investigation of MOF phase formation can provide mechanistic understanding of MOF formation, enable control over phase selection, and inform design principles in forming more complex MOFs. The description of work which follows specifically enumerates on the topics just listed.

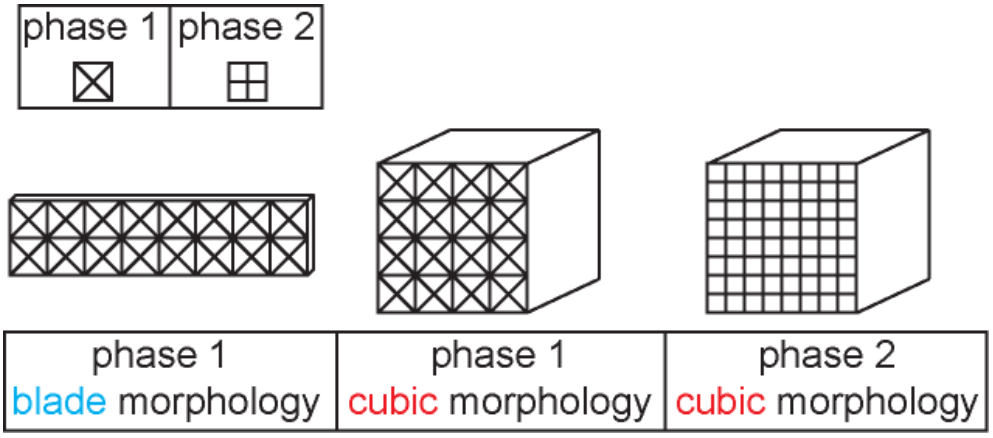

Figure 1.10 Cartoon depiction detailing how differences in phase are determined by chemical or crystallographic differences as opposed to morphological ones.

1.5.1 Chapter 2: Linker Deprotonation and Structural Evolution on the Pathway to MOF-74

MOF synthesis does not necessarily follow classical nucleation theory. Exploration of MOF-74 formation, a framework which employs both oxo and carboxylate coordination, has led to the determination that MOF-74 synthesis proceeds first through the generation of chemically and topologically distinct materials, referred to as phases, displaying exclusively carboxylate coordination, followed by further deprotonation to enable oxo coordination and MOF-74 formation. The synthesis of Mg-MOF-74 at high concentrations of linker and metal enables the stabilization and characterization of the previously unobserved, exclusively carboxylate coordinating phases. *Ex situ* and *in situ* approaches

are leveraged to provide the time-resolved observation of Mg-MOF-74 synthesis and the formation of phases that precede Mg-MOF-74 formation as well as metastable phase dissolution. These data support dissolution and redeposition as the mechanism of MOF-74 formation and provide insight into the formation mechanism of MOFs with multiple linker coordination types.

1.5.2 Chapter 3: Metal–Organic Framework Seeding to Drive Phase Selection and Overcome Synthesis Limitations

Seeding methodology finds application in pharmaceutical settings to select for the formation of target materials by acting as a crystallographic blueprint or by providing a point of nucleation amenable to the formation of the desired phase. Seeding during the synthesis of metal–organic frameworks (MOFs) enhances control over phase expression in synthesis conditions with high concentrations of metal and linker enabling reduced solvent quantities. Dramatic improvements to yield over unseeded conditions are achieved. Phase direction via the seeding method was explored for four different MOFs: Mg-MOF-74, DMOF-1, SNU-70, and UiO-66. The MOFs employed vary in terms of metal identity, secondary building unit, and linker, which demonstrates broad applicability, with one instructive exception, for MOF seeding as a method to drive phase selection and enable MOF production under industrially relevant conditions leading to reduced environmental impact.

1.5.3 Chapter 4: Reagent Reactivity and Solvent Choice Determine Metal–Organic Framework Microstructure during Postsynthetic Modification

Postsynthetic modification is a method of covalently modifying a MOF to form a new material. This method can be thought of as being a tool within the larger toolbox of

postsynthetic methods which are applied to chemically change the MOF after formation. The spatial distribution of MOF functionalization reveals that postsynthetic modification (PSM)-derived microstructures can range from uniform to core–shell, affected by reagent reactivity and solvent choice. A suite of isocyanate reagents with varying reactivity were employed to study the effect of kinetics and experimental conditions on microstructure during PSM. The research demonstrates that a better understanding of the dynamics of PSM can support the design of MOFs with increasingly sophisticated architectures.

1.5.4 Chapter 5: Conclusions and Outlook

The research discussed in this dissertation centers on phase formation in MOFs. Through the research conducted, it is clear that MOF chemistry deviates from molecular chemistry in terms of formation; however, this does not preclude molecular crystallization techniques such as seeding from being efficacious. Postsynthetic modification is also shown to provide meaningful control over phase distribution in MOFs allowing access to advanced MOF forms such as core–shell which may allow for segregated function.

1.6 References

1. Furukawa, H.; Cordova, K. E.; O'Keeffe, M.; Yaghi, O. M. The Chemistry and Applications of Metal-Organic Frameworks. *Science* **2013**, *341* (6149), 1230444.
2. Yaghi, O. M.; Li, G.; Li, H. Selective Binding and Removal of Guests in a Microporous Metal–Organic Framework. *Nature* **1995**, *378* (6558), 703–706.
3. Abrahams, B. F.; Hoskins, B. F.; Michail, D. M.; Robson, R. Assembly of Porphyrin Building-Blocks into Network Structures with Large Channels. *Nature* **1994**, *369* (6483), 727–729.
4. Hoskins, B. F.; Robson, R. Design and Construction of a New Class of Scaffolding-like Materials Comprising Infinite Polymeric Frameworks of 3-D-Linked Molecular Rods - A Reappraisal of the $Zn(CN)_2$ And $Cd(CN)_2$ Structures and the Synthesis and Structure of the Diamond-Related Frameworks $N(CH_3)_4$ $Cu^{I}Zn^{II}(CN)_4$ And Cu^{I} 4,4',4'',4'''-Tetracyanotetraphenylmethane $BF_4.xC_6H_5NO_2$. *J. Am. Chem. Soc.* **1990**, *112* (4), 1546–1554.
5. Freund, R.; Canossa, S.; Cohen, S. M.; Yan, W.; Deng, H.; Guillerm, V.; Eddaoudi, M.; Madden, D. G.; Fairen-Jimenez, D.; Lyu, H.; Macreadie, L. K.; Ji, Z.; Zhang, Y.; Wang, B.; Haase, F.; Wöll, C.; Zaremba, O.; Andreo, J.; Wuttke, S.; Diercks, C. S. 25

Years of Reticular Chemistry. *Angewandte Chemie International Edition* **2021**, *60* (45), 23946–23974.
6. Li, H.; Eddaoudi, M.; O'Keefe, M.; Yaghi, O. M. Design and Synthesis of an Exceptionally Stable and Highly Porous Metal-Organic Framework. *Nature* **1999**, *402*, 276–279.
7. Guo, P.; Dutta, D.; Wong-Foy, A. G.; Gidley, D. W.; Matzger, A. J. Water Sensitivity in Zn4O-Based MOFs Is Structure and History Dependent. *J. Am. Chem. Soc.* **2015**, *137* (7), 2651–2657.
8. Nguyen, J. G.; Cohen, S. M. Moisture-Resistant and Superhydrophobic Metal−Organic Frameworks Obtained via Postsynthetic Modification. *J. Am. Chem. Soc.* **2010**, *132* (13), 4560–4561.
9. Suresh, K.; Matzger, A. J. Enhanced Drug Delivery by Dissolution of Amorphous Drug Encapsulated in a Water Unstable Metal–Organic Framework (MOF). *Angewandte Chemie International Edition* **2019**, *58* (47), 16790–16794.
10. Boissonnault, J. A.; Wong-Foy, A. G.; Matzger, A. J. Core–Shell Structures Arise Naturally During Ligand Exchange in Metal–Organic Frameworks. *Journal of the American Chemical Society* **2017**, *139* (42), 14841–14844.
11. Du Bois, D. R.; Matzger, A. J. Reagent Reactivity and Solvent Choice Determine Metal–Organic Framework Microstructure during Postsynthetic Modification. *J. Am. Chem. Soc.* **2021**, *143* (2), 671–674.
12. Dodson, R. A.; Kalenak, A. P.; Matzger, A. J. Solvent Choice in Metal–Organic Framework Linker Exchange Permits Microstructural Control. *J. Am. Chem. Soc.* **2020**, *142* (49), 20806–20813.
13. Chui, S. S.-Y.; Lo, S. M.-F.; Charmant, J. P. H.; Orpen, A. G.; Williams, I. D. A Chemically Functionalizable Nanoporous Material [Cu3(TMA)2(H2O)3]n. *Science* **1999**, *283* (5405), 1148–1150.
14. Low, J. J.; Benin, A. I.; Jakubczak, P.; Abrahamian, J. F.; Faheem, S. A.; Willis, R. R. Virtual High Throughput Screening Confirmed Experimentally: Porous Coordination Polymer Hydration. *J. Am. Chem. Soc.* **2009**, *131* (43), 15834–15842.
15. Round-two-MOF-commercialization https://cen.acs.org/articles/95/i24/Round-two-MOF-commercialization.html (accessed 2022 -11 -19).
16. A Sponge to Soak Up Carbon Dioxide in the Air https://www.energy.gov/science/articles/sponge-soak-carbon-dioxide-air (accessed 2022 -11 -19).
17. Dodson, R. A.; Wong-Foy, A. G.; Matzger, A. J. The Metal–Organic Framework Collapse Continuum: Insights from Two-Dimensional Powder X-Ray Diffraction. *Chemistry of Materials* **2018**, *30* (18), 6559–6565.
18. Zhang, W.; Hu, Y.; Ge, J.; Jiang, H.-L.; Yu, S.-H. A Facile and General Coating Approach to Moisture/Water-Resistant Metal–Organic Frameworks with Intact Porosity. *J. Am. Chem. Soc.* **2014**, *136* (49), 16978–16981.
19. Ahmed, A.; Seth, S.; Purewal, J.; Wong-Foy, A. G.; Veenstra, M.; Matzger, A. J.; Siegel, D. J. Exceptional Hydrogen Storage Achieved by Screening Nearly Half a Million Metal-Organic Frameworks. *Nature Communications* **2019**, *10* (1), 1568.
20. Ahmed, A.; Liu, Y.; Purewal, J.; Tran, L. D.; Veenstra, M.; Wong-Foy, A.; Matzger, A.; Siegel, D. Balancing Gravimetric and Volumetric Hydrogen Density in MOFs. *Energy Environ. Sci.* **2017**.

21. Erdemir, D.; Lee, A. Y.; Myerson, A. S. Nucleation of Crystals from Solution: Classical and Two-Step Models. *Acc. Chem. Res.* **2009**, *42* (5), 621–629.
22. L. Anderson, S.; Gładysiak, A.; G. Boyd, P.; P. Ireland, C.; Miéville, P.; Tiana, D.; Vlaisavljevich, B.; Schouwink, P.; Beek, W. van; J. Gagnon, K.; Smit, B.; C. Stylianou, K. Formation Pathways of Metal–Organic Frameworks Proceeding through Partial Dissolution of the Metastable Phase. *CrystEngComm* **2017**, *19* (25), 3407–3413.
23. Xing, J.; Schweighauser, L.; Okada, S.; Harano, K.; Nakamura, E. Atomistic Structures and Dynamics of Prenucleation Clusters in MOF-2 and MOF-5 Syntheses. *Nat Commun* **2019**, *10* (1), 3608.
24. Embrechts, H.; Kriesten, M.; Ermer, M.; Peukert, W.; Hartmann, M.; Distaso, M. In Situ Raman and FTIR Spectroscopic Study on the Formation of the Isomers MIL-68(Al) and MIL-53(Al). *RSC Adv.* **2020**, *10* (13), 7336–7348.
25. Wu, Y.; Moorhouse, S. J.; O'Hare, Dermot. Time-Resolved in Situ Diffraction Reveals a Solid-State Rearrangement During Solvothermal MOF Synthesis. *Chem. Mater.* **2015**, *27*, 7236–7239.
26. Embrechts, H.; Kriesten, M.; Hoffmann, K.; Peukert, W.; Hartmann, M.; Distaso, M. Elucidation of the Formation Mechanism of Metal–Organic Frameworks via in-Situ Raman and FTIR Spectroscopy under Solvothermal Conditions. *J. Phys. Chem. C* **2018**, *122* (23), 12267–12278.
27. Du Bois, D. R.; Wright, K. R.; Bellas, M. K.; Wiesner, N.; Matzger, A. J. Linker Deprotonation and Structural Evolution on the Pathway to MOF-74. *Inorg. Chem.* **2022**.
28. Liu, B.; Wong-Foy, A. G.; Matzger, A. J. Rapid and Enhanced Activation of Microporous Coordination Polymers by Flowing Supercritical CO_2. *Chem. Commun.* **2013**, *49*, 1419–1421.
29. Ma, J.; Kalenak, A. P.; Wong-Foy, A. G.; Matzger, A. J. Rapid Guest Exchange and Ultra-Low Surface Tension Solvents Optimize Metal–Organic Framework Activation. *Angewandte Chemie International Edition* **2017**, *56* (46), 14618–14621.
30. Prasad, T. K.; Suh, M. P. Control of Interpenetration and Gas-Sorption Properties of Metal-Organic Frameworks by a Simple Change in Ligand Design. *Chemistry A European Journal* **2012**, *18* (28), 8673–8680.
31. Wright, K. R.; Nath, K.; Matzger, A. J. Superior Metal-Organic Framework Activation with Dimethyl Ether. *Angewandte Chemie International Edition n/a* (n/a).
32. Thommes, M.; Kaneko, K.; Neimark, A. V.; Olivier, J. P.; Rodriguez-Reinoso, F.; Rouquerol, J.; Sing, K. S. W. Physisorption of Gases, with Special Reference to the Evaluation of Surface Area and Pore Size Distribution (IUPAC Technical Report). *Pure and Applied Chemistry* **2015**, *87* (9–10), 1051–1069.
33. Caskey, S. R.; Wong-Foy, A. G.; Matzger, A. J. Dramatic Tuning of Carbon Dioxide Uptake via Metal Substitution in a Coordination Polymer with Cylindrical Pores. *J. Am. Chem. Soc.* **2008**, *130* (33), 10870–10871.
34. Tanabe, K. K.; Wang, Z.; Cohen, S. M. Systematic Functionalization of a Metal−Organic Framework via a Postsynthetic Modification Approach. *Journal of the American Chemical Society* **2008**, *130* (26), 8508–8517.

Chapter 2: Linker Deprotonation and Structural Evolution on the Pathway to MOF-74*

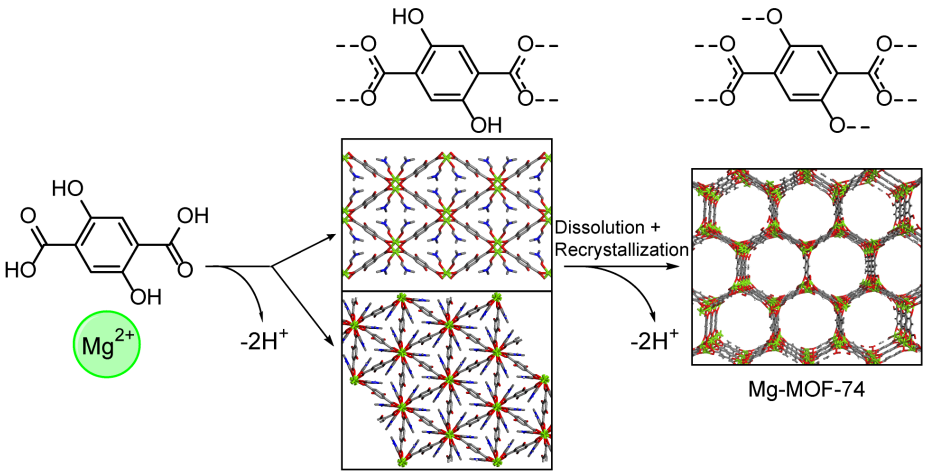

Figure 2.1 Simplified description of Mg-MOF-74 synthesis showing carboxylate coordinating metastable phases which were discovered to precede MOF-74 formation which employs both oxo and carboxylate coordination.

2.1 Publication of This Chapter

Du Bois, D. R.; Wright, K. R.; Bellas, M. K.; Wiesner, N.; Matzger, A. J. Linker Deprotonation and Structural Evolution on the Pathway to MOF-74. *Inorg. Chem.* **2022**, *61*, 4550.

2.2 Introduction

Research into the mechanisms of metal–organic framework (MOF) nucleation and growth contribute to understanding phase selection,[1–3] the origins of defect modes,[4] and inform manufacturability.[5–7] It is understood that the mechanistic phenomena surrounding

*Published with *in situ* instrument setup and measurement performed by Wright, K. R.; single crystal X-ray diffraction by Bellas, M. K.; and PXRD of side product by Wiesner, N.

MOF synthesis are dynamic and can include nucleating with or without the contribution of metastable phases;[7–9] growing incrementally[10–12] or undergoing a structural rearrangement[4,13] to produce the desired phase. As a result, general theories explaining the mechanisms of small molecule growth and nucleation are often not predictive[14] for MOFs. Additionally, analyses typically employed to probe MOF assembly must contend with the limitations associated with *ex situ* analysis, such as material decomposition and short-lived phases, or with *in situ* challenges such as characterizing bulk sample often under solvothermal conditions. The categorization of MOF assembly on a case-by-case basis provides evidence for the creation of more nuanced models[15] that can be leveraged towards the scalable synthesis of MOFs with tailored structure, purity, and defect concentration.

In HKUST-1, *in situ* AFM studies provide compelling evidence that MOF growth occurs from monomer addition of linker and individual addition of the metal cation.[10] In UiO-66, growth has been observed to occur via addition of building units,[16] and there is evidence to support that an amorphous-to-crystalline rearrangement may be involved.[17] Other investigations also suggest that MOF synthesis involves solid-to-solid rearrangements[13,18,19] or the generation of intermediates which undergo Ostwald step changes to arrive at a certain phase.[20–22] Despite mechanistic differences in nucleation and growth, the vast majority of MOFs contain linkers involving exclusively carboxylate coordination chemistry and the pKa differences between coordinating groups are minor. By contrast the MOF-74 family of MOFs is built from 2,5-dioxido-1,4-benzenedicarboxylate (H_4DOBDC in protonated form) where both the aryloxide and the carboxylate coordinate to the metal (Figure 2.2).[23] MOFs that incorporate connectivity to

the metal through multiple coordination types are less common and their mechanistic investigation remains undeveloped. The MOF-74 family displays exceptional properties due to the presence of a high density of coordinatively unsaturated metal sites (CUS). In particular, Mg-MOF-74 excels at CO_2 capture under pressure conditions relevant to flue gas.[24]

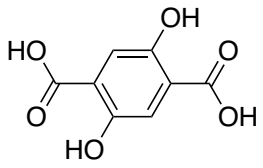

Figure 2.2 H_4DOBDC

2.3 Discussion

Before incorporation into MOF-74, H_4DOBDC undergoes deprotonation of functional groups with pKa values which vary by ~5 units. Base is absent from the original reagent mixture for most MOF syntheses and is generated slowly through solvent decomposition. The expected first two sites for deprotonation of H_4DOBDC are the carboxylic acids, and we reasoned that the dianionic form of the linker should be able to make a MOF. Under synthesis conditions derived from the literature (see section 2.5),[24] no new phases were observed initially; however, when the metal and linker reagents were employed at five times (5×) the normal synthesis concentration, new phases appeared. The synthesis vial was pulled from the oven after 2 h, at which time, multiple MOF phases distinct from Mg-MOF-74 were observed. From this time point, two phases were extracted and their crystal structures solved. Phase 1 crystallizes as yellow cuboctahedrons and phase 2 forms yellow crystals with rhombic prism morphology. Investigating the 1× concentration synthesis with increased attention revealed the presence of phase 1 at 1.25

h which, at that time point, appears alongside Mg-MOF-74. This finding inspired more time-resolved *in situ* methods to determine the order of phase formation.

For context, the asymmetric unit of Mg-MOF-74 contains $Mg(DOBDC)_{0.5}(L)$ and crystallizes in the R-3 space group.[25] The rod secondary building unit (SBU) is a 1D chain which forms a helical structure (Figure 2.3a). Each magnesium is 5-coordinated, connecting with four different linkers and via interactions with three carboxylate oxygens and two oxido oxygens. The linker is fully deprotonated. Each linker coordinates with eight magnesium atoms, and each magnesium atom coordinates an additional ligand (L), that can be removed to expose a coordinatively unsaturated metal site, completing the metal coordination sphere. Each metal is connected along the column by the oxido functionality of one linker and a carboxylate oxygen of another. Along the *c*-axis, large hexagonal pores of diameter 15.19 Å are observed (Figure 2.3b).

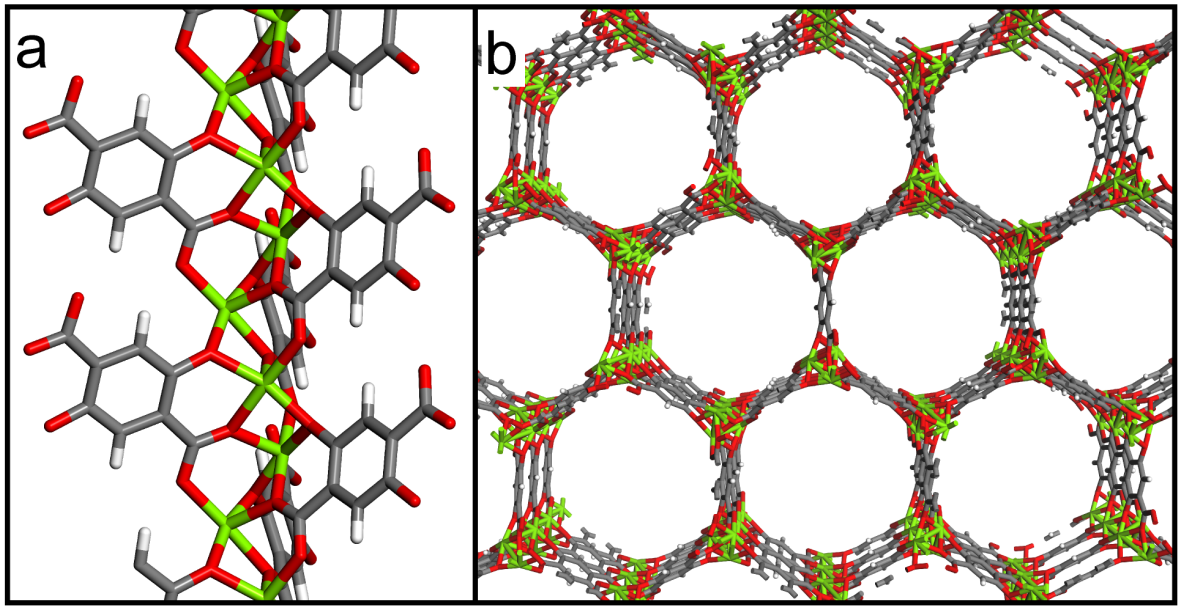

Figure 2.3 (a) A section of the Mg-MOF-74 infinite rod SBU. (b) View along the *c*-axis of hexagonal pores, ligand and protons excluded.

The asymmetric unit of phase 1 contains $Mg_{0.5}(H_2DOBDC)_{0.5}(DMF)$ and crystallizes in the C2/c space group. The linker is deprotonated sufficiently to coordinate using the carboxylate, but not the oxido, functional groups. The structure comprises columns of magnesium arranged in an infinite 1D chain, a rod SBU,[26] wherein each magnesium is coordinated to two DMF molecules and four different linker molecules (Figure 2.4a). Each linker connects two magnesium atoms within a column and two other magnesium atoms within another column. Channels along the *c*-axis are diamond-shaped with DMF coordinated to the metal in the equatorial plane in a cis configuration (Figure 2.4b). This contrasts to a polymorphic framework[27] with DMF coordinated to the metal in a trans configuration[28,29] which was isolated from a subsequent time point analysis of the 5× concentration synthesis as another transient species (Figure 2.5) and verified by SCXRD. Coordinated DMF extends into the channels along the *b*-axis. The pores of the resultant structure are fully occupied by coordinated DMF. H_2DOBDC hydroxy functionalities form intramolecular hydrogen bonds with adjacent carboxylates.

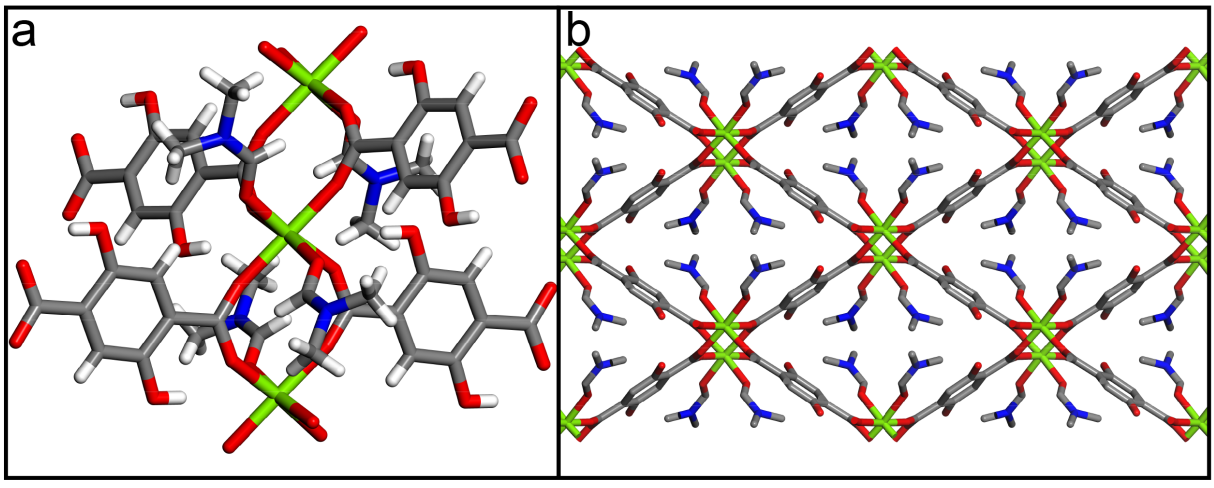

Figure 2.4 (a) Phase 1 contains an infinite rod SBU. (b) View along the *c*-axis of DMF filled pores, protons excluded.

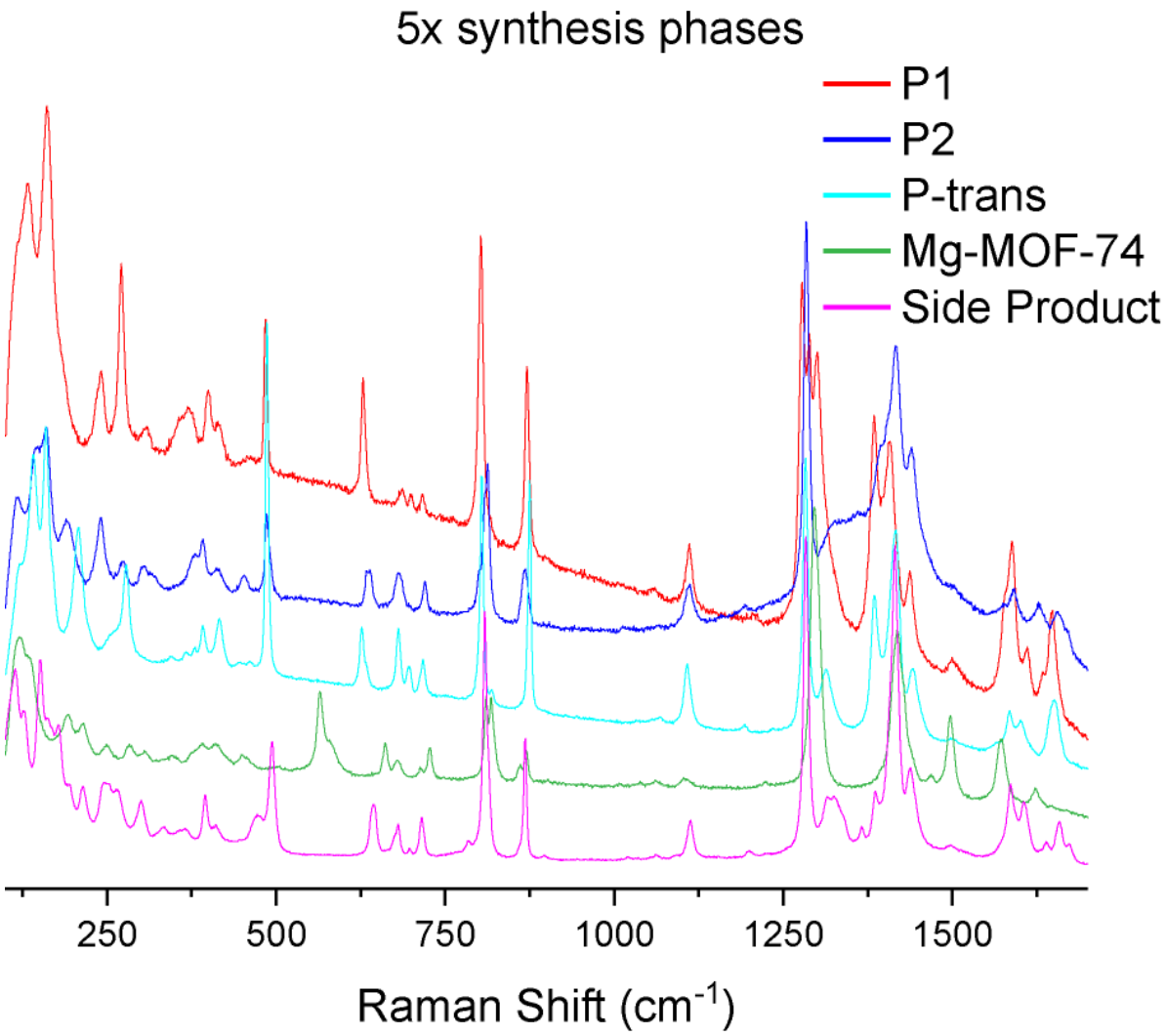

Figure 2.5 Characteristic Raman spectra for phase 1 (red), phase 2 (blue), the trans DMF phase (cyan), Mg-MOF-74 (green), and the white spherical side product (pink).

Phase 2 is a polymorphic framework of phase 1 having the same chemical formula but a different connectivity and overall ratio of chemical residues, thus crystallizing in a different space group- R-3. Like phase 1, the conditions under which phase 2 forms are such that carboxylates form and coordinate to Mg ions while the hydroxyl groups remain protonated. The structure features $Mg_3(-COO)_6(DMF)_6$ SBUs comprised of columns of trinuclear magnesium wherein each magnesium is octahedrally coordinated and connected to each other through the carboxylate of H_2DOBDC linkers (Figure 2.6a).

Terminal magnesium atoms within the trinuclear cluster are bound to three DMF molecules and three H_2DOBDC linkers each. The central magnesium atom is bound to six linker molecules. The trinuclear cluster acts as a 3-connector in the plane with the dicarboxylate linker which leads to hexagonal packing (Figure 2.6b). The trinuclear cluster then connects to another plane of hexagonal sheets. Hexagonal sheets stacked in an ABC arrangement are formed with each trinuclear cluster contributing to two sheets (Figure 2.6c and 2.6d). The vertices of the hexagonal pore are comprised of alternating up and down arrangements of the trinuclear cluster. Channels along the *c* axis are populated by coordinated DMF molecules (Figure 2.6b). Hexagonal pores are bookended in the *c* axis by terminal magnesium atoms with coordinated DMF extending into the pore. The diameter of these hexagonal components is 17.75 Å. The H_2DOBDC hydroxy functionality only interacts intramolecularly.

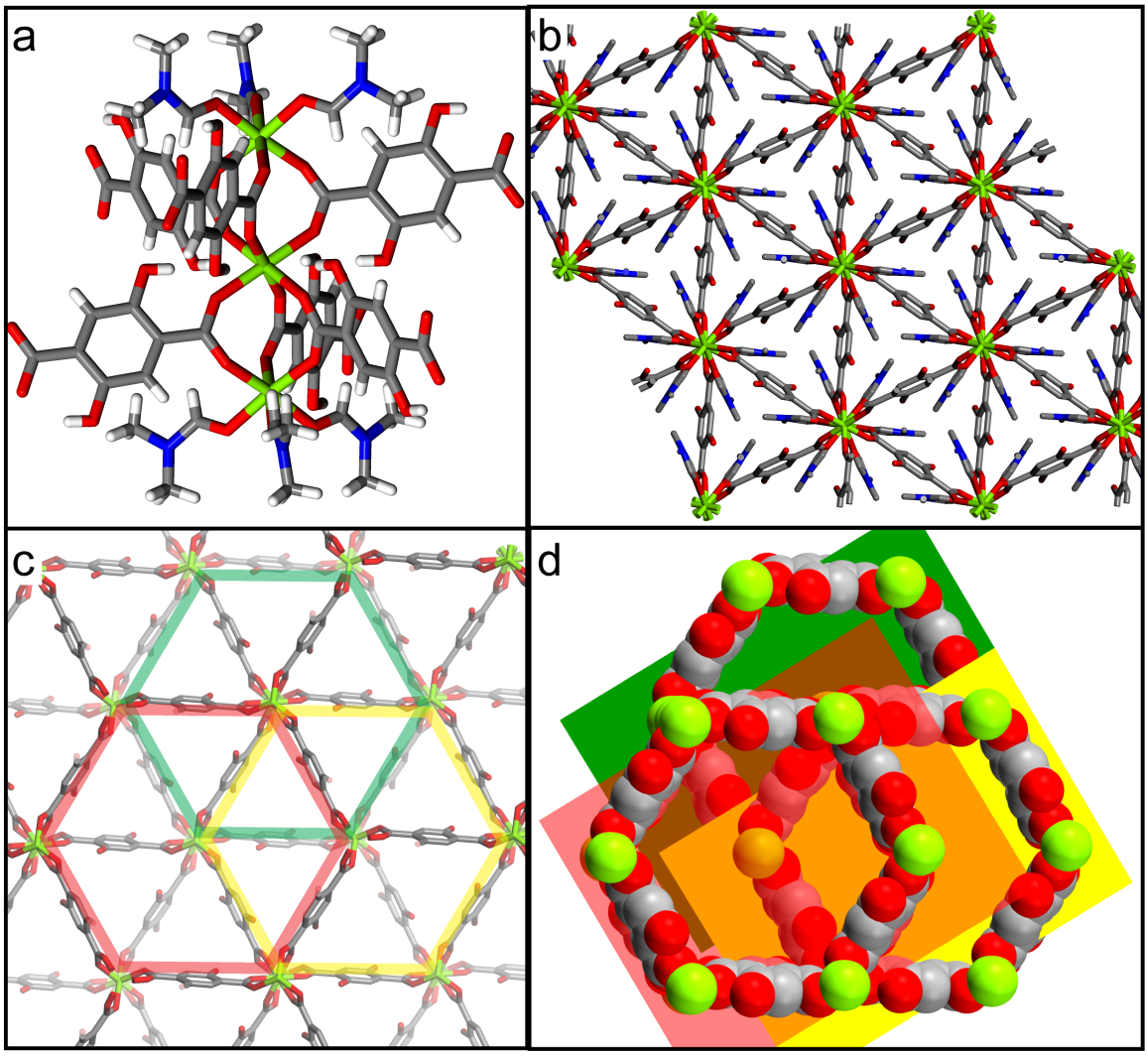

Figure 2.6 (a) Phase 2 contains a trinuclear $Mg_3(-COO)_6(DMF)_6$ SBU. (b) Lattice displayed along *c*-axis with protons excluded. (c) Hexagonal pores are highlighted with protons and DMF excluded. (d) Space-filling model of ABC sheets with planes drawn through the middle.

The appearance of phases 1 and 2 prior to the formation of the MOF-74 structure in the 5× concentration synthesis condition raises questions about the transformation mechanism. In theory, the hexagonal motif and symmetry shared between phase 2 and Mg-MOF-74 suggests that desolvation of the structure followed by increased coordination of metal to linker, incorporating oxido interactions, could result in the formation of Mg-MOF-74. Phase 1 forms with the rod SBU which is in the same class of SBU as MOF-

74; the columnar SBU motif shared by both phases and MOF-74 suggests that formation of these phases can contribute to the formation of the final MOF-74 phase after further deprotonation of H_2DOBDC to DOBDC which occurs with less restriction in the less acidic 1× concentration synthesis. *In situ* optical time-lapse observation of the 1× concentration reaction, indicates the formation of a distinct phase that precedes the generation of the Mg-MOF-74 phase (Figure 2.7. In taking a time point observation of the 1× concentration synthesis conditions, one phase was observed at 1.25 h along with the Mg-MOF-74 phase, and by SCXRD, it was determined as phase 1. We hypothesize that at this concentration of reagents, phase 2 is transient and does not reach optically observable size. The observation of phase 1 in the 1× concentration synthesis of Mg-MOF-74 motivated further time-lapse *in situ* optical studies and Raman spectroscopy of the 1× and 5× concentration synthesis conditions. Time point *ex situ* Raman spectroscopic studies were also performed to isolate individual phases in the 5× concentration synthesis (Figure 2.5). Five phases were isolated over the course of the 5× concentration reaction with a white spherical side product, characterized by Raman spectroscopy and PXRD (Figure A.1), and Mg-MOF-74 being the only observable phases after 20 h (for the mixture of phases at intermediate times, see figures 2.8 for PXRD and A.3 for TGA data).

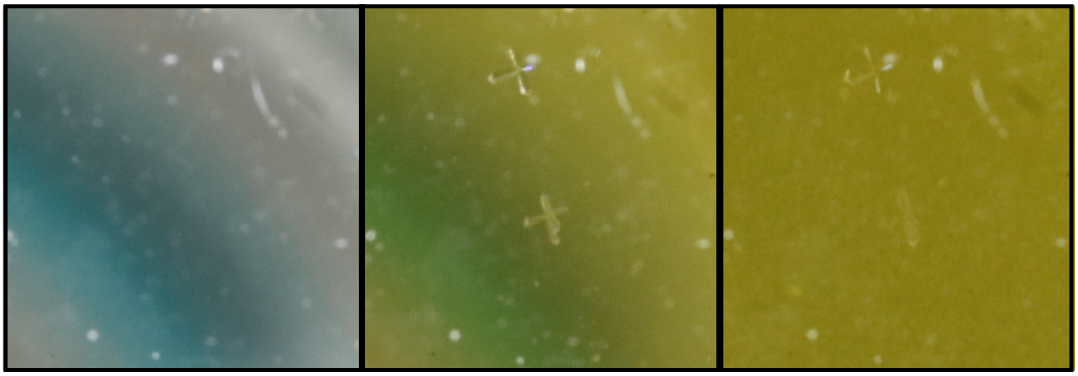

Figure 2.7 1× concentration synthesis showing start of reaction (left), appearance of new phases at 87 minutes (middle), and coverage of vial by Mg-MOF-74 at 101 minutes (right).

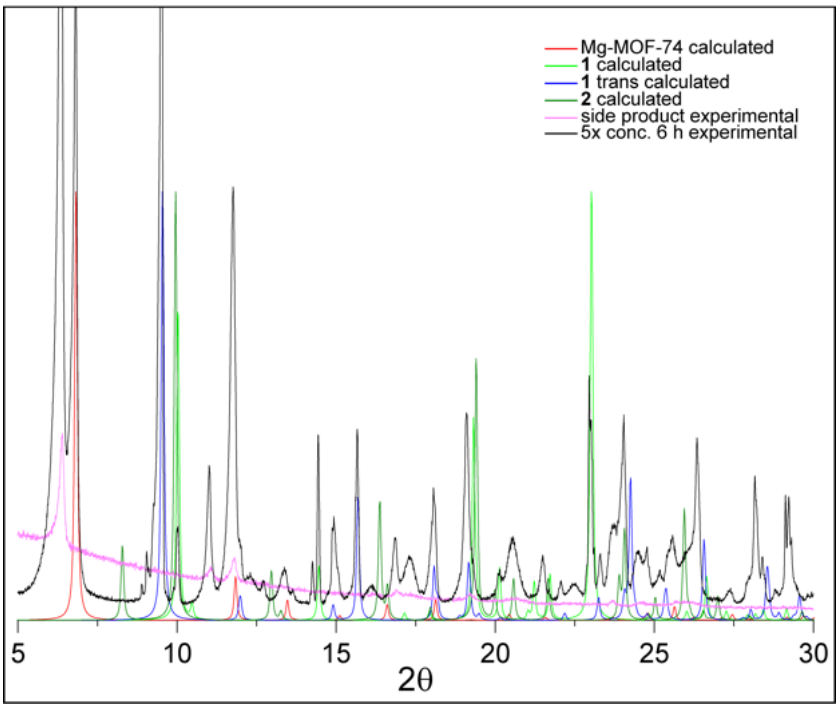

Figure 2.8 Calculated PXRD patterns for phases found in the 5× concentration synthesis compared to experimental data for the bulk after 6 h reaction time.

In situ optical time-lapse studies for both 1× and 5× concentration conditions show the formation of multiple phases preceding the deposition of the microcrystalline solid associated with Mg-MOF-74 (Figures 2.7 and 2.9). The 5× concentration synthesis conditions appear to better stabilize the other phases, and in these conditions, the generation and gradual dissolution of these phases is apparent. Facile observation of

both phases in the 5× concentration synthesis likely results from increased stabilization, relative to the 1× concentration conditions, of the doubly deprotonated H_2DOBDC linker relative to the fully deprotonated DOBDC linker. As a result, the competitive formation of the Mg-MOF-74 phase relative to the other phases is reduced, and the crystals of the other phases are permitted to grow beyond what is allowed under the 1× concentration synthesis conditions. The *in situ* optical time-lapse data indicate that, for the 1× concentration synthesis, other phases precede the final transition to pure Mg-MOF-74 with dissolution and redeposition rather than solid-state transformation being operative.

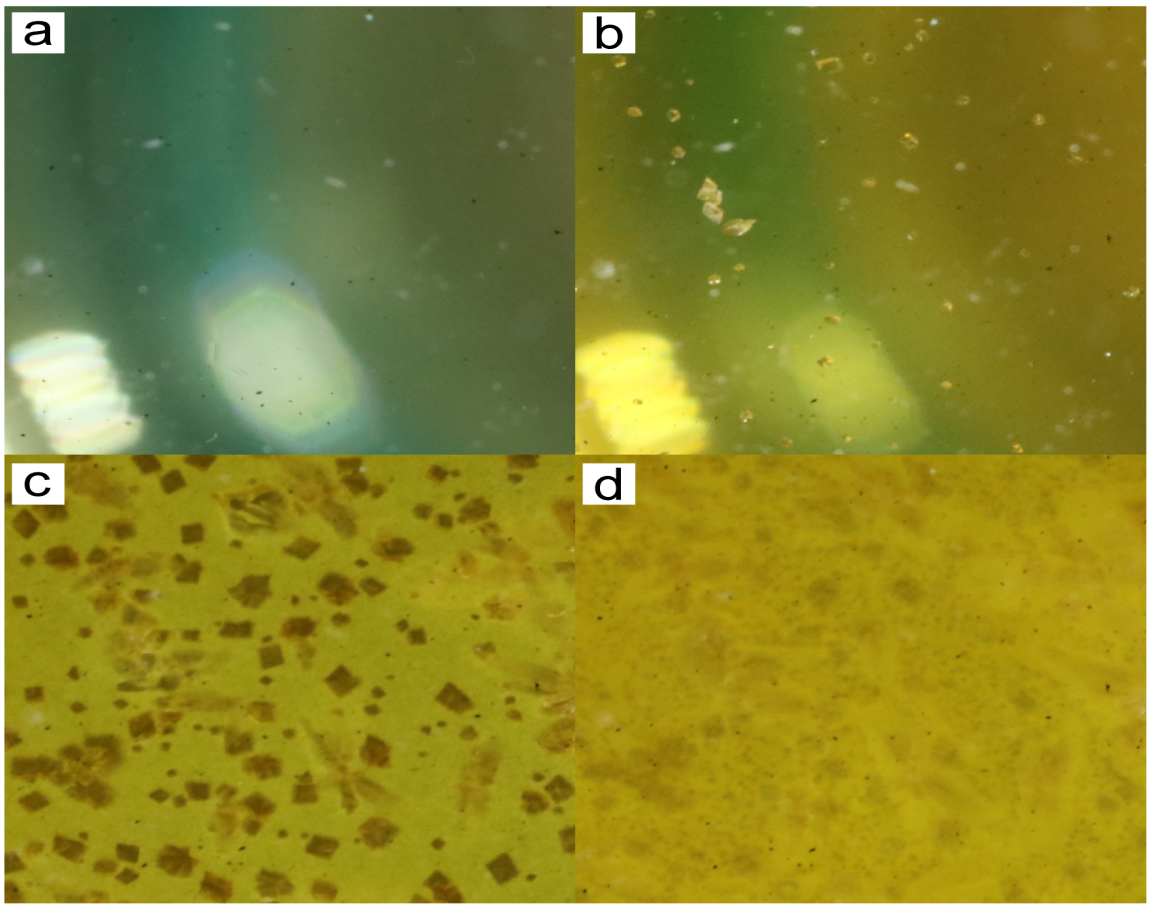

Figure 2.9 5× concentration synthesis showing start of reaction (a), appearance of new phases preceding Mg-MOF-74 formation at 36 minutes (b), Mg-MOF-74 formation at 81 minutes (c), and decreased observation of new phases at 1200 minutes (d).

In situ formation of Mg-MOF-74 was studied in the 5× concentration condition by monitoring the reaction medium through the bottom of the reaction vial by Raman spectroscopy (λ = 785 nm) for 20 hours (See section 2.5.2). At 56 minutes, solid forms, and the spectra are consistent with isolated phase 2: peaks at 484 cm^{-1} and 870 cm^{-1}. Further reaction leads to disappearance of this phase and formation of Mg-MOF-74 after ~14 hours supporting that dissolution and redeposition are operative in the formation of MOF-74 (Figure 2.10). Repeating this process, we saw only growth of the phase pure Mg-MOF-74 at 1× concentration conditions.

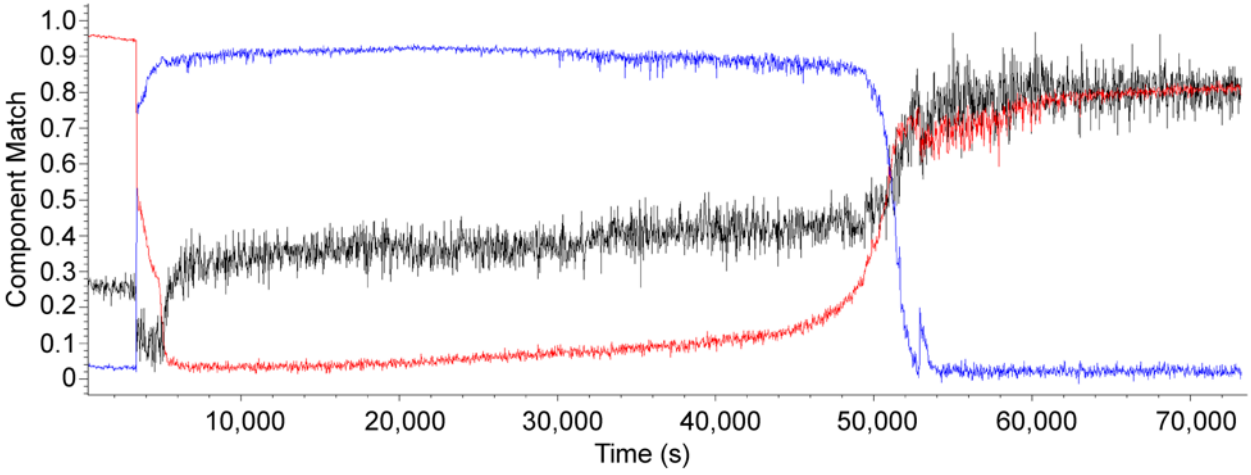

Figure 2.10 Direct classical least squares (DCLS) analysis of Raman spectra from *in situ* growth of 5× concentration Mg-MOF-74 condition. DCLS components from *ex situ* Raman spectra of phase pure Mg-MOF-74 (black trace), phase 2 (blue trace), and solvent mixture (DMF:water:ethanol, red trace) were used as components for analysis.

2.4 Conclusions

Mechanistic studies on MOF formation have demonstrated the variable and rich chemistry surrounding the formation of these materials. It should be no surprise that general theories as well as previous investigations of MOF formation mechanisms[7,30] will require more data and nuance to account for discrepancies[18,31] in a dynamic field where the theoretical limit of manufacturable phases is vast.[32] Through a combination of *ex situ*

and *in situ* techniques, it has been determined that the formation of Mg-MOF-74 is preceded by phases which coordinate exclusively via the carboxylate of the linker before further deprotonation enables coordination to the oxo moiety, and these are expected to be relevant motifs in solution. These phenomena were captured by stabilizing exclusively carboxylate coordinating phases at 5× the concentration of metal and linker during synthesis, and closer examination of the 1× concentration synthesis of Mg-MOF-74 enables observation of phases preceding Mg-MOF-74 formation. Mechanistic insight into the formation of MOFs with multiple coordination types offers pathways to facilitate MOF synthesis with novel coordination modes and improved theoretical understanding of MOF formation enables more robust phase selection, understanding of defect modes, and manufacturability.

2.5 Experimental details

Chemicals were used as purchased without purification unless otherwise noted. Magnesium nitrate hexahydrate certified ACS grade was purchased from Fisher Chemical. DMF which was stored over 4 Å molecular sieves was purchased from Fisher Scientific. 2,5-dihydroxyterepthalic acid (H_4DOBDC) was purchased from HangZhou Trylead Chemical Technology Co., Ltd. Absolute ethanol was purchased from Decon Labs, Inc.

2.5.1 *Synthesis*

Mg-MOF-74 was synthesized using a modified literature procedure.[24]

1× concentration synthesis. To a solid mixture of H_4DOBDC (22.2 mg, 0.112 mmol) and $Mg(NO_3)_2{\cdot}6H_2O$ (57.4 mg, 0.224 mmol) was added a 15:1:1 (v/v/v) mixture of DMF–ethanol–deionized water (10 mL) in a 20-mL scintillation vial which was capped

tightly with Teflon-lined caps. The suspension was sonicated until homogeneous. The reaction vials were placed in an oven at 125 °C. After 20 hours, the sample was removed from the oven and allowed to cool to RT. The mother liquor was decanted from the yellow microcrystalline material and replaced with DMF (10 mL).

5× concentration synthesis. The 5× concentration synthesis of Mg-MOF-74 follows the procedure of the 1× concentration synthesis with the quantity of each of H_4DOBDC and $Mg(NO_3)_2{\cdot}6H_2O$ being multiplied by five. After 20 hours, the sample has microcrystalline Mg-MOF-74 and a white spherical phase characterized by Raman spectroscopy and PXRD (Figures 2.5 and 2.8).

2.5.2 Characterization

Single Crystal X-Ray Structure Determination

Single-crystal X-ray diffraction data were collected using a Rigaku XtaLAB Synergy-S X-ray diffractometer in a kappa goniometer geometry configuration; an Oxford Cryostream 800 low temperature device is also equipped. The X-ray source is a PhotonJet-S microfocus Cu source (λ = 1.54187 Å) operated at 50 kV and 1 mA. X-ray intensities were measured with a HyPix-6000HE detector held 34.00 mm from the sample. The data were processed using CrysAlisPro v38.46 (Rigaku Oxford Diffraction) and were absorption corrected. The structures were determined using OLEX2[33] as well as SHELXT[34] and refined with SHELXL.[35] All non-hydrogen atoms were refined anisotropically with hydrogen atoms placed at idealized positions.

Ex Situ Raman Spectroscopy

Raman spectroscopy was carried out with a Renishaw inVia Raman Microscope equipped with a Leica microscope, 785 nm laser with 1200 lines/mm grating, 65 μm slit, and a Rencam CCD detector.

In Situ Camera Setup

The camera setup comprises the following components: Canon EOS 5DS DSLR camera, Canon MP-E 65mm f/2.8 1.5-5x Macro lens, circular aluminum block with a hole in the center (drilled for 20 mL vial), 4 x 4 x 1/8'' quartz plate, heating tape capable of 313 Watts of power, J-KEM Scientific temperature controller model 210, a thermocouple, red silicone rubber, 1 band clamp, ring light for overhead illumination, and focused fiber optic light source for bottom illumination.

Assembly:

The camera optical station was assembled by fist wrapping the aluminum block with the heat tape. Silicone rubber was wrapped around the tape to ensure thermal insulation. A band clamp was then fastened around the rubber, heat tape, and aluminum immobilize the heating element. This heat block was then placed on top of the quartz plate and equilibrated at 125 °C. Underneath the heated block and quartz plate, was the Canon EOS 5DS DSLR camera fitted with the macro lens. Inside of the through hole of the aluminum cell a vial was inserted along with the thermocouple to monitor temperature of the apparatus.

Experimental Parameters:

Data acquisition was conducted with the vial at 125 °C. The vial containing precursor MOF solution was inserted into the preheated block and held for the duration of synthesis

(~20 hours). The camera was externally hooked up to a desktop computer with the software package DSLR Remote Pro for time-lapse shooting. Specific parameters for time-lapse/ bulb shooting include: 1 frame every 30 seconds for 24 hours, F stop 6.3

In Situ Raman Spectroscopy

The *in situ* Raman setup comprises the following components: Renishaw Virsa Raman spectrometer, 10x Leica microscope objective coupled to a fiber optic probe, circular aluminum block with a hole in the center (for a 20 mL vial) and a hole for a thermocouple, heat heating tape capable of 313 Watts, J-KEM Scientific temperature controller Gemini model, a thermocouple, and red silicone rubber. Data analysis was conducted within WiRe 5.3.

Assembly:

The *in situ* Raman station first had the temperature block assembled similarly to the camera setup with the only change being the temperature controller. Underneath the heated block, backscattered radiation was collected using a 785 nm laser introduced through Leica 10x microscope objective positioned at working distance of 7.3 mm and the backscattered radiation collected. Aluminum foil was wrapped around the whole setup to block ambient light.

Experimental Parameters:

1500 l/mm grating lines with cosmic ray removal on, a center of 750 wavenumbers, and a Renishaw Centrus 2R4P52 – 1040x256 detector were used. Data acquisition was carried out with the Wire 5.3 software package. Specific experimental parameters for *in situ* studies included: 69.9 mW laser power, 3 X 6 second accumulations for 2400 acquisitions using cosmic ray removal.

Powder X-Ray Diffraction

Room-temperature powder X-ray diffraction was performed on a PANalytical Empyrean diffractometer in Bragg–Brentano geometry (Cu $K\alpha$ radiation, 45 kV, and 40 mA). The incident beam was equipped with a Bragg–BrentanoHD X-ray optic using fixed slits/soller slits. X-ray detection was accomplished with a silicon-based linear position sensitive X'Celerator Scientific detector operating in 1D scanning mode. Patterns were collected between 3 – 50 °2θ, with a scan rate of 0.008 ° and 20 seconds per step.

Thermogravimetric Analysis

Thermogravimetric analysis (TGA) thermograms for each sample were recorded on a TA Instruments Q50 TGA. All experiments were conducted on platinum TGA sample pans under a nitrogen purge of 40 mL/min with a heating rate of 2 °C/min, covering a temperature range of ~25 °C to 700 °C. The instrument was calibrated using the Curie points of alumel and nickel standards and all TGA thermograms were analyzed using TA Universal Analysis 2000, V4.5A, build 4.5.0.5.

2.6 Acknowledgements

This work was supported by the U.S. Department of Energy (DE-SC0004888).

2.7 References

1. L. Anderson, S.; Gładysiak, A.; G. Boyd, P.; P. Ireland, C.; Miéville, P.; Tiana, D.; Vlaisavljevich, B.; Schouwink, P.; Beek, W. van; J. Gagnon, K.; Smit, B.; C. Stylianou, K. Formation Pathways of Metal–Organic Frameworks Proceeding through Partial Dissolution of the Metastable Phase. *CrystEngComm*. **2017**, *19* (25), 3407–3413.
2. Embrechts, H.; Kriesten, M.; Ermer, M.; Peukert, W.; Hartmann, M.; Distaso, M. In Situ Raman and FTIR Spectroscopic Study on the Formation of the Isomers MIL-68(Al) and MIL-53(Al). *RSC Adv.* **2020**, *10* (13), 7336–7348.
3. Xing, J.; Schweighauser, L.; Okada, S.; Harano, K.; Nakamura, E. Atomistic Structures and Dynamics of Prenucleation Clusters in MOF-2 and MOF-5 Syntheses. *Nat. Commun*. **2019**, *10* (1), 3608.
4. Embrechts, H.; Kriesten, M.; Hoffmann, K.; Peukert, W.; Hartmann, M.; Distaso, M. Elucidation of the Formation Mechanism of Metal–Organic Frameworks via in-Situ

Raman and FTIR Spectroscopy under Solvothermal Conditions. *J. Phys. Chem. C*. **2018**, *122* (23), 12267–12278.
5. Seoane, B.; Castellanos, S.; Dikhtiarenko, A.; Kapteijn, F.; Gascon, J. Multi-Scale Crystal Engineering of Metal Organic Frameworks. *Coord. Chem. Rev*. **2016**, *307*, 147–187.
6. McKinstry, C.; Cussen, E. J.; Fletcher, A. J.; Patwardhan, S. V.; Sefcik, J. Effect of Synthesis Conditions on Formation Pathways of Metal Organic Framework (MOF-5) Crystals. *Cryst. Growth Des*. **2013**, *13* (12), 5481–5486.
7. Stavitski, E.; Goesten, M.; Juan-Alcañiz, J.; Martinez-Joaristi, A.; Serra-Crespo, P.; Petukhov, A. V.; Gascon, J.; Kapteijn, F. Kinetic Control of Metal-Organic Framework Crystallization Investigated by Time-Resolved In Situ X-Ray Scattering. *Angew. Chem. Int. Ed.* **2011**, *50* (41), 9624–9628.
8. Millange, F.; Medina, M. I.; Guillou, N.; Férey, G.; Golden, K. M.; Walton, R. I. Time-Resolved In Situ Diffraction Study of the Solvothermal Crystallization of Some Prototypical Metal–Organic Frameworks. *Angew. Chem. Int. Ed*. **2010**, *49* (4), 763–766.
9. ĐYeung, H. H.-M.; Sapnik, A. F.; Massingberd-Mundy, F.; Gaultois, M. W.; Wu, Y.; Fraser, D. A. X.; Henke, S.; Pallach, R.; Heidenreich, N.; Magdysyuk, O. V.; Vo, N. T.; Goodwin, A. L. Control of Metal–Organic Framework Crystallization by Metastable Intermediate Pre-Equilibrium Species. *Angew. Chem. Int. Ed*. **2019**, *58* (2), 566–571.
10. Shoaee, M.; Anderson, M. W.; Attfield, M. P. Crystal Growth of the Nanoporous Metal–Organic Framework HKUST-1 Revealed by In Situ Atomic Force Microscopy. *Angew. Chem. Int. Ed*. **2008**, *47* (44), 8525–8528.
11. Wagia, R.; Strashnov, I.; Anderson, M. W.; Attfield, M. P. Determination of the Preassembled Nucleating Units That Are Critical for the Crystal Growth of the Metal–Organic Framework CdIF-4. *Angew. Chem. Int. Ed*. **2016**, *55* (31), 9075–9079.
12. Moh, P. Y.; Cubillas, P.; Anderson, M. W.; Attfield, M. P. Revelation of the Molecular Assembly of the Nanoporous Metal Organic Framework ZIF-8. *J. Am. Chem. Soc.* **2011**, *133* (34), 13304–13307.
13. Wu, Y.; Moorhouse, S. J.; O'Hare, Dermot. Time-Resolved in Situ Diffraction Reveals a Solid-State Rearrangement During Solvothermal MOF Synthesis. *Chem. Mater.* **2015**, *27*, 7236–7239.
14. Ramanan, A.; Whittingham, M. S. How Molecules Turn into Solids: The Case of Self-Assembled Metal−Organic Frameworks. *Cryst. Growth Des*. **2006**, *6* (11), 2419–2421.
15. Biswal, D.; Kusalik, P. G. Probing Molecular Mechanisms of Self-Assembly in Metal–Organic Frameworks. *ACS Nano*. **2017**, *11* (1), 258–268.
16. Xu, H.; Sommer, S.; Broge, N. L. N.; Gao, J.; Iversen, B. B. The Chemistry of Nucleation: In Situ Pair Distribution Function Analysis of Secondary Building Units During UiO-66 MOF Formation. *Chem. Eur. J*. **2019**, *25* (8), 2051–2058.
17. Goesten, M. G.; de Lange, M. F.; Olivos-Suarez, A. I.; Bavykina, A. V.; Serra-Crespo, P.; Krywka, C.; Bickelhaupt, F. M.; Kapteijn, F.; Gascon, J. Evidence for a Chemical Clock in Oscillatory Formation of UiO-66. *Nat. Commun*. **2016**, *7* (1), 11832.

18. Goesten, M. G.; Magusin, P. C. M. M.; Pidko, E. A.; Mezari, B.; Hensen, E. J. M.; Kapteijn, F.; Gascon, J. Molecular Promoting of Aluminum Metal–Organic Framework Topology MIL-101 by N,N-Dimethylformamide. *Inorg. Chem.* **2014**, *53* (2), 882–887.
19. Greer, H. F.; Liu, Y.; Greenaway, A.; Wright, P. A.; Zhou, W. Synthesis and Formation Mechanism of Textured MOF-5. *Cryst. Growth Des*. **2016**, *16* (4), 2104–2111.
20. Yeung, H. H.-M.; Wu, Y.; Henke, S.; Cheetham, A. K.; O'Hare, D.; Walton, R. I. In Situ Observation of Successive Crystallizations and Metastable Intermediates in the Formation of Metal–Organic Frameworks. *Angew. Chem. Int. Ed*. **2016**, *55* (6), 2012–2016.
21. Tanaka, Y.; Kitamura, Y.; Kawano, R.; Shoji, K.; Hiratani, M.; Honma, T.; Takaya, H.; Yoshikawa, H.; Tsuruoka, T.; Tanaka, D. Competing Roles of Two Kinds of Ligand during Nonclassical Crystallization of Pillared-Layer Metal-Organic Frameworks Elucidated Using Microfluidic Systems. *Chem. Eur. J*. **2020**, *26* (41), 8889–8896.
22. Jones, C. L.; Hughes, C. E.; Yeung, H. H.-M.; Paul, A.; Harris, K. D. M.; Easun, T. L. Exploiting in Situ NMR to Monitor the Formation of a Metal–Organic Framework. *Chem. Sci.* **2021**, *12* (4), 1486–1494.
23. Rosi, N. L.; Kim, J.; Eddaoudi, M.; Chen, B.; O'Keeffe, M.; Yaghi, O. M. Rod Packings and Metal−Organic Frameworks Constructed from Rod-Shaped Secondary Building Units. *J. Am. Chem. Soc.* **2005**, *127* (5), 1504–1518.
24. Caskey, S. R.; Wong-Foy, A. G.; Matzger, A. J. Dramatic Tuning of Carbon Dioxide Uptake via Metal Substitution in a Coordination Polymer with Cylindrical Pores. *J. Am. Chem. Soc.* **2008**, *130* (33), 10870–10871.
25. Queen, W. L.; Hudson, M. R.; Bloch, E. D.; Mason, J. A.; Gonzalez, M. I.; Lee, J. S.; Gygi, D.; Howe, J. D.; Lee, K.; Darwish, T. A.; James, M.; Peterson, V. K.; Teat, S. J.; Smit, B.; Neaton, J. B.; Long, J. R.; Brown, C. M. Comprehensive Study of Carbon Dioxide Adsorption in the Metal–Organic Frameworks M_2 (Dobdc) (M = Mg, Mn, Fe, Co, Ni, Cu, Zn). *Chem. Sci.* **2014**, *5* (12), 4569–4581.
26. Schoedel, A.; Li, M.; Li, D.; O'Keeffe, M.; Yaghi, O. M. Structures of Metal–Organic Frameworks with Rod Secondary Building Units. *Chem. Rev.* **2016**, *116* (19), 12466–12535.
27. Caskey, S. R.; Wong-Foy, A. G.; Matzger, A. J. Phase Selection and Discovery among Five Assembly Modes in a Coordination Polymerizationo. *Inorg. Chem*. **2008**, 47 (17), 7751.
28. Cheansirisomboon, A.; Salinas-Uber, J.; Massera, C.; Roubeau, O.; Youngme, S.; Gamez, P. One-Pot Multiple Metal–Organic Framework Formation: Concomitant Generation of Structural Isomers or of Drastically Distinct Materials. *Eur. J. Inorg. Chem*. **2014**, *2014* (26), 4385–4393.
29. Jayaramulu, K.; Kanoo, P.; George, S. J.; Maji, T. K. Tunable Emission from a Porous Metal–Organic Framework by Employing an Excited-State Intramolecular Proton Transfer Responsive Ligand. *Chem. Commun.* **2010**, *46* (42), 7906–7908.
30. Rosnes, M. H.; Mathieson, J. S.; Törnroos, K. W.; Johnsen, R. E.; Cronin, L.; Dietzel, P. D. C. Electrospray Mass Spectrometry Investigation into the Formation of CPO-27. *Cryst. Growth Des*. **2019**, *19* (4), 2089–2096.

31. Friščić, T.; Halasz, I.; Beldon, P. J.; Belenguer, A. M.; Adams, F.; Kimber, S. A. J.; Honkimäki, V.; Dinnebier, R. E. Real-Time and in Situ Monitoring of Mechanochemical Milling Reactions. *Nat. Chem*. **2013**, *5* (1), 66–73.
32. Ahmed, A.; Seth, S.; Purewal, J.; Wong-Foy, A. G.; Veenstra, M.; Matzger, A. J.; Siegel, D. J. Exceptional Hydrogen Storage Achieved by Screening Nearly Half a Million Metal-Organic Frameworks. *Nat. Commun*. **2019**, *10* (1), 1568.
33. Dolomanov, O. V.; Bourhis, L. J.; Gildea, R. J.; Howard, J. a. K.; Puschmann, H. OLEX2: A Complete Structure Solution, Refinement and Analysis Program. *J. Appl. Crystallogr*. **2009**, *42* (2), 339–341.
34. Sheldrick, G. M. SHELXT – Integrated Space-Group and Crystal-Structure Determination. *Acta Crystallogr. A*. **2015**, *71* (1), 3–8.
35. Sheldrick, G. M. Crystal Structure Refinement with SHELXL. *Acta Crystallogr. C*. **2015**, *71* (1), 3–8.

Chapter 3: Metal–Organic Framework Seeding to Drive Phase Selection and Overcome Synthesis Limitations

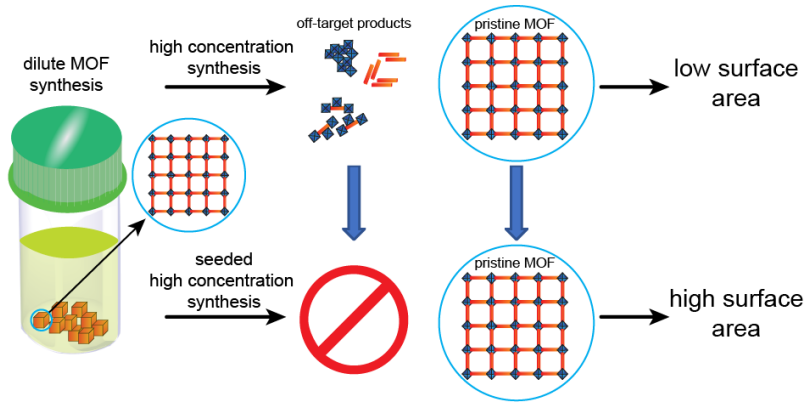

Figure 3.1 Simplified description of Mg-MOF-74 synthesis showing carboxylate coordinating metastable phases which were discovered to precede MOF-74 formation which employs both oxo and carboxylate coordination.

3.1 Publication of This Chapter

Du Bois, D. R.; Matzger, A. J. Metal–Organic Framework Seeding to Drive Phase Selection and Overcome Synthesis Limitations. *Cryst. Growth Des.* **2022**, *22*, 6379.

3.2 Introduction

Seeding in solid-state chemistry finds wide application in both academic research[1–3] and industry,[4,5] notably enabling control over polymorphism, crystal morphology, and yield. In the pharmaceutical setting, polymorph selection through seeding has wide-ranging implications in the pharmacokinetics of many drugs.[6] Silicon wafer fabrication, a process necessitating consistency, is initiated through seeding.[7] Metal–organic framework (MOF) research is only nascent in its incorporation of seeding technology, and

some progress has been made in phase selection,[8] control over morphology,[9] and epitaxial overgrowth.[10] MOF synthesis must advance in terms of yield, solvent choice, and consistent performance for MOFs to fulfill the promise of their sought-after properties. Perhaps the most developed application of seeded growth is in the area of thin films;[11–13] however, it is likely that leveraging such methodology in bulk MOF synthesis will result in increased control over phase selection as well as the ability to increase yield and/or enable increased flexibility in solvent selection, a nontrivial issue when considering the dependency of MOF synthesis on formamide solvents such as DMF that are seeing increased regulatory scrutiny.[14]

MOF synthesis is often performed at dilute concentrations; while this is useful from the perspective of achieving high crystal perfection, future applications will demand large-scale, high-yield syntheses of MOFs while reducing total solvent used. Industry routinely employs seeding to control the kinetics of crystallization and drive phase selection. At high concentrations of metal and linker, it is possible to dramatically improve both throughput and the ratio of MOF generated to solvent used; however, these conditions also cause normally phase pure MOF syntheses to break down,[15] generating off-target phases, increasing defect concentration, and potentially producing amorphous content, all resulting in reduced yield and/or product quality. One possible strategy for phase direction in MOFs to reduce off-target phase production at higher concentrations of metal and linker is seeding, a technique which is hypothesized to enable formation of the desired MOF phase at lower supersaturation. By employing MOFs of the desired phase as seeds, recovery of the target phase at high concentrations of metal and linker is observed in multiple systems, as observed through recovery of surface area, retention of

original morphology, and attenuation of off-target phase reflections by PXRD, and in the case where it fails, *in situ* monitoring of the of the reaction course reveals seed dissolution as an obstacle to phase direction.

3.3 Discussion

Table 3.1 Surface area measurements with associated standard deviation (sample) for unseeded and seeded conditions at various concentrations of metal and linker (see isotherm data in ESI).

System		Unseeded		Seeded	
	Relative concentration	Average surface area (m^2/g)	Std. dev. [population]	Average surface area (m^2/g)	Std. dev. [population]
Mg-MOF-74	1x	1591	120 [3]		
	4.3x	1009	587 [3]	1360	103 [5]
	4.7x	733	592 [9]	1209	182 [9]
	5x	125	34 [3]	1246	230 [3]
DMOF-1	1x	2138	[1]		
	5x	782	35 [3]	1587	88 [3]
UiO-66	1x	1185	32 [3]		
	3x	682	93 [3]	1092	147 [3]

Table 3.2 MOF synthesis conditions and the resulting activated material yields. Synthetic procedures detailed in section 3.5.1.

Target MOF	Relative concentration	Material yield (mg)
Mg-MOF-74	1×	23.0
	5×	214.5
	5× seeded	157.9
DMOF-1	1×	91.7
	5×	745.5
	5× seeded	861.1
UiO-66	1×	455.8
	3×	818.0
	3× seeded	857.1

Mg-MOF-74[16] comprises magnesium ions forming 1-D rod SBUs coordinated to 2,5-dioxido-1,4-benzenedicarboxylate. This MOF possesses desirable properties including coordinatively unsaturated metal sites and high performance in CO_2 capture from low partial pressures relevant to flue gas. Employing a modified literature synthesis[16]

of Mg-MOF-74 results in an average surface area of 1591 m^2/g with the experimental PXRD pattern matching the theoretical pattern (see details in section 3.5.1 and Figure 3.2). At five times (5×) the concentration of metal and linker, the average surface area falls dramatically to 125 m^2/g (Table 3.1, see isotherm data in appendix B.2.2). The seeding method reduces the relative standard deviation and, critically, results in substantial improvements to surface area. Seeding was performed using the MOF crystals from a 1× concentration synthesis. The crystals were ground in a small quantity of DMF with a mortar and pestle; as smaller seed crystal sizes enhance phase direction by providing additional surface area for crystal growth, thus depleting supersaturation more rapidly. Aliquots containing ~4.5 mg of ground crystals (to overcome seed dissolution, Figure B.19) in a small quantity of DMF were employed for 10 mL synthesis scale (see details in section 3.5.1). The improvement to surface area does not arise directly from the presence of Mg-MOF-74 seed crystals, because the material yield at the 5× scale exceeds 150 mg (Table 3.2), and ~4.5 mg of seeds would not account for the substantial increases to surface area observed. PXRD performed before activation reveals that high concentration, unseeded conditions have an increased number of reflections associated with additional expressed phases relative to the seeded conditions (Figure 3.3a and Figure 3.2). Three phases associated with the 5× concentration synthesis condition are DMF solvates, and upon activation, PXRD shows that only peaks associated with Mg-MOF-74 remain, indicating that these phases amorphize during the activation process (Figure 3.2). For the 1× concentration synthesis, scanning-electron microscopy (SEM) shows uniform rod-like crystals that aggregate (Figure 3.3b and Figure B.20 for the bulk distribution). New phases form in the 5× concentration synthesis

including a spherical material (Figure 3.3c and Figure B.21 for the bulk distribution). It has been shown that, at high concentration, multiple phases can be stabilized over the course of a Mg-MOF-74 synthesis, and the increased variability related to the expression of multiple phases is magnified by the stochastic nature of crystal nucleation.[15] Seeding the synthesis of Mg-MOF-74 enables enhanced phase selection as evidenced by PXRD and SEM which shows reduced expression of off-target phases (Figure 3.3a and Figure B.22).

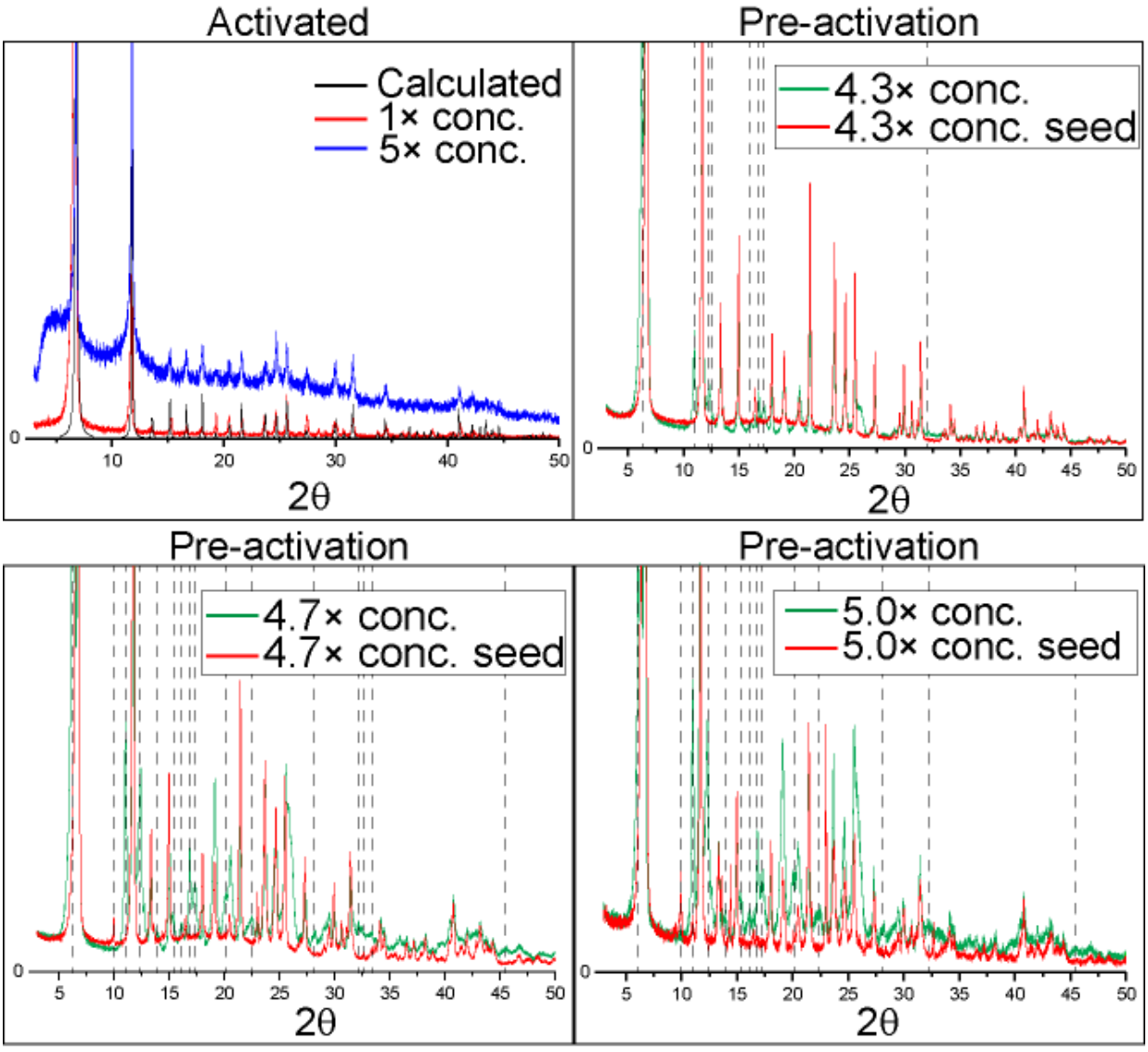

Figure 3.2 (top left) PXRD patterns of the calculated and activated 1× concentration synthesis of Mg-MOF-74 agree. After activation, the powder pattern of the 5×

concentration synthesis also matches Mg-MOF-74, likely due to amorphization of the off-target material. (top right) The PXRD patterns of the unseeded and seeded 4.3× material, only washed in DMF, are compared. Dashed lines highlight peaks showing off-target phase formation. (bottom left) The PXRD patterns of the unseeded and seeded 4.7× material, only washed in DMF, are compared. Dashed lines highlight peaks showing off-target phase formation (bottom right) The PXRD patterns of the unseeded and seeded 5× material, only washed in DMF, are compared. Dashed lines highlight peaks showing off-target phase formation.

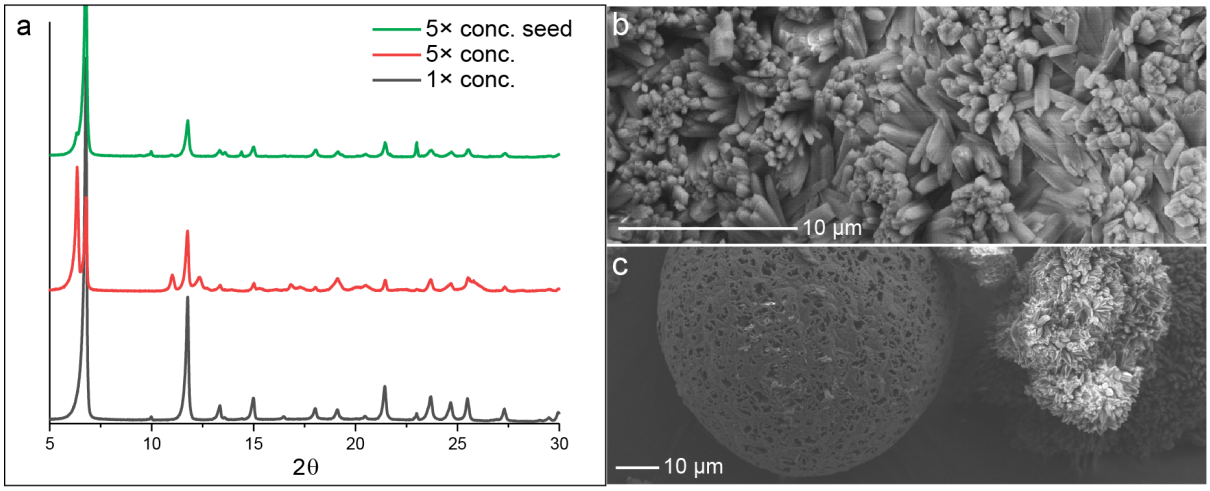

Figure 3.3 (a) PXRD patterns of Mg-MOF-74 synthesized under 1×, 5×, and seeded 5× concentration synthesis conditions. (b) SEM of the 1× concentration synthesis condition showing uniform rod-like crystals. (c) SEM of the 5× concentration synthesis.

To investigate the influence of seeding on a paddlewheel metal cluster motif with multiple linker types, DMOF-1[17] was subjected to a seeding protocol. In this MOF, linkers coordinate to the metal cluster through carboxylate, as terephthalate, and tertiary amine, as 1,4-diazabicyclo[2.2.2.]octane, linkers. The published surface area for DMOF-1 is 1960 m^2/g,[18] and in checking the reproducibility of the synthesis, a surface area of 2138 m^2/g was achieved with the experimental PXRD pattern matching the theoretical pattern (Figure B.1). Under 5× concentration conditions, the synthesis produced a material with an average surface area of 782 m^2/g (Table 3.1, see isotherm data in appendix B.2.2) indicating a significant erosion of material quality. The seeded 5× concentration condition produced a material with an average surface area of 1587 m^2/g. To seed the high concentration synthesis condition, two drops of DMF with suspended seeds (ground with

DMF in mortar and pestle, ~15 mg) from the 1× concentration synthesis were added to the reaction solution (see details in section 3.5.1). The improvement to surface area does not arise directly from the presence of DMOF-1 seed crystals, because the material yield at the 5× scale exceeds 850 mg (Table 3.2), and ~15 mg of seeds would not account for the substantial increases to surface area observed. Comparing the PXRD patterns of the activated material shows that both the seeded and the unseeded 5× concentration synthesis conditions result in additional peaks relative to the 1× condition, corresponding to off-target phase formation; however, the seeded condition preferentially forms DMOF-1, attenuating off-target phase formation (Figure 3.4a). SEM demonstrates that the 1× concentration conditions produce a material with truncated cubic prism morphology that is generally less than 10 μm long (Figure 3.4b and Figure B.23 for the bulk distribution). At 5× concentration, 100 μm striated blocks comprised of aggregated plates form as part of a mixture with the DMOF-1 phase (Figure 3.4c and Figure B.24 for the bulk distribution).

The seeded 5× concentration condition greatly reduces the presence of the off-target phase as reflected in the PXRD and SEM data (Figure 3.4a and Figure B.25).

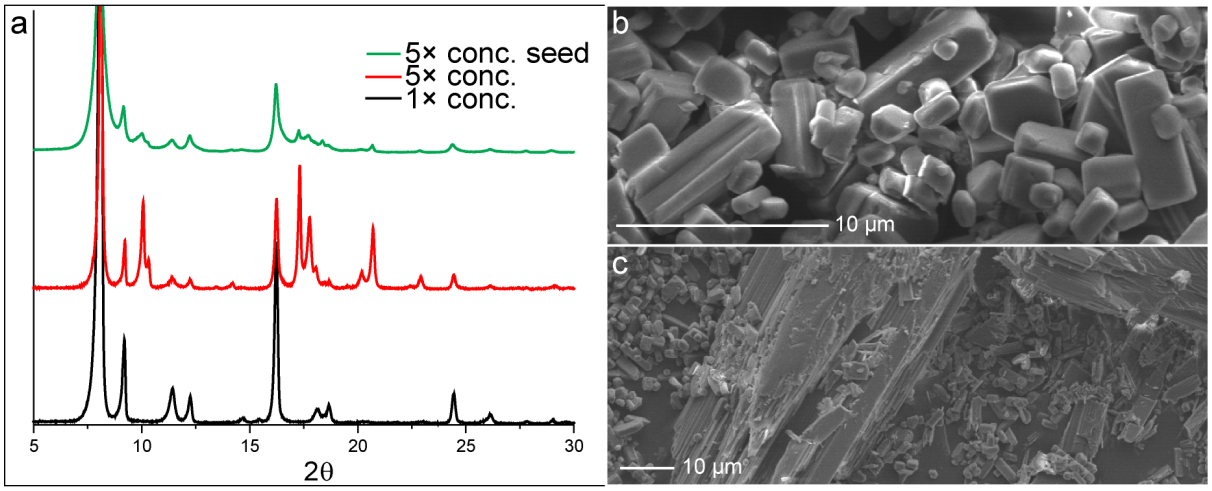

Figure 3.4 (a) PXRD patterns of DMOF-1 synthesized under 1×, 5×, and seeded 5× concentration synthesis conditions. (b) SEM of the 1× concentration synthesis condition showing truncated cubic prism morphology crystals. (c) SEM of the 5× concentration synthesis condition showing off-target phase, a large, striated block comprised of aggregated plates as part of a mixture with the DMOF-1 phase.

SNU-70[19] was investigated because of its high surface area, superb hydrogen storage performance,[20] and its reliance on the widely employed $Zn_4O(-COO)_6$ metal cluster[21] which connects to 4-(2-carboxyvinyl)benzoate linkers.[19] Seeding using multiple methods consistently resulted in a reduction of surface area of the synthesized material. Seed crystals were observed to dissolve by *in situ* optical time-lapse observation (Figure 3.5) which appears to prevent phase direction. The seeding methods attempted to phase direct the 5× concentration synthesis condition employed introduction of variable quantities of seed crystals, introduction of seed crystals at around the time point of nucleation, switching the synthesis solution with a parallel 1× concentration condition which had nucleated, and using the washed contents of a completed 1× concentration synthesis vial to seed the synthesis. Although the methods of seed incorporation used are not exhaustive, SNU-70 clearly does not respond readily to phase direction via the

seeding methods employed and further changes to the synthetic conditions are being explored that potentially inhibit seed dissolution and enable phase direction. The challenges in phase directing SNU-70 formation using the seeding method serves as a reminder that MOF nucleation and growth phenomena are still under active investigation, and as a result, methodology which applies to one or multiple MOF systems may not work for all of them. Surface area, isotherm, and PXRD data are included for consideration (Figures 3.6 and B.13-B.15)

SNU-70 7× concentration seeded synthesis

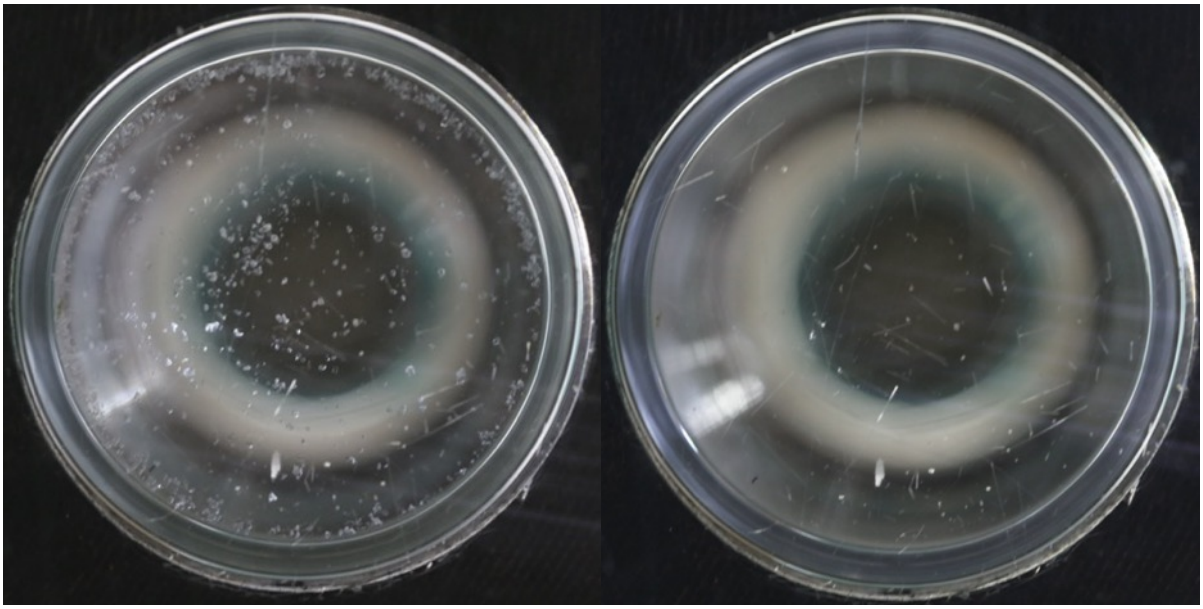

Figure 3.5 One of a variety of conditions explored to implement seeding in the high concentration synthesis of SNU-70: (left) At 0 minutes, seed crystals are added to the 7× reaction mixture. (right) At 30 minutes, seed dissolution is complete.

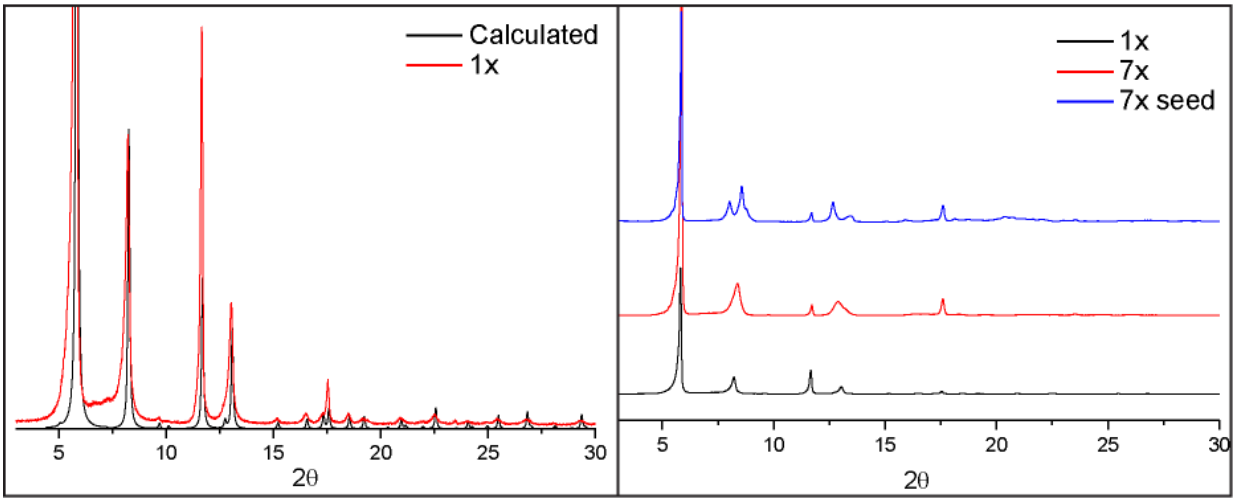

Figure 3.6 (left) PXRD patterns of the calculated and activated 1× concentration synthesis of SNU-70 agree. (right) The PXRD patterns of SNU-70 synthesized under 1×, 7×, and seeded 7× concentration synthesis conditions.

UiO-66,[22] a highly water stable MOF, features cuboctahedral 12-connected Zr_6O_8-core SBUs connected by terepthalate linkers. A synthesis procedure to make "defect-free" UiO-66 was employed,[23] and the average surface area by BET analysis was 1185 m^2/g with the experimental PXRD pattern matching the theoretical pattern (Figure B.2). At 3× concentration synthesis conditions, a surface area of 682 m^2/g was obtained (Table 3.1, see isotherm data in appendix B.2.2). The seeded conditions result in an increased surface area of 1092 m^2/g which arose due to the robust nature of the crystal seeds which remained after employing a washing process (see details in section 3.5.1). PXRD data from the activated materials indicates that at increased concentrations of metal and linker, the synthesis of UiO-66 generates at least one off-target phase (Figure 3.7a). Seeding does not eliminate the off-target phase(s); however, the dramatic increase in surface area provides evidence of its efficacy as a phase director. SEM analysis of the MOF crystals shows formation of aggregates of small crystals with uniform size during the 1× concentration synthesis (Figure 3.7b and Figure B.26 for the bulk distribution). The 3×

concentration synthesis shows the formation of plates in addition to the small crystals with uniform size (Figure 3.7c and Figure B.27 for the bulk distribution). UiO-66 phase-directed synthesis with seeding produces a superior material to the unseeded condition which is observable by PXRD and SEM (Figure 3.7a and Figure B.28 for the bulk distribution).

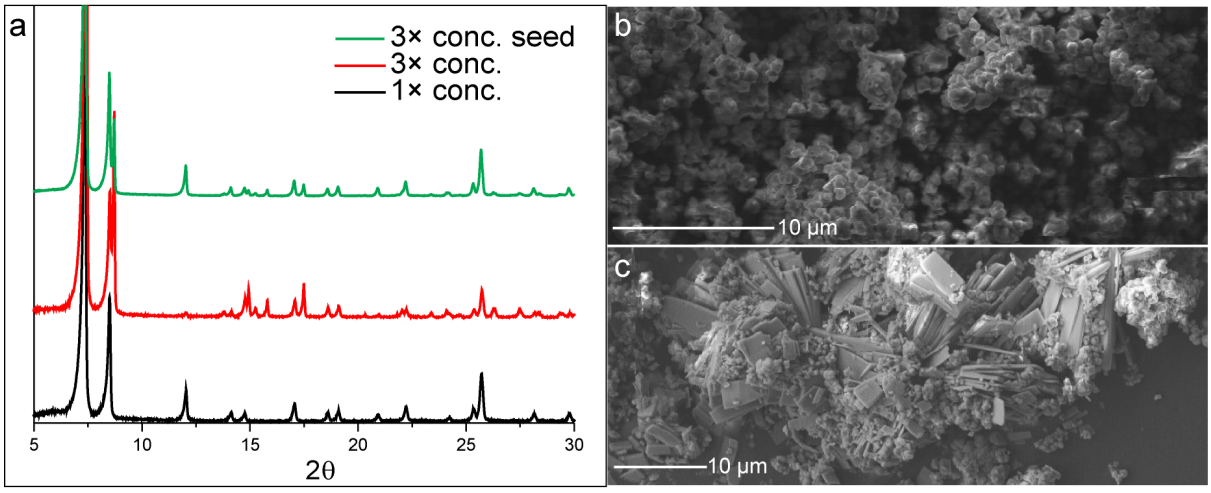

Figure 3.7 (a) PXRD patterns of UiO-66 synthesized under 1×, 5×, and seeded 5× concentration synthesis conditions. (b) SEM of the 1× concentration synthesis condition showing aggregates of small crystals with uniform size. (c) SEM of the 5× concentration synthesis condition showing plate formation along with small crystals of uniform size.

3.4 Conclusions

Seeding MOF syntheses at high concentration represents a general and facile method that enables enhanced production of the desired phase, even under conditions which otherwise result in loss of surface area. The systems employed vary in metal cluster, linker, and connectivity, providing evidence that seeding for phase direction will be applicable to a wide variety of MOFs. Seeding MOF syntheses dramatically improves the yield over the unseeded conditions and reduces variance caused by stochastic processes during crystallization, all while requiring much less solvent overall to produce the desired MOF. Both Mg-MOF-74 and DMOF-1 respond to a straightforward seeding

methodology wherein seed crystals are ground in DMF in a mortar and pestle and introduced directly to the high concentration synthesis solution. In attempting to use seeding to phase direct the synthesis of various MOFs, seed crystal dissolution has been observed, and in the case of SNU-70, synthesis at high concentrations appears resistant to a variety of methods for seeding. BET surface area analysis provides the most direct evidence for the efficacy of the seeding approach, because formation of off-target phases or amorphous materials will result in a loss of surface area, with increased hysteresis also observed. For each of the MOF systems employed, PXRD enables observation of the target MOF as well as attenuation or elimination of off-target phase production when seeding is successfully employed. Microscopy enables observation of deviations in morphology of the target phase during high concentration synthesis and can indicate the presence of off-target phases. The future application of seeding for MOF crystallization requires some exploration of methodology to optimize for phase purity and yield, because current methods drastically reduce but do not eliminate off-target phase formation. Investment into developing system-specific seeding methods will enhance phase purity and facilitate economic scaleup. Applications for the implementation of seeding in MOF synthesis continue to show promise, notably enabling phase selection,[8] generating MOF superstructures,[9] and now in phase-directing the synthesis of MOFs at high concentration.

3.5 Experimental details

Chemicals were used as purchased without purification unless otherwise noted. 1,4-Diazabicyclo[2.2.2]octane (DABCO) and *N,N*-diethylformamide (DEF) were purchased from Acros Organics. Terepthalic acid (H_2BDC) was purchased from Sigma-Aldrich. 4-(2-

Carboxyvinyl)benzoic acid was purchased from AmBeed. Absolute methanol (MeOH), *n*-hexane, concentrated hydrochloric acid (HCl), zinc nitrate hexahydrate, and magnesium nitrate hexahydrate were purchased from Fisher Scientific. Dry chloroform stabilized with amylene was stored over 4 Å molecular sieves as were *N,N*-dimethylformamide (DMF) and methylene chloride. 2,5-Dihydroxyterepthalic acid (H_4DOBDC) was purchased from HangZhou Trylead Chemical Technology Co., Ltd. Absolute ethanol and Contrex AP was purchased from Decon Labs. Zirconium(IV) chloride was purchased from Strem Chemicals. JEOL aluminum specimen mounts were used with PELCO carbon conductive tabs, both from Ted Pella as stages for scanning electron microscopy (SEM).

3.5.1 Synthesis

Mg-MOF-74 was synthesized using a modified literature procedure.[16]

1× concentration synthesis. To a solid mixture of H_4DOBDC (22.2 mg, 0.112 mmol) and $Mg(NO_3)_2{\cdot}6H_2O$ (57.4 mg, 0.224 mmol) in a 20 mL scintillation vial was added a 15:1:1 (v/v/v) mixture of DMF:ethanol:deionized water (10 mL). The vial was capped tightly with a Teflon-lined cap. The suspension was sonicated until homogeneous. The reaction vial was placed in an oven at 125 °C. After 20 hours, the sample was removed from the oven and allowed to cool to room temperature (RT). The mother liquor was decanted and replaced with DMF (3 × 10 mL). PXRD was performed, before activation of the material from MeOH. After PXRD was performed, the remaining material was washed with MeOH (4 × 10 mL) and activated prior to BET surface area analysis and subsequent SEM. Activation of material from MeOH was performed using a Quantachrome MasterPrep Vacuum and Flow Degasser under vacuum at RT for 2 h and at 175 °C for 8 h.

5× concentration synthesis. The 5× concentration synthesis, activation, and analysis of Mg-MOF-74 follows the procedure of the 1× concentration synthesis with the quantity of each of H_4DOBDC and $Mg(NO_3)_2 \cdot 6H_2O$ being multiplied by five.

5× concentration seeded synthesis. The 5× concentration seeded synthesis, activation, and analysis of Mg-MOF-74 follows the procedure of the 1× concentration synthesis with the quantity of each of H_4DOBDC and $Mg(NO_3)_2 \cdot 6H_2O$ being multiplied by five and the reaction mixture having 200 μL less of DMF. Seeds were prepared by grinding all the Mg-MOF-74 from a 1× concentration synthesis vial with a small quantity of DMF and separating into 200 μL aliquots. Seeds (~4.5 mg) were introduced into the reaction vessel and the mixture was sonicated for ~15 s before placement into the oven.

DMOF-1 was synthesized using a modified literature procedure.[18]

1× concentration synthesis. To a solid mixture of BDC (102 mg, 0.614 mmol), DABCO (108 mg, 0.963 mmol), and $Zn(NO_3)_2 \cdot 6H_2O$ (174 mg, 0.585 mmol) in a 20 mL scintillation vial was added 15 mL DMF. The vial was capped tightly with a Teflon-lined cap. The suspension was sonicated for ~5 minutes without reaching homogeneity. The reaction vial was placed in an oven at 120 °C. After 12 hours, the sample was removed from the oven and allowed to cool to RT. The mother liquor was decanted and replaced with DMF (3 × 10 mL) followed by $CHCl_3$ (3 × 10 mL) before activation. Activation of material from $CHCl_3$ was performed using a Quantachrome MasterPrep Vacuum and Flow Degasser under vacuum at RT for 2 h and at 105 °C for 8 h. BET surface area analysis, PXRD, and SEM was performed on the activated material.

5× concentration synthesis. The 5× concentration synthesis, activation, and analysis of DMOF-1 follows the procedure of the 1× concentration synthesis with the quantity of each of BDC, DABCO, and $Zn(NO_3)_2 \cdot 6H_2O$ being multiplied by five.

5× concentration seeded synthesis. The 5× concentration seeded synthesis, activation, and analysis of DMOF-1 follows the procedure of the 1× concentration synthesis with the quantity of each of BDC, DABCO, and $Zn(NO_3)_2 \cdot 6H_2O$ being multiplied by five. Seeds were prepared by grinding all the DMOF-1 from a 1× concentration synthesis vial in a small quantity of DMF. Seeds (~15 mg) were introduced as a suspension in two drops of DMF which were added to the reaction mixture and sonicated for ~15 s before placement in oven.

SNU-70 was synthesized using a modified literature procedure.[19]

1× concentration synthesis. To a solid mixture of 4-(2-carboxyvinyl)benzoic acid (75 mg, 0.390 mmol) and $Zn(NO_3)_2 \cdot 6H_2O$ (150 mg, 0.504 mmol) was added 25 mL DEF. The mixture was sonicated until homogeneous. The mixture was then filtered through a 0.45 μm polytetrafluoroethylene filter into a 60 mL vial (27.5 mm bottom diameter) which was capped tightly with a Teflon-lined cap. The reaction vial was placed in an oven at 105 °C. After 12.5 hours, the sample was removed from the oven and allowed to cool to RT. The mother liquor was decanted and replaced with DMF (3 × 10 mL) followed by CH_2Cl_2 (3 × 10 mL) and *n*-hexane (3 × 10 mL) before activation. Activation of material from *n*-hexane was performed under vacuum at RT overnight. BET surface area analysis was performed on the activated material.

7x concentration synthesis. The 7× concentration synthesis, activation, and analysis of SNU-70 follows the procedure of the 1× concentration synthesis with the quantity of each of 4-(2-carboxyvinyl)benzoic acid and $Zn(NO_3)_2 \cdot 6H_2O$ being multiplied by seven.

7x concentration seeded synthesis. The 7× concentration seeded synthesis, activation, and analysis of SNU-70 follows the procedure of the 1× concentration synthesis with the quantity of each of 4-(2-carboxyvinyl)benzoic acid and $Zn(NO_3)_2 \cdot 6H_2O$ being multiplied by seven. Seeds were prepared and introduced to the reaction vessel using a variety of methods as described in the section 3.3.

UiO-66 was synthesized using a literature procedure.[23]

1× concentration synthesis. In sequence, DMF (9.74 mL) was added to $ZrCl_4$ (378 mg, 1.62 mmol), the mixture was sonicated, and HCl (286 μL) was added with additional sonication until homogeneity is reached.H_2BDC (539 mg, 3.24 mmol) was added to the mixture with ~5 minutes of sonication afterwards. The mixture was pipetted into a Teflon-lined hydrothermal autoclave reactor. The reaction vessel was placed in an oven at 220 °C. After 20 hours, the sample was removed from the oven and allowed to cool to RT. The mother liquor was decanted and replaced with DMF (3 × 10 mL), aided by centrifugation, followed by MeOH (4 × 10 mL) before activation. Activation of material from MeOH was performed using a Quantachrome MasterPrep Vacuum and Flow Degasser under vacuum at RT for 2 h and at 150 °C for 8 h. BET surface area analysis, PXRD, and SEM was performed on the activated material.

3× concentration synthesis. The 3× concentration synthesis, activation, and analysis of UiO-66 follows the procedure of the 1× concentration synthesis with the quantity of each of 4-(2-carboxyvinyl)benzoic acid and $Zn(NO_3)_2 \cdot 6H_2O$ being multiplied by three.

3× concentration seeded synthesis. The 3× concentration seeded synthesis, activation, and analysis of SNU-70 follows the procedure of the 1× concentration synthesis with the quantity of each of 4-(2-carboxyvinyl)benzoic acid and $Zn(NO_3)_2 \cdot 6H_2O$ being multiplied by three. Seeds were left adhered to the reaction vessel and subjected to washing with Contrex AP (majority component: sodium carbonate) and water, scrubbed with a bottle brush, washed with acetone, and left in an oven to dry overnight before the vessel containing the seeds was used for synthesis.

3.5.2 Characterization

Brunauer, Emmett, and Teller (BET) Surface Area Analysis

BET surface areas were calculated from the nitrogen adsorption isotherm at 77 K. Measurements were taken from 0.005 to 1 bar using a NOVA e-series 4200 surface area analyzer from Quantachrome Instruments.

Powder X-Ray Diffraction

Powder X-ray diffraction was performed on a PANalytical Empyrean diffractometer in Bragg–Brentano geometry (Cu $K\alpha$ radiation, 45 kV, and 40 mA). The incident beam was equipped with a Bragg–BrentanoHD X-ray optic using fixed slits/soller slits. X-ray detection was accomplished with a silicon-based linear position sensitive X'Celerator Scientific detector operating in 1D scanning mode. Patterns were collected between 3 – 50 °2θ, with a scan rate of 0.008 ° and 20 seconds per step.

Scanning electron microscopy (SEM)

A JEOL JSM-7800FLV scanning electron microscope operating with an accelerating voltage of 20 kV was used for SEM experiments. Samples were carbon coated prior to analysis.

In situ camera setup

The camera setup comprises the following components: Canon EOS 5DS DSLR camera, Canon MP-E 65mm f/2.8 1.5-5x Macro lens, circular aluminum block with a hole in the center (drilled for 20 mL vials), 4 × 4 × 1/8'' quartz plate, heating tape capable of 313 Watts of power, J-KEM Scientific temperature controller model 210, a thermocouple, red silicone rubber, 1 band clamp, ring light for overhead illumination, and focused fiber optic light source for bottom illumination.

Assembly:

The camera optical station was assembled by fist wrapping the aluminum block with the heat tape. Silicone rubber was wrapped around the tape to ensure thermal insulation. A band clamp was then fastened around the rubber, heat tape, and aluminum to immobilize the heating element. This heat block was then placed on top of the quartz plate and equilibrated at the MOF synthesis temperature. Underneath the heated block and quartz plate, was the Canon EOS 5DS DSLR camera fitted with the macro lens. Inside of the through hole of the aluminum cell a vial was inserted along with the thermocouple to monitor the temperature of the apparatus.

Experimental Parameters:

Data acquisition was conducted with the vial at MOF synthesis temperature. The vial containing precursor MOF solution was inserted into the preheated block and held for a preset time. The camera was externally hooked up to a desktop computer with the

software package DSLR Remote Pro for time-lapse shooting. Specific parameters for time-lapse/ bulb shooting include: 1 frame every 30 seconds for the duration of acquisition, F stop 6.3.

3.6 Acknowledgements

This work was supported by the U.S. Department of Energy (DE-SC0004888). SEM work was conducted at the Robert B. Mitchell Electron Microbeam Analysis Lab, part of the University of Michigan's Department of Earth & Environmental Sciences.

3.7 References

1. Xia, Y.; Xia, X.; Peng, H.-C. Shape-Controlled Synthesis of Colloidal Metal Nanocrystals: Thermodynamic versus Kinetic Products. *J. Am. Chem. Soc.* **2015**, *137* (25), 7947–7966.
2. Iyoki, K.; Itabashi, K.; Okubo, T. Progress in Seed-Assisted Synthesis of Zeolites without Using Organic Structure-Directing Agents. *Microporous Mesoporous Mater.* **2014**, *189*, 22–30.
3. Coquerel, G. Preferential Crystallization. In *Novel Optical Resolution Technologies*; Sakai, K., Hirayama, N., Tamura, R., Eds.; Topics in Current Chemistry; Springer: Berlin, Heidelberg, 2007; pp 1–51.
4. Bauer, J.; Spanton, S.; Henry, R.; Quick, J.; Dziki, W.; Porter, W.; Morris, J. Ritonavir: An Extraordinary Example of Conformational Polymorphism. *Pharm. Res.* **2001**, *18* (6), 859–866.
5. Beckmann, W. Seeding the Desired Polymorph: Background, Possibilities, Limitations, and Case Studies. *Org. Process Res. Dev.* **2000**, *4* (5), 372–383.
6. Lee, E. H. A Practical Guide to Pharmaceutical Polymorph Screening & Selection. *Asian J. Pharm. Sci.* **2014**, *9* (4), 163–175.
7. Scheel, H. J. Historical Aspects of Crystal Growth Technology. *J. Cryst. Growth* **2000**, *211* (1), 1–12.
8. Xu, H.-Q.; Wang, K.; Ding, M.; Feng, D.; Jiang, H.-L.; Zhou, H.-C. Seed-Mediated Synthesis of Metal–Organic Frameworks. *J. Am. Chem. Soc.* **2016**, *138* (16), 5316–5320.
9. Feng, L.; Wang, K.-Y.; Yan, T.-H.; Zhou, H.-C. Seed-Mediated Evolution of Hierarchical Metal–Organic Framework Quaternary Superstructures. *Chem. Sci.* **2020**, *11* (6), 1643–1648.
10. Koh, K.; Wong-Foy, A. G.; Matzger, A. J. MOF@MOF: Microporous Core-Shell Architectures. *Chem. Commun.* **2009**, No. 41, 6162–6164.
11. Zhang, F.; Zou, X.; Gao, X.; Fan, S.; Sun, F.; Ren, H.; Zhu, G. Hydrogen Selective NH2-MIL-53(Al) MOF Membranes with High Permeability. *Adv. Funct. Mater.* **2012**, *22* (17), 3583–3590.

12. Yoo, Y.; Lai, Z.; Jeong, H.-K. Fabrication of MOF-5 Membranes Using Microwave-Induced Rapid Seeding and Solvothermal Secondary Growth. *Microporous Mesoporous Mater.* **2009**, *123* (1), 100–106.
13. Gascon, J.; Aguado, S.; Kapteijn, F. Manufacture of Dense Coatings of Cu3(BTC)2 (HKUST-1) on α-Alumina. *Microporous Mesoporous Mater.* **2008**, *113* (1), 132–138.
14. *Commission Regulation (EU) 2021/2030 of 19 November 2021 Amending Annex XVII to Regulation (EC) No 1907/2006 of the European Parliament and of the Council Concerning the Registration, Evaluation, Authorisation and Restriction of Chemicals (REACH) as Regards N,N-Dimethylformamide (Text with EEA Relevance)*; 2021; Vol. 415.
15. Du Bois, D. R.; Wright, K. R.; Bellas, M. K.; Wiesner, N.; Matzger, A. J. Linker Deprotonation and Structural Evolution on the Pathway to MOF-74. *Inorg. Chem.* **2022**. *61*, 11, 4550–4554
16. Caskey, S. R.; Wong-Foy, A. G.; Matzger, A. J. Dramatic Tuning of Carbon Dioxide Uptake via Metal Substitution in a Coordination Polymer with Cylindrical Pores. *J. Am. Chem. Soc.* **2008**, *130* (33), 10870–10871.
17. Lee, J. Y.; Olson, D. H.; Pan, L.; Emge, T. J.; Li, J. Microporous Metal-Organic Frameworks with High Gas Sorption and Separation Capacity. *Adv. Funct. Mater.* **2007**, *17* (8), 1255–1262.
18. Schoenecker, P. M.; Carson, C. G.; Jasuja, H.; Flemming, C. J. J.; Walton, K. S. Effect of Water Adsorption on Retention of Structure and Surface Area of Metal–Organic Frameworks. *Ind. Eng. Chem. Res.* **2012**, *51* (18), 6513–6519.
19. Prasad, T. K.; Suh, M. P. Control of Interpenetration and Gas-Sorption Properties of Metal-Organic Frameworks by a Simple Change in Ligand Design. *Chem. Eur. J.* **2012**, *18* (28), 8673–8680.
20. Ahmed, A.; Seth, S.; Purewal, J.; Wong-Foy, A. G.; Veenstra, M.; Matzger, A. J.; Siegel, D. J. Exceptional Hydrogen Storage Achieved by Screening Nearly Half a Million Metal-Organic Frameworks. *Nat. Commun.* **2019**, *10* (1), 1568.
21. Eddaoudi, M.; Kim, J.; Rosi, N.; Vodak, D.; Wachter, J.; O'Keeffe, M.; Yaghi, O. M. Systematic Design of Pore Size and Functionality in Isoreticular MOFs and Their Application in Methane Storage. *Science* **2002**, *295* (5554), 469–472.
22. Cavka, J. H.; Jakobsen, S.; Olsbye, U.; Guillou, N.; Lamberti, C.; Bordiga, S.; Lillerud, K. P. A New Zirconium Inorganic Building Brick Forming Metal Organic Frameworks with Exceptional Stability. *J. Am. Chem. Soc.* **2008**, *130* (42), 13850–13851.
23. Shearer, G. C.; Chavan, S.; Ethiraj, J.; Vitillo, J. G.; Svelle, S.; Olsbye, U.; Lamberti, C.; Bordiga, S.; Lillerud, K. P. Tuned to Perfection: Ironing Out the Defects in Metal–Organic Framework UiO-66. *Chem. Mater.* **2014**, *26* (14), 4068–4071.

Chapter 4: Reagent Reactivity and Solvent Choice Determine Metal–Organic Framework Microstructure during Postsynthetic Modification

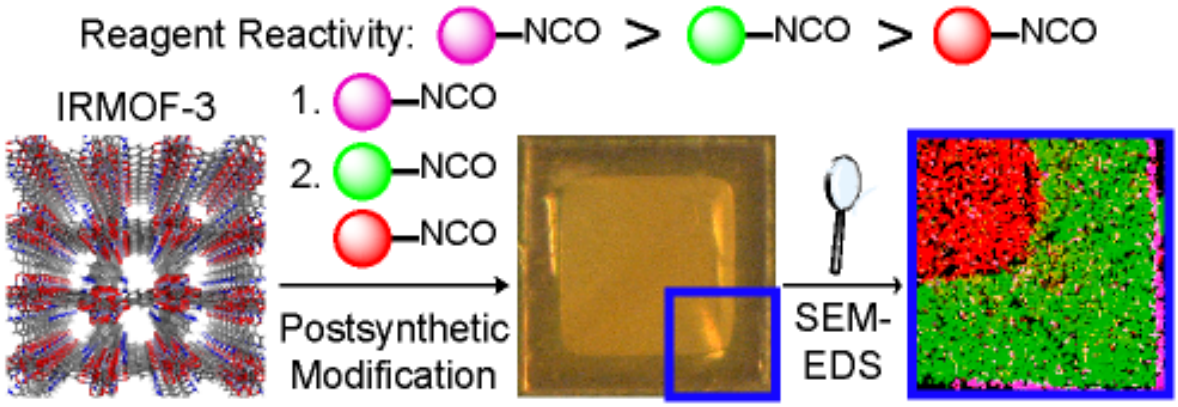

Figure 4.1 Simplified description of microstructure modification via postsynthetic modification. The resulting three-layer structure consists of IRMOF-3, covalently modified by three distinct isocyanates.

4.1 Publication of This Chapter

Du Bois, D. R.; Matzger, A. J. Reagent Reactivity and Solvent Choice Determine Metal–Organic Framework Microstructure during Postsynthetic Modification. *J. Am. Chem. Soc.* **2021**, *143*, 671.

4.2 Introduction

Leveraging controlled microstructure manipulation is viewed as a means to introduce advanced functionality such as sequential catalysis, size-selective catalysis, and separations capabilities to metal–organic frameworks (MOFs).[1–3] Postsynthetic methods enable access to MOFs with modified ligands, metals, and functional groups that are otherwise difficult to obtain by direct synthesis. Clever manipulation of the various

classes of postsynthetic methods[4–7] have given rise to sophisticated MOFs,[1,8–14] demonstrating internal and external control over the MOF crystal. Crystal overgrowth is a common method by which MOF microstructure is controlled;[6,10,15,16] this technique is incorporated into the creation of advanced forms including hollow,[17] Matryoshka,[18,19] and double-shell hollow[1,20] MOFs. Postsynthetic linker exchange[12,21–24] and transmetalation[25] have also been shown to affect MOF microstructure. This expansion in the usage of postsynthetic methods has led to a growing list of structurally diversified MOFs capable of performing multiple tasks and displaying increased performance.[10,21,26–29] Despite continuing success in using postsynthetic methods to increase the complexity of MOF architecture, postsynthetic modification (PSM), the covalent postsynthetic method, is underutilized. The utility of PSM in affecting MOF domain stratification is presented here, providing evidence that PSM can be a powerful tool towards designing MOFs with increasingly sophisticated microstructures by simple and scalable synthetic approaches.

In theory, during PSM, the spatial distribution of substituents added to the MOF framework will follow one of two limiting outcomes: 1) the reagent will react with the MOF linkers faster than it can diffuse through the MOF, resulting in the formation of a core–shell microstructure, or 2) the reagent will diffuse through the MOF more quickly than it can react with the MOF, leading to a uniform microstructure with random functional group distribution throughout the framework (Figure 4.2). At one extreme, PSM restricted to the MOF surface has been reported, often by employing bulky substituents that inhibit reagent diffusion beyond the MOF surface.[30–35] What has not been explored is the effect of reactivity on the spatial distribution of new substituents within the MOF. Here we demonstrate that by varying reactivity through reagent and solvent choice, both

core–shell and uniform microstructures can be obtained, and intermediate distributions of new functionality can be induced as well. This provides a complement to postsynthetic exchange methods and allows the incorporation of alternative functionalities.

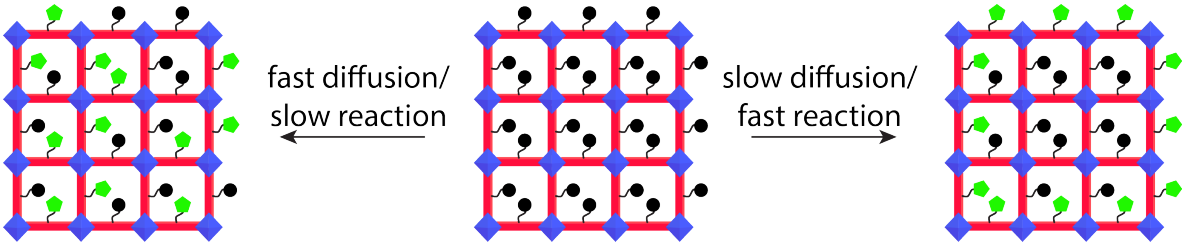

Figure 4.2 Diagram of expected PSM MOF products depending on relative rates of diffusion and reaction. Left: fast diffusion relative to reaction yields a product with randomly distributed new functionality. Right: slow diffusion relative to reaction yields a product with a core-shell distribution of new functionality.

4.3 Discussion

IRMOF-3, comprised of Zn_4O metal clusters and 2-aminobenzene dicarboxylate linkers, was chosen as the model system for investigation, because it forms large crystals which enable spatially resolved observations on the distribution of new functionality, and it has large pore apertures (9.0 Å)[36] that allow diffusion for a variety of molecules used for PSM. Halogenated reagents were chosen for the PSM of IRMOF-3 (Scheme 4.1), allowing for the determination of their spatial distribution by energy-dispersive X-ray spectroscopy (EDS) in conjunction with scanning electron microscopy (SEM) on cross sections of crystals. Electronically differentiated isocyanates were chosen to model differences in reagent reactivity and their effect on microstructure after PSM. PSM was conducted in chloroform and toluene to determine the effect of solvent polarity on microstructure.

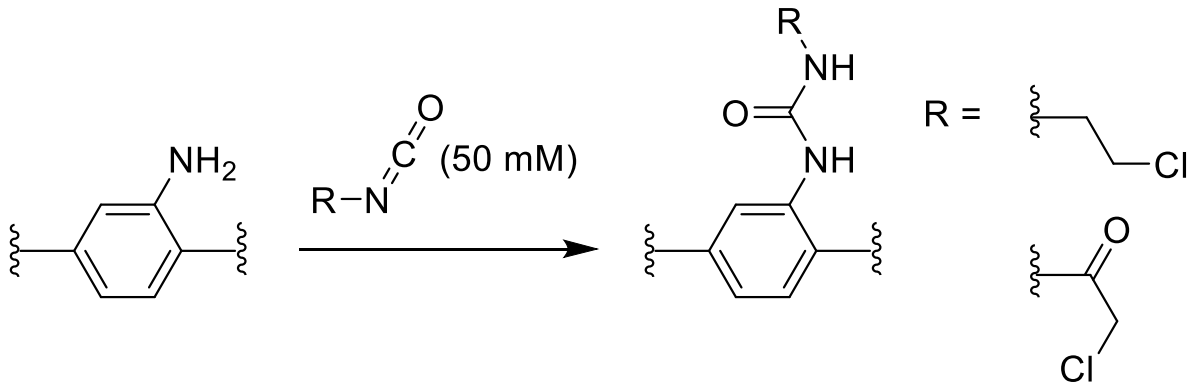

Scheme 4.1 2-aminobenzene dicarboxylate linkers of IRMOF-3 modified via PSM with halogenated isocyanates.

SEM-EDS images of MOF cross sections after PSM with either of two electronically differentiated isocyanates, 2-chloroethyl isocyanate or chloroacetyl isocyanate, show differences in the spatial distribution of new substituents: more uniform microstructure after PSM with 2-chloroethyl isocyanate and core–shell microstructure after PSM with chloroacetyl isocyanate (Figure 4.3). Solvent choice does not change the resultant microstructure for either 2-chloroethyl isocyanate or chloroacetyl isocyanate; however, SEM-EDS mapping and linescan data show solvent effects in the extent of PSM for both reagents (Figures C.1 through C.16). In order to compare the relative reactivity of 2-chloroethyl isocyanate and chloroacetyl isocyanate towards IRMOF-3, FTIR kinetic studies were performed with these reagents on a model compound, butyl anthranilate, in both chloroform and toluene. After mixing 2-chloroethyl isocyanate with butyl anthranilate, the peak corresponding to the urethane product steadily increases over three days (Figures C.17 and C.18). For the reaction of chloroacetyl isocyanate and butyl anthranilate, the peak corresponding to the urethane product appears immediately (for details, see appendix C.2.2). Together, the kinetic and SEM-EDS data support the hypothesis that fast reaction rates result in core–shell microstructure and slow reaction

rates result in uniform microstructure. Additionally, ^{1}H NMR of digested IRMOF-3 after PSM shows that in both chloroform and toluene, chloroacetyl isocyanate achieves a higher percent conversion of the linker than 2-chloroethyl isocyanate at all time points taken from 3 to 24 hours (Figures C.19 through C.34), also supporting the conclusion that chloroacetyl isocyanate reacts with amine functionality at a faster rate than does 2-chloroethyl isocyanate. Conversion percent by ^{1}H NMR and the relative intensities of chlorine to zinc by SEM-EDS linescans show that solvent choice affects the dynamics of PSM. In the case of chloroacetyl isocyanate, the use of chloroform increases the depth of penetration of PSM relative to toluene as shown by SEM-EDS linescans, and these data agree with ^{1}H NMR data which show increased conversion in PSM conditions using chloroform (Figures C.9 through C.16 and Figure 4.4). For PSM with 2-chloroethyl isocyanate, a different trend was observed wherein the relative intensity of chlorine to zinc in SEM-EDS and percent conversion in ^{1}H NMR both show increased conversion for PSM in toluene relative to PSM in chloroform (Figures C.1 through C.8 and Figure 4.4). It was initially hypothesized that the greater solvent polarity of chloroform relative to toluene would result in an increased rate of PSM for both reagents; however, experimental results indicate that solvent polarity alone cannot fully explain the role of solvent choice in affecting the dynamics of PSM.[37] Additional studies were conducted using different solvents and temperatures as well as increased reagent concentration (Figures C.35 through C.38). The data support the conclusion that reagent reactivity is the main determinant of resultant microstructure.

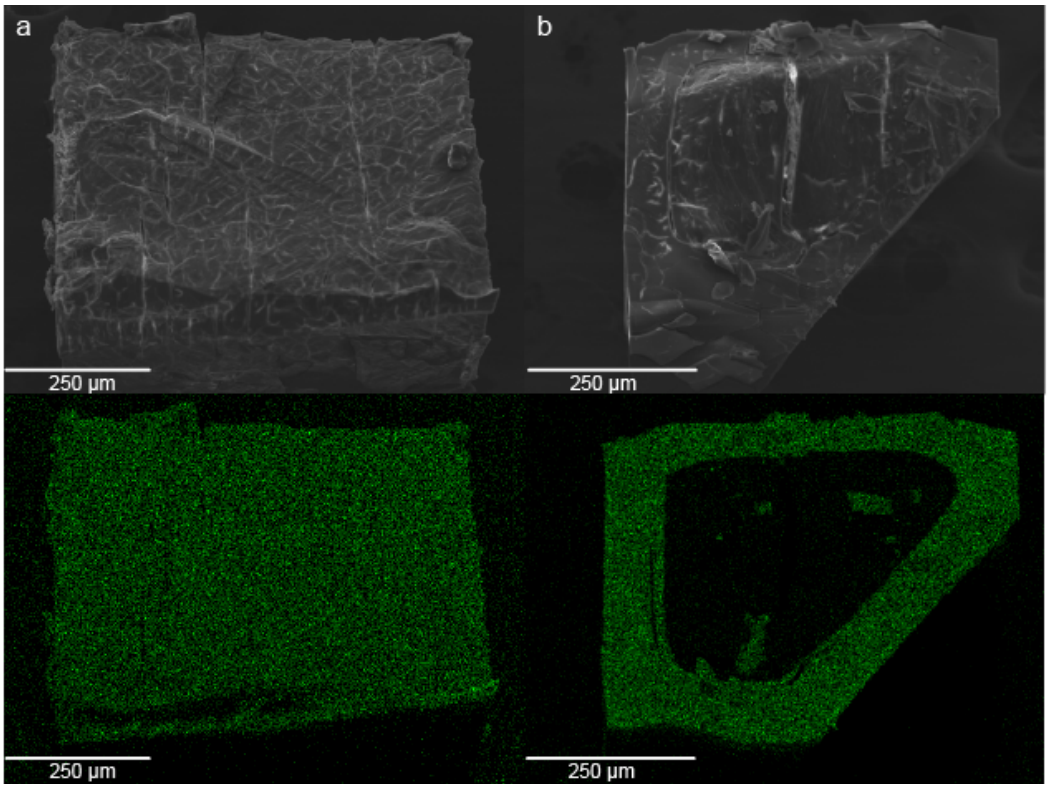

Figure 4.3 SEM images of IRMOF-3 cross sections after PSM with a) 2-chloroethyl isocyanate with an EDS map showing uniform distribution of chlorine in green below and b) chloroacetyl isocyanate with an EDS map showing core–shell distribution of chlorine in green below.

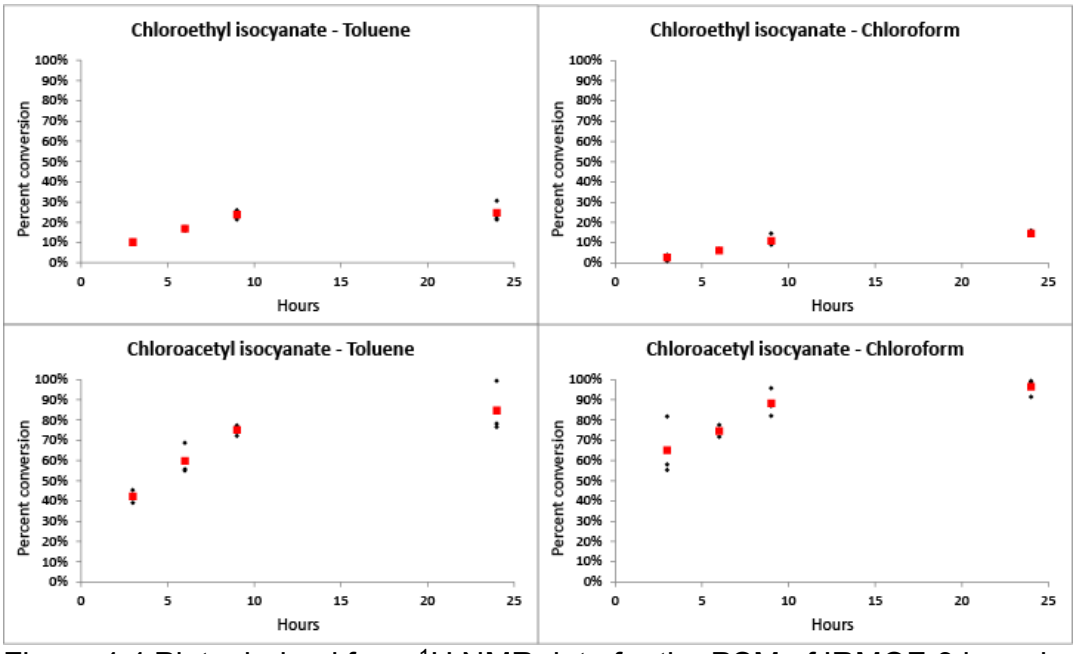

Figure 4.4 Plots derived from ^{1}H NMR data for the PSM of IRMOF-3 in various conditions where black dots indicate individual trial data and red squares indicate the average of the trial data.

Focusing on the influence of solvent choice on microstructure, it was observed that PSM with 2-chloroethyl isocyanate for 24 hours in chloroform, a polar solvent, resulted in a slight increase in core–shell character compared to PSM in toluene, a less polar solvent (Figures C.4 and C.8). It was hypothesized that solvent polarity affects microstructure during PSM by changing the reaction rate between reagent and linker, however other factors affecting diffusion such as the diffusion coefficient of the reagent,[23] solvent molecule size, and intermolecular interactions could play a role in affecting microstructure. Because the data show that solvent choice does affect the dynamics of PSM, 4-bromophenyl isocyanate was used as a reagent with reactivity intermediate to 2-chloroethyl isocyanate and chloroacetyl isocyanate to further investigate the use of solvent choice during PSM as a meaningful parameter to affect MOF microstructure. This is desirable as enhanced control over microstructure during PSM can provide a pathway towards the design of increasingly sophisticated MOF architectures. PSM was performed for 3 hours under dry conditions in toluene, chloroform, and a 1:1 mixture of each. SEM-EDS linescans of IRMOF-3 cross sections show that PSM of 4-bromophenyl isocyanate in toluene results in a uniform distribution of new functionality (Figure 4.5a). PSM in chloroform shows microstructure with increased core–shell character (Figure 4.5b). PSM in the 1:1 mixture of toluene and chloroform displays increased core–shell character relative to toluene and reduced overall reactivity compared to chloroform (Figure 4.5c). Additional experiments wherein a 1:5 ratio of anhydrous DMF to toluene was used for PSM show that adding anhydrous DMF to toluene increases the core–shell character of the resultant MOF while suppressing core functionalization (Figure 4.5d). Collectively, the above results support the hypothesis that altering the solvent used for PSM is a viable

method to influence the resultant microstructure of the functionalized MOF, best thought of as a sliding scale between uniform distribution and core–shell.

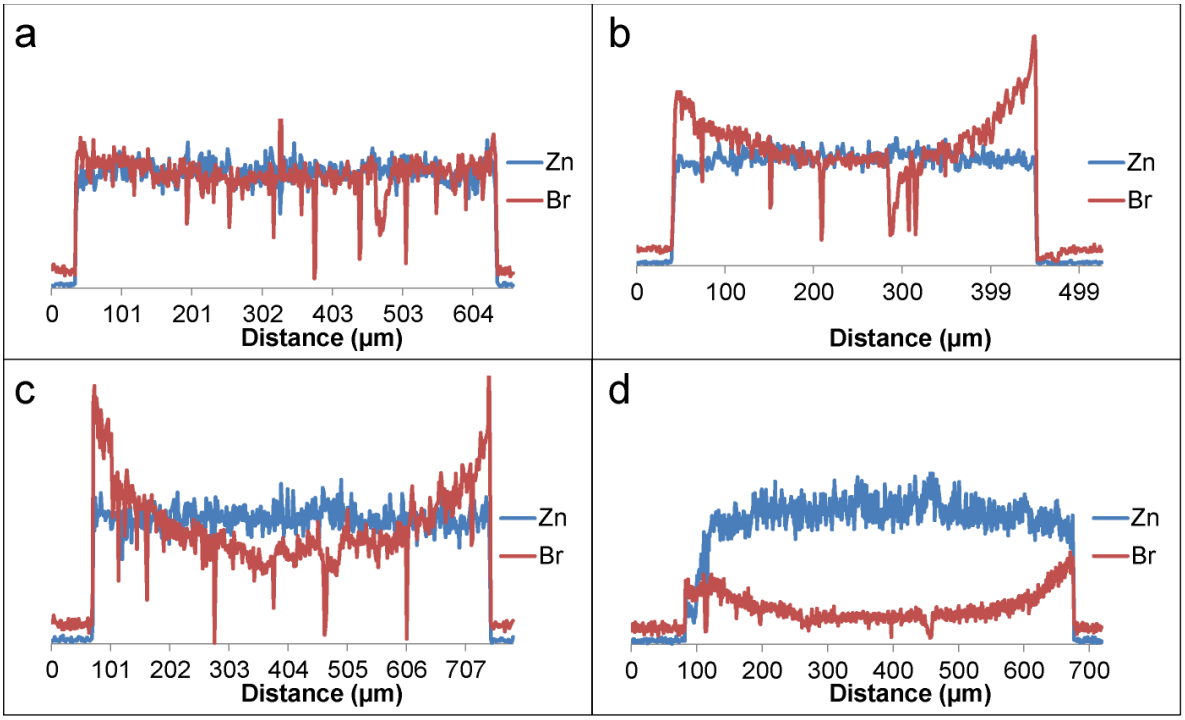

Figure 4.5 SEM-EDS linescans of IRMOF-3 cross sections after PSM with 4-bromophenyl isocyanate in a) toluene, b) chloroform, c) a 1:1 mixture of toluene and chloroform, and d) a 1:5 mixture of DMF and toluene.

In order to demonstrate the utility of understanding the dynamics of PSM, a one-pot core–shell MOF was generated through PSM with a mixture of chloroacetyl isocyanate and 4-bromophenyl isocyanate (Figure 4.6a). It was anticipated that the differences in reactivity between chloroacetyl isocyanate and 4-bromophenyl isocyanate would lead to an unequal distribution of the two compounds throughout the MOF during PSM. The experimental result is dramatic in that the demarcation between the chloroacetyl isocyanate functionalized zone (shell) and the 4-bromophenyl isocyanate functionalized zone (core) is sharp. Encouraged by these results, a more complex MOF microstructure was derived using stepwise functionalizations wherein trifluoroacetyl

isocyanate (very high reactivity) is first used to functionalize the shell of the MOF followed by a self-sorting reaction with chloroacetyl isocyanate and 4-bromophenyl isocyanate. This generates a Matryoshka microstructure (Figure 4.6b). PSM with trifluoroacetyl isocyanate does not block the diffusion of chloroacetyl isocyanate and 4-bromophenyl isocyanate, nor does it alter the previously observed dynamic which leads to the formation of a bifunctional core–shell MOF.

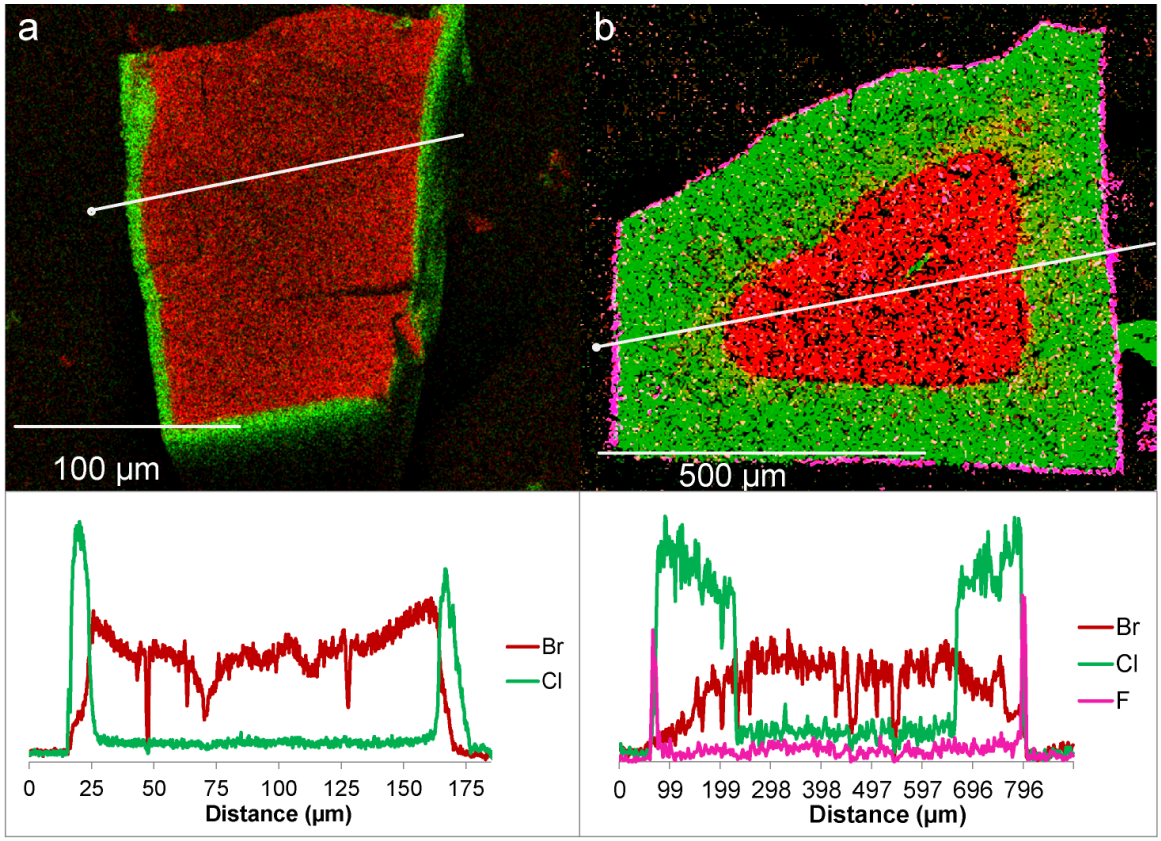

Figure 4.6 SEM-EDS maps and linescans of cross sections of IRMOF-3 after PSM with a) chloroacetyl isocyanate and bromophenyl isocyanate (core–shell) and b) trifluoroacetyl isocyanate, chloroacetyl isocyanate, and 4-bromophenyl isocyanate (Matryoshka).

4.4 Conclusions

MOFs with tunable microstructure can be attained through judicious choice of postsynthetic modification (PSM) strategy. Controlling the degree and spatial distribution

of functionalization by adjusting reagent reactivity and the solvent used represents a novel and simple route to complex materials with potential applications in fields where separations based on chemical or steric attributes is a necessity such as sequential catalysis, chromatography, and chemical sensing.

4.5 Experimental Details

Chemicals were used as purchased without purification unless otherwise noted. 2-Aminoterepthalic acid, 4-bromophenyl isocyanate, chloroacetyl isocyanate, 2-chloroethyl isocyanate, deuterium chloride 35% in D_2O, and 1,2-dichloroethane were purchased from Sigma Aldrich. Anhydrous *N,N*-dimethyl formamide (DMF) purchased from Sigma Aldrich was stored over activated 3 Å molecular sieves in a glove box where it was kept for 3 to 4 days before use. Dry acetonitrile, dry chloroform stabilized with amylene, DMF dried over 4 Å molecular sieves, anhydrous toluene, and zinc nitrate hexahydrate were purchased from Fisher Scientific. Trifluoroacetyl isocyanate was purchased from Enamine. Butyl anthranilate was purchased from TCI chemicals. Carbon tetrachloride and methyl sulfoxide-d_6 were purchased from Acros Organics. Trichloroethylene was purchased from Alfa Aesar. Chloroform-D + silver foil was purchased from Cambridge Isotope Laboratories, Inc. JEOL aluminum specimen mounts were used with PELCO carbon conductive tabs, both from Ted Pella Inc., as stages for scanning electron microscopy (SEM) in conjunction with energy-dispersive X-ray spectroscopy (EDS). A JEOL JSM-7800FLV scanning electron microscope operating with an accelerating voltage of 20 kV was used for SEM-EDS experiments. After PSM, IRMOF- 3 samples were prepared for SEM-EDS analysis by sectioning crystals in toluene parallel to the 100 plane using a razor blade and placing the crystal cross sections with the cut side up on

the carbon tape adhered to the aluminum stage, followed by activation under vacuum. Mid-infrared spectroscopy was performed using a Thermo Scientific Nicolet iS50 FT-IR in transmission mode with a SmartSeal Trans Cell with 0.05 mm CaF_2 windows made by PIKE Technologies. ^1H NMR spectra were recorded on a Varian vnmrs 500 MHz spectrometer. For each ^1H NMR experiment, approximately 8.6 mg of IRMOF-3 modified with either 2- chloroethyl isocyanate or chloroacetyl isocyanate were digested by sonication in 600 µL of DMSO-d_6 and 2.3 µL of 35% deuterium chloride in D_2O. Upon dissolution of the crystals, this solution was filtered through a 0.45 µm Nylon filter and used for ^1H NMR analysis.

4.5.1 Synthesis

IRMOF-3 was synthesized using a modified literature procedure.[32] $Zn(NO_2)_3 \cdot 6H_2O$ (478 mg, 1.61 mmol) and 2-aminobenzenedicarboxylic acid (100 mg, 0.552 mmol) were dissolved in 20 mL of DMF. The solution was divided into 2 mL portions and transferred into 10 vials (1 dram, ~3.7 mL capacity). The vials were placed in an oven set to 100 oC. The temperature was held overnight, after which the oven was turned off and left to cool with the door slightly ajar for 20-30 minutes. The mother liquor from each vial was pipetted out, and the crystals were washed with DMF (3 × 3 mL). The crystals were then washed in toluene or chloroform (3 × 3 mL) to reflect the post-synthetic modification (PSM) solution conditions used next. The average yield of dried IRMOF-3 per vial was determined to be approximately 8.6 mg (~57% yield).

4.5.2 Postsynthetic modification

Each PSM reaction was performed on ~8.6 mg of IRMOF-3 using 3 mL of reaction solution in a 1 dram vial. For analysis by SEM-EDS, each vial of functionalized

IRMOF-3 was washed in toluene (3 × 3 mL) as the final step before cutting and activating the crystals. Toluene was chosen as the solvent to cut crystals from, because it has sufficiently low volatility to allow the sectioning of crystals with a razor before complete evaporation (allowing for cleaner cuts) and also does not leave trace chlorine to interfere with SEM-EDS.

PSM with either chloroacetyl isocyanate or 2-chloroethyl isocyanate was conducted at 50 mM in either chloroform or toluene. These reactions progressed for 3, 6, 9, or 24 hours before the reaction solution was pipetted out and the crystals were washed in the solvent used for PSM (3 × 3 mL). For conditions involving washes with chloroform, toluene was also used to wash the crystals (3 × 3 mL). For PSM conditions using only 4-bromophenyl isocyanate as the reagent, 50 mM of 4-bromophenyl isocyanate were used in either chloroform, toluene, a 1:1 mixture of chloroform and toluene, or a 1:5 mixture of anhydrous DMF (to prevent reagent consumption due to residual water) and toluene. Dry DMF was used after PSM to wash the crystals (3 × 3 mL). The DMF washing step was followed by washes in toluene (3 × 3 mL). For PSM of IRMOF-3 to form a dual functionalized core–shell structure, a solution containing 50 mM each of 4- bromophenyl isocyanate and chloroethyl isocyanate in chloroform was used. After 1 hour, the solution was pipetted out, and the functionalized crystals were washed in chloroform (3 × 3 mL) and then toluene (3 × 3 mL). For PSM of IRMOF-3 to form a Matryoshka MOF with 3 separate functionalities, a two-step reaction process was used wherein 50 mM of trifluoroacetyl isocyanate in fresh deuterated chloroform was used in the first step for 16 hours, followed by washing in chloroform (3 × 3 mL). In the second step, 50 mM of 4- bromophenyl isocyanate and 5 mM of chloroacetyl isocyanate in

choloroform were used for PSM over 21 hours, followed by washing in chloroform (3 × 3 mL) and then toluene (3 × 3 mL).

4.5 Acknowledgements

This work was supported by the United States Department of Energy (DE-SC0004888). SEM work was conducted at the Robert B. Mitchell Electron Microbeam Analysis Lab, part of the University of Michigan's Department of Earth & Environmental Sciences.

4.7 References

1. Lee, J.; Kwak, J. H.; Choe, W. Evolution of Form in Metal–Organic Frameworks. *Nat. Commun.* **2017**, *8*, 1–8.
2. Cohen, S. M. The Postsynthetic Renaissance in Porous Solids. *J. Am. Chem. Soc.* **2017**, *139*, 2855–2863.
3. Jiang, J.; Zhao, Y.; Yaghi, O. M. Covalent Chemistry beyond Molecules. *J. Am. Chem. Soc.* **2016**, *138*, 3255–3265.
4. Cohen, S. M. Postsynthetic Methods for the Functionalization of Metal-Organic Frameworks. *Chem. Rev.* **2012**, *112*, 970–1000.
5. Islamoglu, T.; Goswami, S.; Li, Z.; Howarth, A. J.; Farha, O. K.; Hupp, J. T. Postsynthetic Tuning of Metal–Organic Frameworks for Targeted Applications. *Acc. Chem. Res.* **2017**, *50*, 805–813.
6. Burrows, A. D. Mixed-Component Metal–Organic Frameworks (MC-MOFs): Enhancing Functionality through Solid Solution Formation and Surface Modifications. *CrystEngComm.* **2011**, *13*, 3623.
7. Yin, Z.; Wan, S.; Yang, J.; Kurmoo, M.; Zeng, M.-H. Recent Advances in Post-Synthetic Modification of Metal–Organic Frameworks: New Types and Tandem Reactions. *Coord. Chem. Rev.* **2019**, *378*, 500–512.
8. Gadzikwa, T.; Farha, O. K.; Malliakas, C. D.; Kanatzidis, M. G.; Hupp, J. T.; Nguyen, S. T. Selective Bifunctional Modification of a Non-Catenated Metal−Organic Framework Material via "Click" Chemistry. *J. Am. Chem. Soc.* **2009**, *131*, 13613–13615.
9. Gadzikwa, T.; Lu, G.; Stern, C. L.; Wilson, S. R.; Hupp, J. T.; Nguyen, S. T. Covalent Surface Modification of a Metal–Organic Framework: Selective Surface Engineering via CuI-Catalyzed Huisgen Cycloaddition. *Chem. Commun.* **2008**, *43*, 5493–5495.
10. Li, T.; Sullivan, J. E.; Rosi, N. L. Design and Preparation of a Core-Shell Metal-Organic Framework for Selective CO_2 Capture. *J. Am. Chem. Soc.* **2013**, *135*, 9984–9987.
11. Furukawa, S.; Hirai, K.; Takashima, Y.; Nakagawa, K.; Kondo, M.; Tsuruoka, T.; Sakata, O.; Kitagawa, S. A Block PCP Crystal: Anisotropic Hybridization of Porous Coordination Polymers by Face-Selective Epitaxial Growth. *Chem. Commun.* **2009**, *34*, 5097–5099.
12. Liu, C.; Zeng, C.; Luo, T.-Y.; Merg, A. D.; Jin, R.; Rosi, N. L. Establishing Porosity Gradients within Metal–Organic Frameworks Using Partial Postsynthetic Ligand Exchange. *J. Am. Chem. Soc.* **2016**, *138*, 12045–12048.

13. McDonald, K. A.; Feldblyum, J. I.; Koh, K.; Wong-Foy, A. G.; Matzger, A. J. Polymer@MOF@MOF: “Grafting from” Atom Transfer Radical Polymerization for the Synthesis of Hybrid Porous Solids. *Chem. Commun.* **2015**, *51*, 11994–11996.
14. Feng, L.; Yuan, S.; Li, J.-L.; Wang, K.-Y.; Day, G. S.; Zhang, P.; Wang, Y.; Zhou, H.-C. Uncovering Two Principles of Multivariate Hierarchical Metal–Organic Framework Synthesis via Retrosynthetic Design. *ACS Cent. Sci.* **2018**, *4*, 1719–1726.
15. Luo, T.-Y.; Liu, C.; Gan, X. Y.; Muldoon, P. F.; Diemler, N. A.; Millstone, J. E.; Rosi, N. L. Multivariate Stratified Metal–Organic Frameworks: Diversification Using Domain Building Blocks. *J. Am. Chem. Soc.* **2019**, *141*, 2161–2168.
16. Peng, H.; Raya, J.; Richard, F.; Baaziz, W.; Ersen, O.; Ciesielski, A.; Samorì, P. Synthesis of Robust MOFs@COFs Porous Hybrid Materials via an Aza-Diels–Alder Reaction: Towards High-Performance Supercapacitor Materials. *Angew. Chem. Int. Ed.* **2020**, *132*, 19770–19777.
17. Liu, D.; Wan, J.; Pang, G.; Tang, Z. Hollow Metal–Organic-Framework Micro/Nanostructures and Their Derivatives: Emerging Multifunctional Materials. *Adv. Mater.* **2019**, *31*, 1803291.
18. Koh, K.; Wong-Foy, A. G.; Matzger, A. J. MOF@MOF: Microporous Core-Shell Architectures. *Chem. Commun.* **2009**, *41*, 6162–6164.
19. Zhan, G.; Zeng, H. C. Hydrogen Spillover through Matryoshka-Type (ZIFs@) N−1 ZIFs Nanocubes. *Nat. Commun.* **2018**, *9*, 1–12.
20. Wan, M.; Zhang, X.; Li, M.; Chen, B.; Yin, J.; Jin, H.; Lin, L.; Chen, C.; Zhang, N. Hollow Pd/MOF Nanosphere with Double Shells as Multifunctional Catalyst for Hydrogenation Reaction. *Small.* **2017**, *13*, 1701395.
21. Liu, X.; Li, Y.; Ban, Y.; Peng, Y.; Jin, H.; Bux, H.; Xu, L.; Caro, J.; Yang, W. Improvement of Hydrothermal Stability of Zeolitic Imidazolate Frameworks. *Chem. Commun.* **2013**, *49*, 9140–9142.
22. Jayachandrababu, K. C.; Sholl, D. S.; Nair, S. Structural and Mechanistic Differences in Mixed-Linker Zeolitic Imidazolate Framework Synthesis by Solvent Assisted Linker Exchange and de Novo Routes. *J. Am. Chem. Soc.* **2017**, *139*, 5906–5915.
23. Boissonnault, J. A.; Wong-Foy, A. G.; Matzger, A. J. Core–Shell Structures Arise Naturally During Ligand Exchange in Metal–Organic Frameworks. *J. Am. Chem. Soc.* **2017**, *139*, 14841–14844.
24. Kim, S.; Lee, J.; Jeoung, S.; Moon, H. R.; Kim, M. Surface-Deactivated Core–Shell Metal–Organic Framework by Simple Ligand Exchange for Enhanced Size Discrimination in Aerobic Oxidation of Alcohols. *Chem. Eur. J.* **2020**, *26*, 7568–7572.
25. Song, X.; Kim, T. K.; Kim, H.; Kim, D.; Jeong, S.; Moon, H. R.; Lah, M. S. Post-Synthetic Modifications of Framework Metal Ions in Isostructural Metal–Organic Frameworks: Core–Shell Heterostructures via Selective Transmetalations. *Chem. Mater.* **2012**, *24*, 3065–3073.
26. Fukushima, T.; Horike, S.; Kobayashi, H.; Tsujimoto, M.; Isoda, S.; Foo, M. L.; Kubota, Y.; Takata, M.; Kitagawa, S. Modular Design of Domain Assembly in Porous Coordination Polymer Crystals via Reactivity-Directed Crystallization Process. *J. Am. Chem. Soc.* **2012**, *134*, 13341–13347.
27. Hirai, K.; Furukawa, S.; Kondo, M.; Uehara, H.; Sakata, O.; Kitagawa, S. Sequential Functionalization of Porous Coordination Polymer Crystals. *Angew. Chem. Int. Ed.* **2011**, *50*, 8057–8061.

28. Zhao, M.; Deng, K.; He, L.; Liu, Y.; Li, G.; Zhao, H.; Tang, Z. Core–Shell Palladium Nanoparticle@Metal–Organic Frameworks as Multifunctional Catalysts for Cascade Reactions. *J. Am. Chem. Soc.* **2014**, *136*, 1738–1741.
29. Huang, Y.-B.; Liang, J.; Wang, X.-S.; Cao, R. Multifunctional Metal–Organic Framework Catalysts: Synergistic Catalysis and Tandem Reactions. *Chem. Soc. Rev.* **2017**, *46*, 126–157.
30. McGuire, C. V.; Forgan, R. S. The Surface Chemistry of Metal-Organic Frameworks. *Chem. Commun.* **2015**, *51*, 5199–5217.
31. Forgan, R. S. The Surface Chemistry of Metal–Organic Frameworks and Their Applications. *Dalton Trans.* **2019**, *48*, 9037–9042.
32. Tanabe, K. K.; Wang, Z.; Cohen, S. M. Systematic Functionalization of a Metal−Organic Framework via a Postsynthetic Modification Approach. *J. Am. Chem. Soc.* **2008**, *130*, 8508–8517.
33. Zhang, H.-F.; Li, M.; Wang, X.-Z.; Luo, D.; Zhao, Y.-F.; Zhou, X.-P.; Li, D. Fine-Tuning Metal–Organic Framework Performances by Spatially-Differentiated Postsynthetic Modification. *J. Mater. Chem.* **2018**, *6*, 4260–4265.
34. Mohmeyer, A.; Schäfer, M.; Schaate, A.; Locmelis, S.; Schneider, A. M.; Behrens, P. Inside/Outside: Post-Synthetic Modification of the Zr-Benzophenonedicarboxylate Metal–Organic Framework. *Chem. Eur. J.* **2020**, *26*, 2222–2232.
35. Sun, Q.; He, H.; Gao, W.-Y.; Aguila, B.; Wojtas, L.; Dai, Z.; Li, J.; Chen, Y.-S.; Xiao, F.-S.; Ma, S. Imparting Amphiphobicity on Single-Crystalline Porous Materials. *Nat. Commun.* **2016**, *7*, 13300.
36. Eddaoudi, M.; Kim, J.; Rosi, N.; Vodak, D.; Wachter, J.; O'Keeffe, M.; Yaghi, O. M. Systematic Design of Pore Size and Functionality in Isoreticular MOFs and Their Application in Methane Storage. *Science.* **2002**, *295*, 469–472.
37. A further complication is the potential for background reactivity with adventitious water.

Chapter 5 Conclusions and Outlook

5.1 Synopsis

Descriptions of MOF phases, characterized through a variety of analytical methods, comprise the bulk of this dissertation. MOFs present tantalizing physical properties, capturing the imaginations of researchers from various fields, with particular interest in applications such as fuel storage, catalysis, and separations. Once activated, MOFs possess intrinsic porosity with structural stability sufficient to withstand a vacuum. Additionally, MOFs contain metal SBUs, often catalytically active, and organic linkers which are often targets for postsynthetic methods.

An investigation of Mg-MOF-74 provided insight into MOF formation involving multiple coordination types. Multiple metastable phases employing only carboxylate coordination were observed preceding MOF formation at high concentrations of metal and linker. These conditions stabilized metastable phases and allowed their observation. *In situ* Raman spectroscopy enabled observation of one of the metastable phases dissolving with later deposition of the MOF-74 phase and resulted in the conclusion that MOF-74 formation proceeds through dissolution of the metastable phase and redeposition of the MOF-74 phase. Within the context of the MOF field, the dissolution and redeposition mechanism of MOF-74 formation supports treatment of MOFs as materials which form through a variety of mechanisms. No competent unifying theory of MOF formation has been proposed, and given the variety of mechanisms of MOF formation published, MOF formation should be treated as system dependent.

At high concentrations of metal and linker, MOF synthesis results in a mixture of phases and an overall reduction in material quality, as measured by surface area

analysis, PXRD, and SEM. High concentration syntheses of MOFs represent a method to reduce solvent waste, specifically the use of formamide solvents. By using a seeding approach with the desired MOF as the seed to phase-direct synthesis towards the desired MOF, the synthesis results in improvements to surface area with increased expression of the desired MOF phase as measured via PXRD and SEM. Four MOF systems featuring different linker and SBU types were selected to test the seeding approach. Three MOFs responded to phase direction via seeding. SNU-70 did not respond to seeding, and *in situ* observation of the synthesis supports seed dissolution as the cause. While seeding represents a facile way to drastically increase expression of the desired phase, optimization of seeding methodology will be required to exert full control over phase expression.

Postsynthetic modification (PSM) is one method by which a new MOF can be created by functionalizing a preexisting MOF. The target of PSM is the linker which undergoes chemical transformation. Before the published work, it was unknown whether PSM would result in core–shell or uniform microstructures in MOFs. Using a suite of halogen-tagged isocyanates and monitoring the distribution of functionalization using SEM in conjunction with EDS, core–shell microstructures were found to form preferentially with more reactive reagents and in more polar solvents for PSM, while uniform microstructures formed preferentially from less reactive reagents and less polar solvents. The microstructure of the resulting material can range from uniform to core–shell with intermediate distributions of functionalization being accessible through judicious choice of reagent and solvent during PSM.

5.2 Outlook

The topics covered in this dissertation provide direction for future MOF research. As with MOF-74, most MOFs do not follow classical nucleation theory during formation. While mechanisms of MOF formation defy simple categorization, research thrusts that aim to incorporate inclusions or control MOF formation at the nucleation and/or growth stages must account for how the MOF forms. Some MOFs have multiple demonstrated mechanisms of formation dependent on the synthetic conditions employed.[1] Despite many publications which provide mechanistic understanding of MOF formation, MOF synthesis is still conducted in a primarily phenomenological manner. As the variety of MOFs continues to increase, the MOF field would benefit from more studies of MOF formation with the goal of classifying and categorizing MOFs by their mode of formation. Determining MOF formation patterns which may result from the choice of SBU, linker, solvent system, etc. will enable an increase in the accuracy and precision of effort towards the synthesis and functionalization of MOFs. Additionally, a granular understanding of the steps towards the formation of a particular MOF enables exploitation of the underlying chemistry. In other fields of chemical research, mechanistic understanding of a reaction is a requirement which enables directed experimentation; MOF researchers would benefit in a similar fashion.

Phase direction via seeding was explored as a method to reduce solvent waste during MOF synthesis. The underlying issue remains: MOF synthesis must be scalable to achieve industrial relevance. To support the statements touting the relevance of mechanistic understanding of MOF formation made in the previous paragraph, seeding methodology bypasses the nucleation phase, ideally providing a crystallographic

blueprint which can act as a site for continued MOF growth. It was demonstrated that with seeding, MOF formation can proceed, even under previously prohibitive conditions. Considering the broader MOF field, seeded synthesis methodology should also be applied to mixed solvent systems. Specifically, substituting in green solvents while reducing the concentration of formamide would enable greater sustainability in MOF synthesis while reducing cost.

As the number of MOFs theorized and synthesized continues to grow, a larger contingent of researchers begins to increase the complexity of these MOF systems with the aim of generating MOFs of niche or multiple function.[2] While synthesizing multiple MOFs at high concentrations of metal and linker, it was observed that crystalline aggregates formed as off-target phases. Characterizing one of these aggregates in Mg-MOF-74 resulted in the discovery that multiple publications had been written about them as 'hierarchical MOFs'.[3–5] The materials which result from these high concentration syntheses have reduced surface area and material quality (ie. stability) and may not merit attention from the perspective of leveraging those important properties. However, the increased morphological complexity of the resulting materials presents consistently and can be explored to determine what properties they possess which can be leveraged in the future. At the outset, these hierarchical MOFs may be able to leverage morphological properties for, for example, drug delivery, or hierarchical MOFs may open possibilities in designing complex materials which can perform spatially resolved functions. On the second point, the following paragraph will show what MOFs with multiple functionalities would look like. Mechanistic understanding of the formation of these aggregates will also enhance our understanding of MOF formation, specifically providing insight into the

pathways for off-target phase formation, which can then be addressed and either targeted for enhanced expression or removal during synthesis.

While exploring the distribution of functionalization during PSM, core–shell microstructures were observed. Core–shell is a microstructure in which two distinct phases are distributed through the material as a core phase and a shell phase. When considering catalytic applications, a core–shell material has advantages. Specifically, any reagent must travel through the shell to encounter the core. The Matzger laboratory has also demonstrated that core–shell microstructures can be achieved with postsynthetic ligand exchange as well. Future research in the field should leverage these discoveries towards creating MOFs which contain multiple functioning zones within a single crystal (Figure 5.1). Researchers who pursue this direction will benefit, because holding two functions in proximity at the microscale is intrinsically desirable, and the literature precedent for MOFs which perform tandem functions is limited.

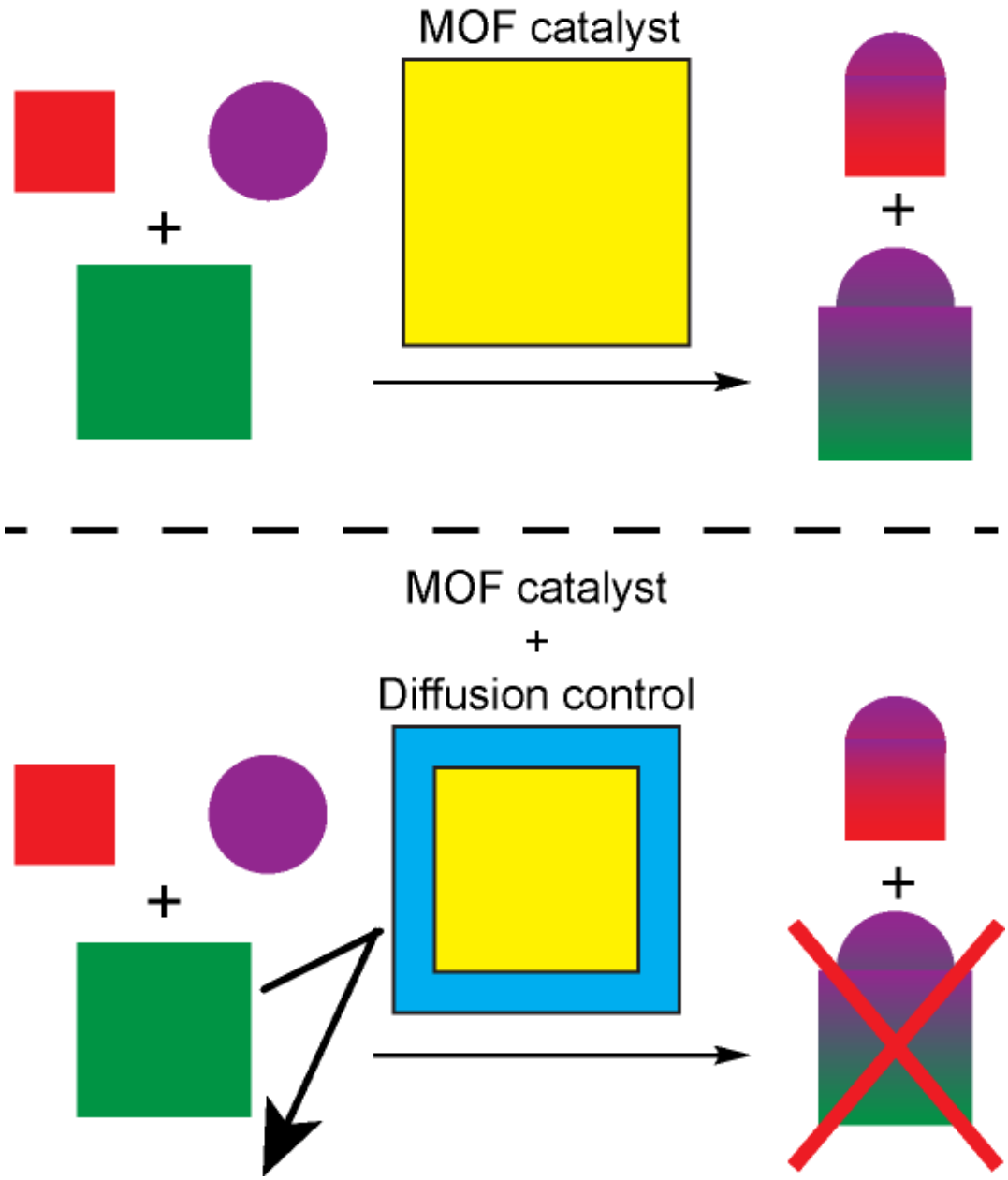

Figure 5.1 Cartoon representation of how diffusion control at the shell can enable selective catalysis at the core.

Generally, MOF research remains nascent when considering the possibilities. The outlook presented here remains close to the content of the dissertation; however, the field will likely continue to grow at an exciting rate, carried forward by the prospect of utilizing incredible material properties.

5.3 References

1. McKinstry, C.; Cussen, E. J.; Fletcher, A. J.; Patwardhan, S. V.; Sefcik, J. Effect of Synthesis Conditions on Formation Pathways of Metal Organic Framework (MOF-5) Crystals. *Crystal Growth & Design* **2013**, *13* (12), 5481–5486.
2. Feng, L.; Wang, K.-Y.; Willman, J.; Zhou, H.-C. Hierarchy in Metal–Organic Frameworks. *ACS Cent. Sci.* **2020**, *6* (3), 359–367.
3. Feng, L.; Wang, K.-Y.; Yan, T.-H.; Zhou, H.-C. Seed-Mediated Evolution of Hierarchical Metal–Organic Framework Quaternary Superstructures. *Chem. Sci.* **2020**, *11* (6), 1643–1648.
4. Feng, L.; Wang, K.-Y.; Yan, T.-H.; Zhou, H.-C. Porous Crystalline Spherulite Superstructures. *Chem* **2020**, *6* (2), 460–471.
5. Feng, L.; Li, J.-L.; Day, G. S.; Lv, X.-L.; Zhou, H.-C. Temperature-Controlled Evolution of Nanoporous MOF Crystallites into Hierarchically Porous Superstructures. *Chem* **2019**, *5* (5), 1265–1274.

Appendices

Appendix A Linker Deprotonation and Structural Evolution on the Pathway to MOF-74

A.1 Publication of This Chapter

Du Bois, D. R.; Wright, K. R.; Bellas, M. K.; Wiesner, N.; Matzger, A. J. Linker Deprotonation and Structural Evolution on the Pathway to MOF-74. *Inorg. Chem.* **2022**, *61*, 4550.

A.2 Supporting Data

A.2.1 Crystallographic Data Table

Table A.1 Crystal structure data

Parameter	*1*	*2*
a (Å)	17.0520 (22)	17.75500 (16)
b (Å)	10.33180 (12)	17.75500 (16)
c (Å)	9.22563 (13)	14.80132 (16)
α *(°)*	90	90
β *(°)*	98.0882 (12)	90
γ *(°)*	90	120
v (Å^3)	1609.18 (3)	4040.85 (9)
Z/Z'	4/0.5	9/0.5
$R_{int.}$ *(%)*	4.79	3.39
R_1 *(%)*	4.63	5.13
$_wR_2$ *(%)*	12.97	14.77
GOF	1.088	1.042
Chemical Formula	$C_{14}H_8MgN_2O_8$	$C_{14}H_8MgN_2O_8$
Crystal System	monoclinic	Trigonal
Space Group	C_2/c (#15)	$R\bar{3}$ (#148)
Formula weight (g/mol)	366.61	366.61
$\rho_{calc.}$ *(g/cm^3)*	1.513	1.356
F (000)	768	1728
μ *(mm^{-1})*	1.407	1.260
Total Reflections	14366	27569
Unique reflections	1676	1585
Observed Reflections	1578	1571
Variables	124	128

A.2.2 Table showing times when phases appear by Raman spectroscopy

Table A.2 Green indicates the presence of a phase at a given time point by Raman spectroscopy at 5x synthesis conditions.*

Phase	3 h	6 h	9 h	12 h	20 h
1					
2					
1 trans					
Mg-MOF-74					
Side product					

*Due to the stochastic nature of MOF synthesis, the observation of a phase at a given time point does not ensure its observation at that time point for each synthesis.

A.2.3 PXRD data

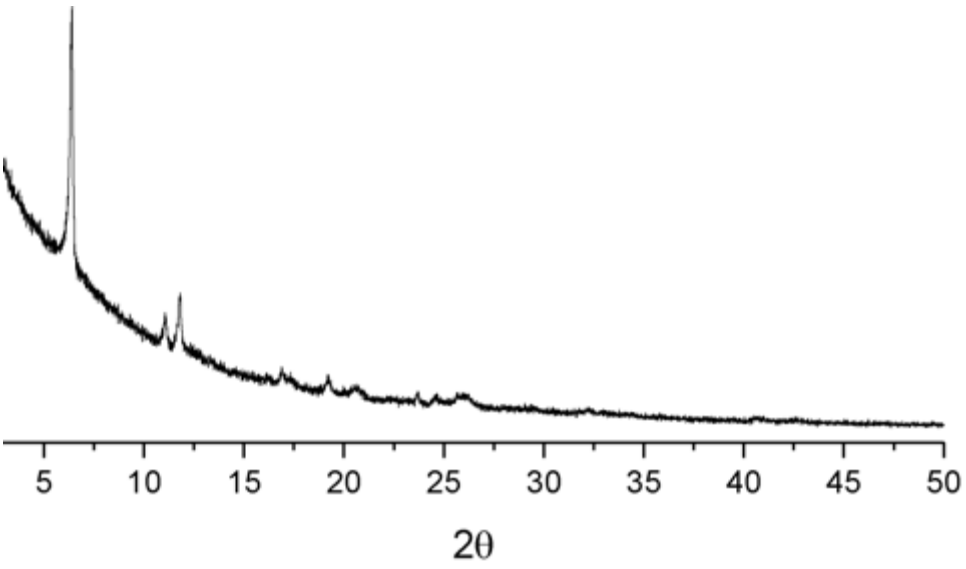

Figure A.1 PXRD pattern of side product of 5x concentration synthesis conditions.

A.2.4 In situ Raman data

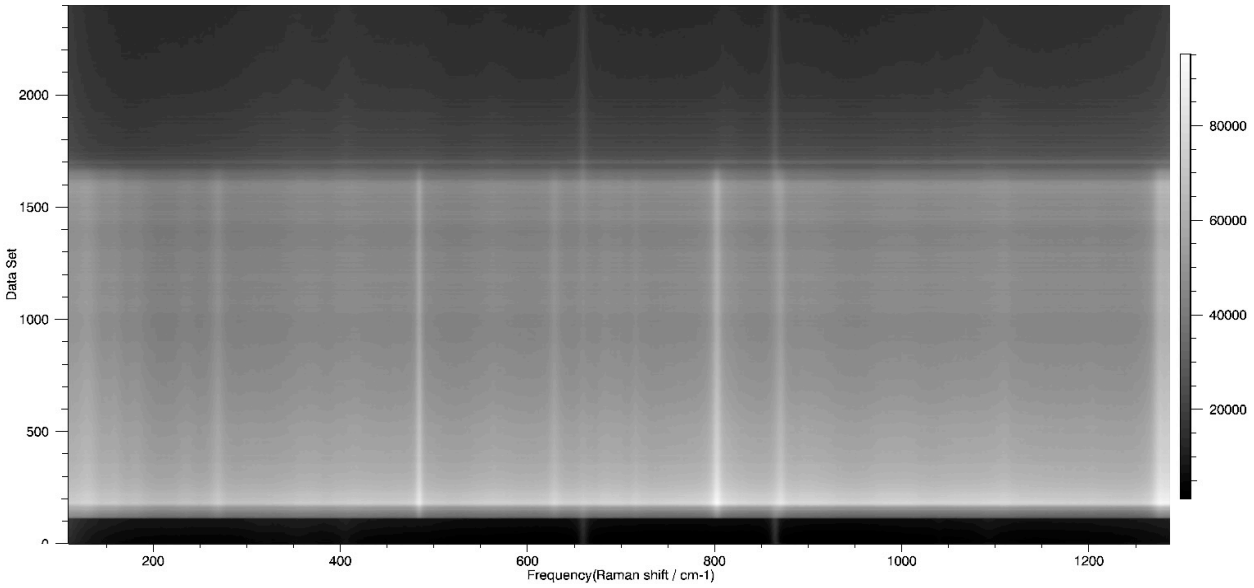

Figure A.2 3D plot of *in situ* Raman data acquired from the 5x concentration synthesis of Mg-MOF-74. Each data set took 30 s to acquire with no intervening time between collections. The data correspond to the location of approximately one crystal and do not show all phase changes occurring.

A.2.5 Thermogram data

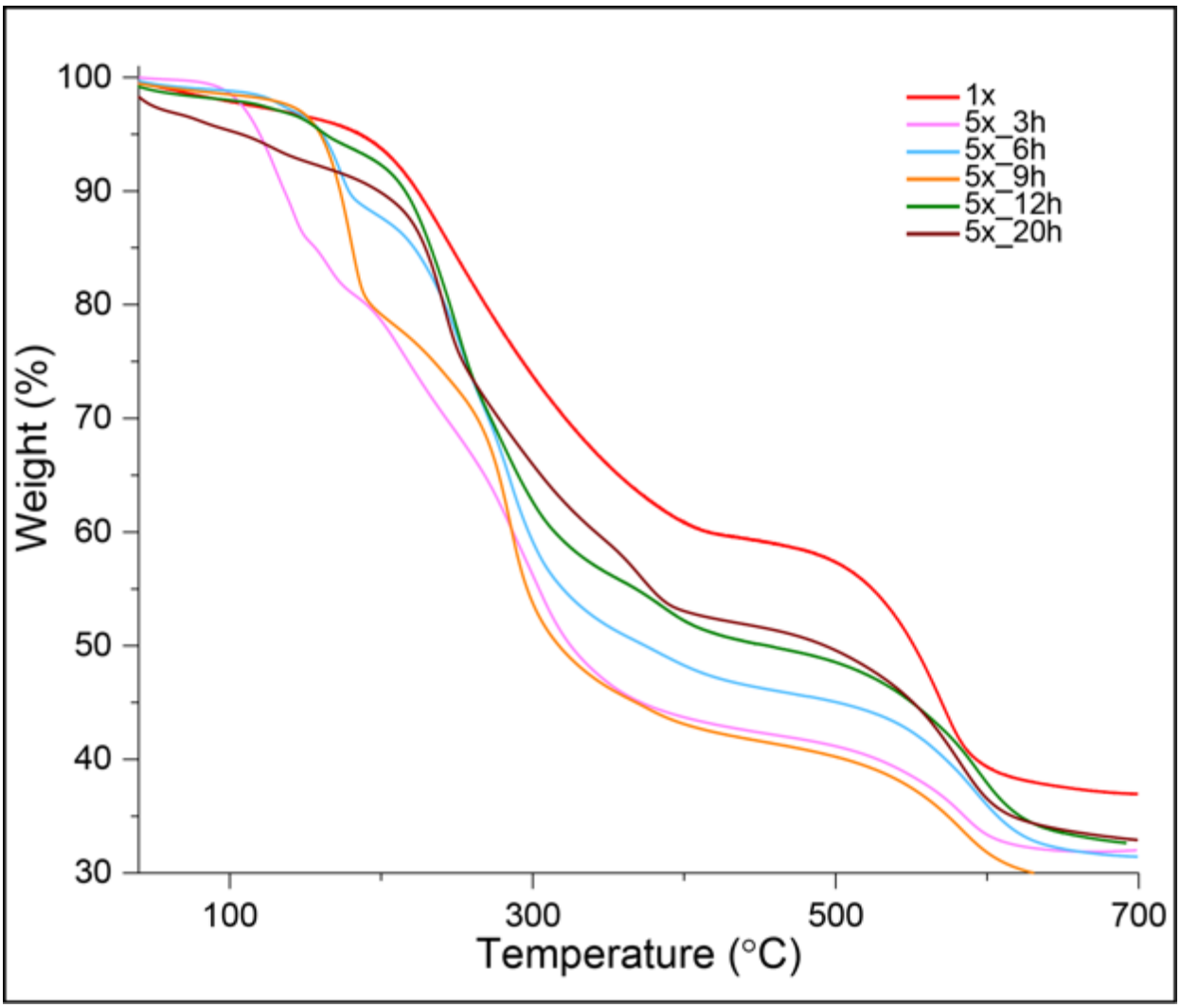

Figure A.3 TGA traces of Mg-MOF-74 5x concentration synthesis at various times of synthesis where the 1x concentration synthesis condition is the TGA trace for pure Mg-MOF-74. The greater solvent content, as evidenced by lower temperature mass losses in the TGA trace, is consistent with the production of more solvated phases at early stages in the reaction.

Appendix B Metal–Organic Framework Seeding to Drive Phase Selection and Overcome Synthesis Limitations

B.1 Publications of This Chapter

Du Bois, D. R.; Matzger, A. J. Metal–Organic Framework Seeding to Drive Phase Selection and Overcome Synthesis Limitations. *Cryst. Growth Des.* **2022**, *22*, 6379.

B.2 Supporting Data

B.2.1 PXRD data

DMOF-1

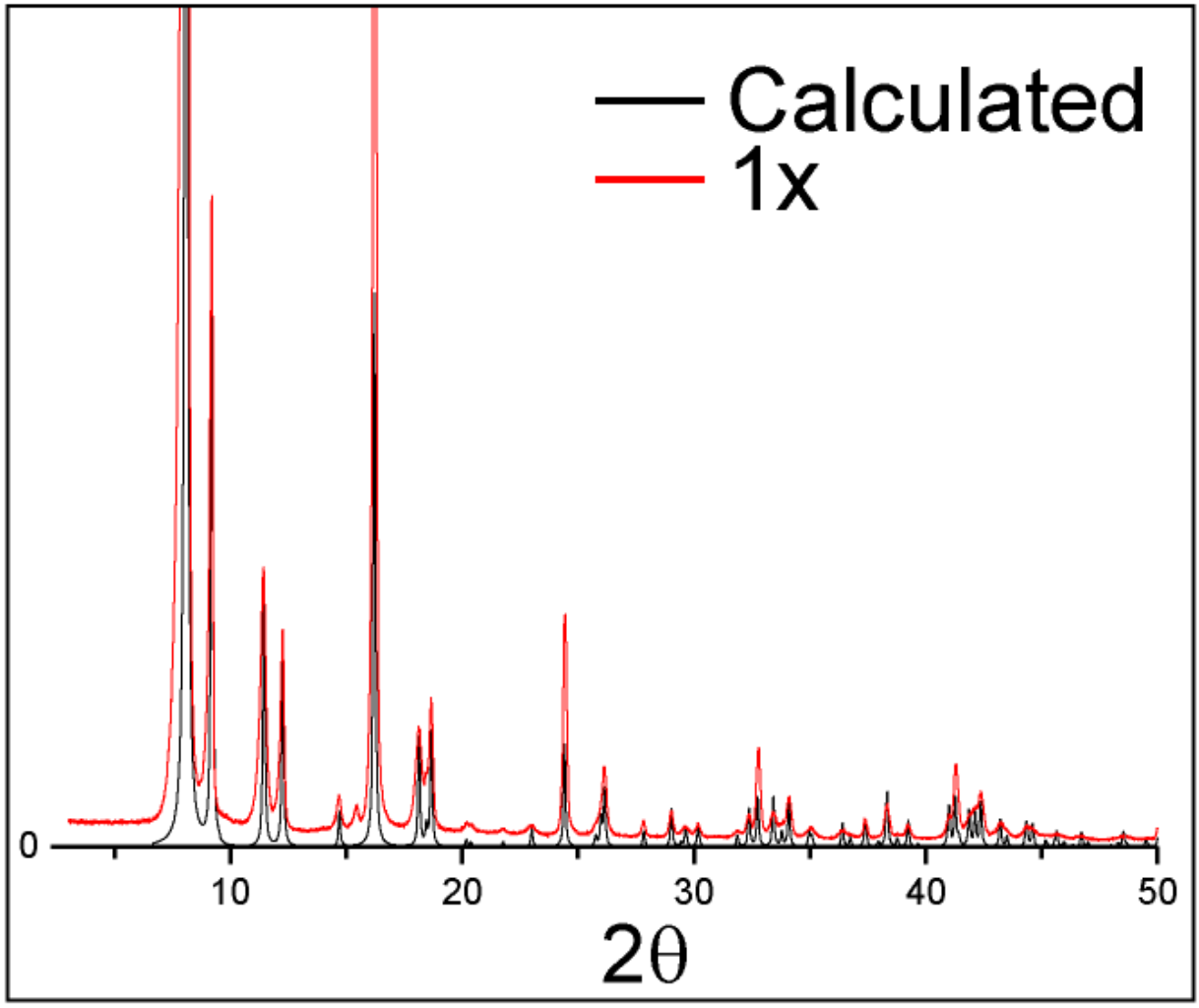

Figure B.1 PXRD patterns of the calculated and activated 1× concentration synthesis of DMOF-1 agree.

UiO-66

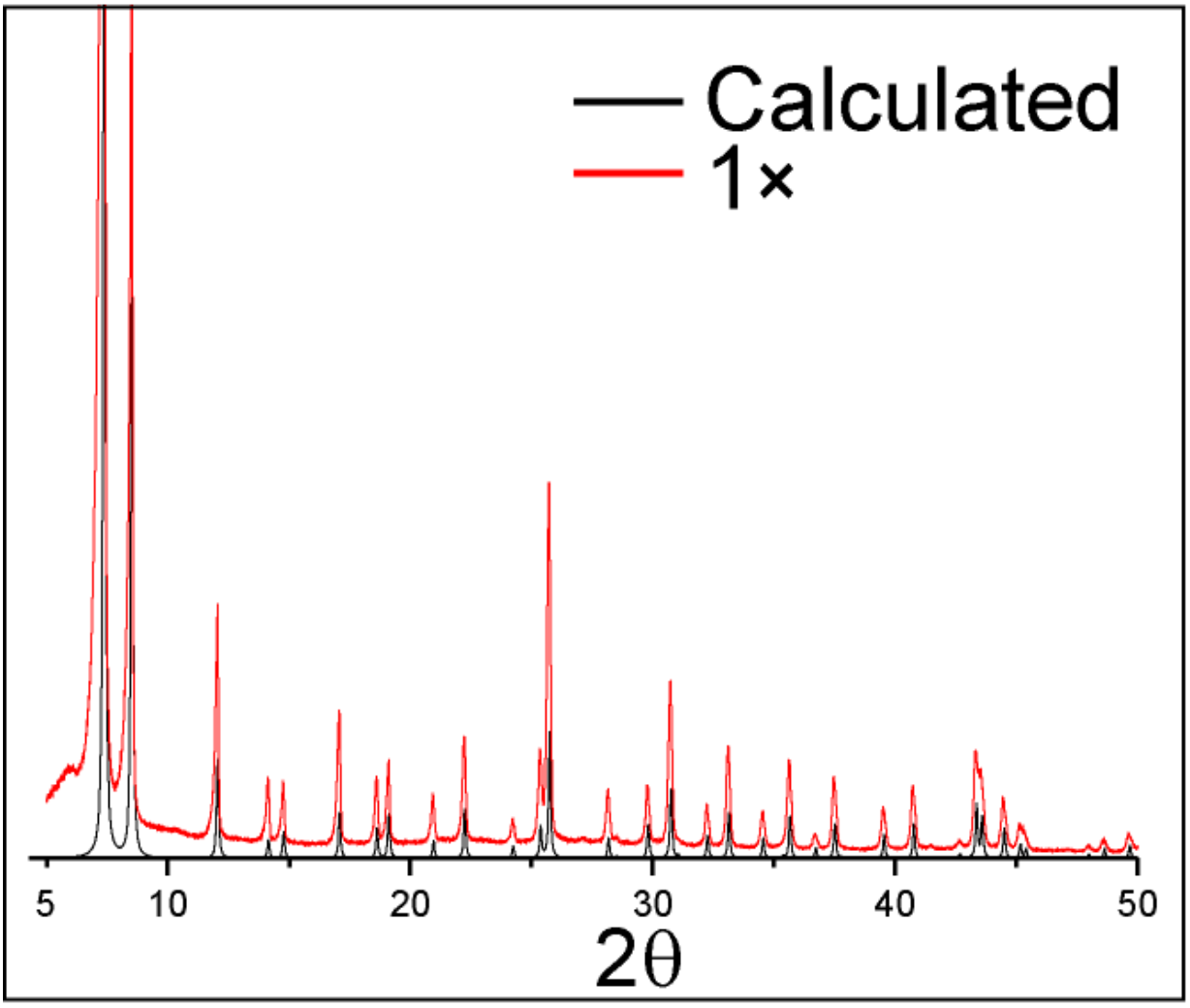

Figure B.2 PXRD patterns of the calculated and activated 1× concentration synthesis of UiO-66 agree.

B.2.2 Measured nitrogen adsorption isotherms

Mg-MOF-74 1×

BET surface area = 1422 m^2/g
C constant = 7585.059
Correlation coefficient = 0.999999
BET fitting range = [0.0045, 0.0233]

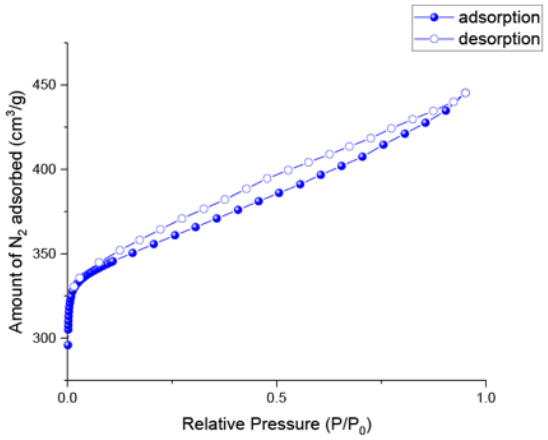

BET surface area = 1672 m^2/g
C constant = 6958.694
Correlation coefficient = 0.999999
BET fitting range = [0.0069, 0.0245]

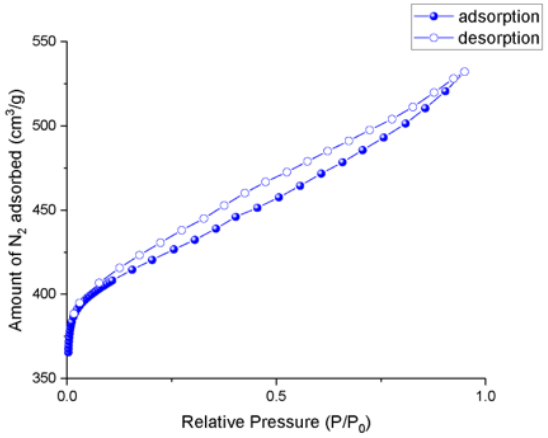

BET surface area = 1680 m^2/g
C constant = 5641.207
Correlation coefficient = 0.999999
BET fitting range = [0.0039, 0.0239]

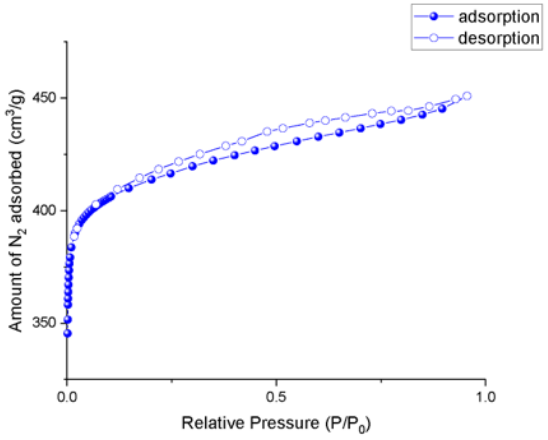

Figure B.3 Nitrogen adsorption-desorption isotherm at 77 K for activated Mg-MOF-74 1×, measurements for three samples shown.

Mg-MOF-74 4.3×

BET surface area = 1236 m²/g
C constant = 6818.794
Correlation coefficient = 0.999998
BET fitting range = [0.0066, 0.0251]

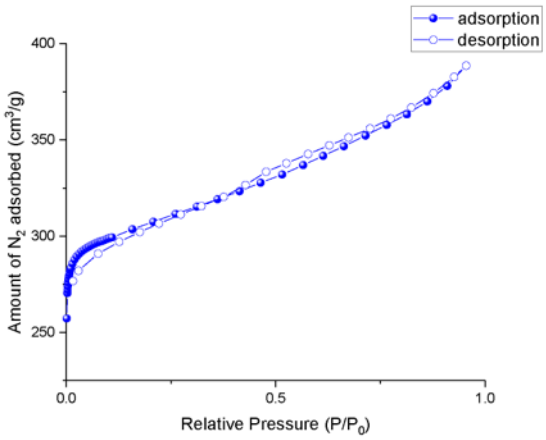

BET surface area = 1586 m²/g
C constant = 8950.921
Correlation coefficient = 0.999999
BET fitting range = [0.00606, 0.219]

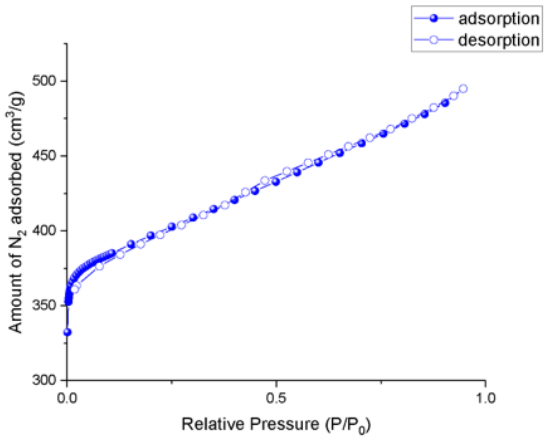

BET surface area = 204 m²/g
C constant = 108.736
Correlation coefficient = 0.999981
BET fitting range = [0.0921, 0.2581]

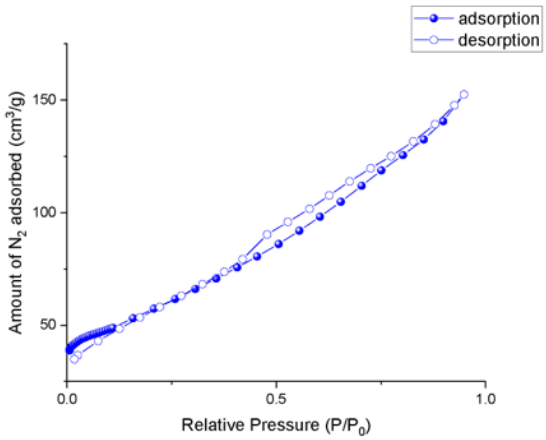

Figure B.4 Nitrogen adsorption-desorption isotherm at 77 K for activated Mg-MOF-74 4.3×, measurements for three samples shown.

Mg-MOF-74 4.3× seeded

BET surface area = 1332 m²/g
C constant = 4182.951
Correlation coefficient = 0.999999
BET fitting range = [0.010, 0.0409]

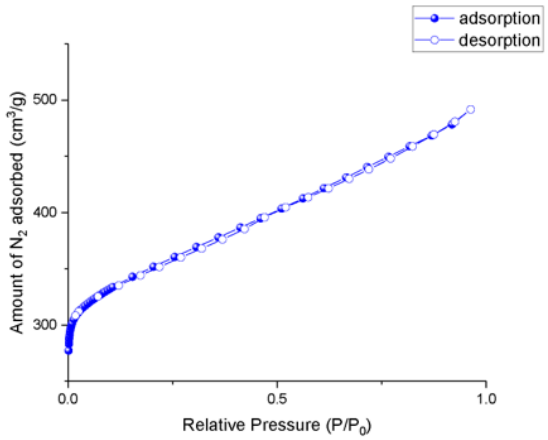

BET surface area = 1536 m²/g
C constant = 11159.101
Correlation coefficient = 0.999999
BET fitting range = [0.0051, 0.0177]

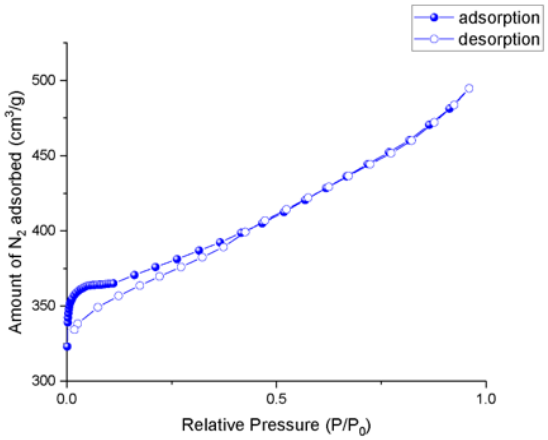

BET surface area = 1335 m²/g
C constant = 9796.893
Correlation coefficient = 0.999999
BET fitting range = [0.00640, 0.0227]

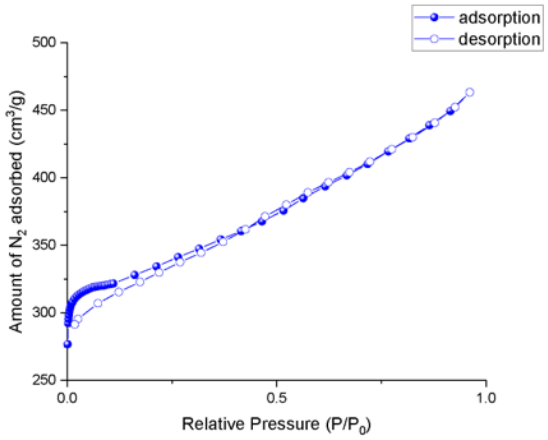

BET surface area = 1277 m²/g
C constant = 6165.301
Correlation coefficient = 0.999999
BET fitting range = [0.0081, 0.0296]

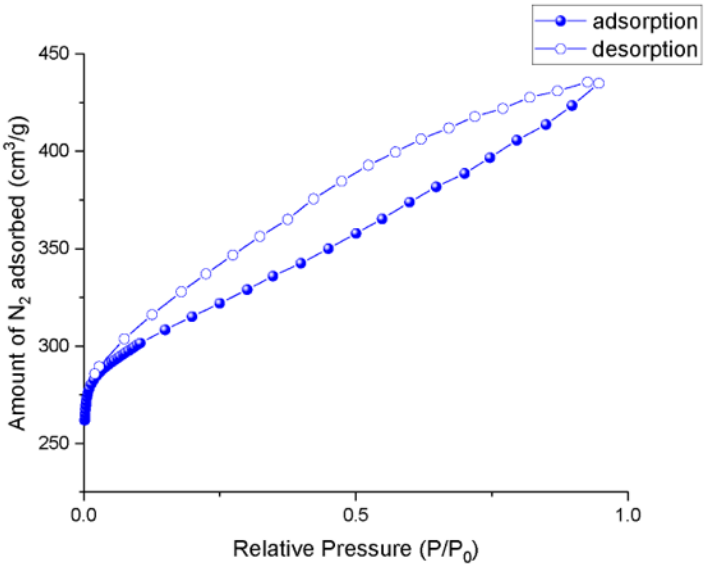

BET surface area = 1158 m²/g
C constant = 7730.680
Correlation coefficient = 1.0
BET fitting range = [0.0053, 0.0204]

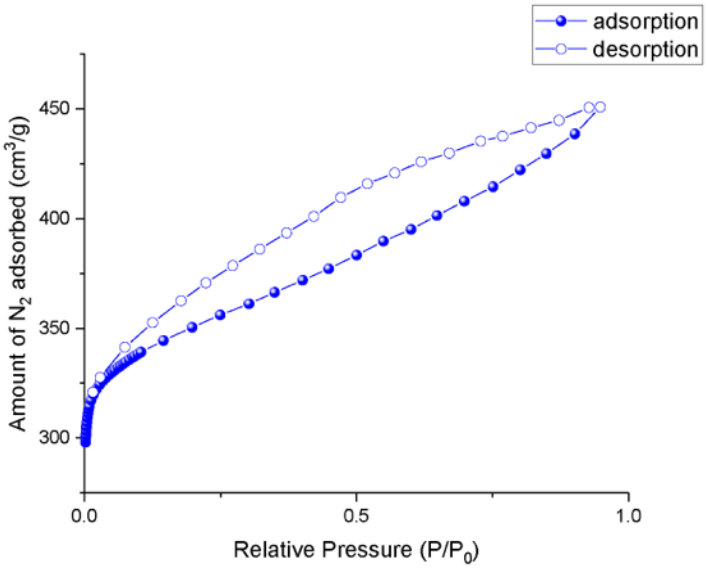

Figure B.5 Nitrogen adsorption-desorption isotherm at 77 K for activated Mg-MOF-74 4.3× seeded conditions, measurements for five samples shown.

Mg-MOF-74 4.7×

BET surface area = 80 m²/g
C constant = 49.860
Correlation coefficient = 0.999972
BET fitting range = [0.00934, 0.2992]

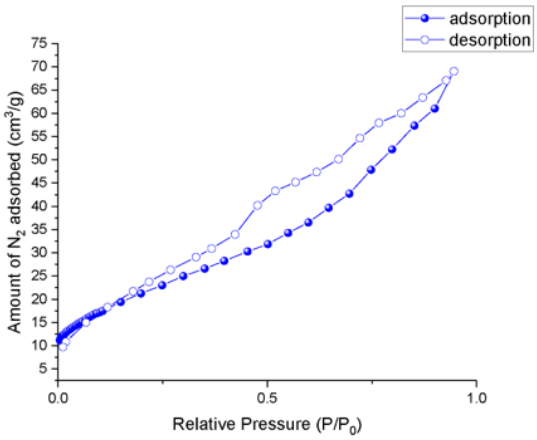

BET surface area = 337 m²/g
C constant = 1347.044
Correlation coefficient = 0.999992
BET fitting range = [0.00626, 0.0945]

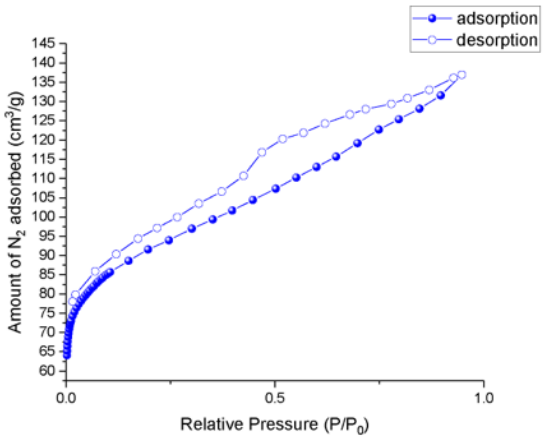

BET surface area = 64 m²/g
C constant = 73.634
Correlation coefficient = 0.99975
BET fitting range = [0.0852, 0.2017]

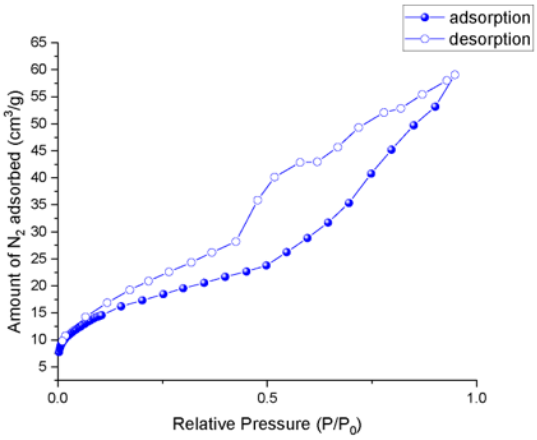

BET surface area = 422 m²/g
C constant = 600.352
Correlation coefficient = 0.999999
BET fitting range = [0.00402, 0.0720]

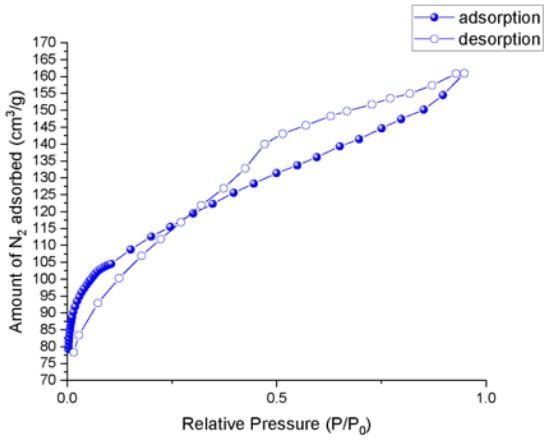

BET surface area = 1533 m²/g
C constant = 6409.321
Correlation coefficient = 0.999999
BET fitting range = [0.0080, 0.0209]

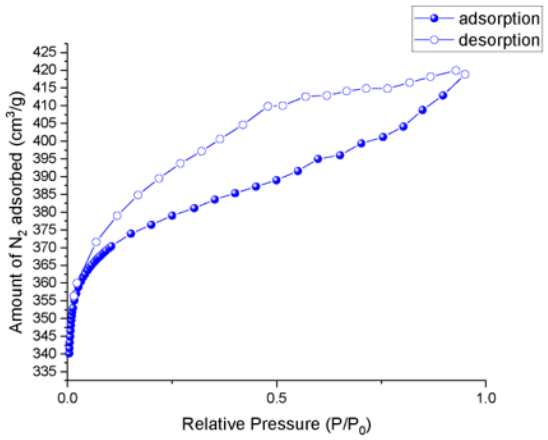

BET surface area = 1421 m²/g
C constant = 8273.511
Correlation coefficient = 0.999999
BET fitting range = [0.0057, 0.0229]

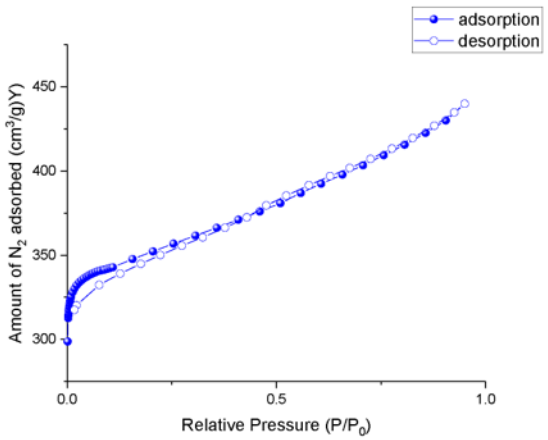

BET surface area = 1557 m²/g
C constant = 8600.864
Correlation coefficient = 1.000000
BET fitting range = [0.00364, 0.0170]

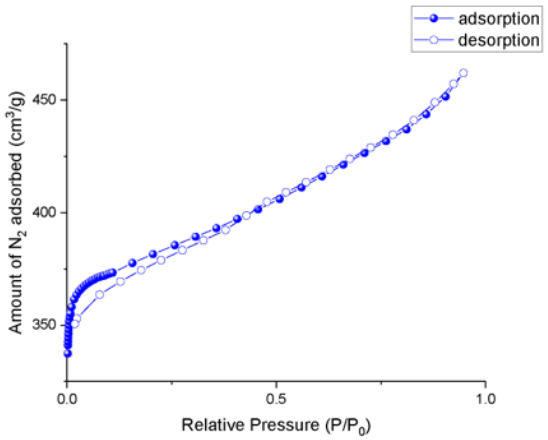

BET surface area = 901 m²/g
C constant = 5033.559
Correlation coefficient = 0.999999
BET fitting range = [0.00674, 0.0291]

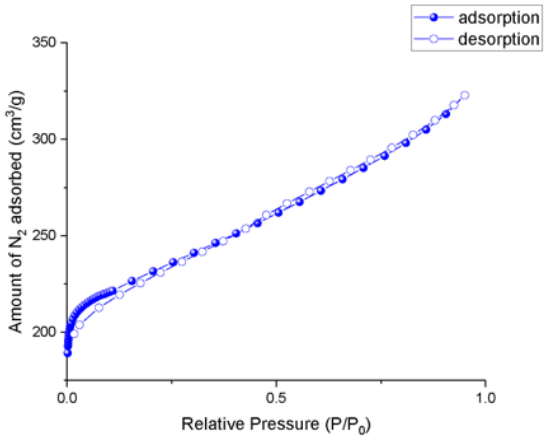

BET surface area = 281 m²/g
C constant = 920.314
Correlation coefficient = 0.999997
BET fitting range = [0.0641, 0.0928]

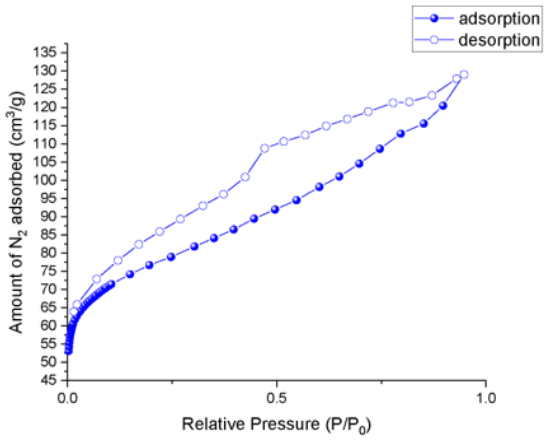

Figure B.6 Nitrogen adsorption-desorption isotherm at 77 K for activated Mg-MOF-74 4.7×, measurements for nine samples shown.

Mg-MOF-74 4.7× seeded

BET surface area = 1335 m²/g
C constant = 3062.598
Correlation coefficient = 0.999999
BET fitting range = [0.00556, 0.02389]

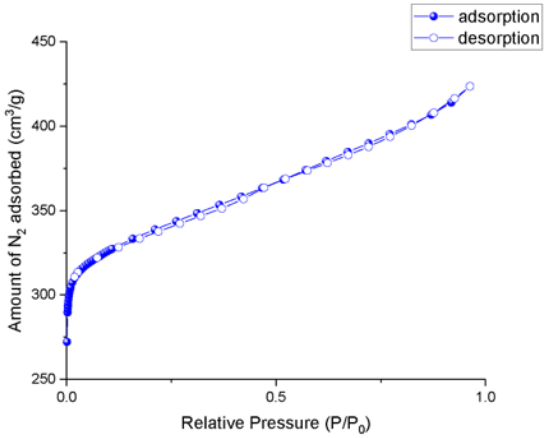

BET surface area = 1277 m²/g
C constant = 6165.301
Correlation coefficient = 0.999999
BET fitting range = [0.00815, 0.0296]

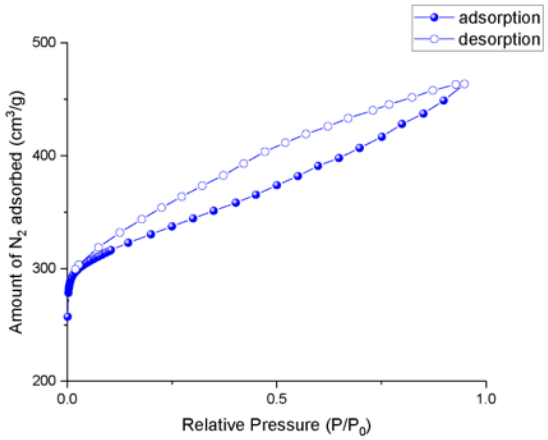

BET surface area = 1158 m²/g
C constant = 7730.680
Correlation coefficient = 1.000000
BET fitting range = [0.0053, 0.0204]

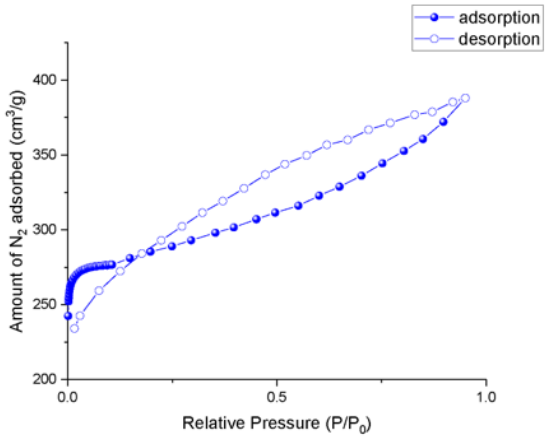

BET surface area = 1266 m²/g
C constant = 6101.485
Correlation coefficient = 0.999998
BET fitting range = [0.0067, 0.0257]

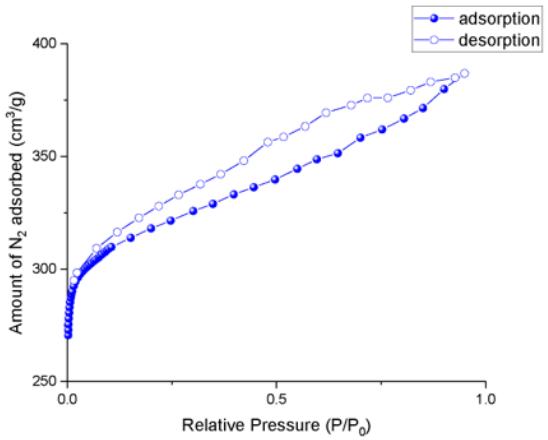

BET surface area = 1494 m²/g
C constant = 6741.642
Correlation coefficient = 0.999999
BET fitting range = [0.0042, 0.0220]

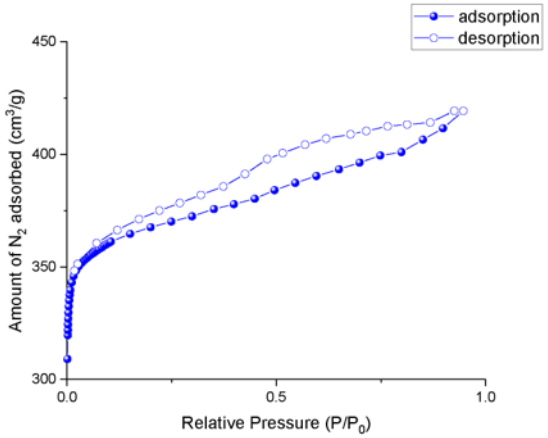

BET surface area = 828 m²/g
C constant = 4434.612
Correlation coefficient = 0.999998
BET fitting range = [0.0099, 0.0316]

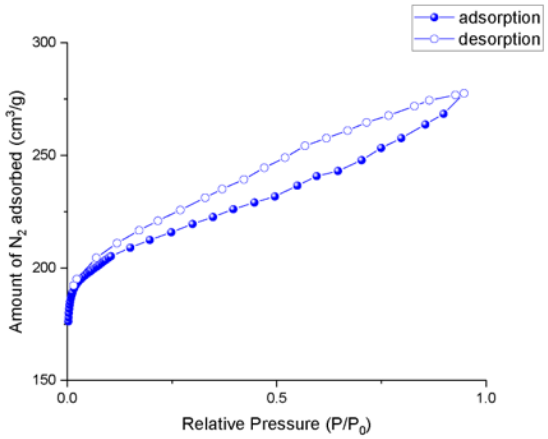

BET surface area = 1291 m²/g
C constant = 5736.556
Correlation coefficient = 0.999999
BET fitting range = [0.0033, 0.0226]

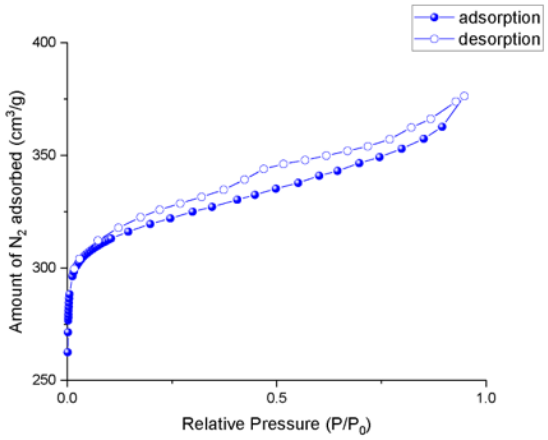

BET surface area = 1014 m²/g
C constant = 5196.832
Correlation coefficient = 0.999999
BET fitting range = [0.0053, 0.0266]

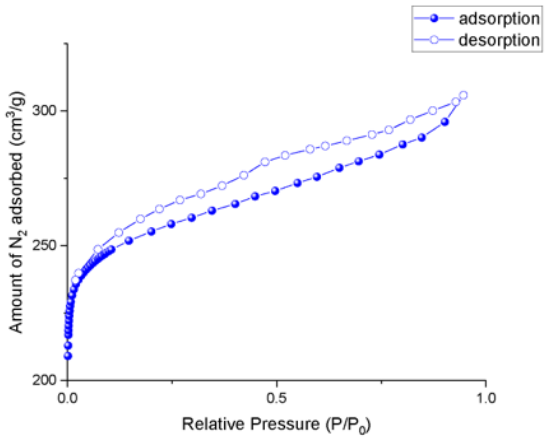

BET surface area = 1217 m²/g
C constant = 5163.064
Correlation coefficient = 0.999999
BET fitting range = [0.0044, 0.0270]

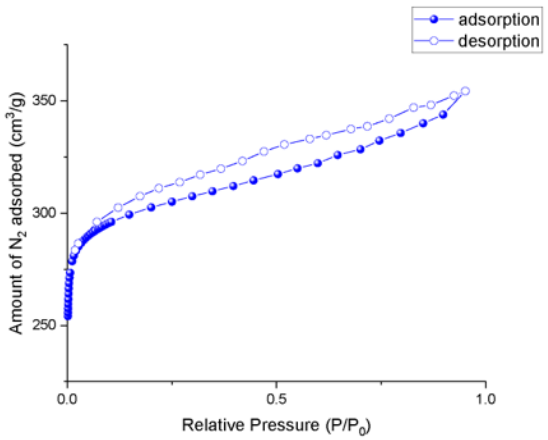

Figure B.7 Nitrogen adsorption-desorption isotherm at 77 K for activated Mg-MOF-74 4.7× seeded conditions, measurements for nine samples shown.

Mg-MOF-74 5×

BET surface area = 98.6 m^2/g
C constant = 49.290
Correlation coefficient = 0.999977
BET fitting range = [0.095, 0.296]

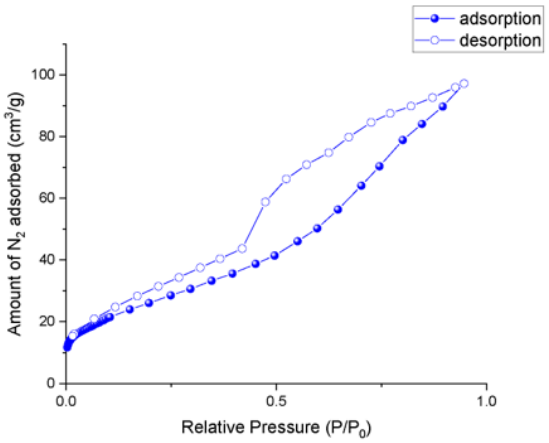

BET surface area = 103 m^2/g
C constant = 54.736
Correlation coefficient = 0.999949
BET fitting range = [0.090, 0.250]

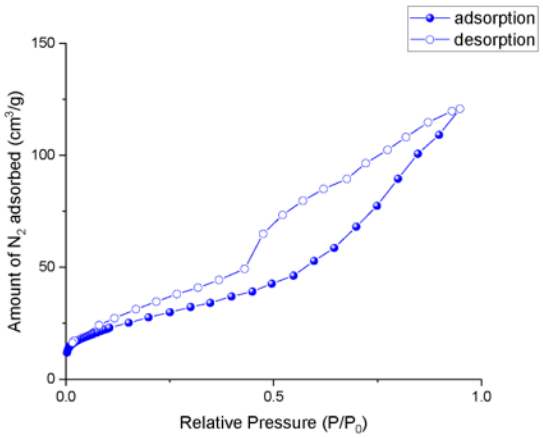

BET surface area = 173 m^2/g
C constant = 26.310
Correlation coefficient = 0.999934
BET fitting range = [0.048, 0.2978]

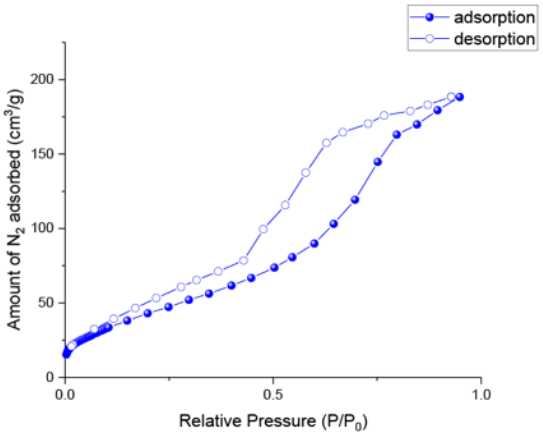

Figure B.8 Nitrogen adsorption-desorption isotherm at 77 K for activated Mg-MOF-74 5×, measurements for three samples shown.

Mg-MOF-74 5× seeded

BET surface area = 1494 m^2/g
C constant = 7174.822
Correlation coefficient = 0.999999
BET fitting range = [0.0056, 0.0235]

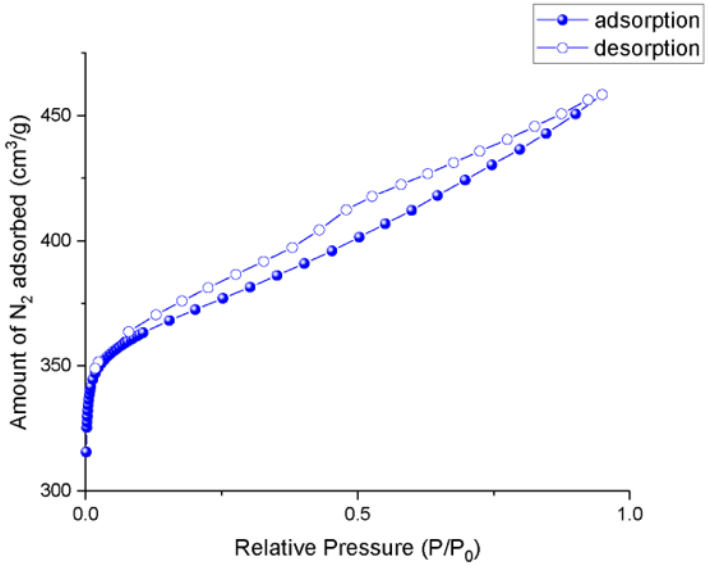

Figure B.9 Nitrogen adsorption-desorption isotherm at 77 K for activated Mg-MOF-74 5× seeded conditions, measurements for one sample shown. Data for the other two samples is unavailable.

DMOF-1 1×

BET surface area = 2138 m²/g
C constant = 4196.300
Correlation coefficient = 0.999979
BET fitting range = [0.0036, 0.0184]

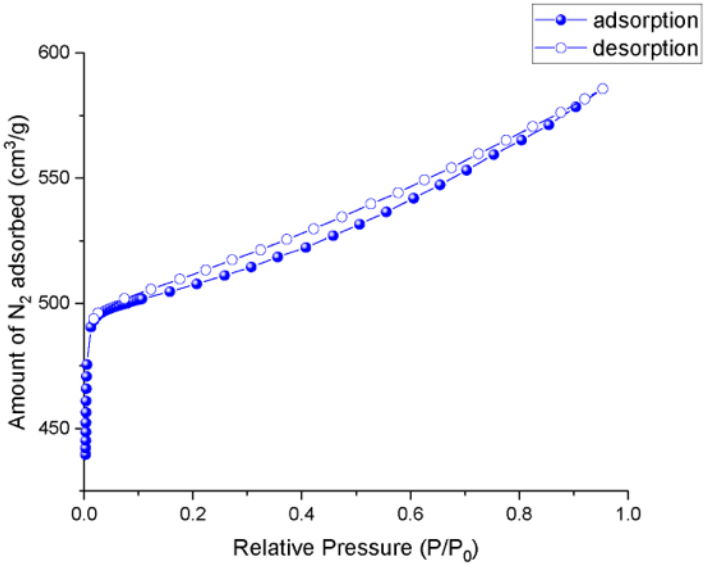

Figure B.10 Nitrogen adsorption-desorption isotherm at 77 K for activated DMOF-1 1×, measurements for one sample shown.

DMOF-1 5×

BET surface area = 768 m²/g
C constant = 5577.222
Correlation coefficient = 0.999987
BET fitting range = [0.0046, 0.0157]

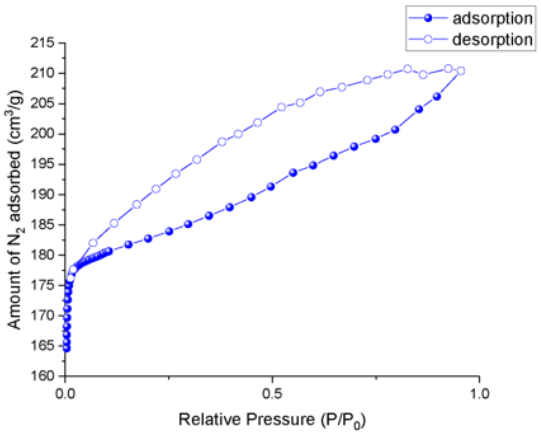

BET surface area = 749 m²/g
C constant = 4733.725
Correlation coefficient = 0.999981
BET fitting range = [0.0042, 0.0149]

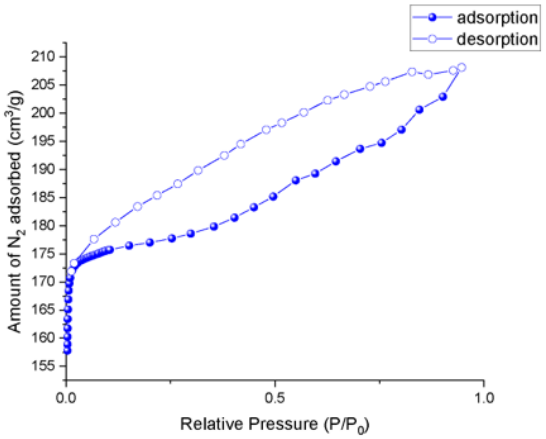

BET surface area = 830 m²/g
C constant = 4110.265
Correlation coefficient = 0.999950
BET fitting range = [0.0036, 0.0177]

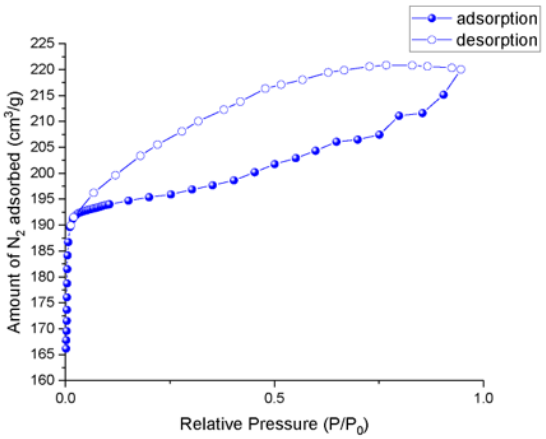

Figure B.11 Nitrogen adsorption-desorption isotherm at 77 K for activated DMOF-1 5×, measurements for three samples shown.

DMOF-1 5× seeded

BET surface area = 1463 m²/g
C constant = 6893.229
Correlation coefficient = 0.999998
BET fitting range = [0.0074, 0.0144]

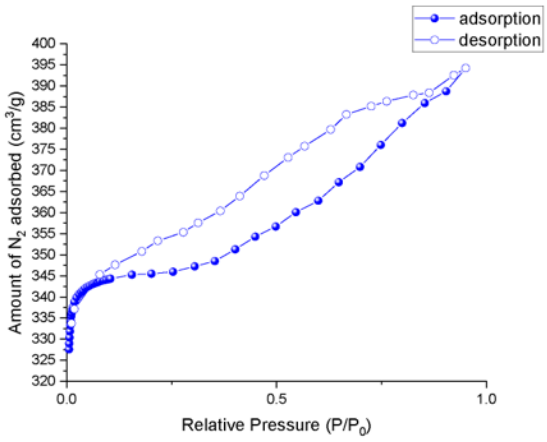

BET surface area = 1642 m²/g
C constant = 4014.777
Correlation coefficient = 0.999975
BET fitting range = [0.0037, 0.0184]

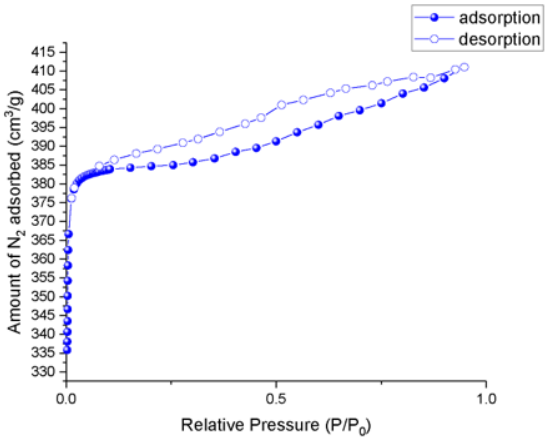

BET surface area = 1656 m²/g
C constant = 6379.501
Correlation coefficient = 0.999992
BET fitting range = [0.0060, 0.0163]

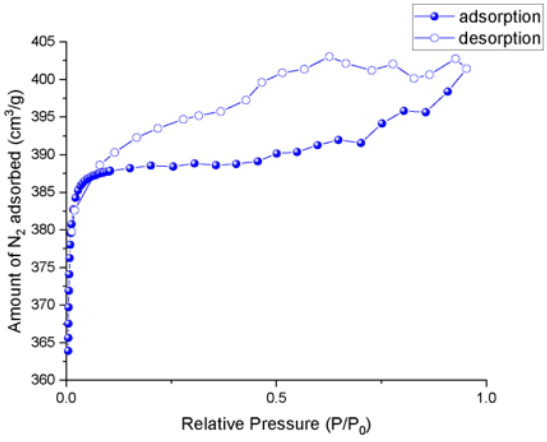

Figure B.12 Nitrogen adsorption-desorption isotherm at 77 K for activated DMOF-1 5× seeded conditions, measurements for three samples shown.

SNU-70 1×

BET surface area = 5173 m²/g
C constant = 222.872
Correlation coefficient = 0.999695
BET fitting range = [0.046, 0.076]

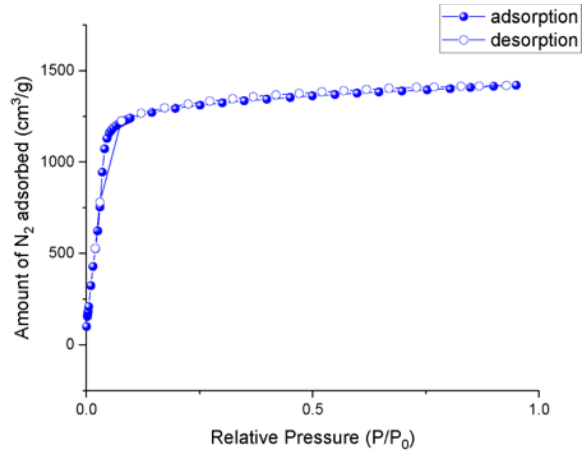

BET surface area = 5144 m²/g
C constant = 226.815
Correlation coefficient = 0.999622
BET fitting range = [0.045, 0.078]

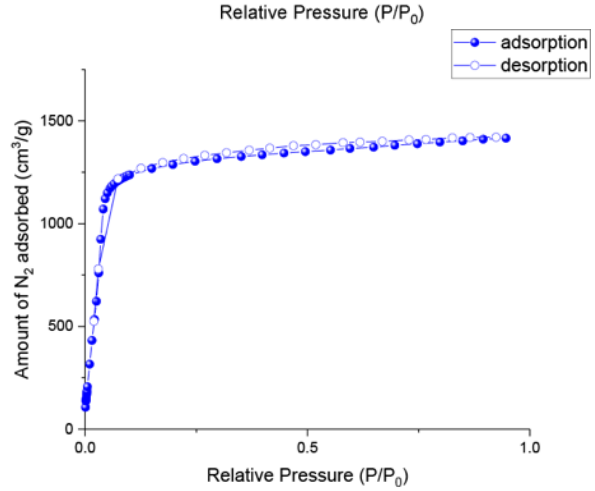

Figure B.13 Nitrogen adsorption-desorption isotherm at 77 K for activated SNU-70 1×, measurements for two samples shown.

SNU-70 7×

BET surface area = 2056 m²/g
C constant = 1930.676
Correlation coefficient = 0.999996
BET fitting range = [0.015, 0.046]

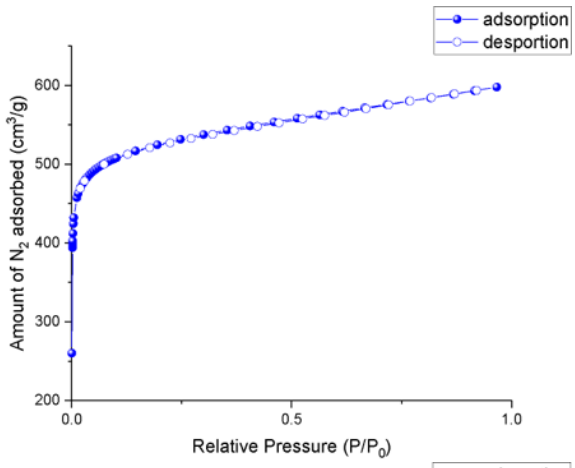

BET surface area = 2032 m²/g
C constant = 1796.718
Correlation coefficient = 0.999995
BET fitting range = [0.016, 0.046]

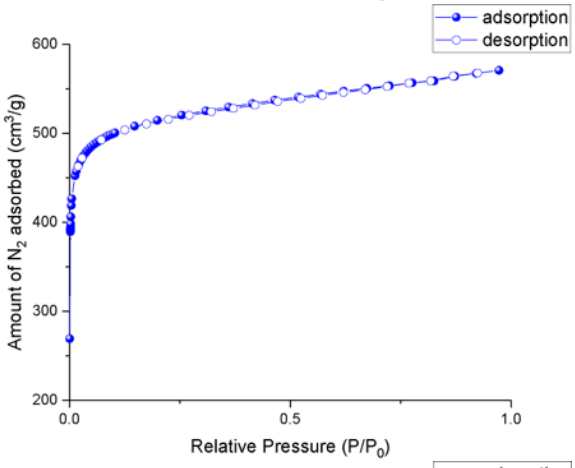

BET surface area = 2040 m²/g
C constant = 1881.562
Correlation coefficient = 0.999995
BET fitting range = [0.016, 0.046]

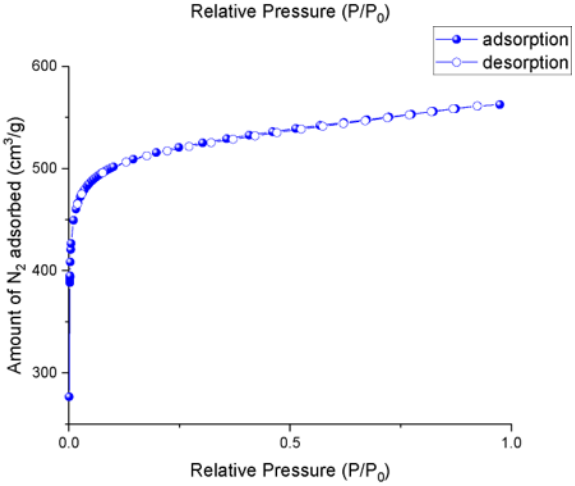

Figure B.14 Nitrogen adsorption-desorption isotherm at 77 K for activated SNU-70 7×, measurements for three samples shown.

SNU-70 7× seeded

BET surface area = 2057 m^2/g
C constant = 1267.342
Correlation coefficient = 0.999995
BET fitting range = [0.016, 0.046]

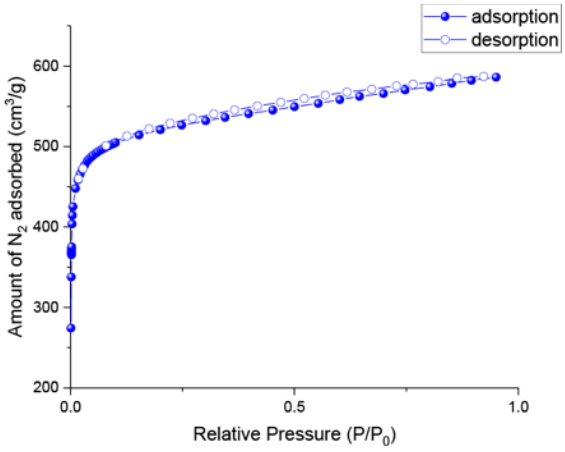

BET surface area = 1513 m^2/g
C constant = 1985.407
Correlation coefficient = 0.999995
BET fitting range = [0.016, 0.047]

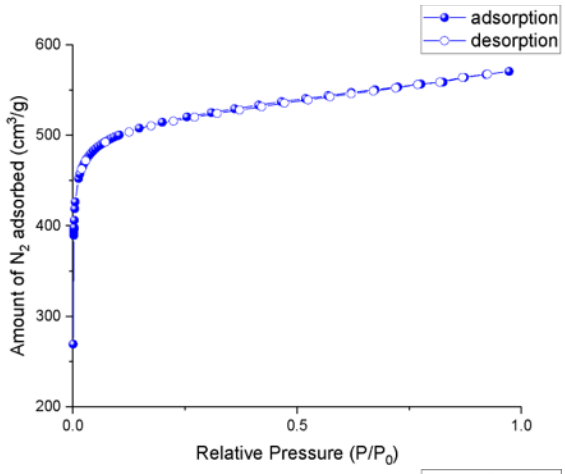

BET surface area = 2033 m^2/g
C constant = 1916.761
Correlation coefficient = 0.999997
BET fitting range = [0.014, 0.041]

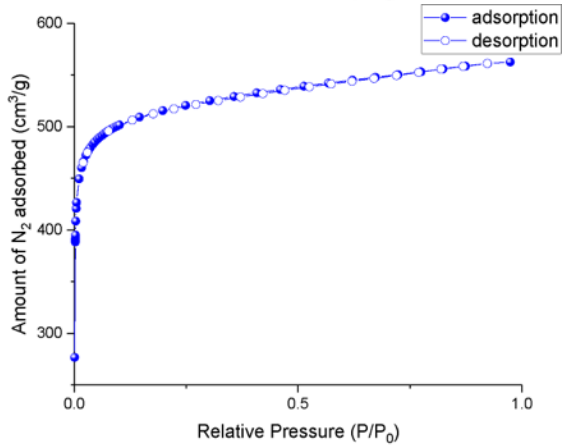

Figure B.15 Nitrogen adsorption-desorption isotherm at 77 K for activated SNU-70 7× seeded conditions, measurements for three samples shown.

UiO-66 1×

BET surface area = 1184 m²/g
C constant = 3961.936
Correlation coefficient = 0.999998
BET fitting range = [0.003382, 0.02689]

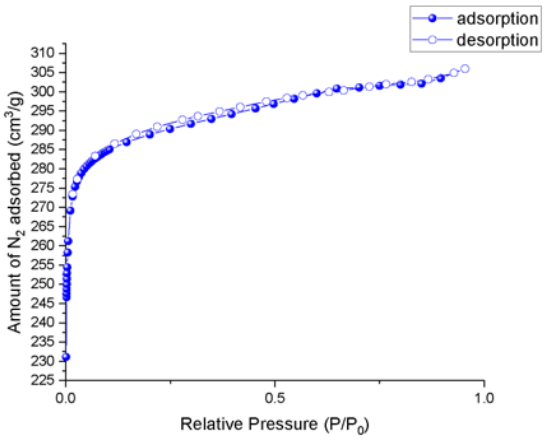

BET surface area = 1223 m²/g
C constant = 3020.216
Correlation coefficient = 0.999999
BET fitting range = [0.00404, 0.026496]

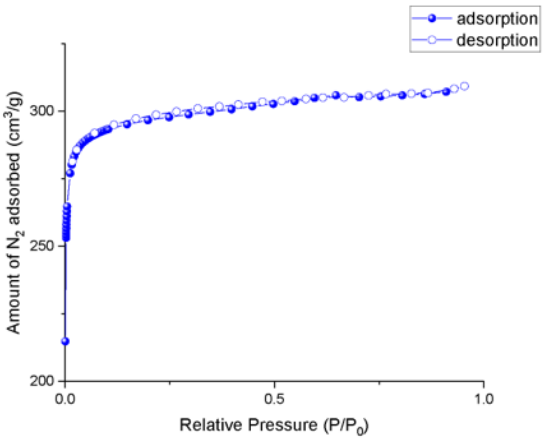

BET surface area = 1146 m²/g
C constant = 3745.551
Correlation coefficient = 0.999995
BET fitting range = [0.004953, 0.026152]

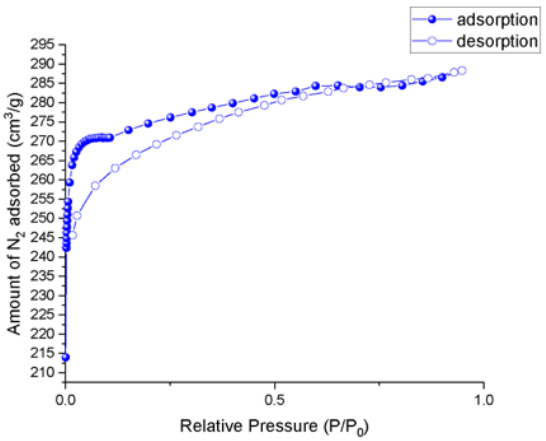

Figure B.16 Nitrogen adsorption-desorption isotherm at 77 K for activated UiO-66 1×, measurements for three samples shown.

UiO-66 3×

BET surface area = 805 m²/g
C constant = 2875.601
Correlation coefficient = 0.999993
BET fitting range = [0.0188, 0.0491]

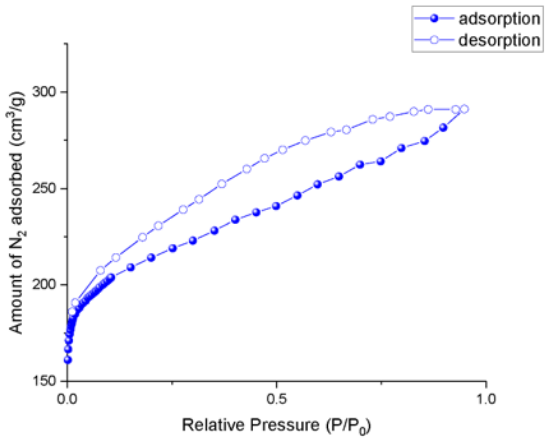

BET surface area = 579 m²/g
C constant = 9697.066
Correlation coefficient = 0.999999
BET fitting range = [0.0047, 0.0162]

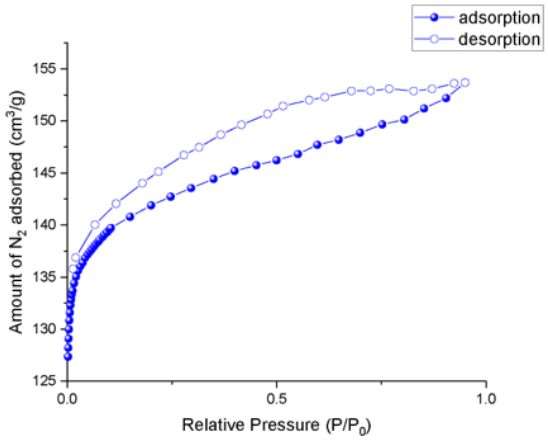

BET surface area = 663 m²/g
C constant = 3129.835
Correlation coefficient = 0.999998
BET fitting range = [0.0050, 0.030832]

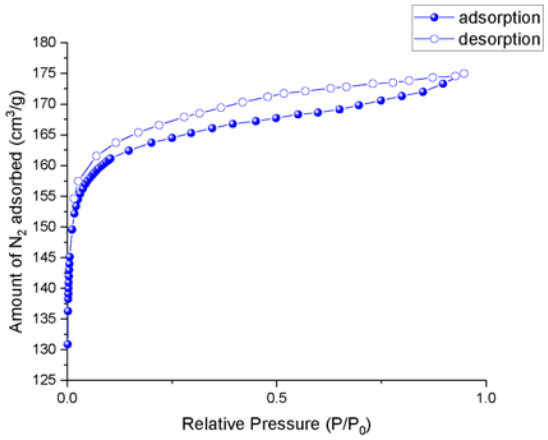

Figure B.17 Nitrogen adsorption-desorption isotherm at 77 K for activated UiO-66 3×, measurements for three samples shown.

UiO-66 3× seeded

BET surface area = 1041 m^2/g
C constant = 8973.000
Correlation coefficient = 0.999999
BET fitting range = [0.0107, 0.0240]

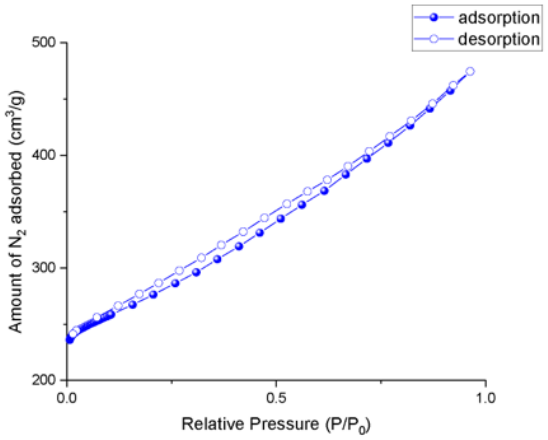

BET surface area = 943 m^2/g
C constant = -13036.639
Correlation coefficient = 0.999999
BET fitting range = [0.0099, 0.01977]

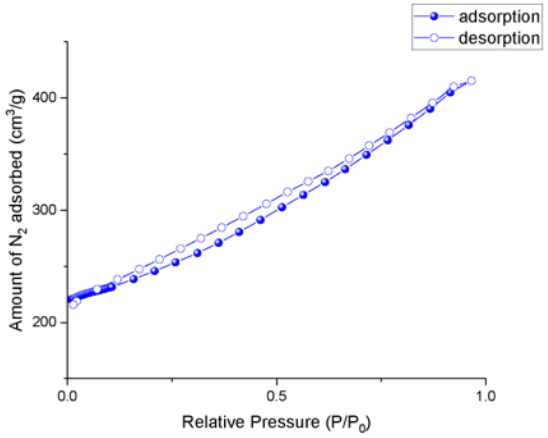

BET surface area = 1292 m^2/g
C constant = 455.714
Correlation coefficient = 0.999982
BET fitting range = [0.0714, 0.1029]

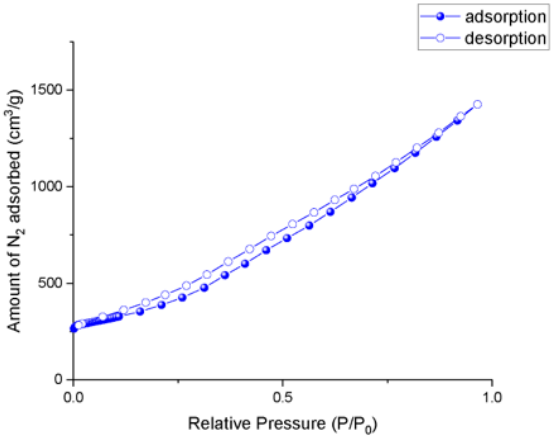

Figure B.18 Nitrogen adsorption-desorption isotherm at 77 K for activated UiO-66 3× seeded conditions, measurements for three samples shown.

B.2.3 Time-lapse photography

Mg-MOF-74 5× concentration seeded synthesis

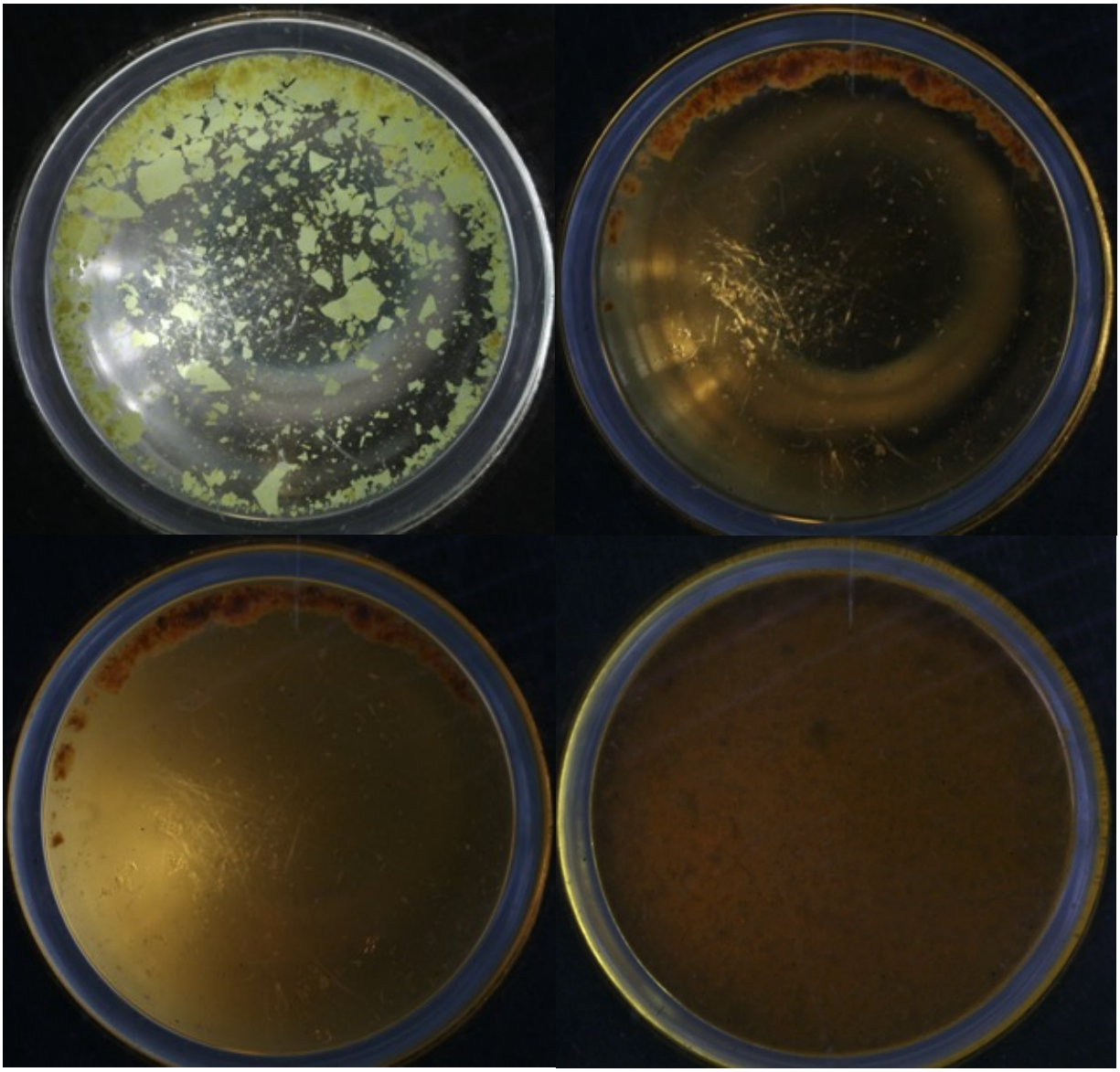

Figure B.19 (top left) At 0 minutes, seed crystals are added to the 5× reaction mixture. (top right) At 44 minutes, seed dissolution has progressed to its maximum extent. (bottom left) At 59 minutes, microcrystalline Mg-MOF-74 begins to form, observed as a loss of transparency when observed from the bottom of the reaction vial. (bottom right) At 20 h, material formation has resulted in a significant loss to transparency when observed from the bottom of the reaction vial.

B.2.4 SEM data

Mg-MOF-74

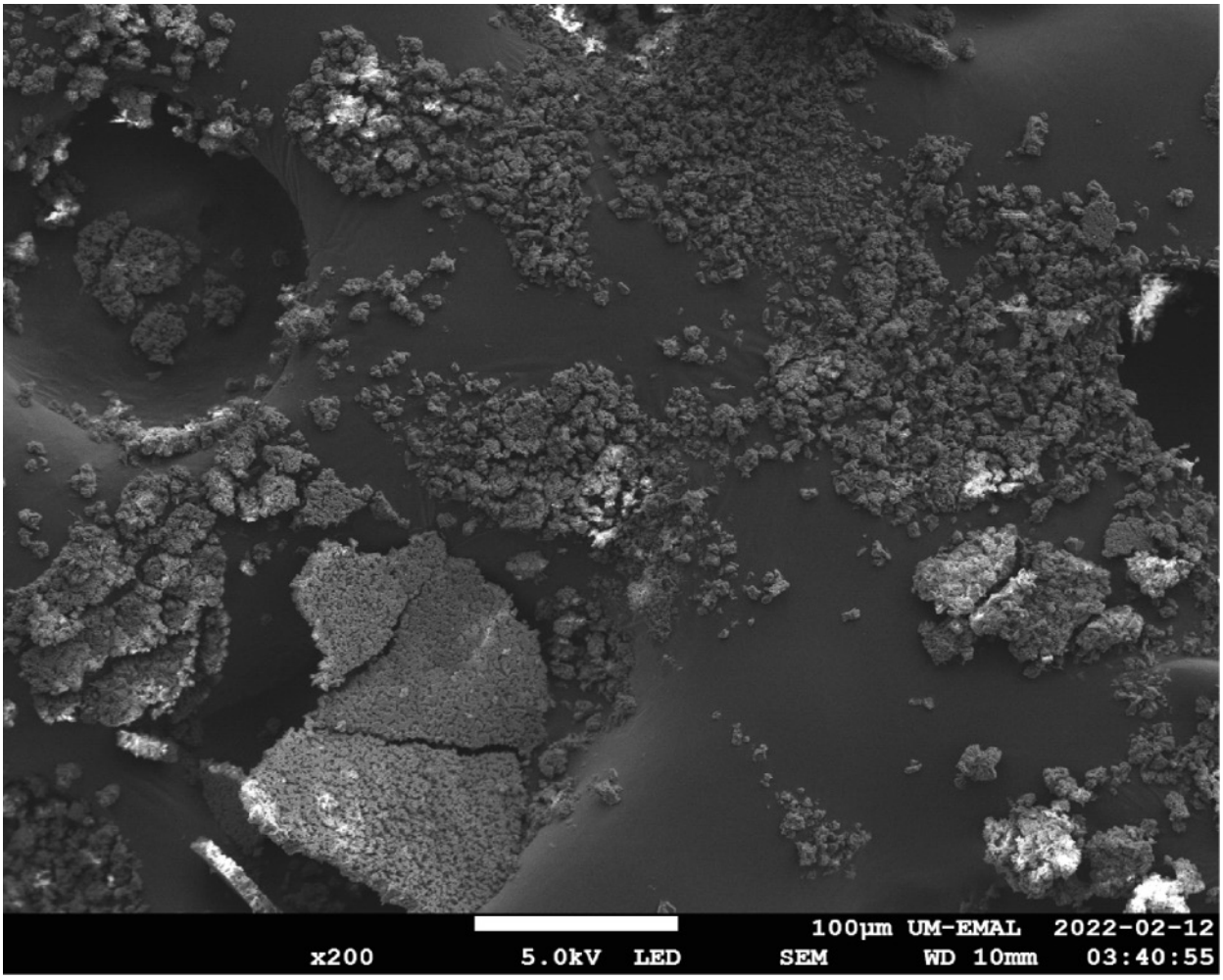

Figure B.20 SEM of the bulk Mg-MOF-74 1× concentration synthesis material.

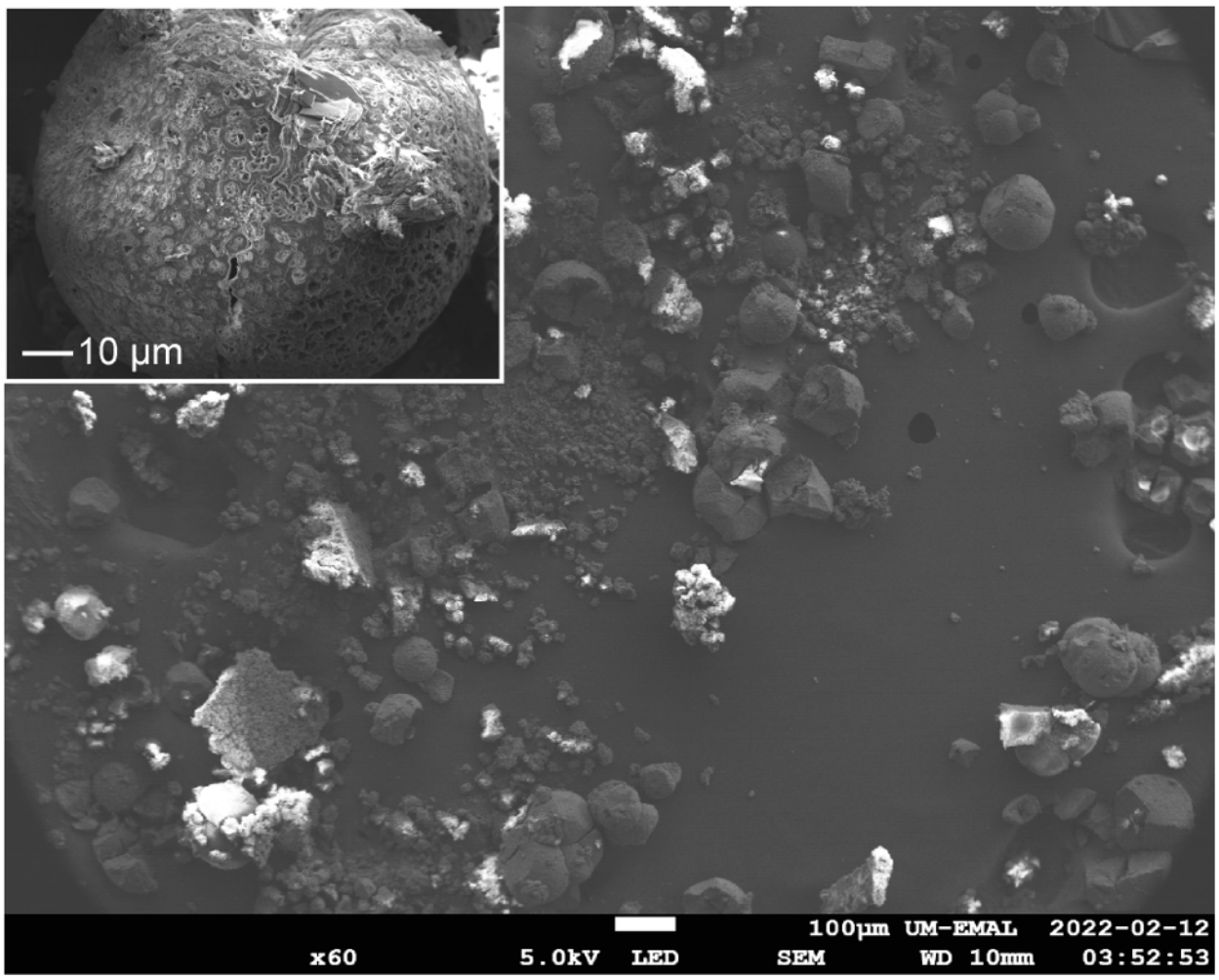

Figure B.21 SEM of the bulk Mg-MOF-74 5× concentration synthesis material with inset showing the spherical phase and plate crystal formation adhered to the spherical material.

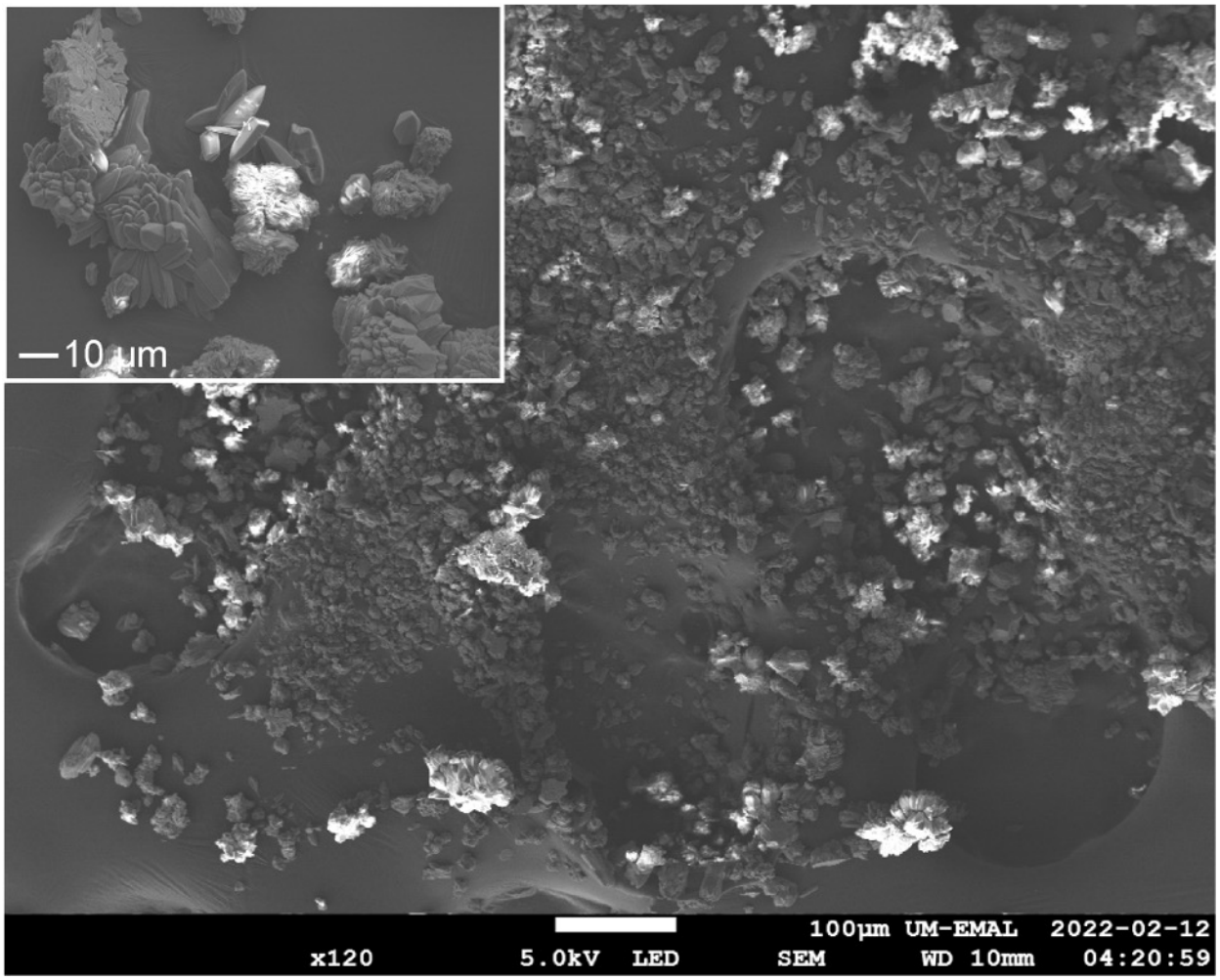

Figure B.22 SEM of the bulk Mg-MOF-74 5× concentration seeded synthesis material with inset showing retention of plate crystal phase along with Mg-MOF-74 phase.

DMOF-1

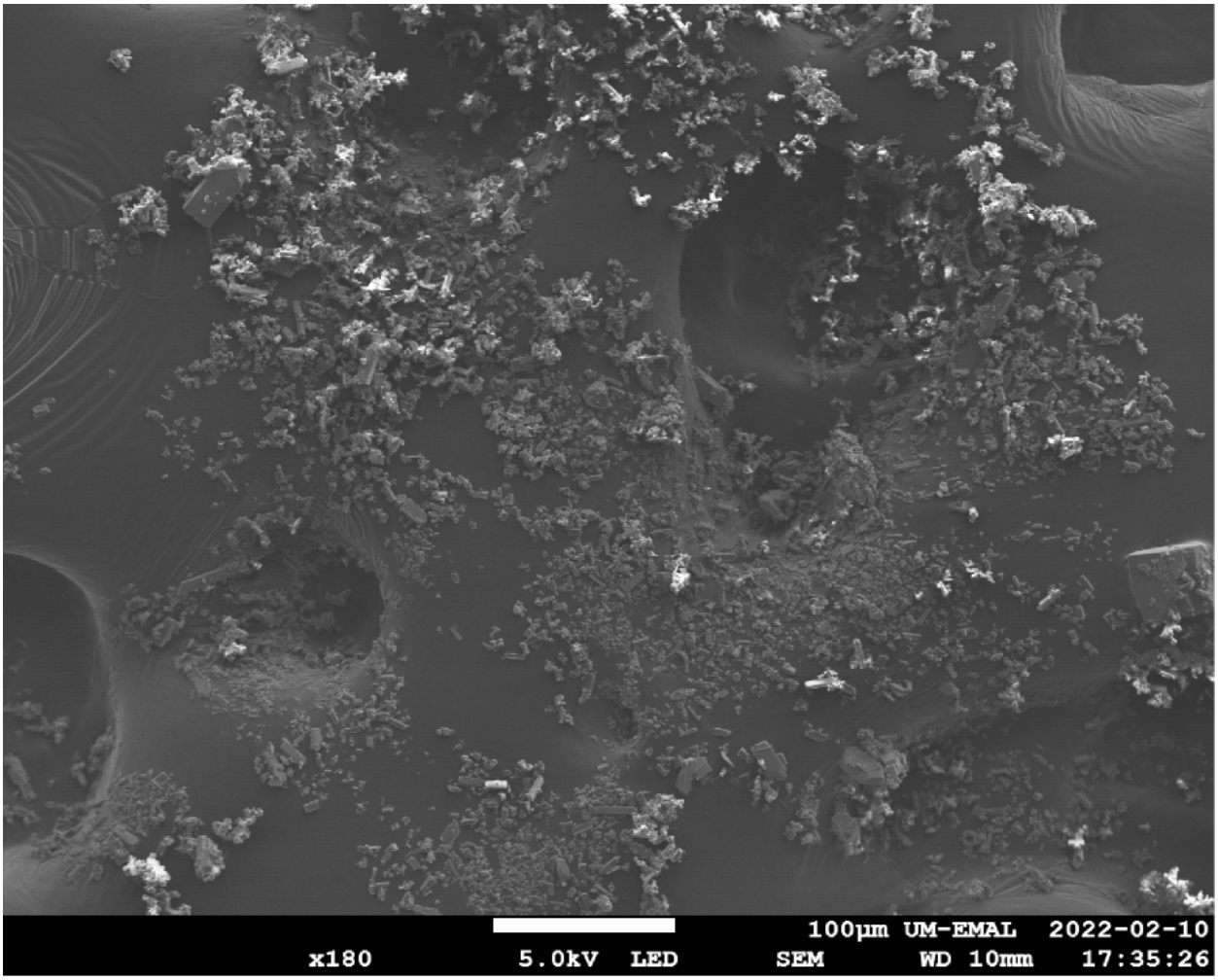

Figure B.23 SEM of the bulk DMOF-1 1× concentration synthesis material.

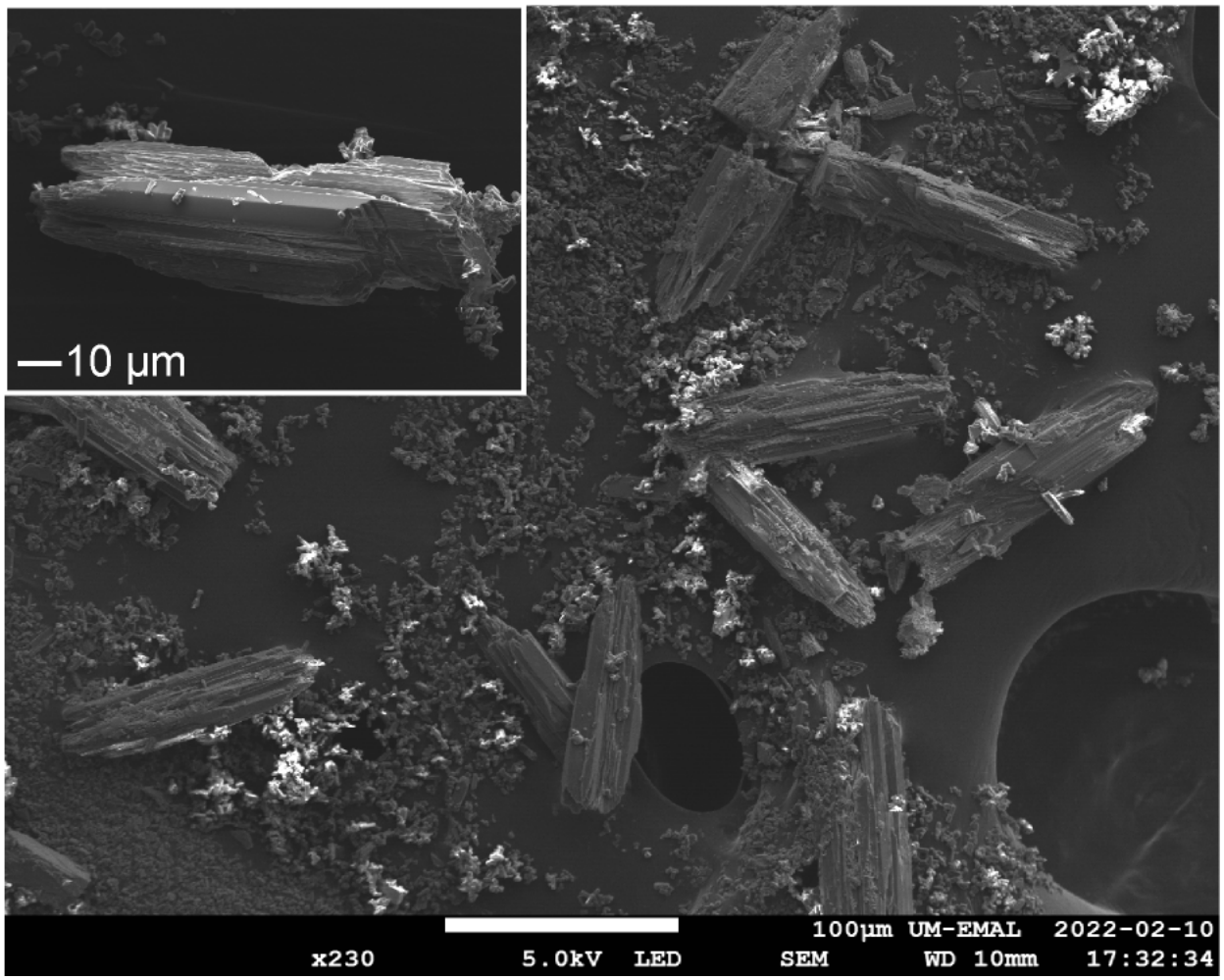

Figure B.24 SEM of the bulk DMOF-1 5× concentration synthesis material with inset showing off-target phase, a large, striated block comprised of aggregate plates.

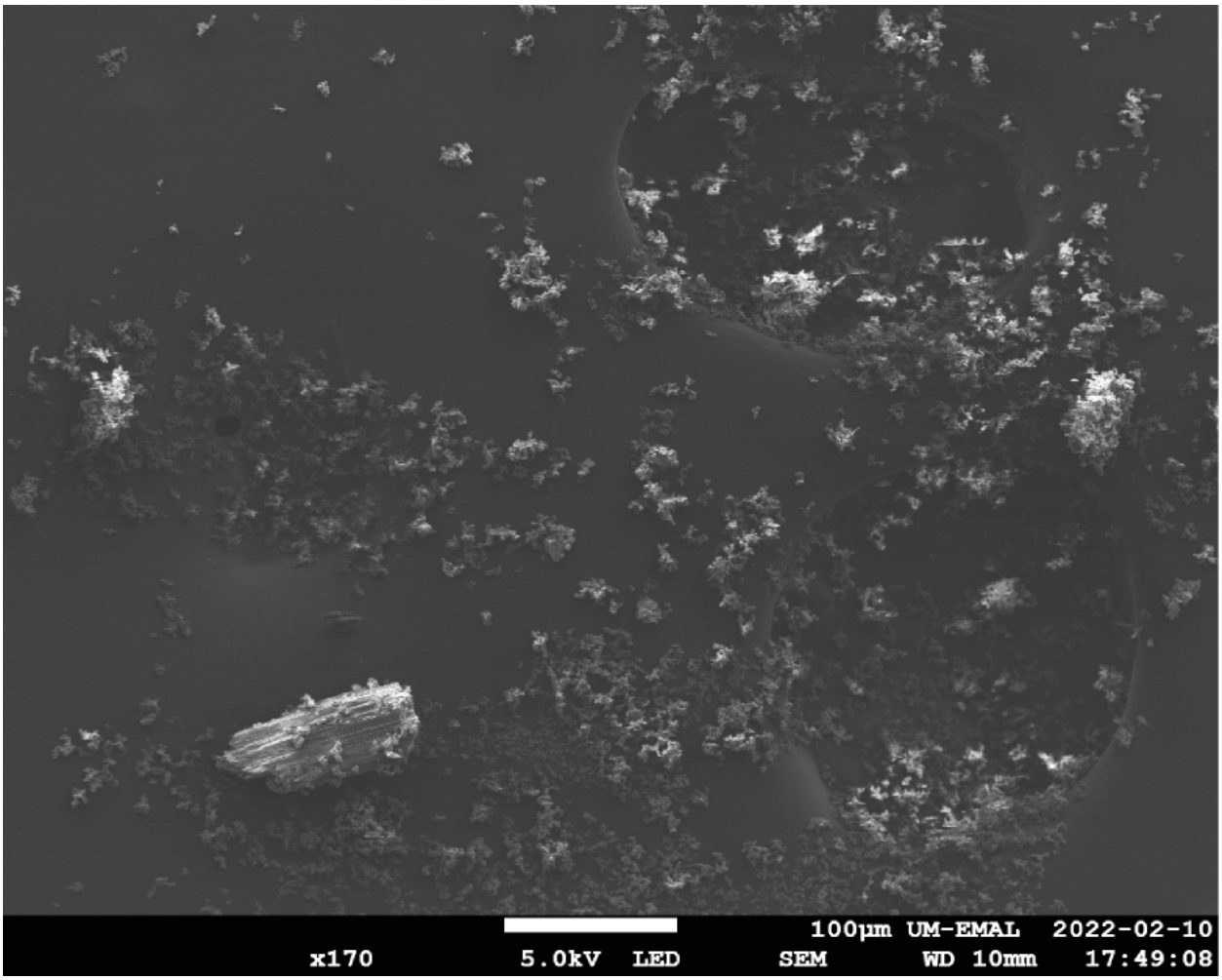

Figure B.25 SEM of the bulk DMOF-1 5× concentration seeded synthesis material.

UiO-66

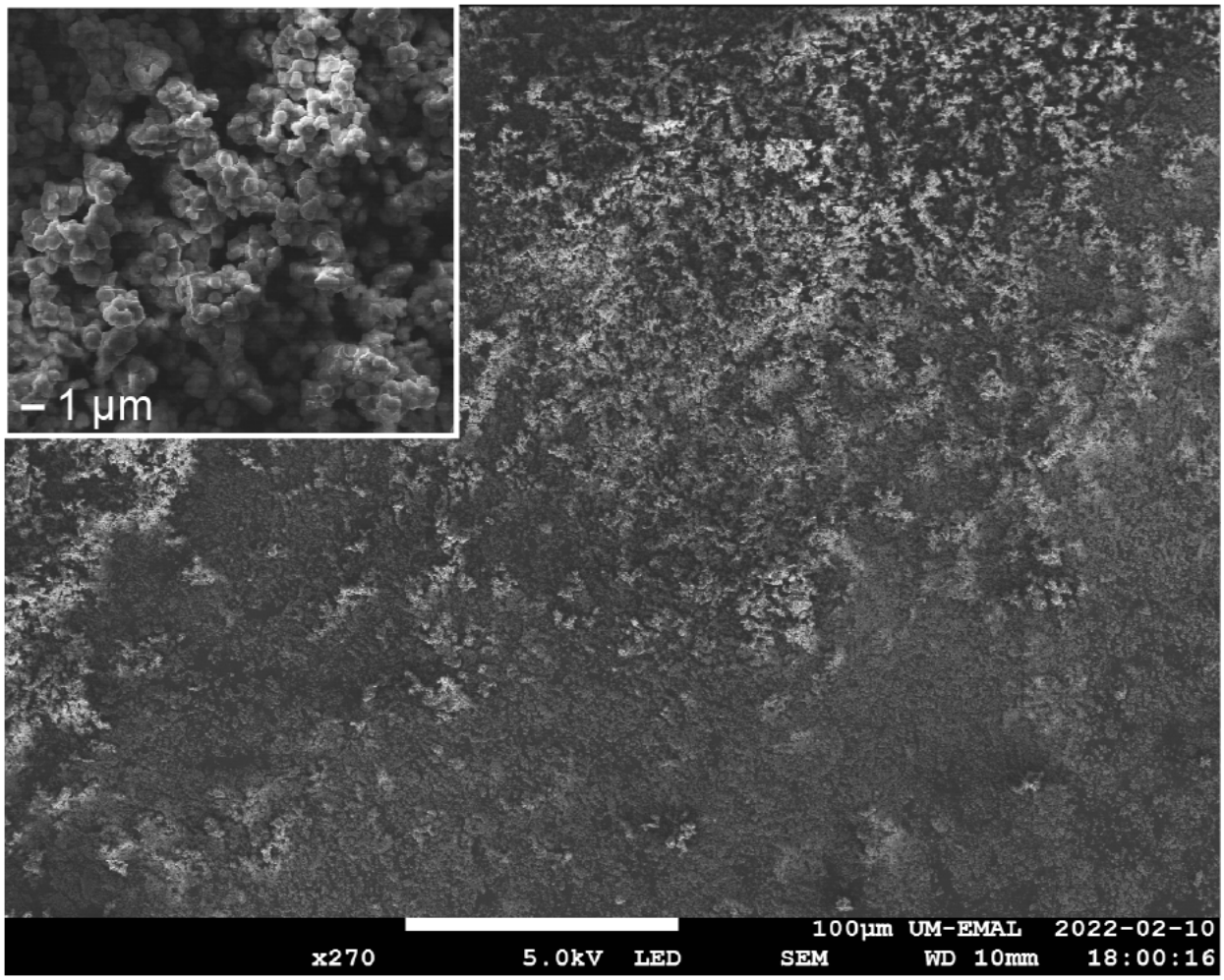

Figure B.26 SEM of the bulk UiO-66 1× concentration synthesis material with inset showing aggregates of small crystals with uniform size.

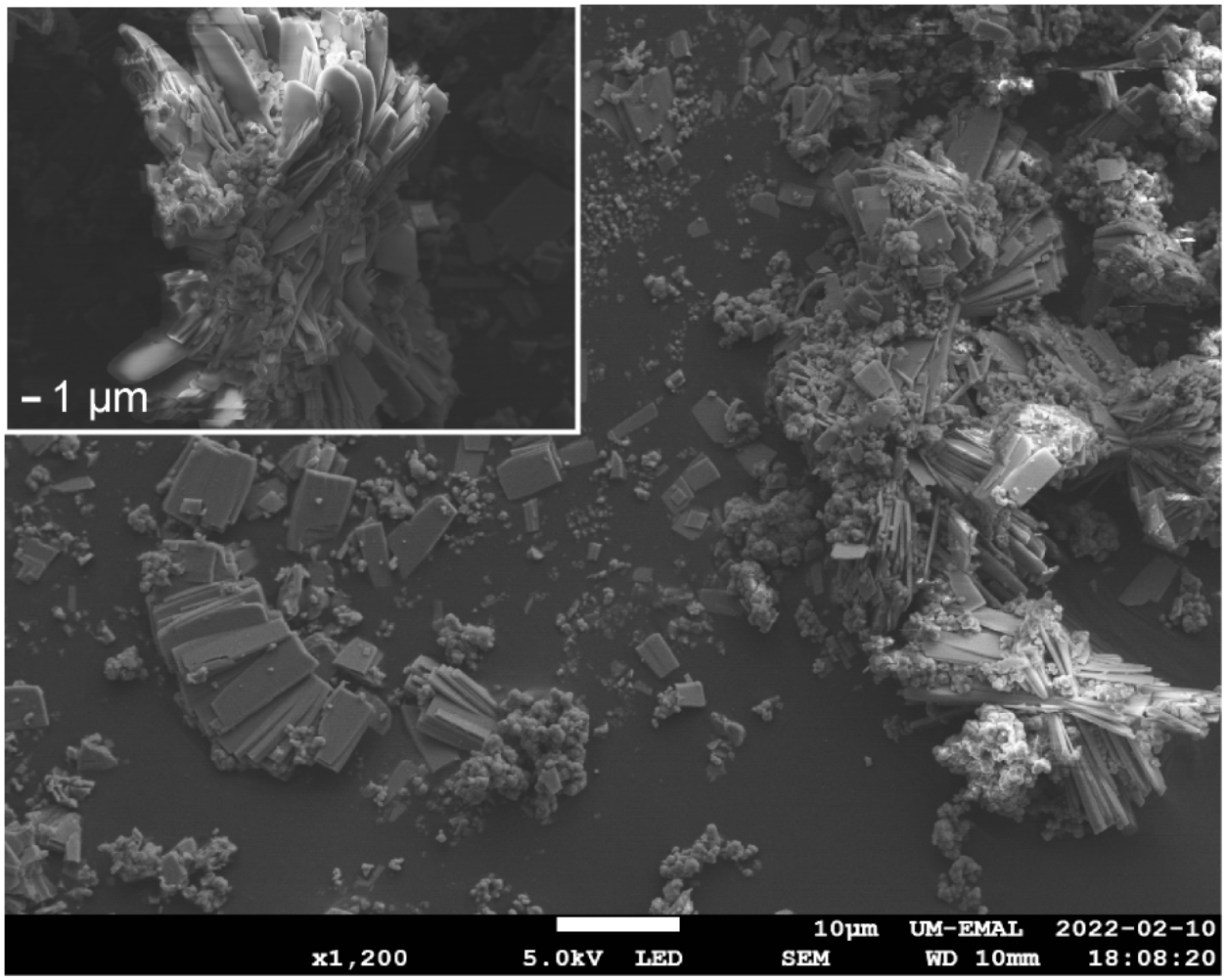

Figure B.27 SEM of the bulk UiO-66 3× concentration synthesis material with inset showing plate formation along with small crystals of uniform size.

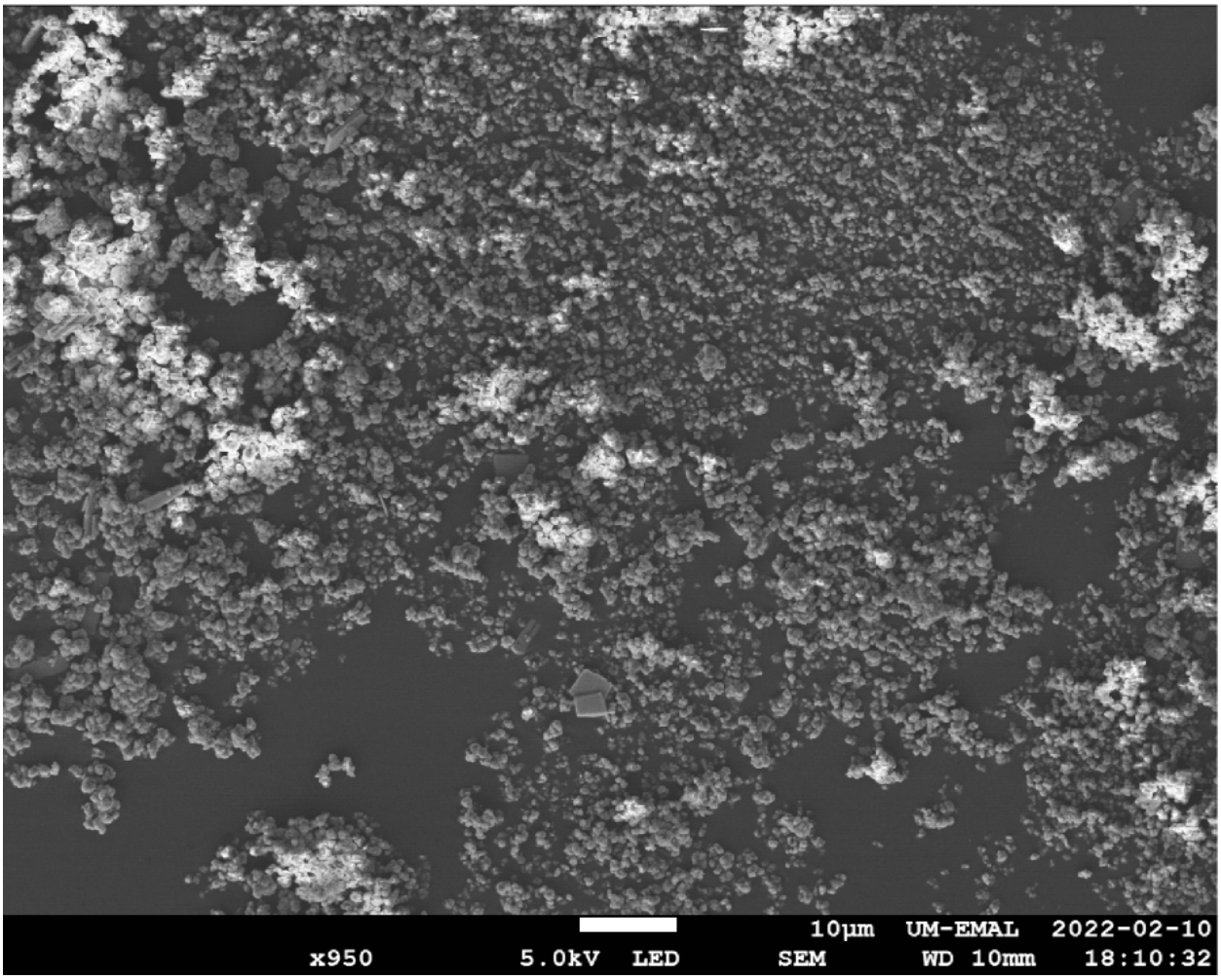

Figure B.28 SEM of the bulk UiO-66 3× concentration seeded synthesis material.

Appendix C Reagent Reactivity and Solvent Choice Determine Metal–Organic Framework Microstructure during Postsynthetic Modification

C.1 Publication of This Chapter

Du Bois, D. R.; Matzger, A. J. Reagent Reactivity and Solvent Choice Determine Metal–Organic Framework Microstructure during Postsynthetic Modification. *J. Am. Chem. Soc.* **2021**, *143*, 671.

C.2 Supporting Data

C.2.1 Experimental SEM-EDS Data

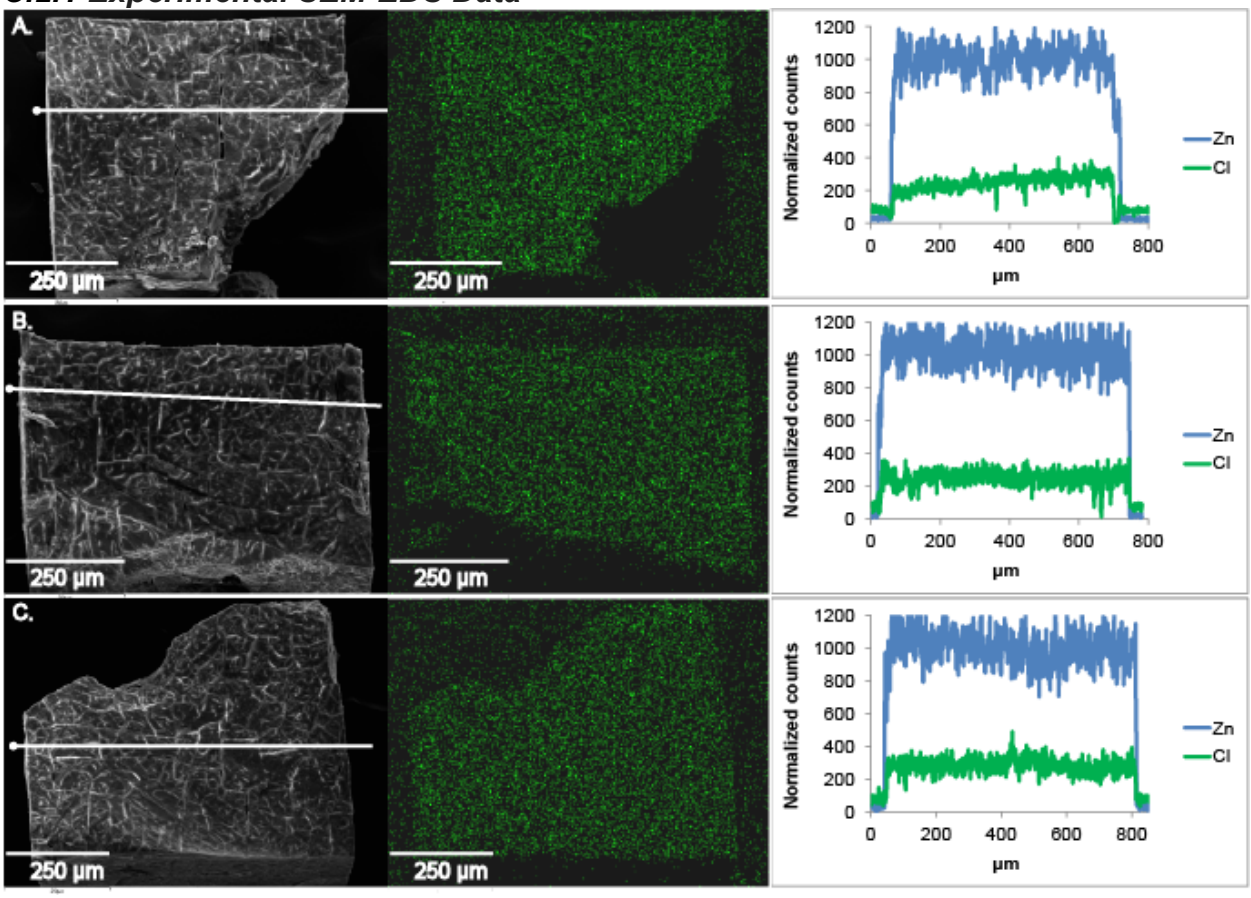

Figure C.1 SEM images, EDS maps, and EDS linescans for three trials of PSM on IRMOF-3 with 2-chloroethyl isocyanate for 3 hours in toluene, resulting in a uniform microstructure. Zinc counts on linescans normalized to average 1000.

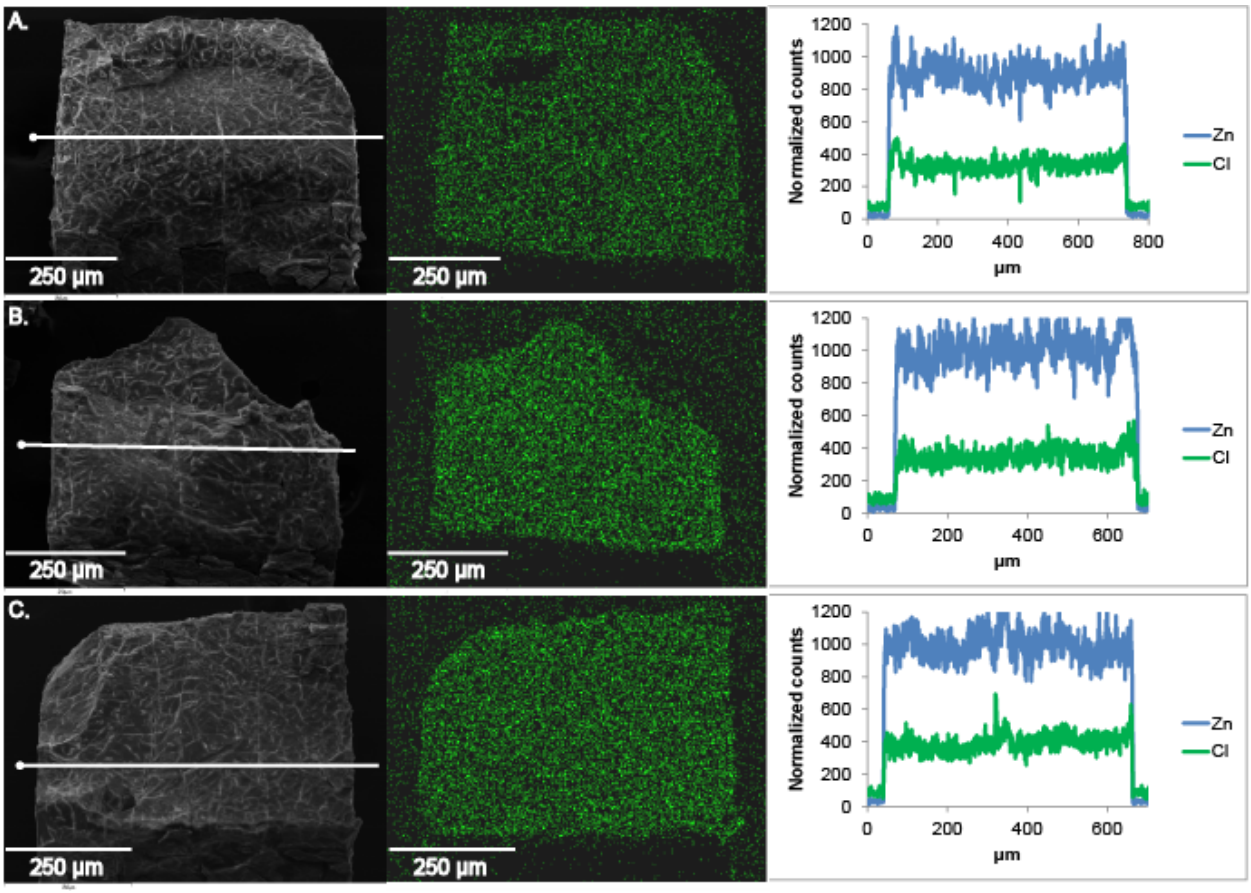

Figure C.2 SEM images, EDS maps, and EDS linescans for three trials of PSM on IRMOF-3 with 2-chloroethyl isocyanate for 6 hours in toluene, resulting in a uniform microstructure. Zinc counts on linescans normalized to average 1000.

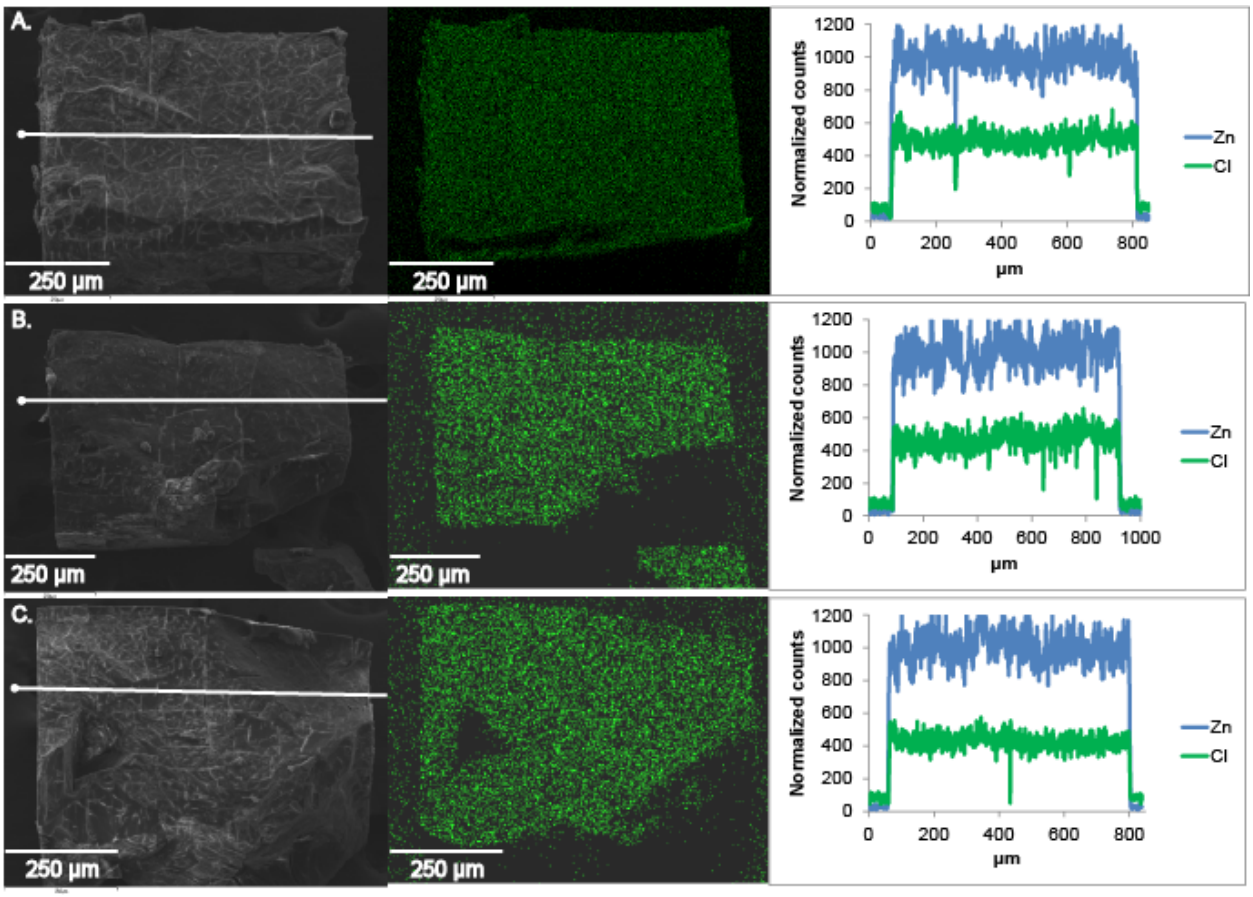

Figure C.3 SEM images, EDS maps, and EDS linescans for three trials of PSM on IRMOF-3 with 2-chloroethyl isocyanate for 9 hours in toluene, resulting in a uniform microstructure. Zinc counts on linescans normalized to average 1000.

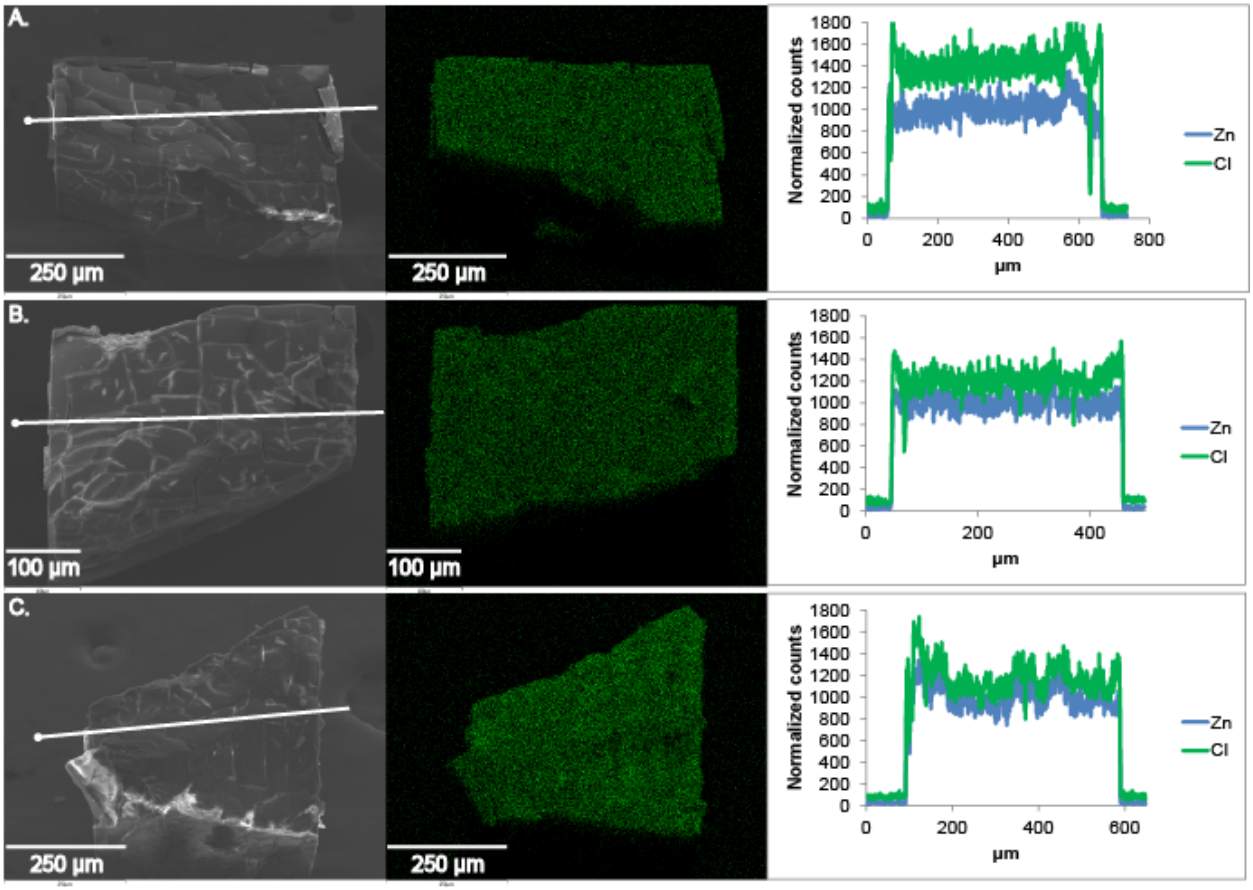

Figure C.4 SEM images, EDS maps, and EDS linescans for three trials of PSM on IRMOF-3 with 2-chloroethyl isocyanate for 24 hours in toluene, resulting in a uniform microstructure. Zinc counts on linescans normalized to average 1000.

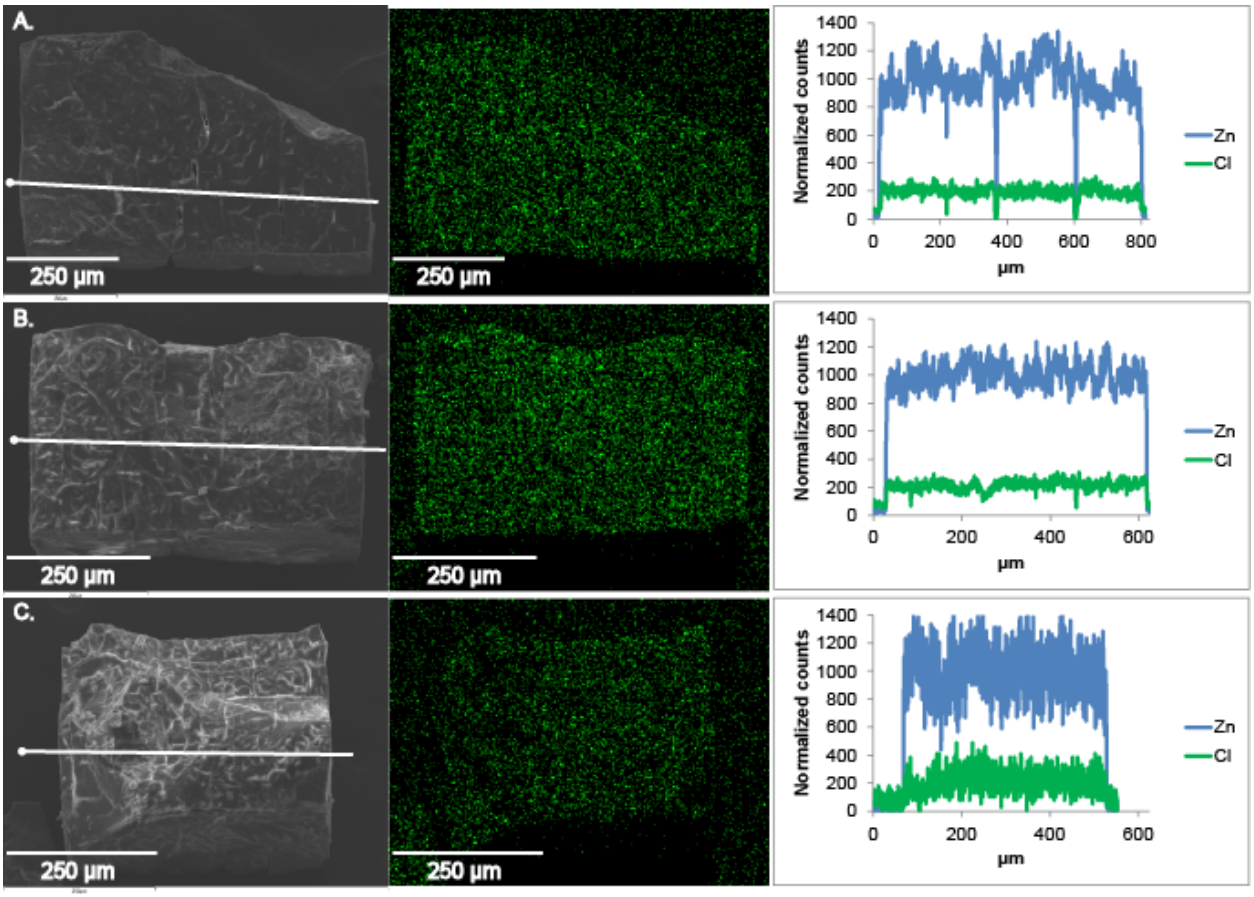

Figure C.5 SEM images, EDS maps, and EDS linescans for three trials of PSM on IRMOF-3 with 2-chloroethyl isocyanate for 3 hours in chloroform, resulting in a uniform microstructure. Zinc counts on linescans normalized to average 1000.

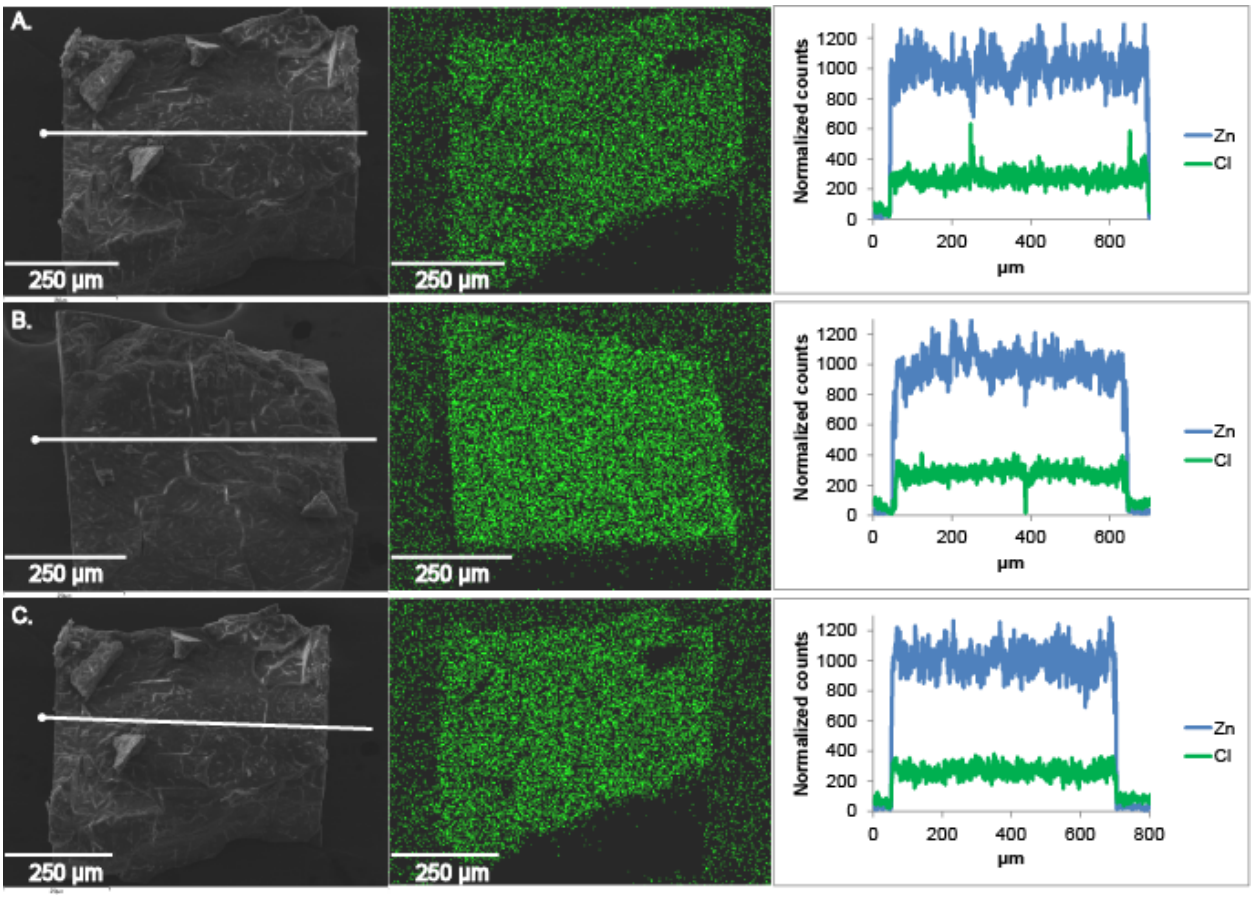

Figure C.6 SEM images, EDS maps, and EDS linescans for three trials of PSM on IRMOF-3 with 2-chloroethyl isocyanate for 6 hours in chloroform, resulting in a uniform microstructure. Zinc counts on linescans normalized to average 1000.

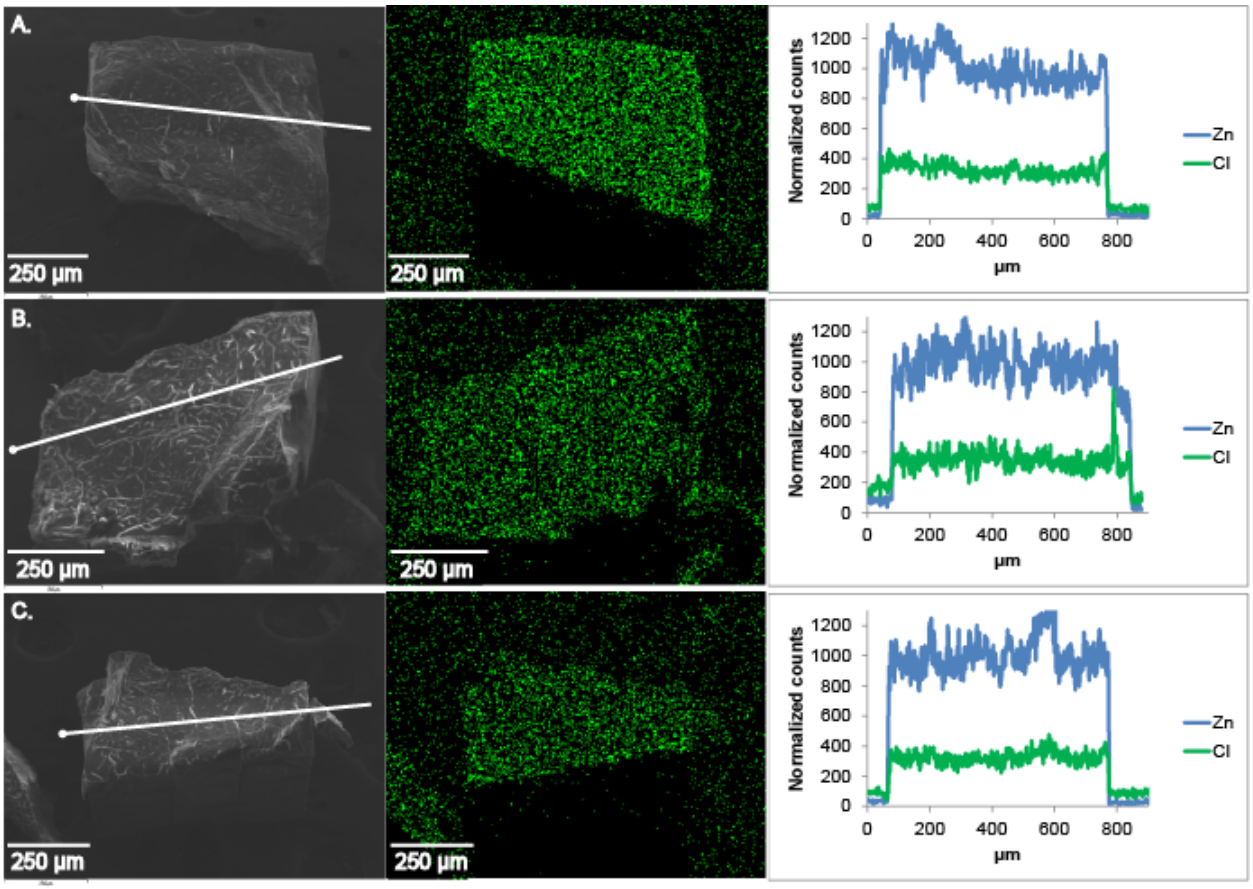

Figure C.7 SEM images, EDS maps, and EDS linescans for three trials of PSM on IRMOF-3 with 2-chloroethyl isocyanate for 9 hours in chloroform, resulting in a uniform microstructure. Zinc counts on linescans normalized to average 1000.

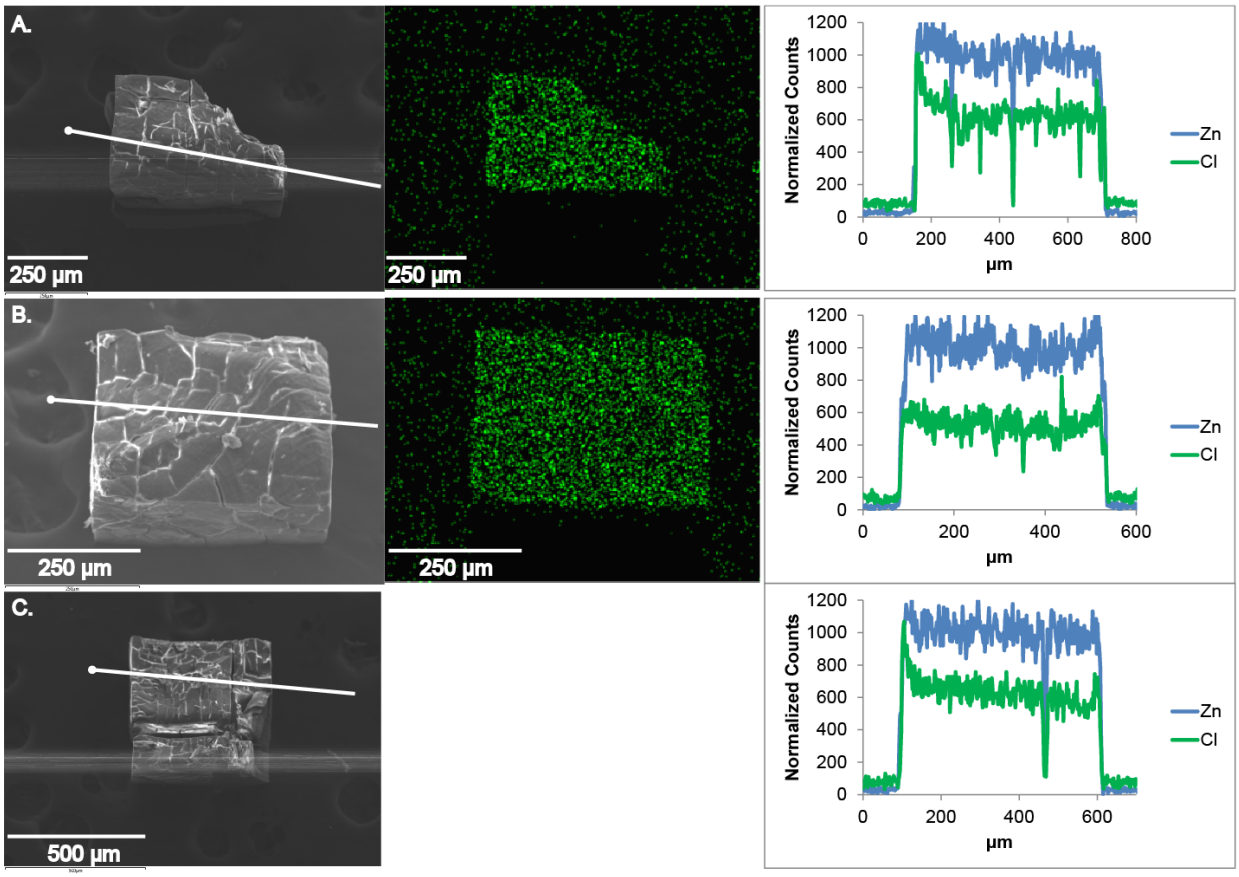

Figure C.8 SEM images, EDS maps, and EDS linescans for three trials of PSM on IRMOF-3 with 2-chloroethyl isocyanate for 24 hours in chloroform, resulting in a uniform microstructure. Zinc counts on linescans normalized to average 1000. EDS mapping data was not collected for trial c.

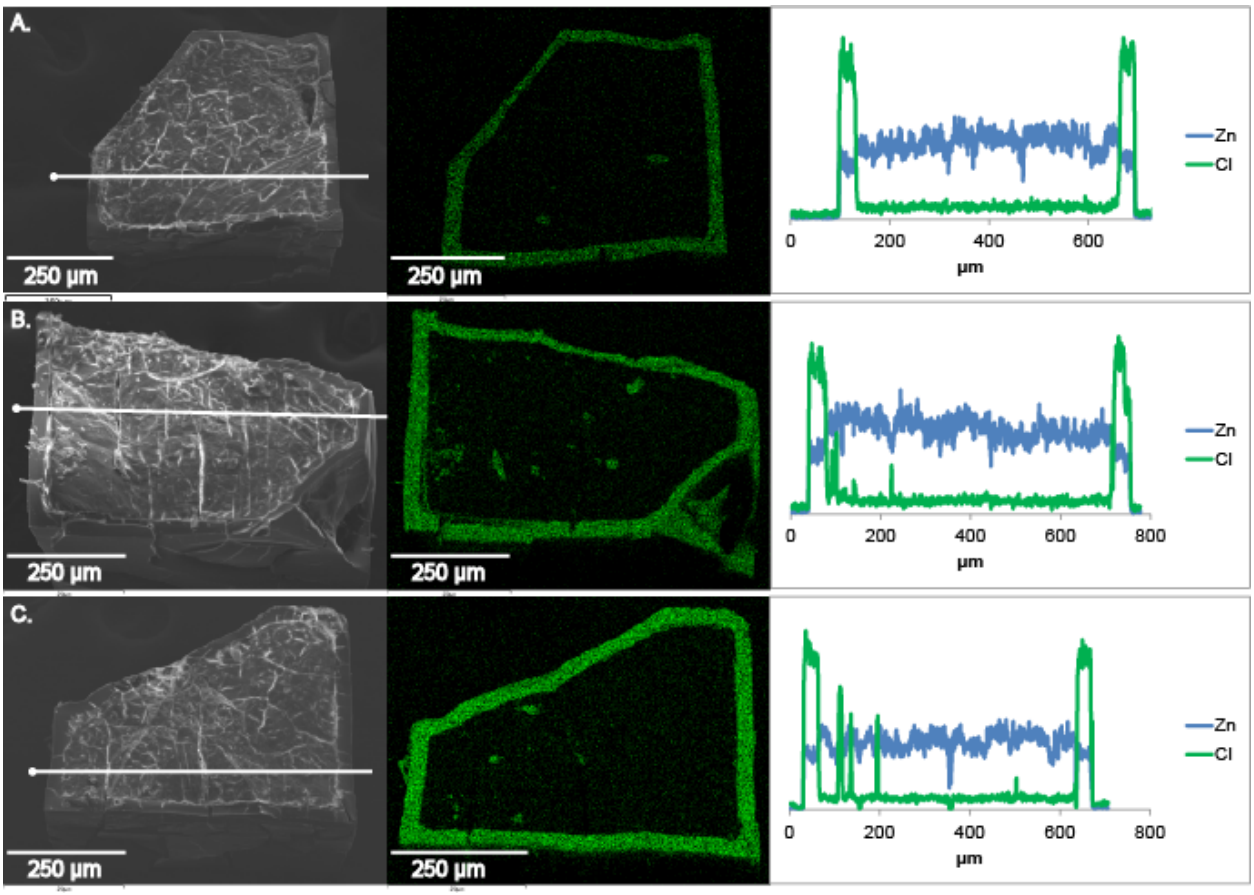

Figure C.9 SEM images, EDS maps, and EDS linescans for three trials of PSM on IRMOF-3 with chloroacetyl isocyanate for 3 hours in toluene, resulting in a core–shell microstructure.

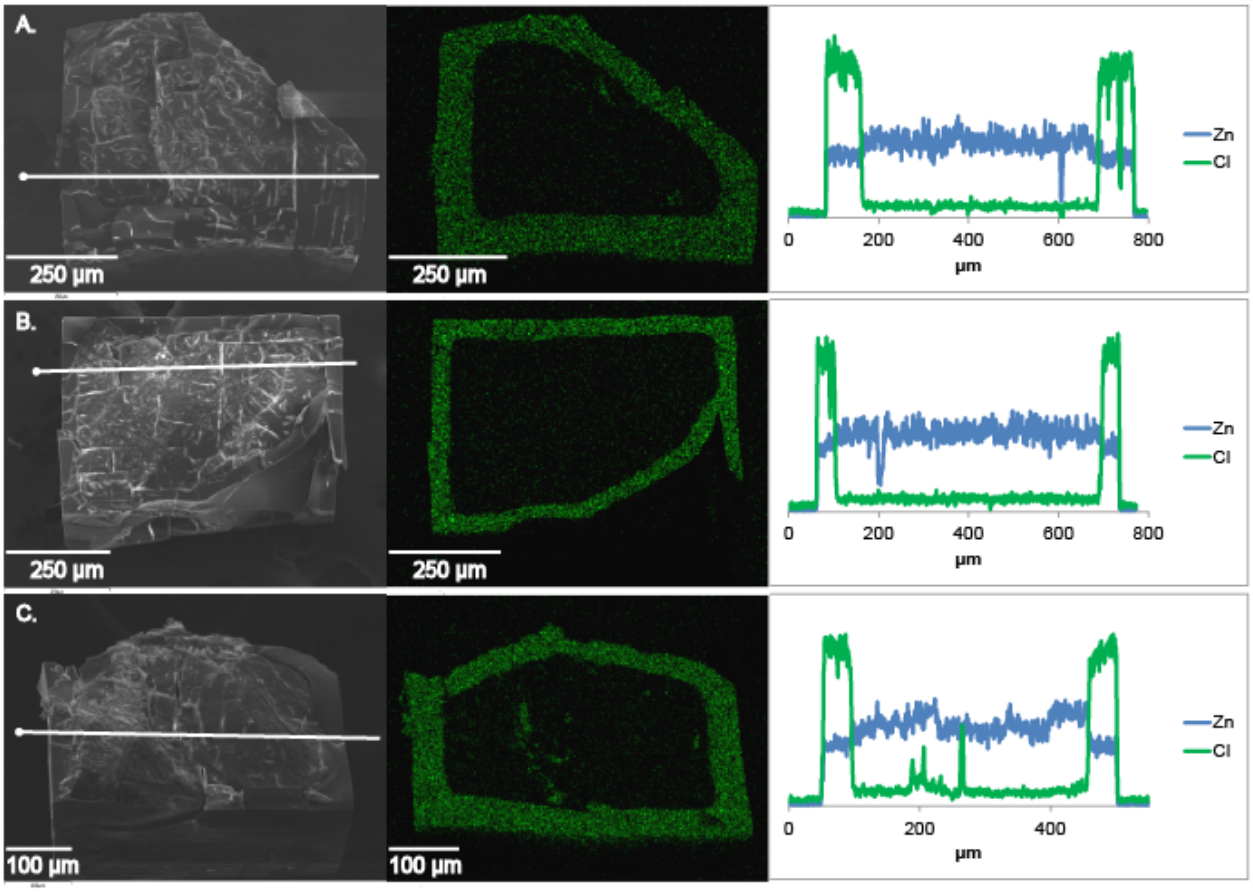

Figure C.10 SEM images, EDS maps, and EDS linescans for three trials of PSM on IRMOF-3 with chloroacetyl isocyanate for 6 hours in toluene, resulting in a core–shell microstructure.

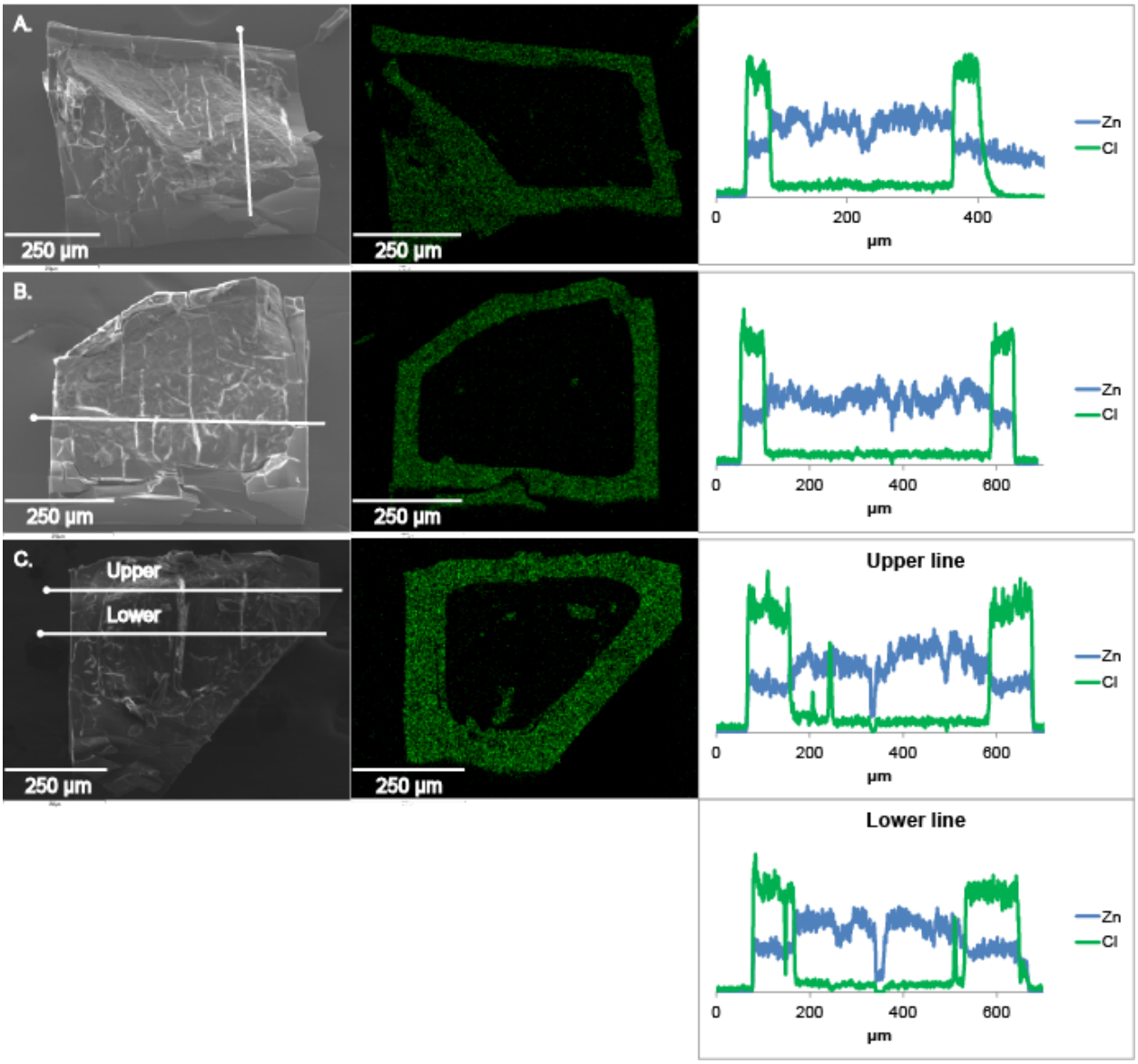

Figure C.11 SEM images, EDS maps, and EDS linescans for three trials of PSM on IRMOF-3 with chloroacetyl isocyanate for 9 hours in toluene, resulting in a core–shell microstructure. Trial C has two linescans to ensure accurate depictions of the depth of functionalization with two measured regions that are perpendicular to the edge of the MOF.

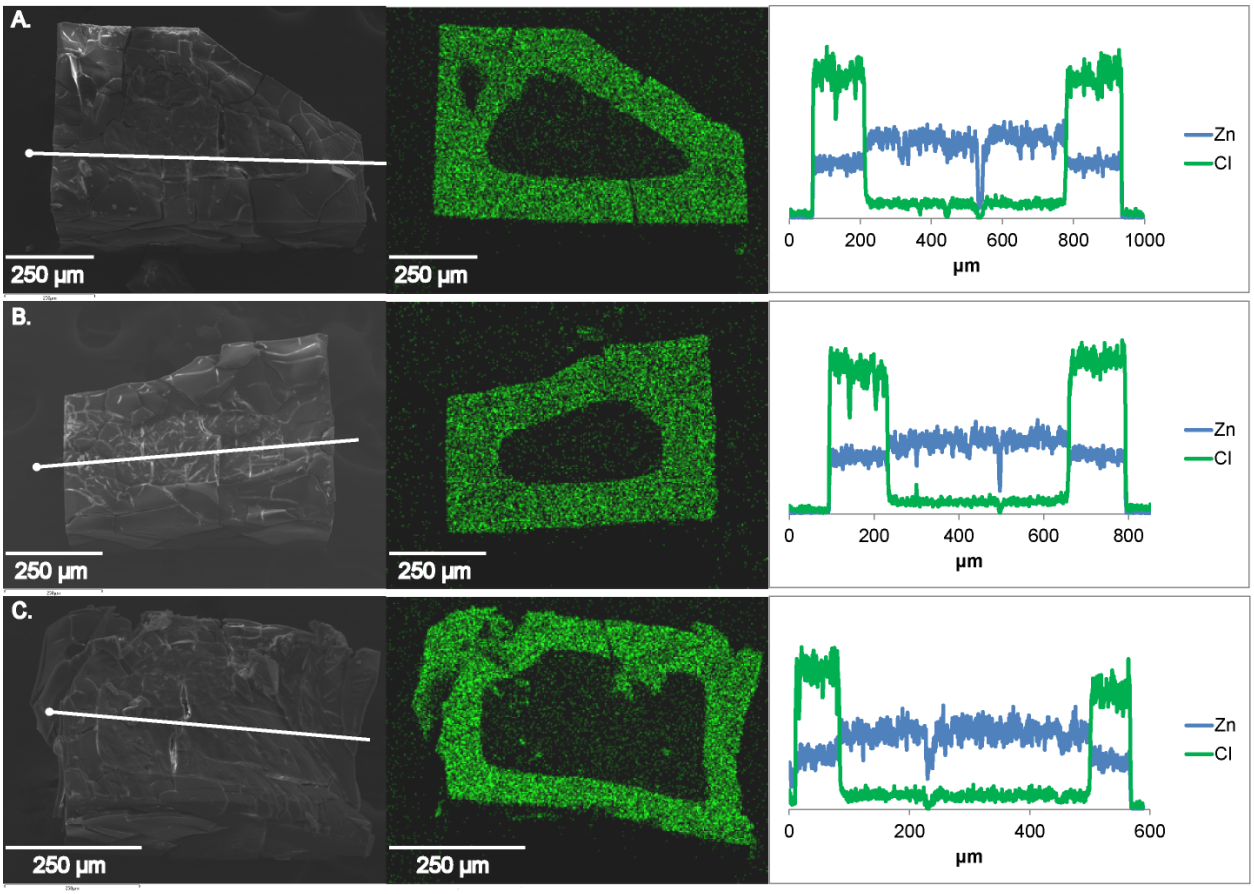

Figure C.12 SEM images, EDS maps, and EDS linescans for three trials of PSM on IRMOF-3 with chloroacetyl isocyanate for 24 hours in toluene, resulting in a core–shell microstructure.

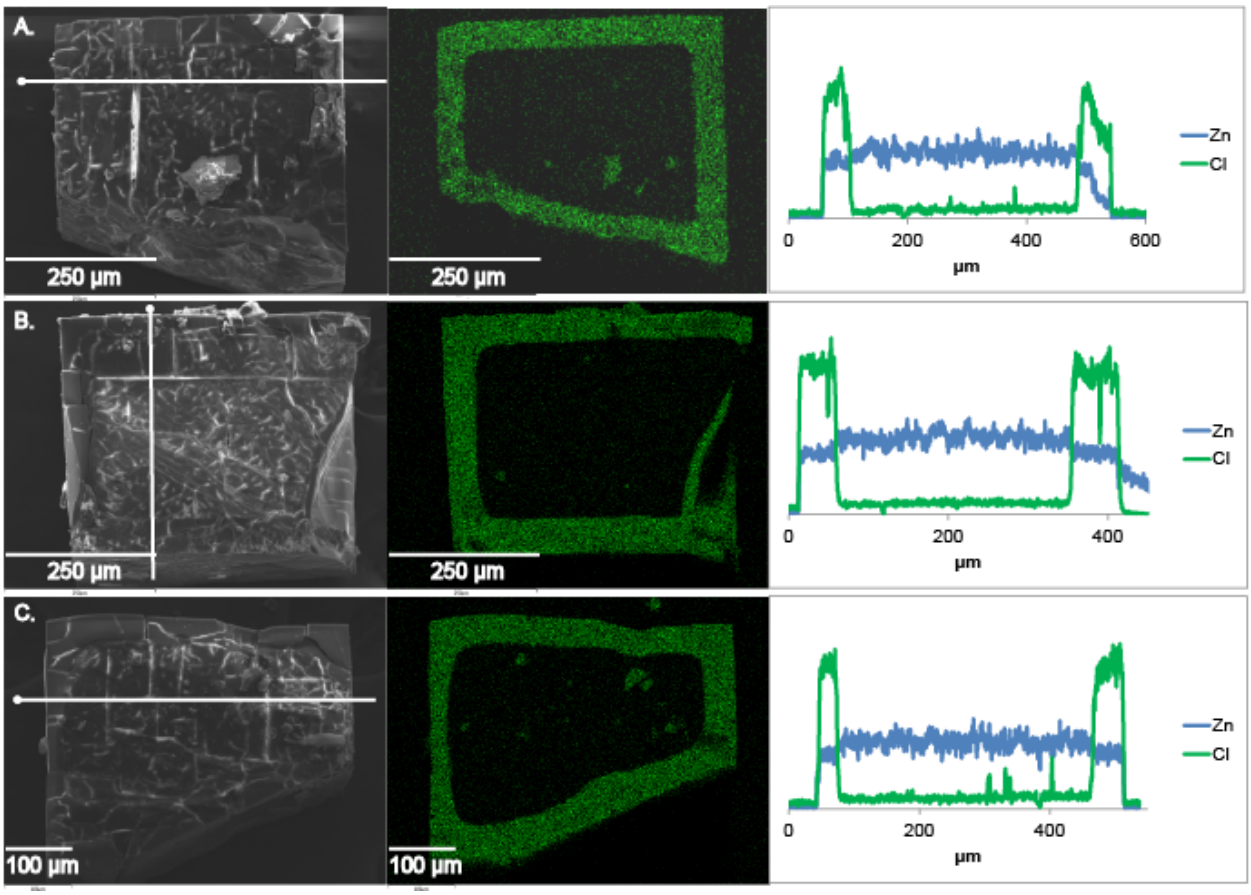

Figure C.13 SEM images, EDS maps, and EDS linescans for three trials of PSM on IRMOF-3 with chloroacetyl isocyanate for 3 hours in chloroform, resulting in a core–shell microstructure.

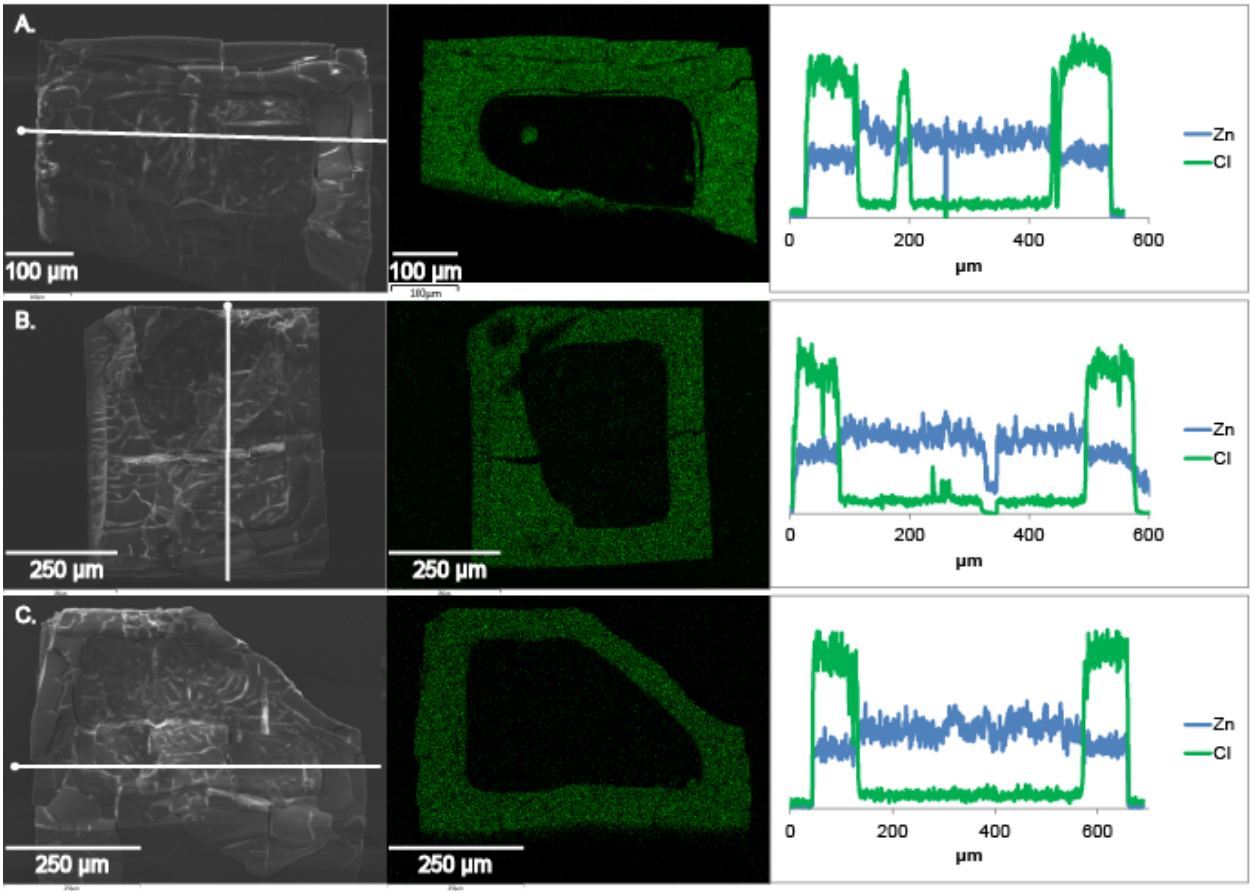

Figure C.14 SEM images, EDS maps, and EDS linescans for three trials of PSM on IRMOF-3 with chloroacetyl isocyanate for 6 hours in chloroform, resulting in a core–shell microstructure.

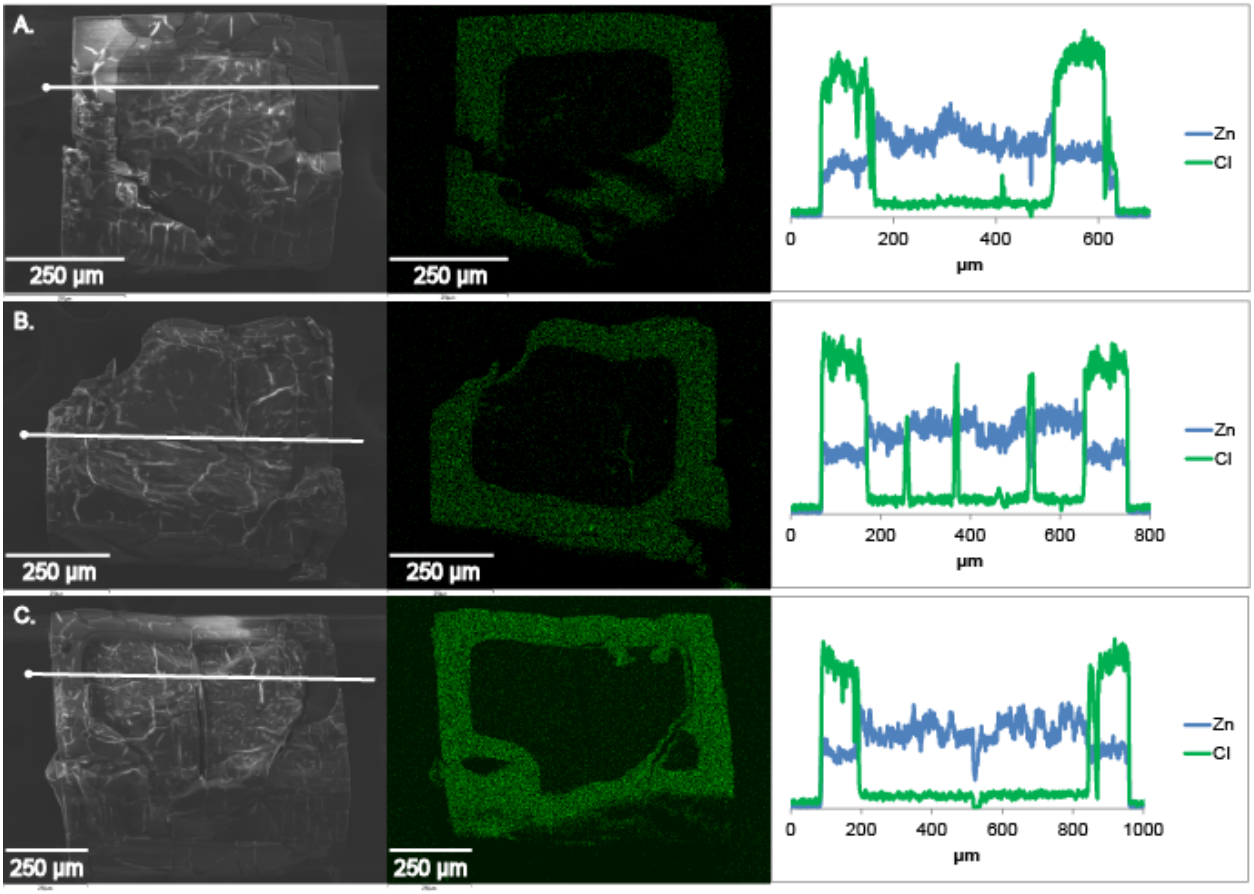

Figure C.15 SEM images, EDS maps, and EDS linescans for three trials of PSM on IRMOF-3 with chloroacetyl isocyanate for 9 hours in chloroform, resulting in a core–shell microstructure.

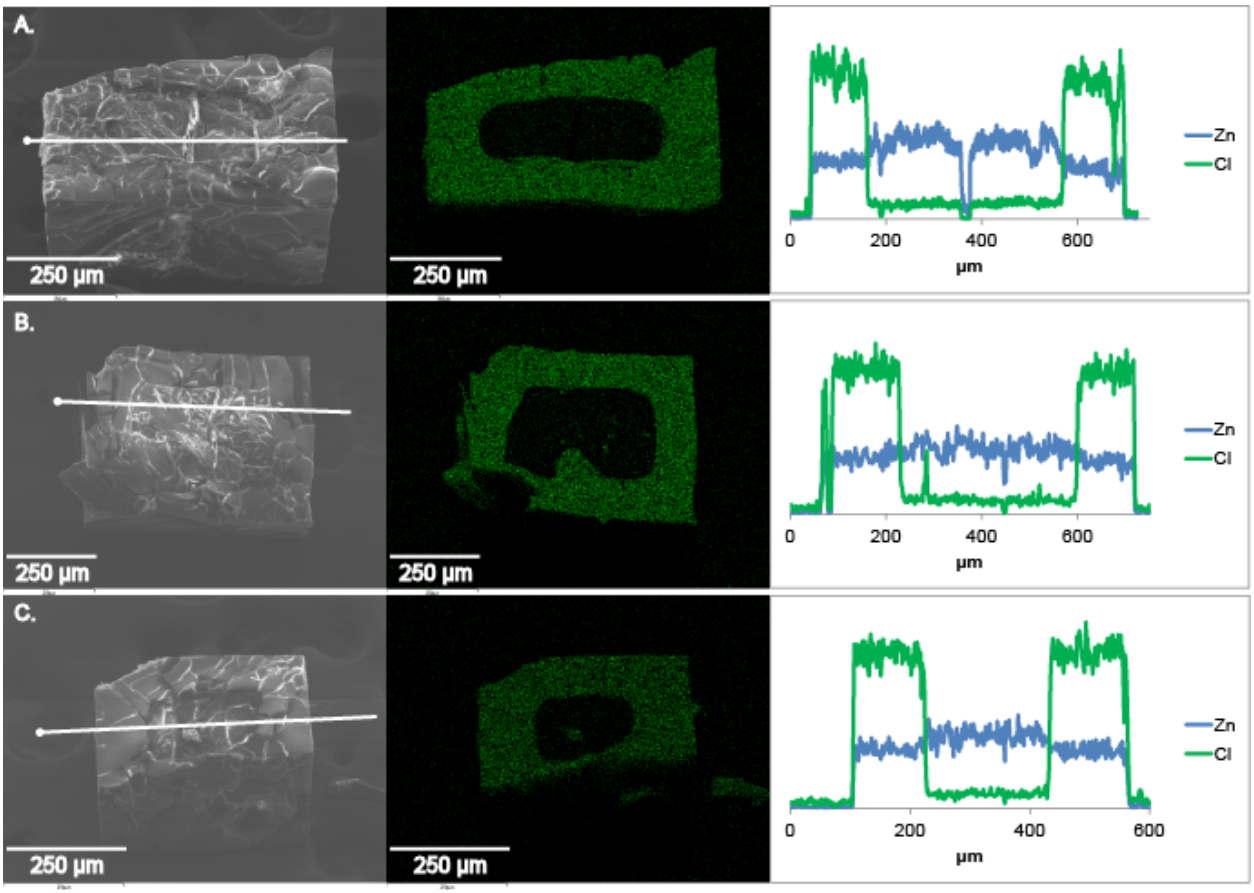

Figure C.16 SEM images, EDS maps, and EDS linescans for three trials of PSM on IRMOF-3 with chloroacetyl isocyanate for 24 hours in chloroform, resulting in a core–shell microstructure.

C.2.2 Experimental IR Kinetics Data

Reaction of chloroacetyl isocyanate and butyl anthranilate, 40 mM each:

IR spectra show that after mixing chloroacetyl isocyanate with butyl anthranilate, the isocyanate peak at 2252.5 cm^{-1} in toluene and 2254.4 cm^{-1} in chloroform disappears immediately. The urethane product peak at 1531.2 cm^{-1} in toluene and 1533.2 cm^{-1} in chloroform appears immediately.

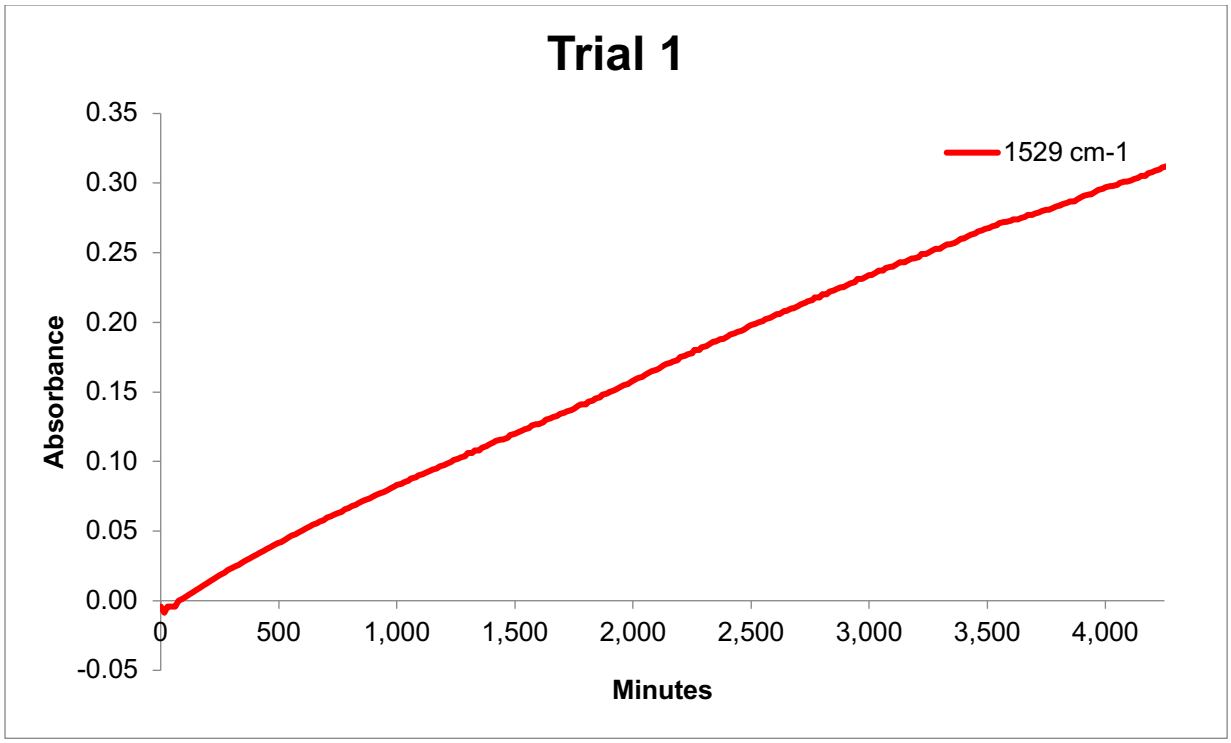

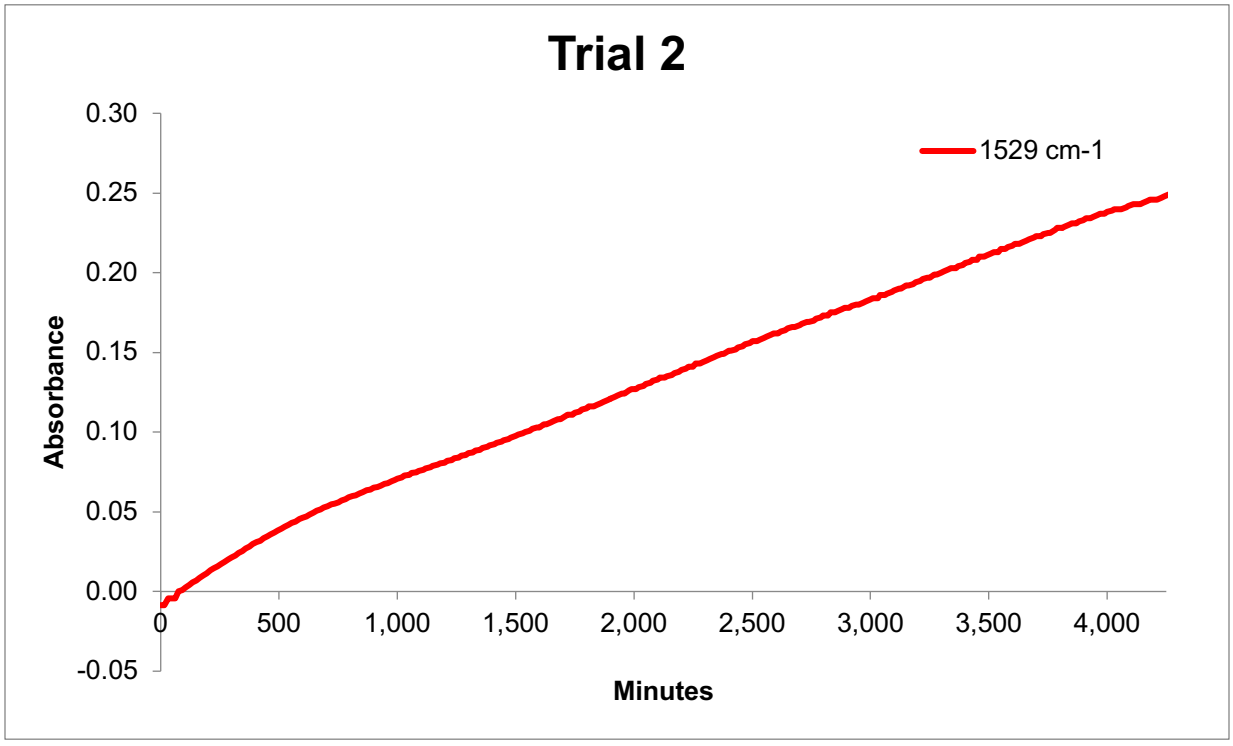

Figure C.17 FTIR kinetic measurements for the generation of product, tracked using the peak at 1529 cm^{-1}, for the reaction between butyl anthranilate and 2-chloroethyl isocyanate in toluene, 200 mM each.

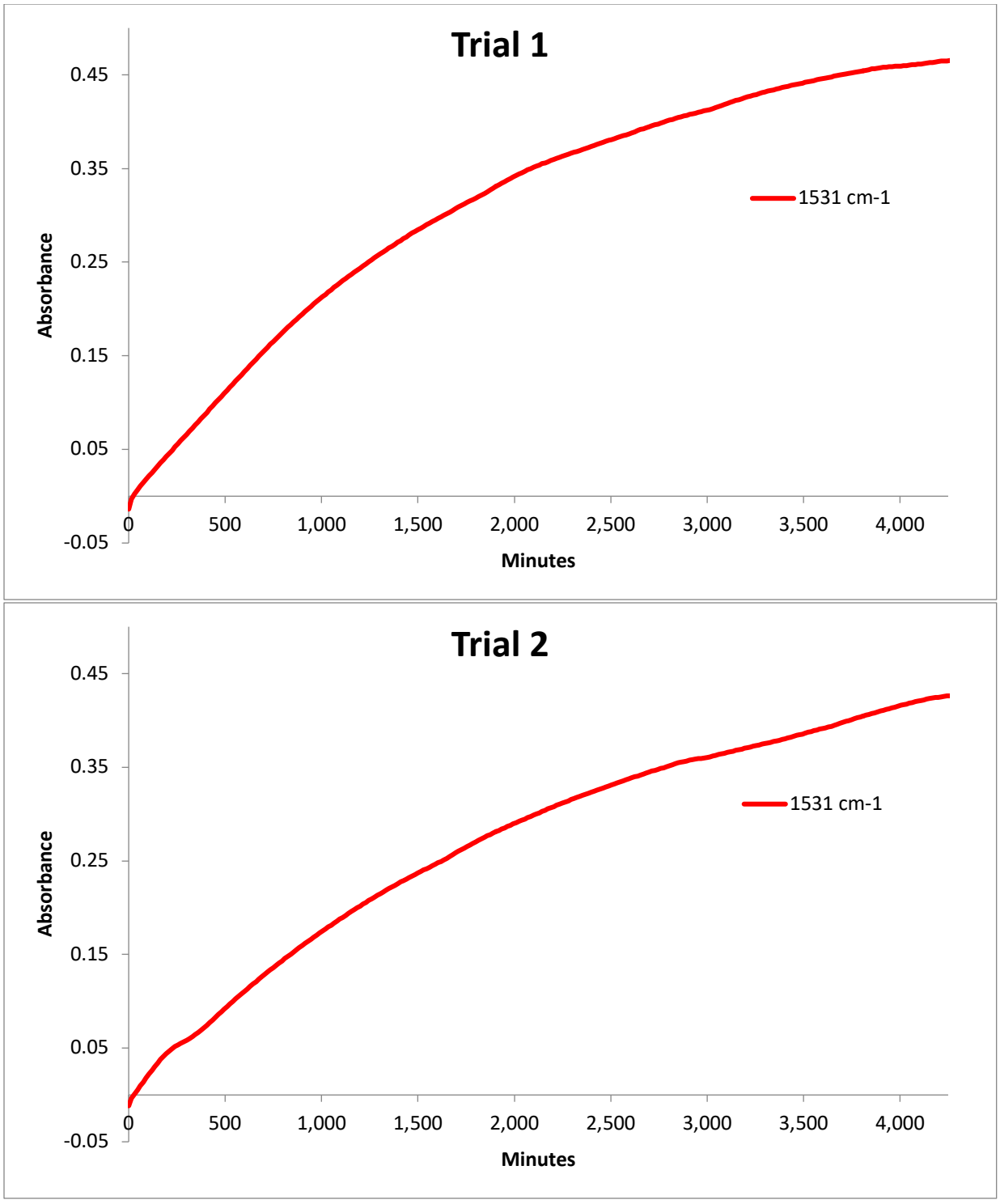

Figure C.18 FTIR kinetic measurements for the generation of product, tracked using the peak at 1531 cm^{-1}, for the reaction between butyl anthranilate and 2-chloroethyl isocyanate in chloroform, 200 mM each.

C.2.3 Experimental ^{1}H NMR Spectroscopy Data

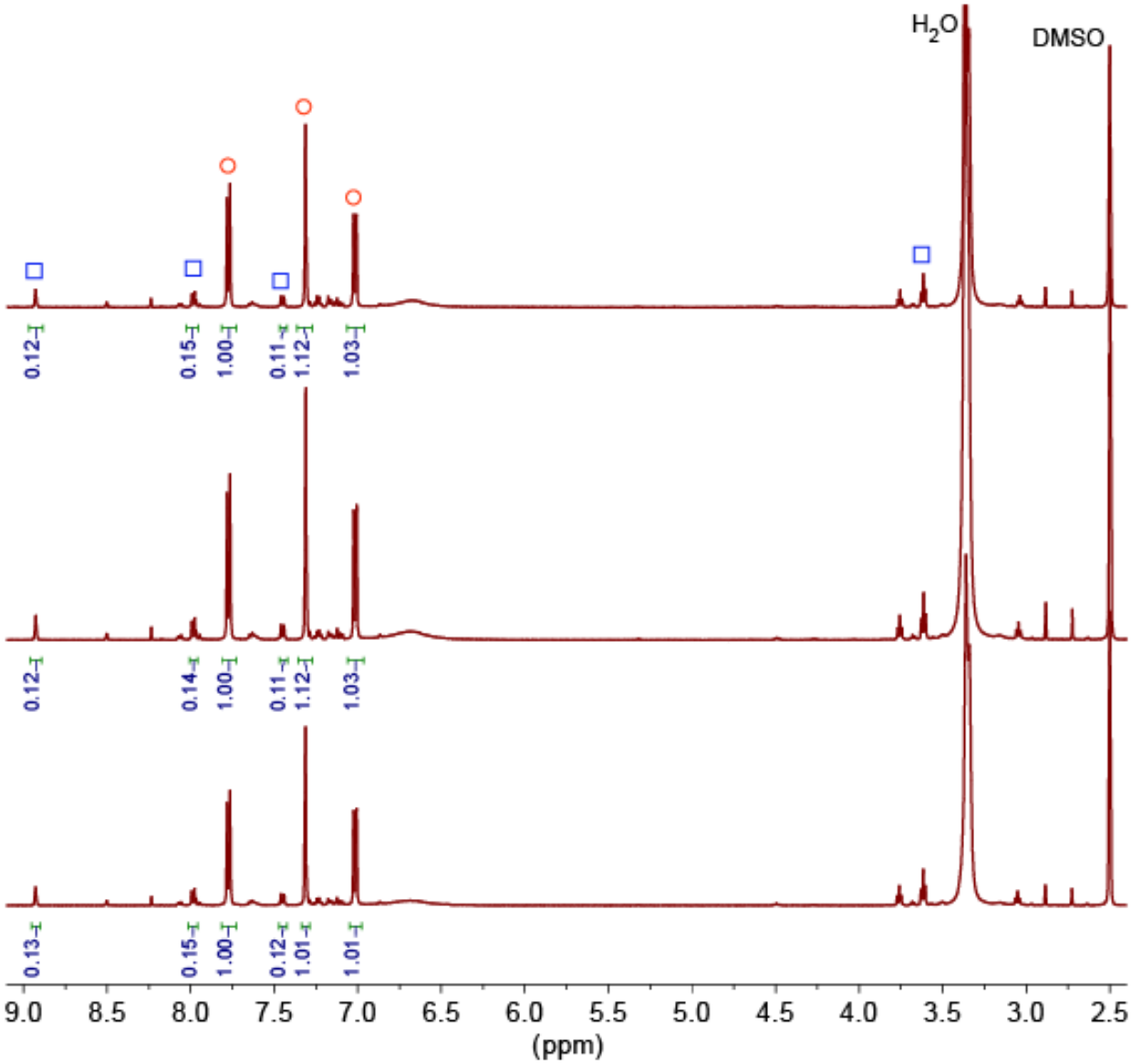

Figure C.19 ^{1}H NMR spectra for three trials of digested IRMOF-3 modified with 2-chloroethyl isocyanate in toluene for 3 h. Red circles mark peaks related to unmodified IRMOF-3, and blue squares mark peaks related to IRMOF-3 after PSM with 2-chloroethyl isocyanate. Integration values for the determination of conversion percentage are taken from peaks at 7.78 ppm for IRMOF-3 and 7.45 ppm for IRMOF-3 after PSM.

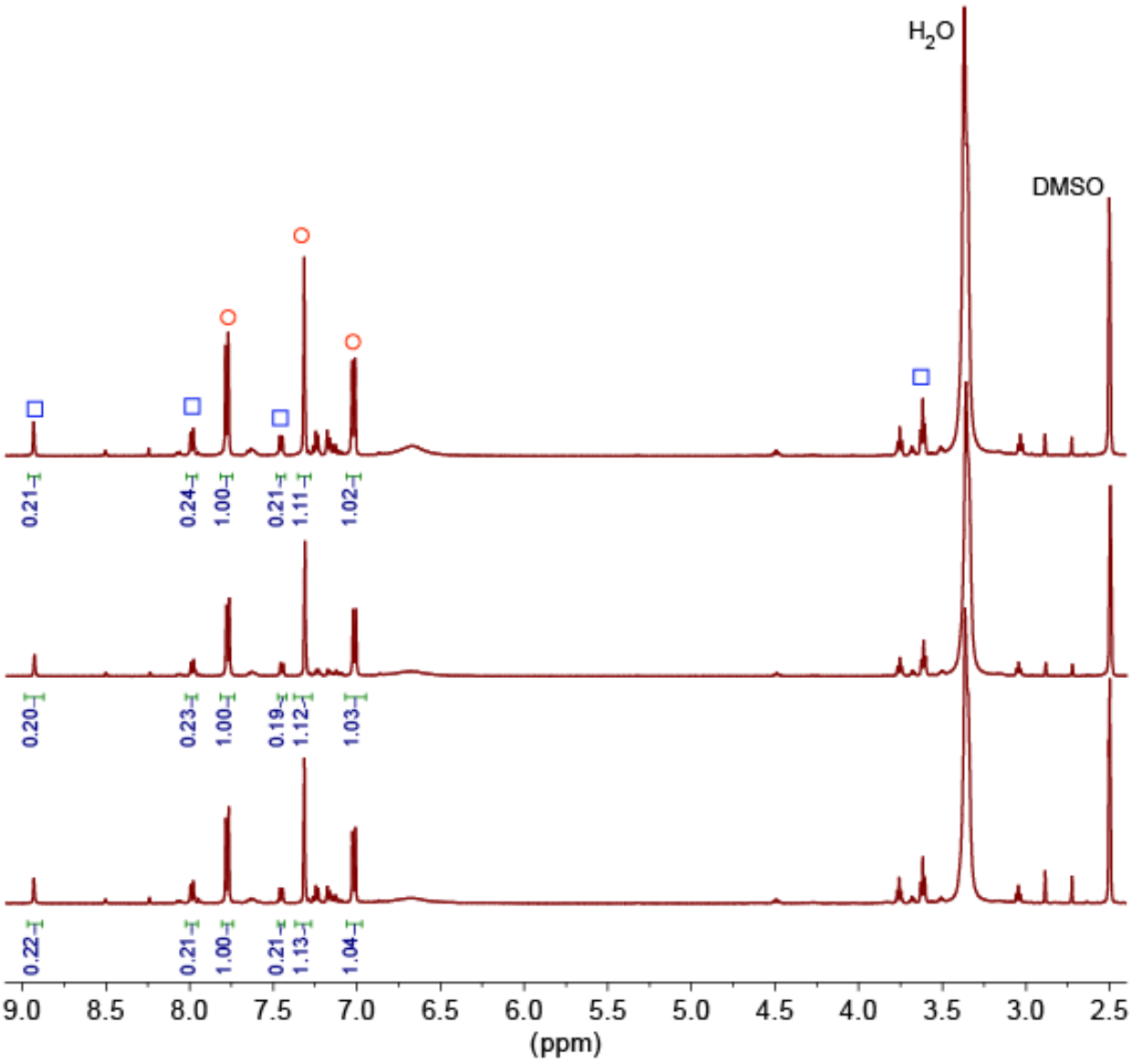

Figure C.20 ^{1}H NMR spectra for three trials of digested IRMOF-3 modified with 2-chloroethyl isocyanate in toluene for 6 h. Red circles mark peaks related to unmodified IRMOF-3, and blue squares mark peaks related to IRMOF-3 after PSM with 2-chloroethyl isocyanate. Integration values for the determination of conversion percentage are taken from peaks at 7.78 ppm for IRMOF-3 and 7.45 ppm for IRMOF-3 after PSM.

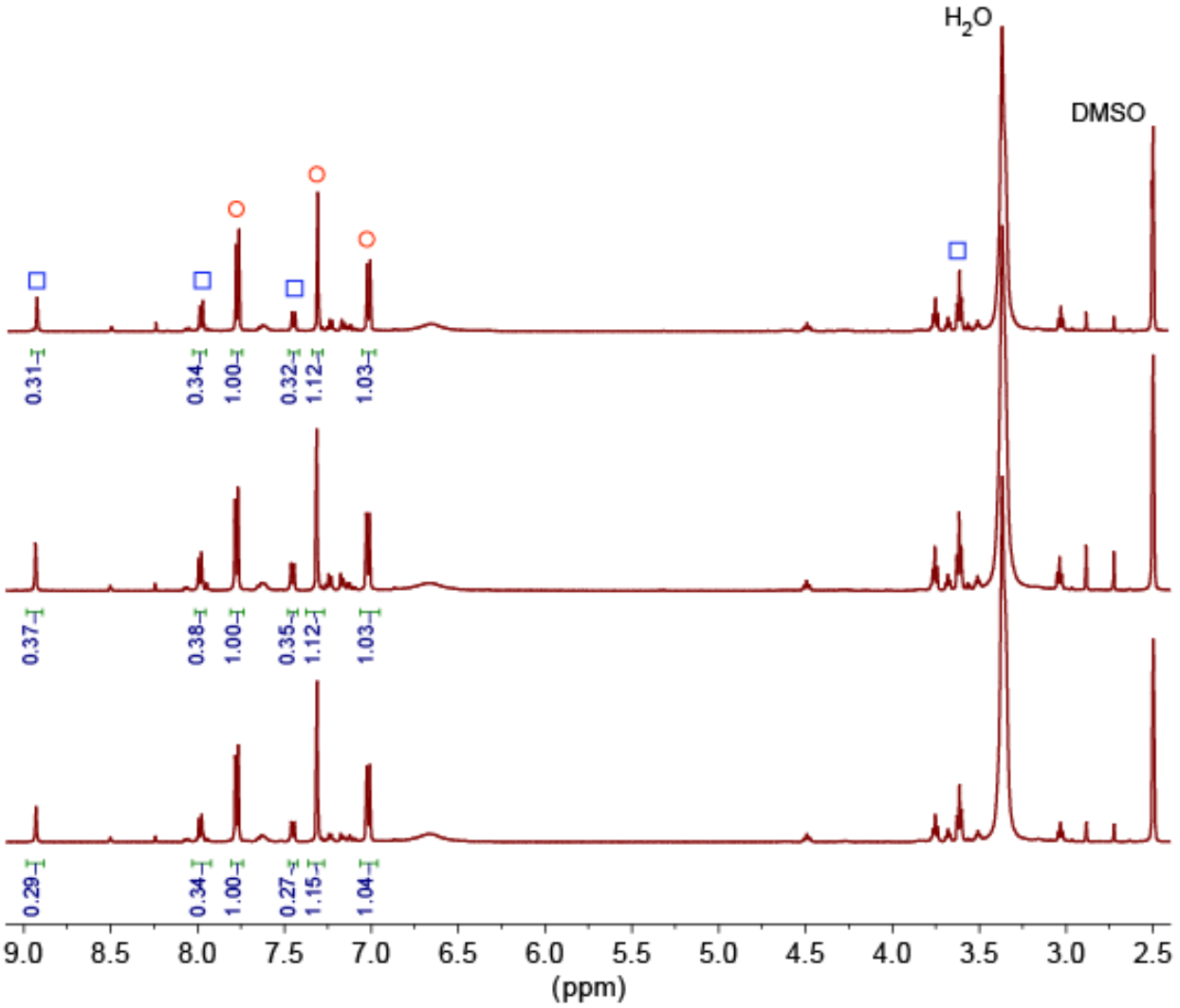

Figure C.21 ^{1}H NMR spectra for three trials of digested IRMOF-3 modified with 2-chloroethyl isocyanate in toluene for 9 h. Red circles mark peaks related to unmodified IRMOF-3, and blue squares mark peaks related to IRMOF-3 after PSM with 2-chloroethyl isocyanate. Integration values for the determination of conversion percentage are taken from peaks at 7.78 ppm for IRMOF-3 and 7.45 ppm for IRMOF-3 after PSM.

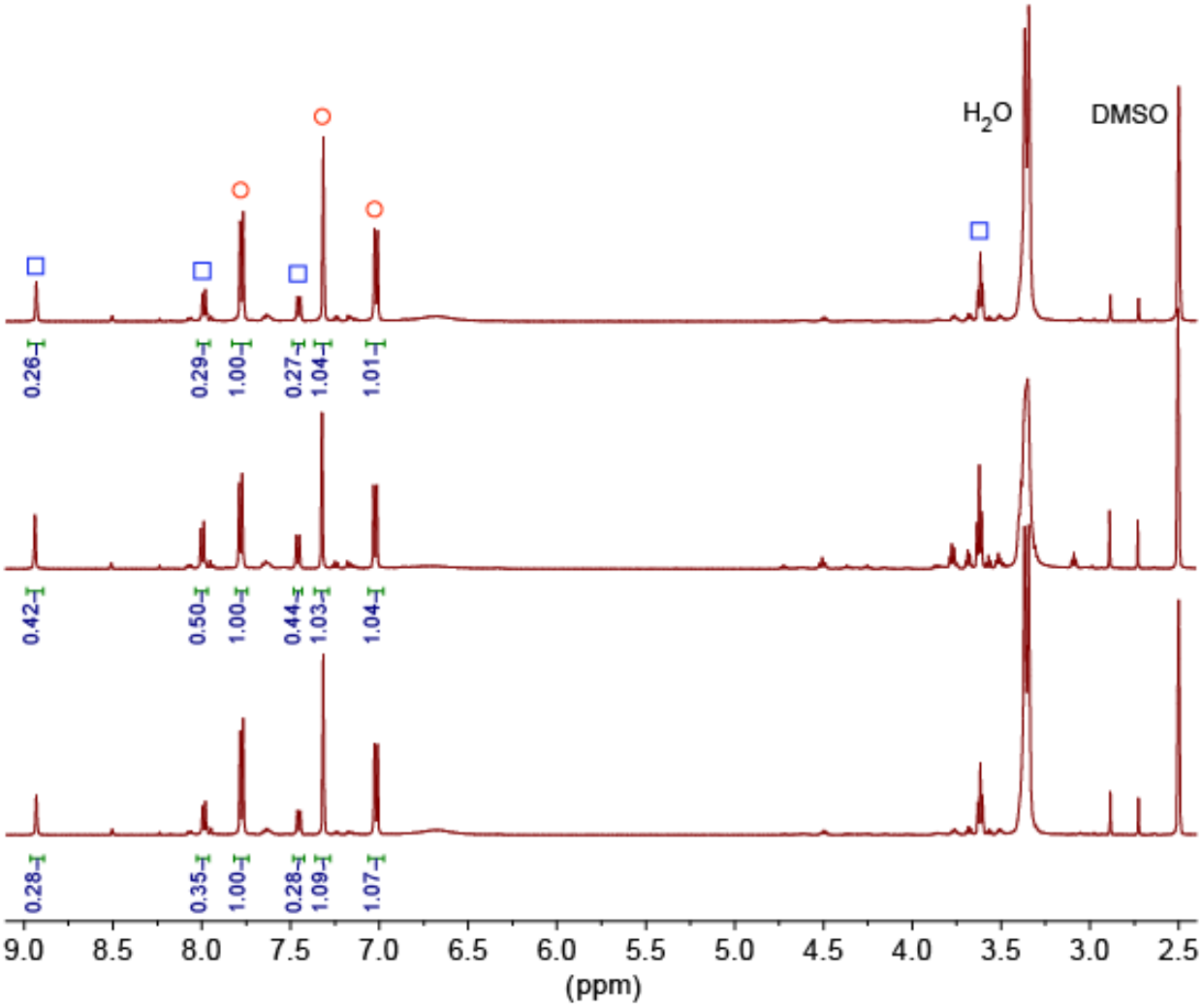

Figure C.22 ^{1}H NMR spectra for three trials of digested IRMOF-3 modified with 2-chloroethyl isocyanate in toluene for 24 h. Red circles mark peaks related to unmodified IRMOF-3, and blue squares mark peaks related to IRMOF-3 after PSM with 2-chloroethyl isocyanate. Integration values for the determination of conversion percentage are taken from peaks at 7.78 ppm for IRMOF-3 and 7.45 ppm for IRMOF-3 after PSM.

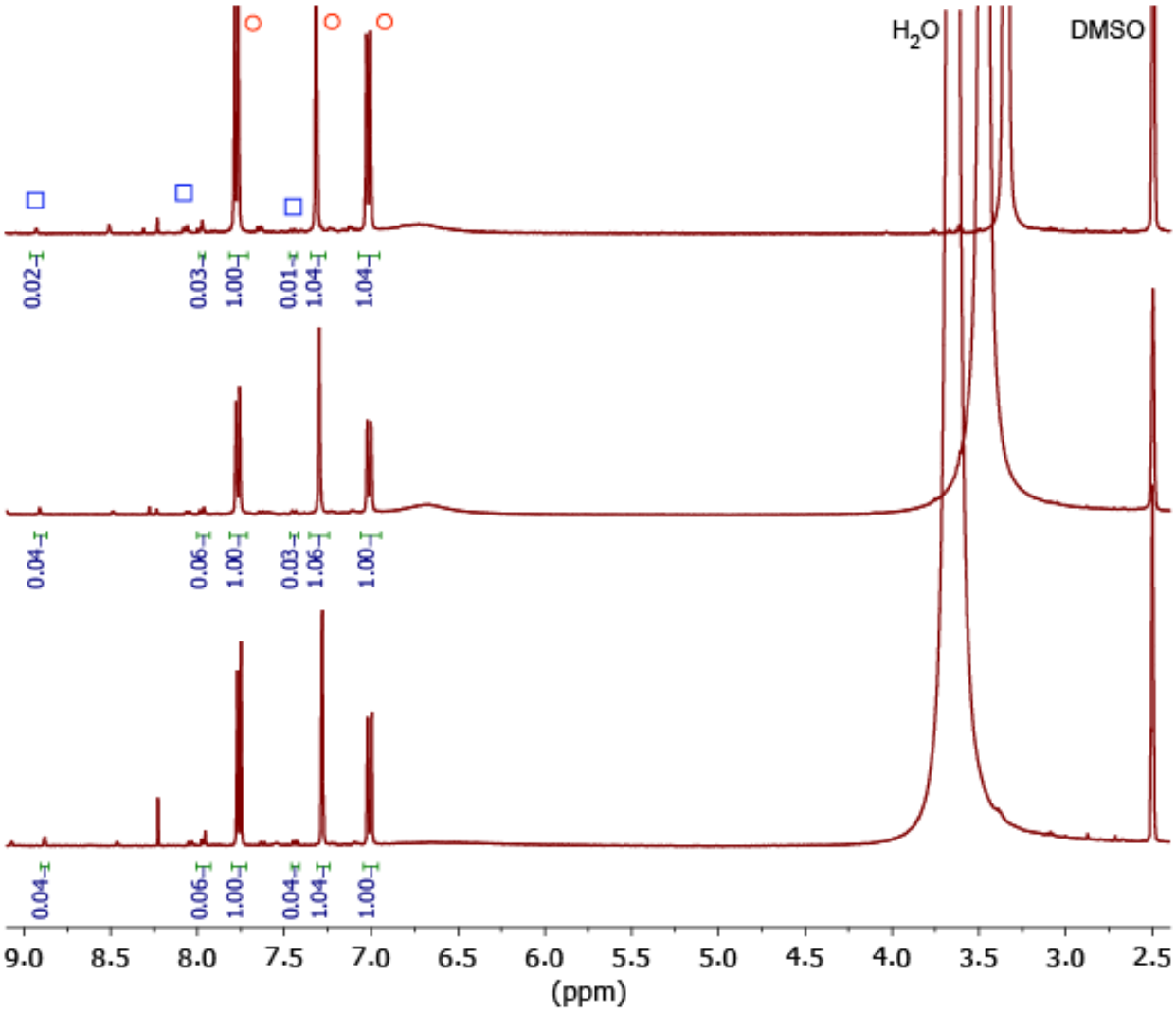

Figure C.23 ^{1}H NMR spectra for three trials of digested IRMOF-3 modified with 2-chloroethyl isocyanate in chloroform for 3 h. Red circles mark peaks related to unmodified IRMOF-3, and blue squares mark peaks related to IRMOF-3 after PSM with 2-chloroethyl isocyanate. Integration values for the determination of conversion percentage are taken from peaks at 7.78 ppm for IRMOF-3 and 7.45 ppm for IRMOF-3 after PSM.

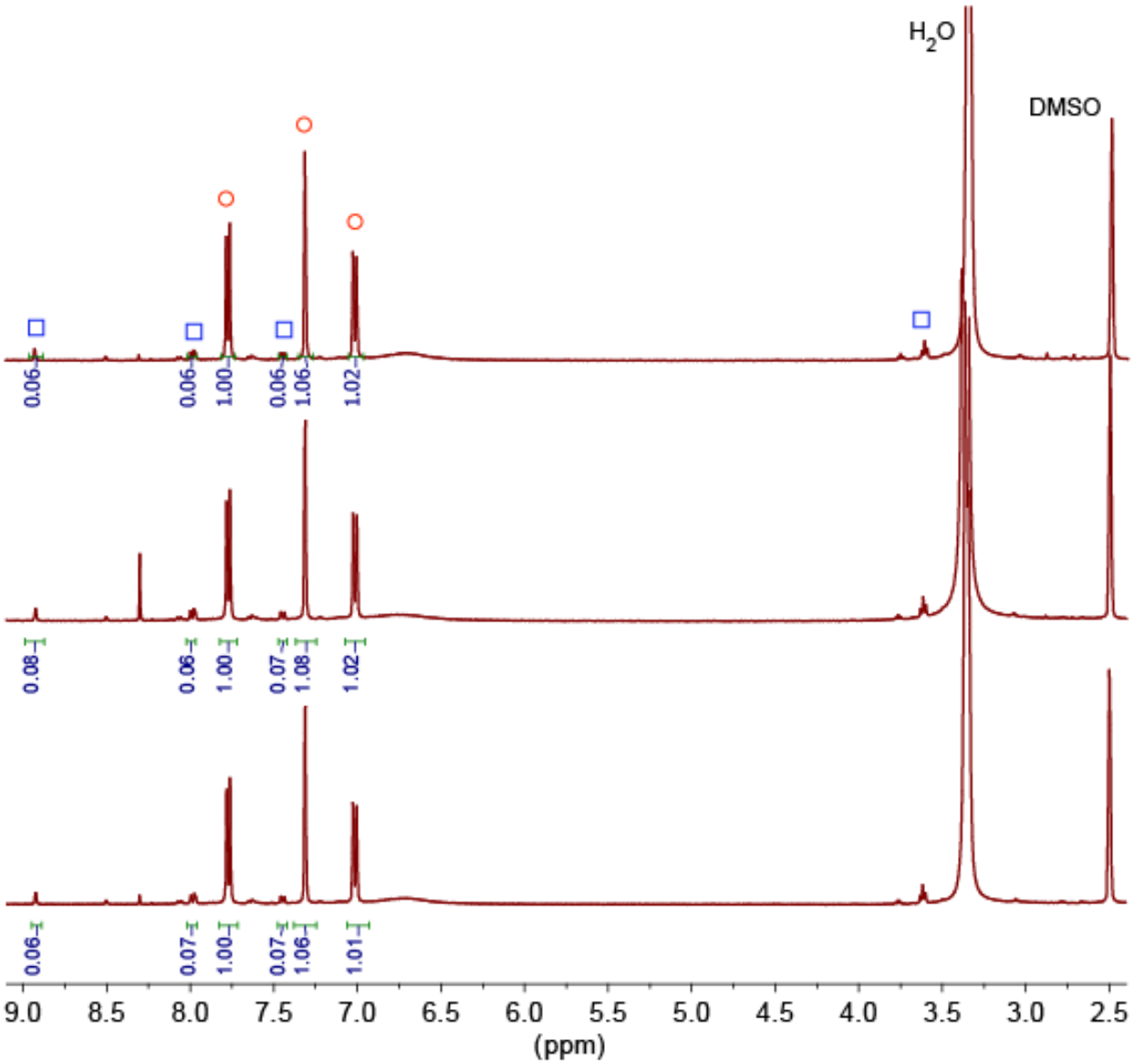

Figure C.24 ^{1}H NMR spectra for three trials of digested IRMOF-3 modified with 2-chloroethyl isocyanate in chloroform for 6 h. Red circles mark peaks related to unmodified IRMOF-3, and blue squares mark peaks related to IRMOF-3 after PSM with 2-chloroethyl isocyanate. Integration values for the determination of conversion percentage are taken from peaks at 7.78 ppm for IRMOF-3 and 7.45 ppm for IRMOF-3 after PSM.

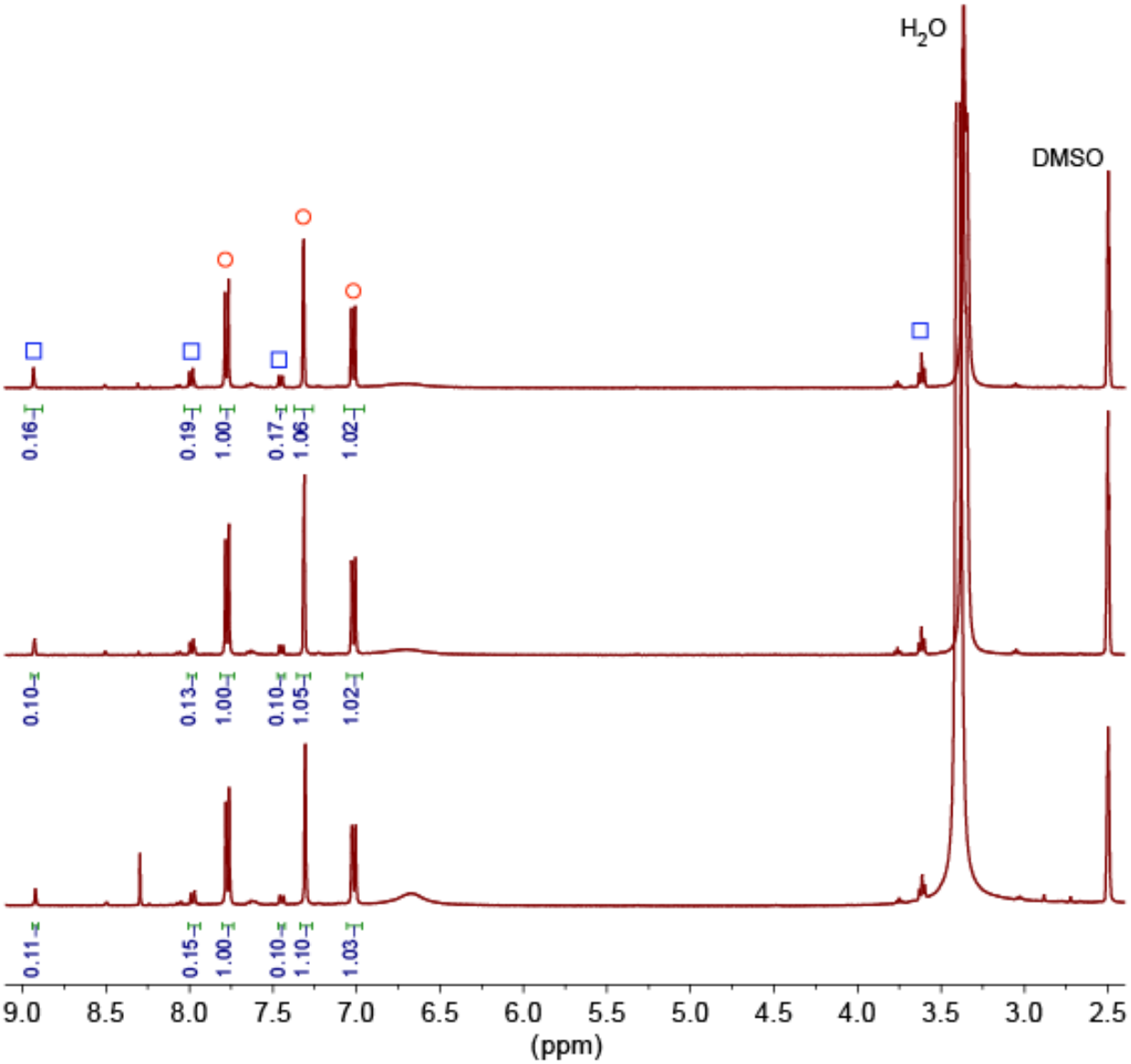

Figure C.25 ^{1}H NMR spectra for three trials of digested IRMOF-3 modified with 2-chloroethyl isocyanate in chloroform for 9 h. Red circles mark peaks related to unmodified IRMOF-3, and blue squares mark peaks related to IRMOF-3 after PSM with 2-chloroethyl isocyanate. Integration values for the determination of conversion percentage are taken from peaks at 7.78 ppm for IRMOF-3 and 7.45 ppm for IRMOF-3 after PSM.

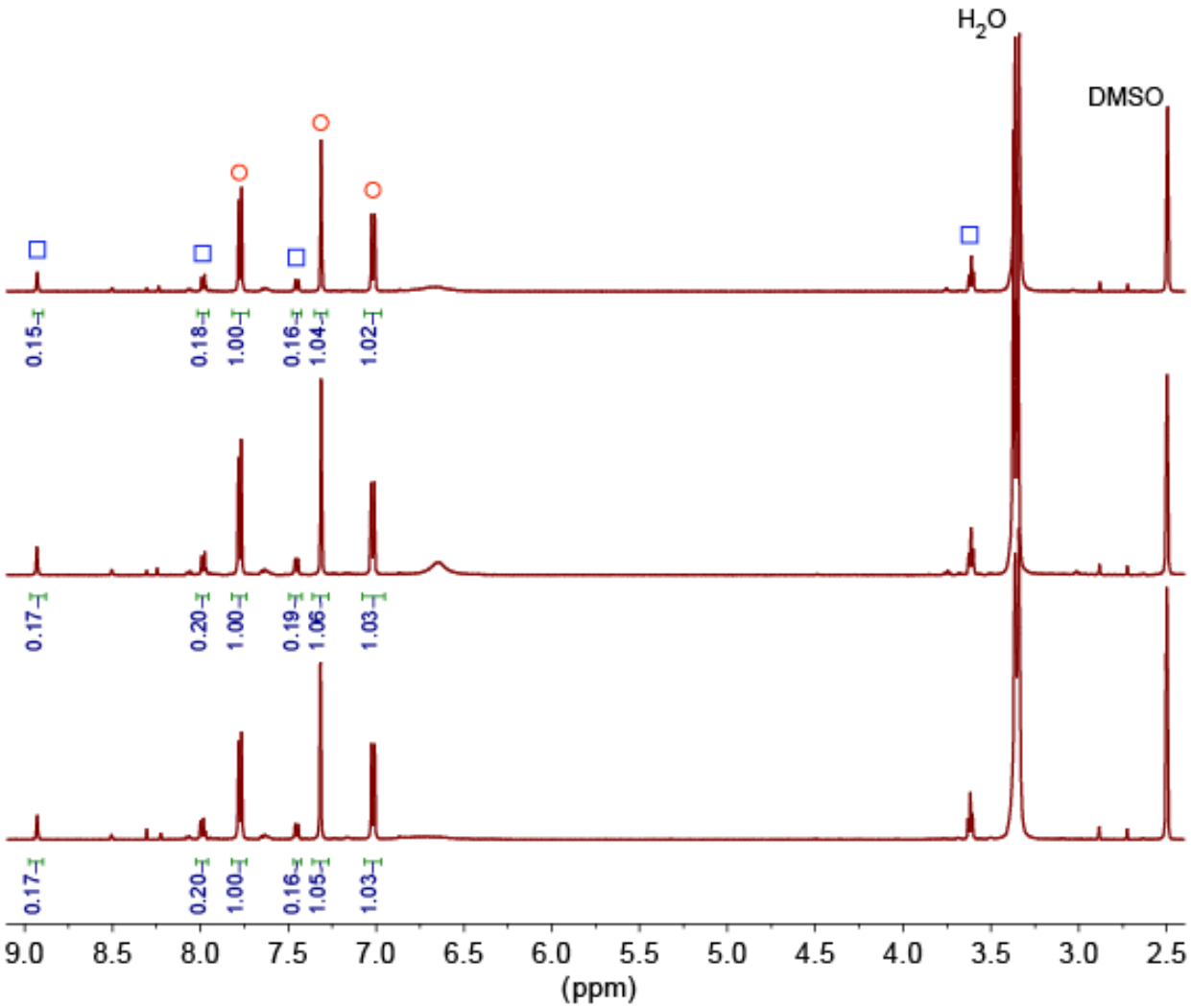

Figure C.26 ^{1}H NMR spectra for three trials of digested IRMOF-3 modified with 2-chloroethyl isocyanate in chloroform for 24 h. Red circles mark peaks related to unmodified IRMOF-3, and blue squares mark peaks related to IRMOF-3 after PSM with 2-chloroethyl isocyanate. Integration values for the determination of conversion percentage are taken from peaks at 7.78 ppm for IRMOF-3 and 7.45 ppm for IRMOF-3 after PSM.

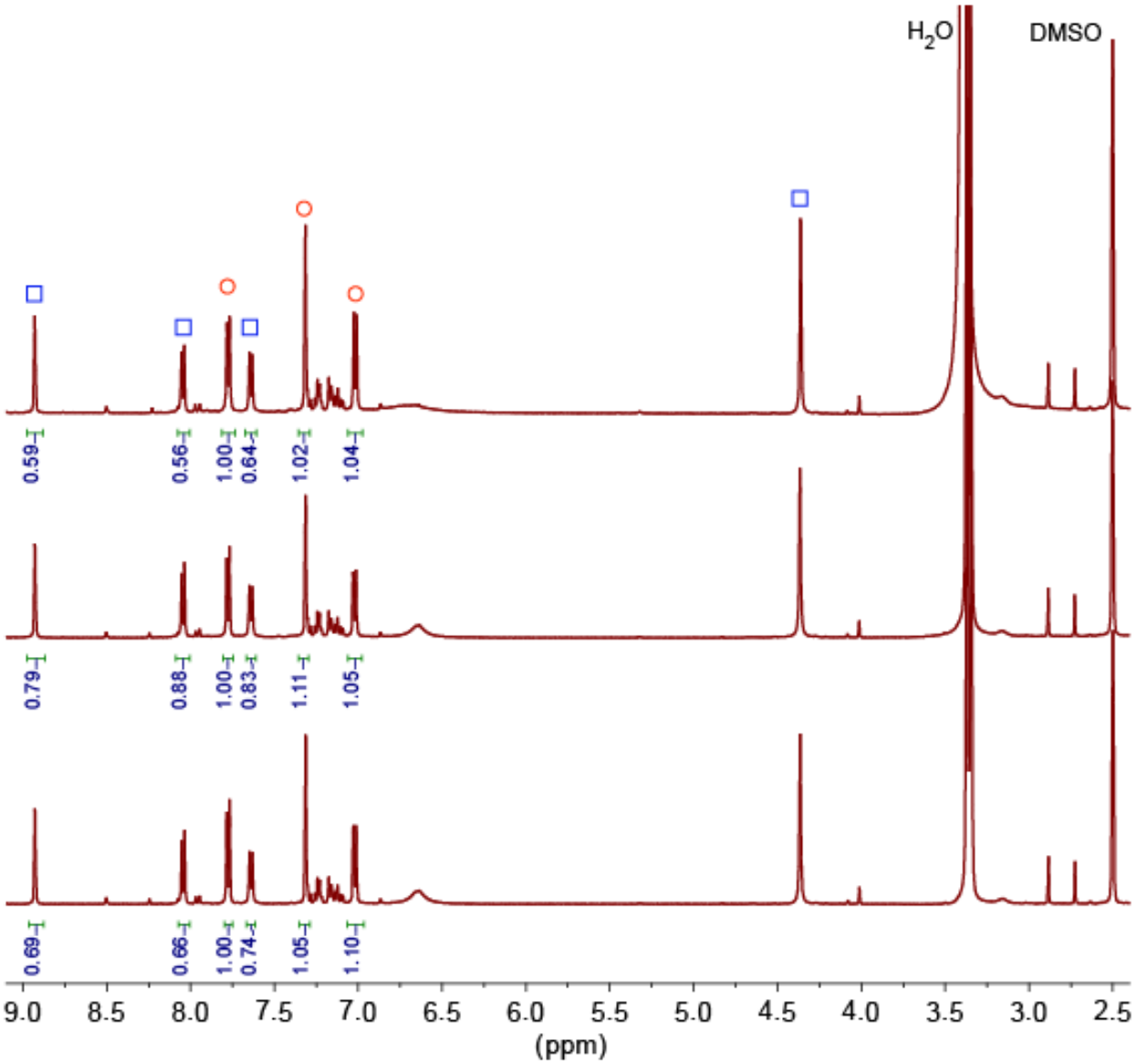

Figure C.27 ^{1}H NMR spectra for three trials of digested IRMOF-3 modified with chloroacetyl isocyanate in toluene for 3 h. Red circles mark peaks related to unmodified IRMOF-3, and blue squares mark peaks related to IRMOF-3 after PSM with chloroacetyl isocyanate. Integration values for the determination of conversion percentage are taken from peaks at 7.78 ppm for IRMOF-3 and 7.65 ppm for IRMOF-3 after PSM.

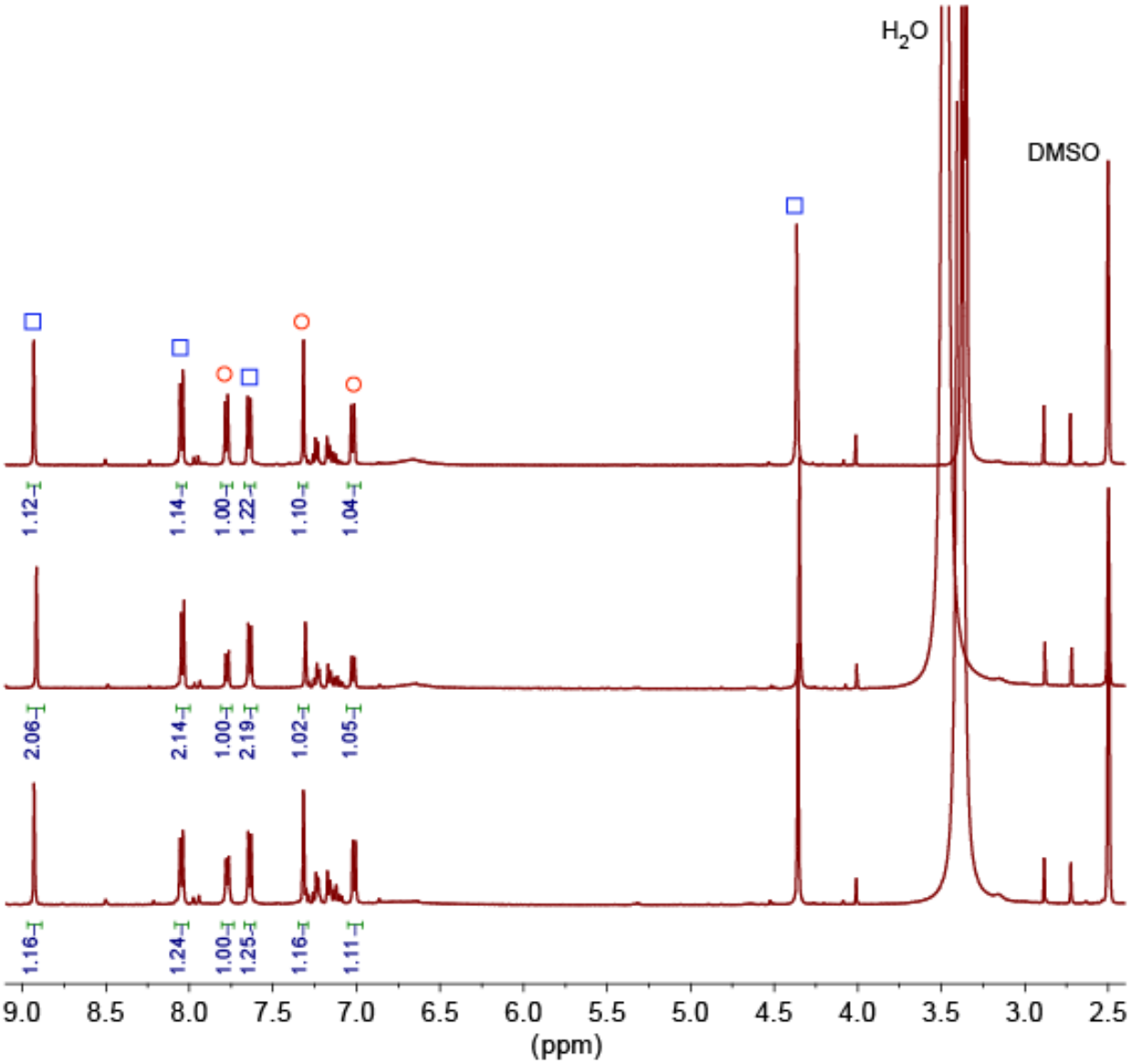

Figure C.28 ^{1}H NMR spectra for three trials of digested IRMOF-3 modified with chloroacetyl isocyanate in toluene for 6 h. Red circles mark peaks related to unmodified IRMOF-3, and blue squares mark peaks related to IRMOF-3 after PSM with chloroacetyl isocyanate. Integration values for the determination of conversion percentage are taken from peaks at 7.78 ppm for IRMOF-3 and 7.65 ppm for IRMOF-3 after PSM.

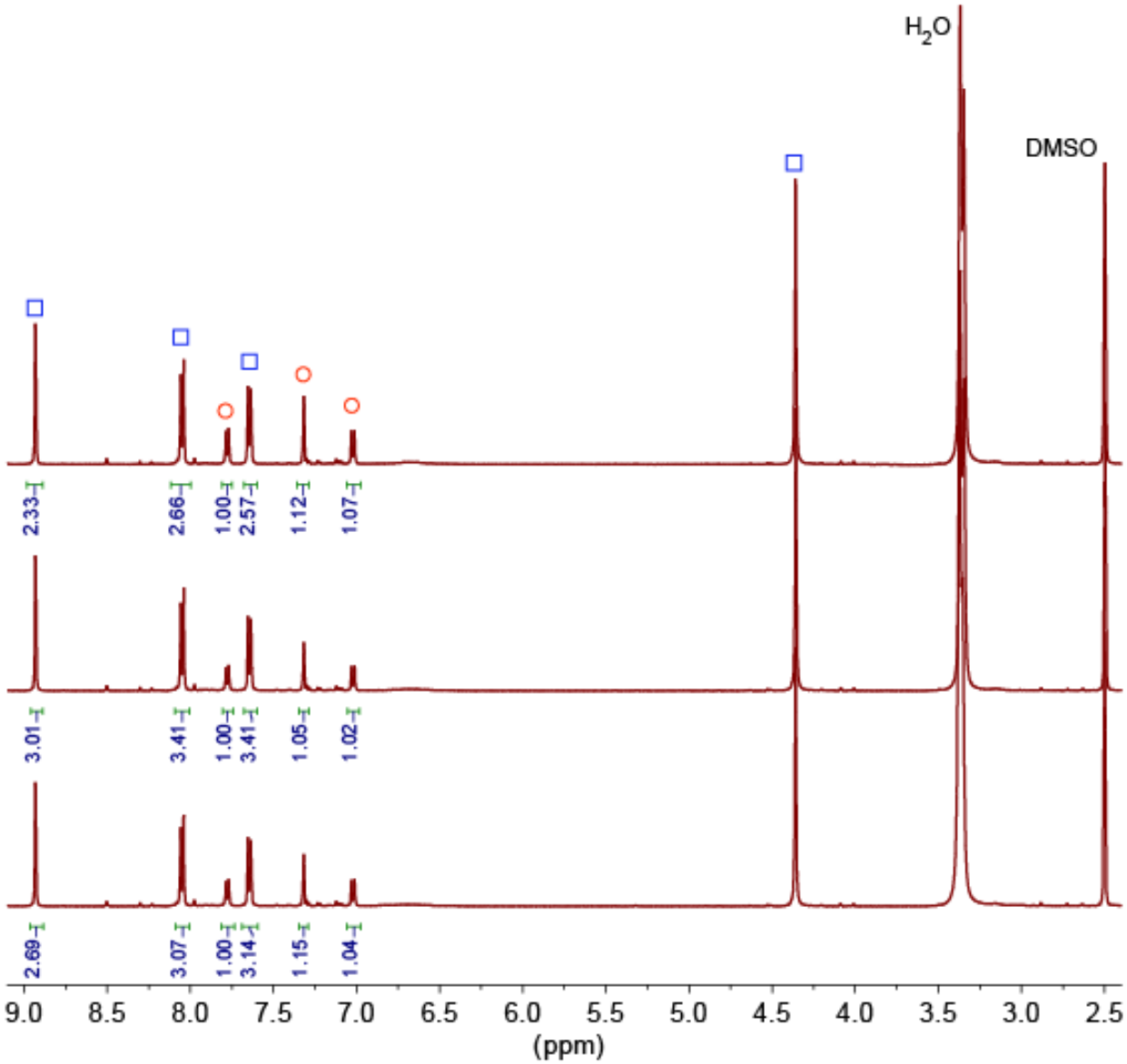

Figure C.29 ^{1}H NMR spectra for three trials of digested IRMOF-3 modified with chloroacetyl isocyanate in toluene for 9 h. Red circles mark peaks related to unmodified IRMOF-3, and blue squares mark peaks related to IRMOF-3 after PSM with chloroacetyl isocyanate. Integration values for the determination of conversion percentage are taken from peaks at 7.78 ppm for IRMOF-3 and 7.65 ppm for IRMOF-3 after PSM.

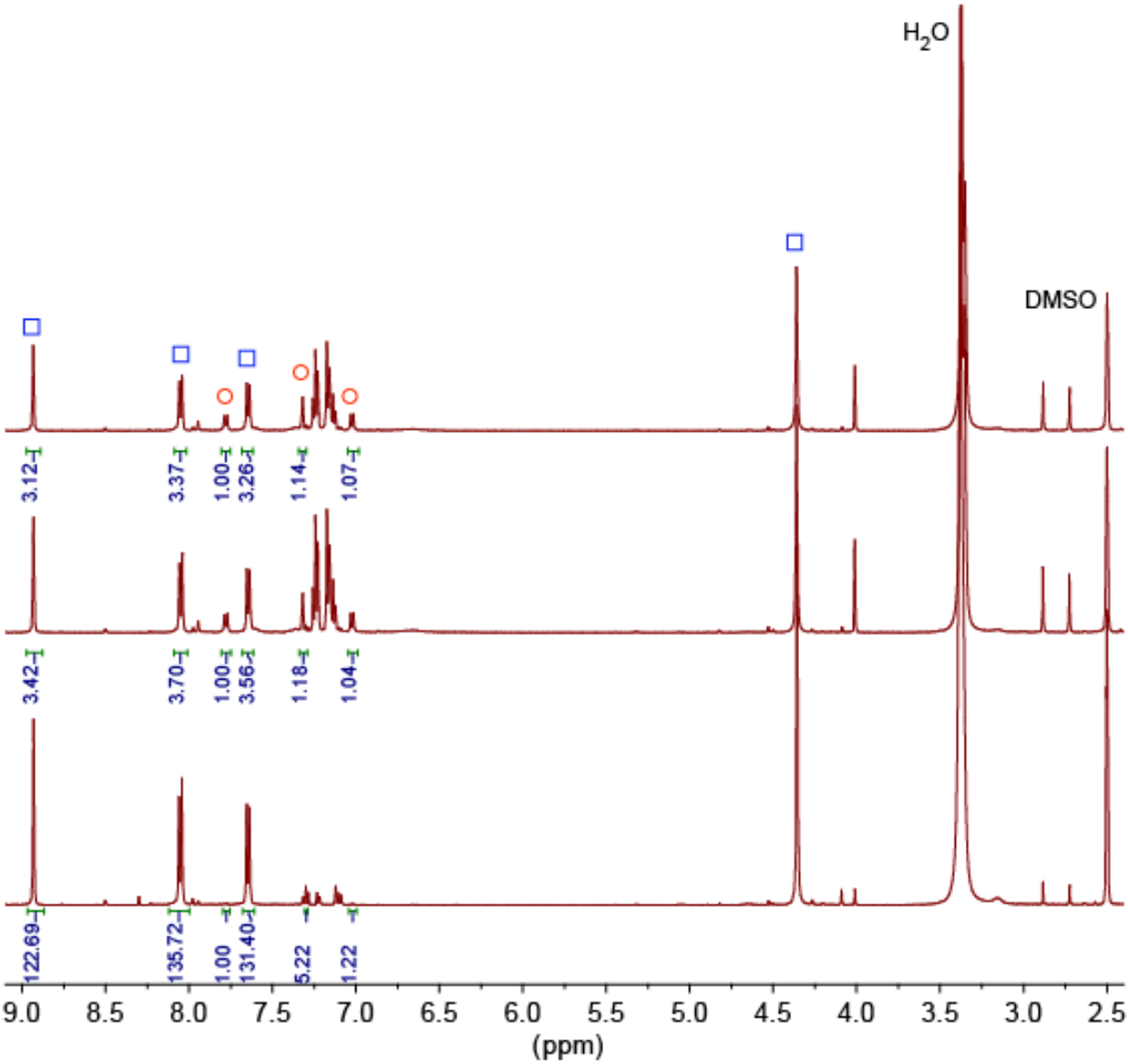

Figure C.30 ^{1}H NMR spectra for three trials of digested IRMOF-3 modified with chloroacetyl isocyanate in toluene for 24 h. Red circles mark peaks related to unmodified IRMOF-3, and blue squares mark peaks related to IRMOF-3 after PSM with chloroacetyl isocyanate. Integration values for the determination of conversion percentage are taken from peaks at 7.78 ppm for IRMOF-3 and 7.65 ppm for IRMOF-3 after PSM.

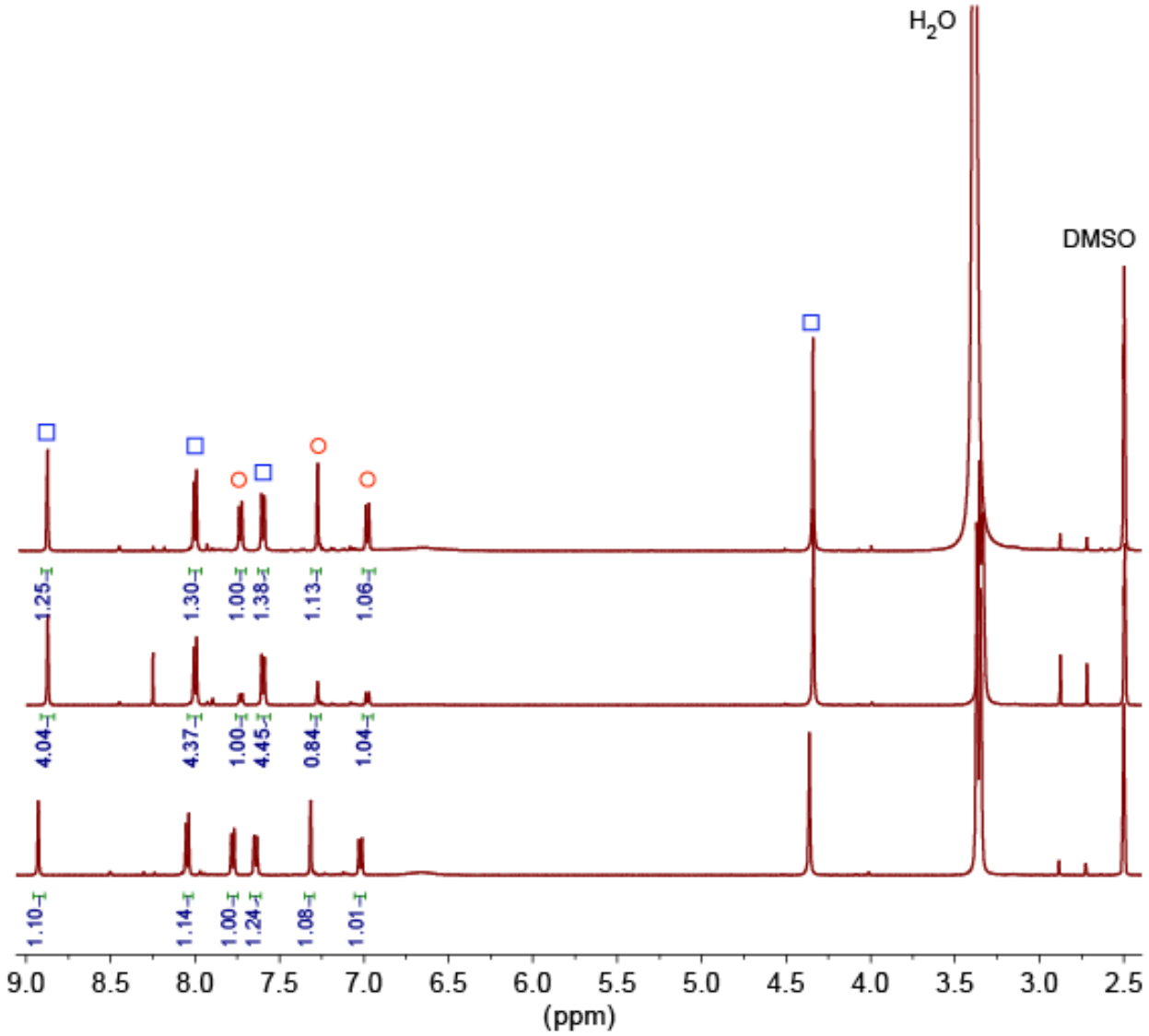

Figure C.31 ^{1}H NMR spectra for three trials of digested IRMOF-3 modified with chloroacetyl isocyanate in chloroform for 3 h. Red circles mark peaks related to unmodified IRMOF-3, and blue squares mark peaks related to IRMOF-3 after PSM with chloroacetyl isocyanate. Integration values for the determination of conversion percentage are taken from peaks at 7.78 ppm for IRMOF-3 and 7.65 ppm for IRMOF-3 after PSM.

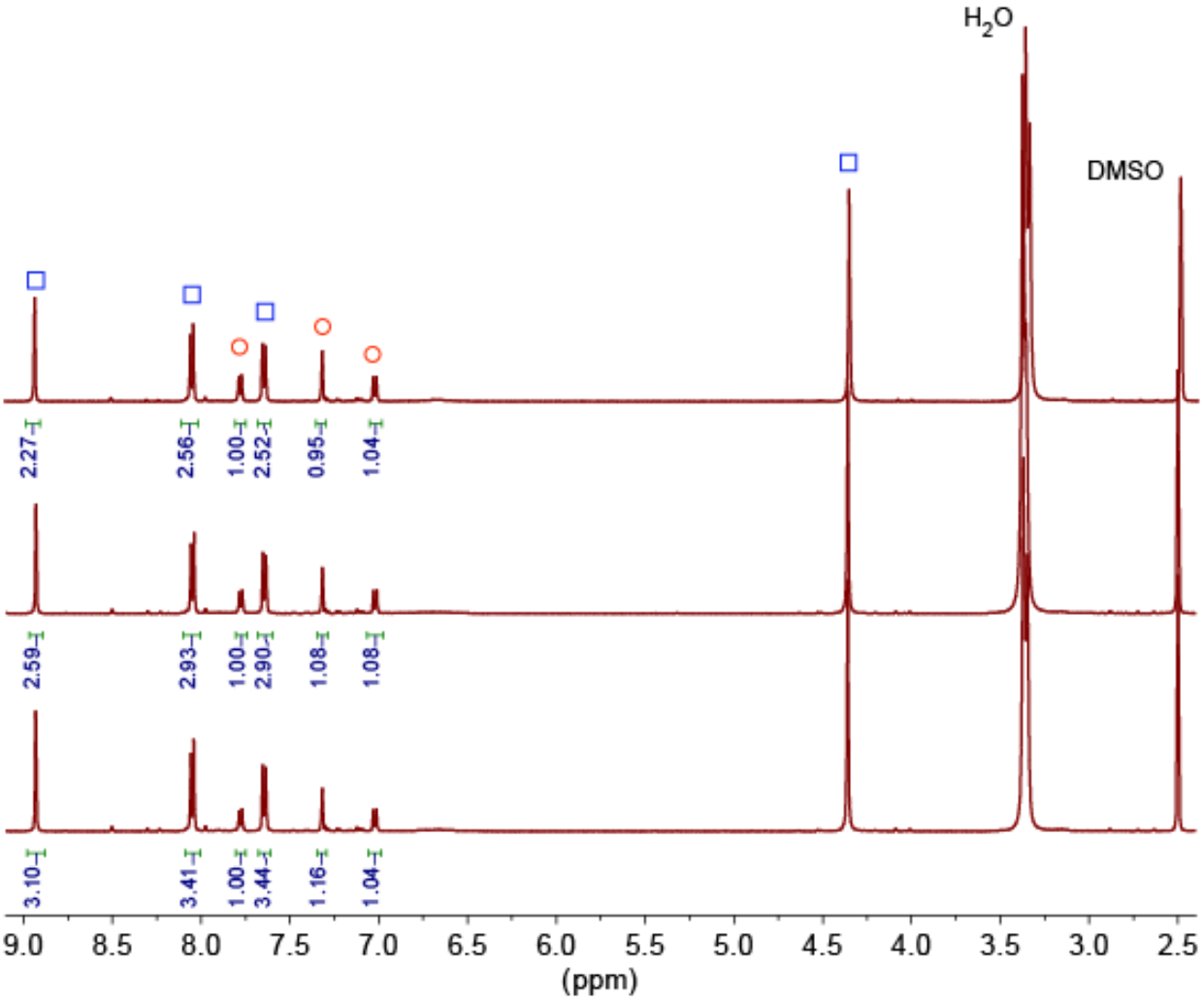

Figure C.32 ^{1}H NMR spectra for three trials of digested IRMOF-3 modified with chloroacetyl isocyanate in chloroform for 6 h. Red circles mark peaks related to unmodified IRMOF-3, and blue squares mark peaks related to IRMOF-3 after PSM with chloroacetyl isocyanate. Integration values for the determination of conversion percentage are taken from peaks at 7.78 ppm for IRMOF-3 and 7.65 ppm for IRMOF-3 after PSM.

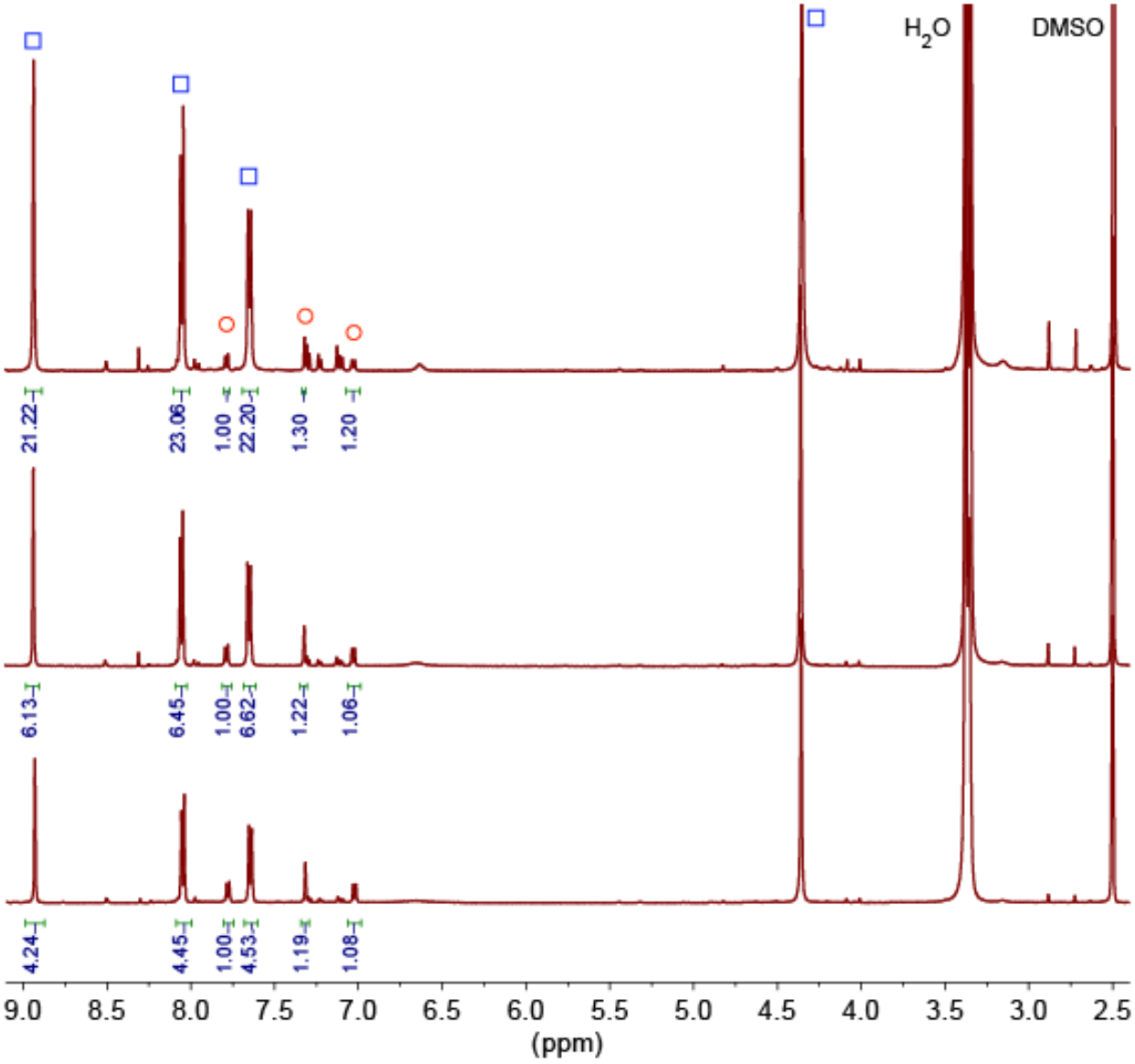

Figure C.33 ^{1}H NMR spectra for three trials of digested IRMOF-3 modified with chloroacetyl isocyanate in chloroform for 9 h. Red circles mark peaks related to unmodified IRMOF-3, and blue squares mark peaks related to IRMOF-3 after PSM with chloroacetyl isocyanate. Integration values for the determination of conversion percentage are taken from peaks at 7.78 ppm for IRMOF-3 and 7.65 ppm for IRMOF-3 after PSM.

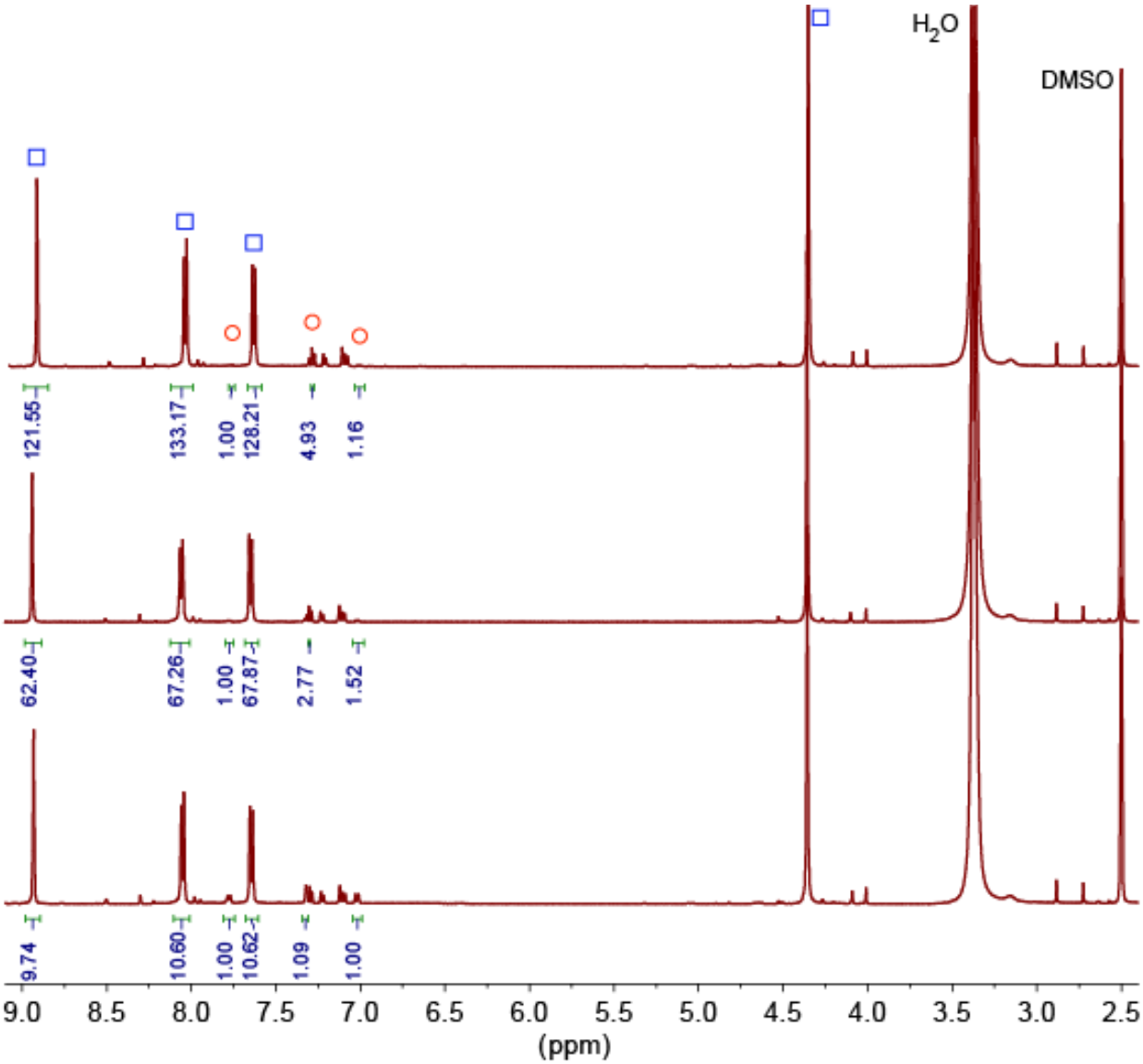

Figure C.34 ^{1}H NMR spectra for three trials of digested IRMOF-3 modified with chloroacetyl isocyanate in chloroform for 24 h. Red circles mark peaks related to unmodified IRMOF-3, and blue squares mark peaks related to IRMOF-3 after PSM with chloroacetyl isocyanate. Integration values for the determination of conversion percentage are taken from peaks at 7.78 ppm for IRMOF-3 and 7.65 ppm for IRMOF-3 after PSM.

C.2.4 Additional SEM-EDS Data

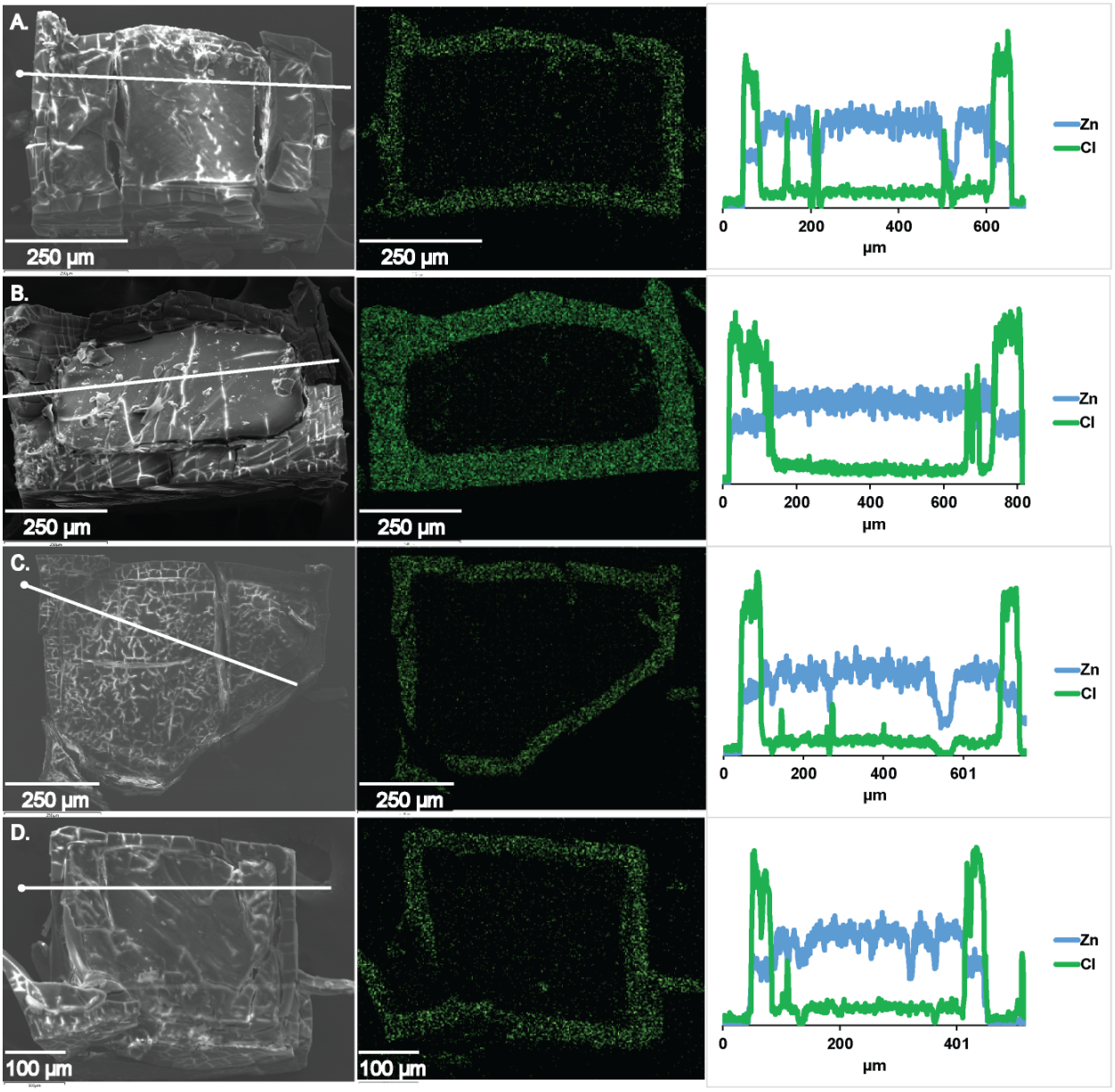

Figure C.35 SEM images, EDS maps, and EDS linescans for PSM on IRMOF-3 with chloroacetyl isocyanate in A) carbon tetrachloride for 3 hours, B) trichloroethylene for 3 hours, C) 1,2-dichloroethane for 1 hour, and D) acetonitrile for 1 hour.

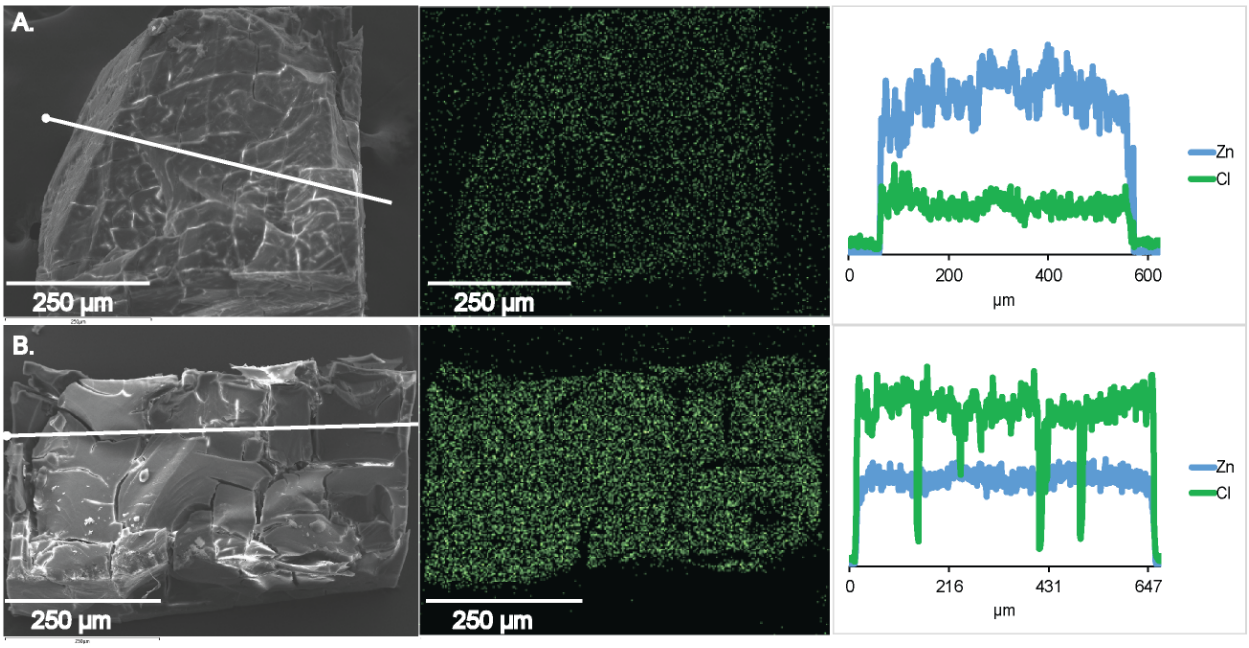

Figure C.36 SEM images, EDS maps, and EDS linescans for PSM on IRMOF-3 with 2-chloroethyl isocyanate in carbon tetrachloride for A) 1 hour and B) 48 hours.

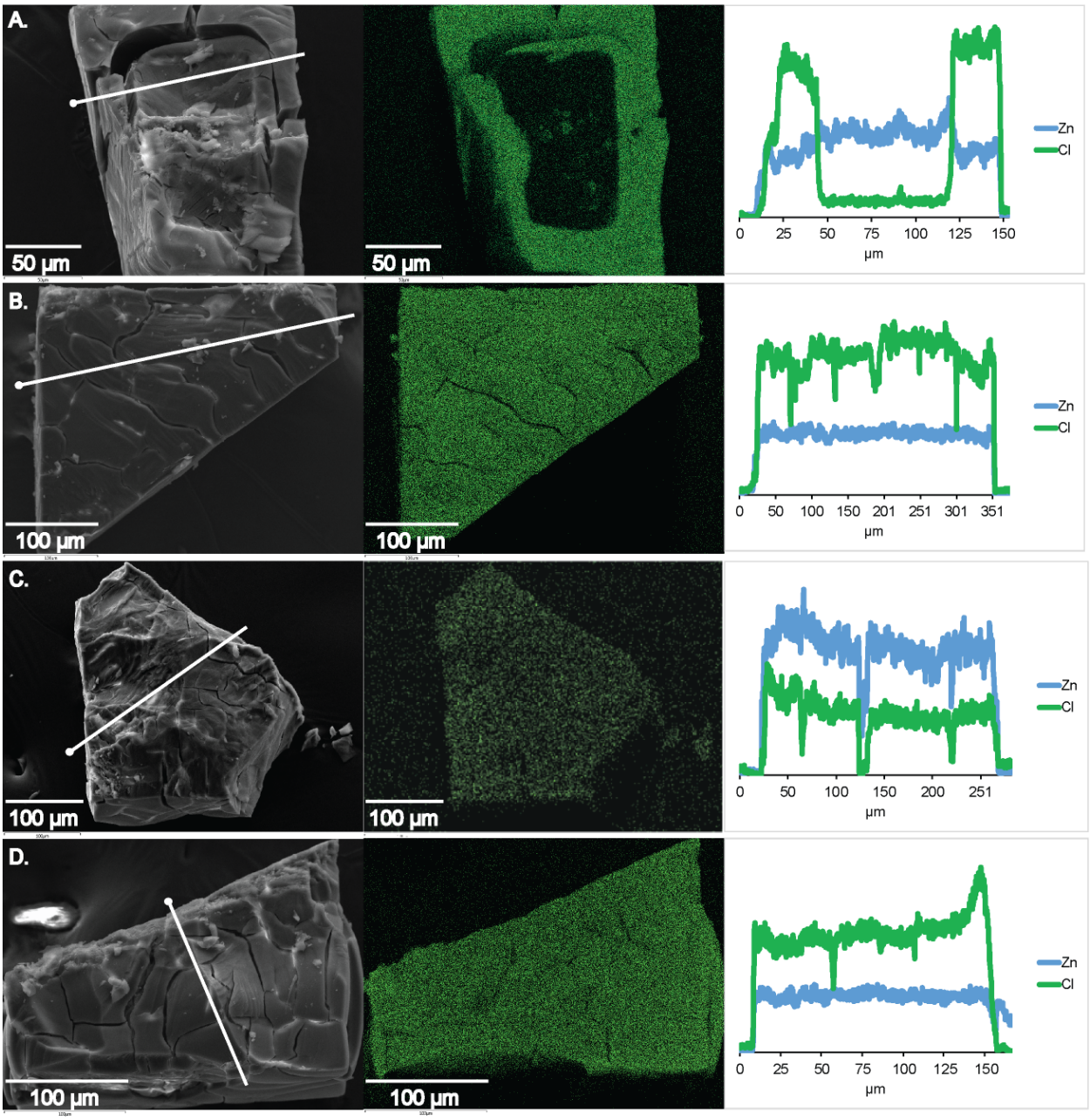

Figure C.37 SEM images, EDS maps, and EDS linescans for PSM on IRMOF-3 in chloroform overnight with A) chloroacetyl isocyanate at -18.8 °C, B) chloroacetyl isocyanate at 50 °C, C) 2-chloroethyl isocyanate at -18.8 °C, and D) 2-chloroethyl isocyanate at 50 °C.

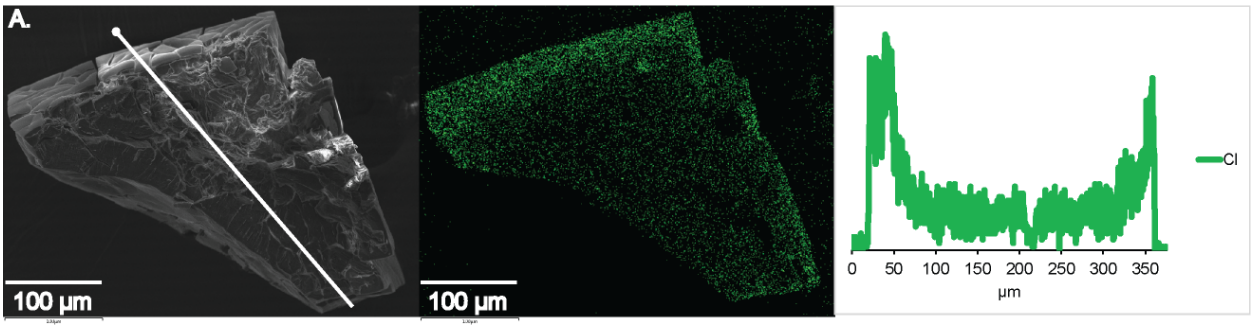

Figure C.38 An SEM image, EDS map, and EDS linescan for PSM on IRMOF-3 with 500 mM 2-chloroethyl isocyanate in chloroform for 1 hour. The zinc signal is excluded for clarity.